

STR FILE COPY

AFWAL-TR-89-3008

AD-A210 824



FATIGUE GROWTH AND CLOSURE OF SHORT CRACKS

Nagaraja S. Iyyer and Norman E. Dowling  
Virginia Polytechnic Institute and State University  
Blacksburg, Virginia 24061.

June 1989

Final Report for Period Jun 85 - Dec 88

Approved for public release; distribution unlimited

FLIGHT DYNAMICS LABORATORY  
AIR FORCE WRIGHT AERONAUTICAL LABORATORIES  
AIR FORCE SYSTEMS COMMAND  
WRIGHT-PATTERSON AIR FORCE BASE, OHIO 45433-6553

DTIC  
1989 1989  
A  
A

89

8

01

114



REPORT DOCUMENTATION PAGE

Form Approved  
OMB No. 0704-0188

1. PART SECURITY CLASSIFICATION Unclassified		1b. RESTRICTIVE MARKINGS	
2a. SECURITY CLASSIFICATION AUTHORITY		3. DISTRIBUTION/AVAILABILITY OF REPORT Approved for public release; Distribution unlimited	
2b. DECLASSIFICATION/DOWNGRADING SCHEDULE		5. MONITORING ORGANIZATION REPORT NUMBER(S) AFWAL-TR-89-3008	
4. PERFORMING ORGANIZATION REPORT NUMBER(S)		7a. NAME OF MONITORING ORGANIZATION Flight Dynamics Laboratory (AFWAL/FDSEC) AF Wright Aeronautical Laboratories	
6a. NAME OF PERFORMING ORGANIZATION Virginia Polytechnic Institute and State University	6b. OFFICE SYMBOL (if applicable)	7b. ADDRESS (City, State, and ZIP Code) Wright-Patterson AFB, OH 45433-6553	
6c. ADDRESS (City, State, and ZIP Code) Blacksburg, VA 24061		9. PROCUREMENT INSTRUMENT IDENTIFICATION NUMBER F33615-85-K-3210	
8a. NAME OF FUNDING / SPONSORING ORGANIZATION Flight Dynamics Laboratory	8b. OFFICE SYMBOL (if applicable) AFWAL/FIBEC	10. SOURCE OF FUNDING NUMBERS	
8c. ADDRESS (City, State, and ZIP Code) Wright-Patterson AFB, OH 45433-6553		PROGRAM ELEMENT NO. 61102F	PROJECT NO. 2302
		TASK NO. N1	WORK UNIT ACCESSION NO. 01
11. TITLE (Include Security Classification) FATIGUE GROWTH AND CLOSURE OF SHORT CRACKS			
12. PERSONAL AUTHOR(S) Nagaraja S. Iyyer and Norman E. Dowling			
13a. TYPE OF REPORT Final Report	13b. TIME COVERED FROM 85 Jun to 88 Dec	14. DATE OF REPORT (Year, Month, Day) 3 June 1989	15. PAGE COUNT 281
16. SUPPLEMENTARY NOTATION			
17. COSATI CODES		18. SUBJECT TERMS (Continue on reverse if necessary and identify by block number)	
FIELD	GROUP	SUB-GROUP	→ Short Cracks, Crack Closure, Fracture Mechanics, Crack Growth Rate, Stereoimaging, and Durability & Damage Toleranc
11	06		
19. ABSTRACT (Continue on reverse if necessary and identify by block number) A study has been carried out to investigate the growth and closure behavior of short cracks in 2024-T351 aluminum alloy and four different conditions of 4340 steel using through thickness cracks of straight fronts. The experiments were carried out to study the influence of stress level, stress ratio, yield strength and prior austenitic grain sizes in notched and unnotched specimens. The stereoimaging technique was developed and adapted to obtain crack closing and opening points, and also near tip displacement fields. Experimental results are presented with a general discussion. It was found that long cracks showed good correlation when analyzed in terms of effective stress intensity range. However, correlations were poor for short cracks. It was found that short cracks show less closure behavior than long cracks. The estimates of initial crack lengths based on linear elastic data were made. These estimates differed significantly from the actual initial crack lengths for completely reversed cycling tests. Suggestions have been made to the equivalent initial flaw size approach and conclusions have been drawn.			
20. DISTRIBUTION/AVAILABILITY OF ABSTRACT <input checked="" type="checkbox"/> UNCLASSIFIED/UNLIMITED <input type="checkbox"/> SAME AS RPT. <input type="checkbox"/> DTIC USERS		21. ABSTRACT SECURITY CLASSIFICATION Unclassified	
22a. NAME OF RESPONSIBLE INDIVIDUAL Capt. Christopher J. Mazur		22b. TELEPHONE (Include Area Code) 513-255-6104	22c. OFFICE SYMBOL AFWAL/FDSEC

# Contents

## 1. INTRODUCTION AND LITERATURE REVIEW

<i>1.1 RATIONALIZATION OF SHORT CRACK GROWTH</i>	2
<i>1.2 PLASTICITY AND CLOSURE</i>	5
<i>1.3 MICROSTRUCTURAL EFFECTS</i>	13
<i>1.4 OTHER FACTORS CONTRIBUTING TO 'SHORT CRACK EFFECT'</i>	15
<i>1.5 IMPORTANCE OF SHORT CRACKS IN AIRCRAFT INDUSTRY</i>	17
<i>1.6 DISCUSSION AND SIGNIFICANCE OF THE PRESENT STUDY</i>	17

## 2. EXPERIMENTAL PROGRAM

<i>2.1 MATERIALS AND HEAT TREATMENT</i>	27
<i>2.2 SPECIMENS</i>	28
<i>2.3 FATIGUE TESTS</i>	30
<i>2.4 TESTING PROCEDURE AND METHODOLOGY</i>	31

## 3. EXPERIMENTAL PROCEDURES

<i>3.1 HEAT TREATMENT</i>	43
<i>3.2 PRECRACKING</i>	46

3.3 RESIDUAL STRESSES AND ELECTROCHEMICAL POLISHING	49
3.4 STEREOIMAGING	51
<b>4. EXPERIMENTAL RESULTS</b>	
4.1 MICROSTRUCTURAL CHARACTERIZATION	79
4.2 MECHANICAL PROPERTIES	80
4.3 LONG CRACK FATIGUE TESTS	81
4.4 SHORT CRACK FATIGUE TESTS	87
4.5 SHORT CRACK FATIGUE TESTS IN NOTCHED SPECIMENS	101
<b>5. DISCUSSION</b>	
5.1 DURABILITY ANALYSIS - EQUIVALENT INITIAL FLAW SIZE	232
5.2 SHORT CRACK GROWTH UNDER GROSS PLASTIC DEFORMATION	236
5.3 RATIONALIZATION OF LONG CRACK GROWTH	240
5.4 RATIONALIZATION OF SHORT CRACK GROWTH	240
5.5 IMPLICATIONS OF FATIGUE SHORT CRACK GROWTH STUDIES	243
<b>6. SUMMARY AND CONCLUSIONS</b>	271
<b>REFERENCES</b>	275

## List of Figures

Fig. 1.1	Typical crack growth rate versus stress intensity range .....	21
Fig. 1.2	Basis of Linear Elastic Fracture Mechanics, LEFM [4]. .....	22
Fig. 1.3	Crack growth rate versus stress intensity range for short cracks [5]. ....	23
Fig. 1.4	Schematic diagram illustrating different mechanisms of closure .....	24
Fig. 1.5	Schematic diagram illustrating the residual strains in the wake of crack.	25
Fig. 2.1	Geometry of compact tension specimen of 2024-T351 aluminum. ....	39
Fig. 2.2	Specimen geometries of short crack test (SCT) specimens. ....	40
Fig. 2.3	Specimen geometry of notched specimen of aluminum. ....	41
Fig. 2.4	Geometry of single hole end configuration specimens of steel. ....	42
Fig. 3.1	Typical crack length versus cycles data for cracks growing under far field cyclic compression. ....	63
Fig. 3.2	Crack growth rate as a function of crack length. ....	64
Fig. 3.3	Schematic diagram illustrating the region of residual strains in front of the notch under far field cyclic compression. ....	65
Fig. 3.4	Thickness of the material removed as a function of time. ....	66
Fig. 3.5	Residual stresses on the surface as a function of the thickness of the material removed. ....	67
Fig. 3.6	Principle of stereoscopic viewing. ....	68
Fig. 3.7	Schematic diagram of a mirror stereoscope. ....	69
Fig. 3.8	Schematic diagram of the experimental set-up. ....	70
Fig. 3.9	Schematic diagram illustrating the principle of "floating mark.". ....	71

Fig. 3.10	Schematic diagram of the parallax bar. ....	72
Fig. 3.11	Schematic diagram illustrating the eye-brain visual relationship. ....	73
Fig. 3.12	Schematic diagram illustrating the technique of detecting crack opening point. ....	74
Fig. 3.13	Comparison of the opening levels determined by stereoimaging with Elber's [17] empirical relation in 2024-T351 aluminum alloy. ....	75
Fig. 3.14	Pictures (x86) of crack tip vicinity at minimum and maximum points of the loading cycle. ....	76
Fig. 3.15	Relative displacement in a direction perpendicular to the crack axis between the minimum and maximum points of the loading cycle corresponding to Fig. 3.14. ....	77
Fig. 3.16	Crack opening displacement as a function of crack length at maximum and opening points of the loading cycle corresponding to Fig. 3.14. ....	78
Fig. 4.1	Microstructure (x100) of low strength fine grain size condition of steel (LF). ....	109
Fig. 4.2	Microstructure (x100) of high strength fine grain size condition of steel (HF). ....	110
Fig. 4.3	Microstructure (x50) of low strength coarse grain size condition of steel (LC) ....	111
Fig. 4.4	Microstructure (x50) of high strength coarse grain size condition of steel (HC). ....	112
Fig. 4.5	Comparison of the prior austenitic grain sizes with the data reported in the literature [74]. ....	113
Fig. 4.6	Geometry of the tensile specimen. ....	114
Fig. 4.7	Crack growth rate as a function of the applied stress intensity range for LF condition of steel at $R = 0.1$ . ....	115
Fig. 4.8	Crack growth rate as a function of the applied stress intensity range for HF condition of steel at $R = 0.1$ ....	116
Fig. 4.9	Crack growth rate as a function of the applied stress intensity range for LC condition of steel at $R = 0.1$ . ....	117
Fig. 4.10	Crack growth rate as a function of the applied stress intensity range for HC condition of steel at $R = 0.1$ ....	118

Fig. 4.11	Crack growth rate as a function of the applied stress intensity range for aluminum at $R = 0.1$ .....	119
Fig. 4.12	Crack growth rate, as a function of the applied stress intensity range for LF condition of steel at $R = 0.4$ .....	120
Fig. 4.13	Crack growth rate as a function of the applied stress intensity range for HF condition of steel at $R = 0.4$ .....	121
Fig. 4.14	Crack growth rate as a function of the applied stress intensity range for LC condition of steel at $R = 0.4$ .....	122
Fig. 4.15	Crack growth rate as a function of the applied stress intensity range for HC condition of steel at $R = 0.4$ .....	123
Fig. 4.16	Crack growth rate as a function of the applied stress intensity range for aluminum at $R = 0.4$ .....	124
Fig. 4.17	Crack growth rate as a function of the applied stress intensity range for aluminum at $R = 0.7$ .....	125
Fig. 4.18	Crack growth rate as a function of the applied stress intensity range for LF condition of steel at $R = -1.0$ .....	126
Fig. 4.19	Crack growth rate as a function of the applied stress intensity range for HF condition of steel at $R = -1.0$ .....	127
Fig. 4.20	Crack growth rate as a function of the applied stress intensity range for LC condition of steel at $R = -1.0$ .....	128
Fig. 4.21	Crack growth rate as a function of the applied stress intensity range for HC condition of steel at $R = -1.0$ .....	129
Fig. 4.22	Crack growth rate as a function of the applied stress intensity range for aluminum at $R = -1.0$ .....	130
Fig. 4.23	Crack growth rate as a function of the effective stress intensity range for LF condition of steel at $R = 0.1$ .....	131
Fig. 4.24	Crack growth rate as a function of the effective stress intensity range for HF condition of steel at $R = 0.1$ .....	132
Fig. 4.25	Crack growth rate as a function of the effective stress intensity range for LC condition of steel at $R = 0.1$ .....	133
Fig. 4.26	Crack growth rate as a function of the effective stress intensity range for HC condition of steel at $R = 0.1$ .....	134
Fig. 4.27	Crack growth rate as a function of the effective stress intensity range for aluminum at $R = 0.1$ .....	135

Fig. 4.28	Crack growth rate as a function of the effective stress intensity range for LF condition of steel at $R = 0.4$ .....	136
Fig. 4.29	Crack growth rate as a function of the effective stress intensity range for HF condition of steel at $R = 0.4$ .....	137
Fig. 4.30	Crack growth rate as a function of the effective stress intensity range for LC condition of steel at $R = 0.4$ .....	138
Fig. 4.31	Crack growth rate as a function of the effective stress intensity range for HC condition of steel at $R = 0.4$ .....	139
Fig. 4.32	Crack growth rate as a function of the effective stress intensity range for aluminum at $R = 0.4$ .....	140
Fig. 4.33	Crack growth rate as a function of the effective stress intensity range for aluminum at $R = 0.7$ .....	141
Fig. 4.34	Crack growth rate as a function of the effective stress intensity range for LF condition of steel at $R = -1.0$ .....	142
Fig. 4.35	Crack growth rate as a function of the effective stress intensity range for HF condition of steel at $R = -1.0$ .....	143
Fig. 4.36	Crack growth rate as a function of the effective stress intensity range for LC condition of steel at $R = -1.0$ .....	144
Fig. 4.37	Crack growth rate as a function of the effective stress intensity range for HC condition of steel at $R = -1.0$ .....	145
Fig. 4.38	Crack growth rate as a function of the effective stress intensity range for aluminum at $R = -1.0$ .....	146
Fig. 4.39	$da/dn$ as a function of effective stress intensity range for LF condition of steel at all R ratios .....	147
Fig. 4.40	$da/dn$ as a function of effective stress intensity range for HF condition of steel at all R ratios .....	148
Fig. 4.41	$da/dn$ as a function of effective stress intensity range for LC condition of steel at all R ratios .....	149
Fig. 4.42	$da/dn$ as a function of effective stress intensity range for HC condition of steel at all R ratios .....	150
Fig. 4.43	$da/dn$ as a function of effective stress intensity range for aluminum at all R ratios .....	151
Fig. 4.44	$da/dn$ as a function of effective stress intensity range for all four conditions of steel at different R ratios. ....	152

Fig. 4.45	Growth rate of short cracks in LF condition of steel at low and high stress levels at R ratio of 0.1 .....	153
Fig. 4.46	Growth rate of short cracks in HF condition of steel at low and high stress levels at R ratio of 0.1 .....	154
Fig. 4.47	Growth rate of short cracks in LC condition of steel at low and high stress levels at R ratio of 0.1 .....	155
Fig. 4.48	Growth rate of short cracks in HC condition of steel at low and high stress levels at R ratio of 0.1 .....	156
Fig. 4.49	Growth rate of short cracks in aluminum at low and high stress levels at R ratio of 0.1 .....	157
Fig. 4.50	Growth rate of short cracks in LF condition of steel at low and high stress levels at R ratio of 0.4 .....	158
Fig. 4.51	Growth rate of short cracks in HF condition of steel at low and high stress levels at R ratio of 0.4 .....	159
Fig. 4.52	Growth rate of short cracks in LC condition of steel at low and high stress levels at R ratio of 0.4 .....	160
Fig. 4.53	Growth rate of short cracks in HC condition of steel at low and high stress levels at R ratio of 0.4 .....	161
Fig. 4.54	Growth rate of short cracks in aluminum at low and high stress levels at R ratio of 0.4 .....	162
Fig. 4.55	Growth rate of short cracks in LF condition of steel at low and high stress levels at R ratio of 0.7 .....	163
Fig. 4.56	Growth rate of short cracks in HF condition of steel at low and high stress levels at R ratio of 0.7 .....	164
Fig. 4.57	Growth rate of short cracks in LC condition of steel at low and high stress level at R ratio of 0.7 .....	165
Fig. 4.58	Growth rate of short cracks in HC condition of steel at low and high stress levels at R ratio of 0.7 .....	166
Fig. 4.59	Growth rate of short cracks in aluminum at low and high stress levels at R ratio of 0.7 .....	167
Fig. 4.60	Growth rate of short cracks in LF condition of steel at low and high stress levels at R ratio of -1.0 .....	168
Fig. 4.61	Growth rate of short cracks in HF condition of steel at low and high stress levels at R ratio of -1.0 .....	169

Fig. 4.62	Growth rate of short cracks in LC condition of steel at low and high stress level at R ratio of -1.0 .....	170
Fig. 4.63	Growth rate of short cracks in HC condition of steel at low and high stress levels at R ratio of -1.0 .....	171
Fig. 4.64	Effective stress fraction, U, as a function of crack length, a, in LF, HF, LC, and HC conditions of steel at R = 0.1 (low stress level) .....	172
Fig. 4.65	Effective stress fraction, U, as a function of crack length, a, in LF, HF, LC and HC conditions of steel at R = 0.4 (low stress level) .....	173
Fig. 4.66	Effective stress fraction, U, as a function of crack length, a, in LF, HF, LC and HC conditions of steel at R = 0.7 (low stress level) .....	174
Fig. 4.67	Effective stress fraction, U, as a function of crack length, a, in LF, HF, LC and HC conditions of steel at R = -1.0 (low stress level) .....	175
Fig. 4.68	Effective stress fraction, U, as a function of crack length, a, in aluminum at different R ratios (low stress level). .....	176
Fig. 4.69	Ratio of stress fractions, U/U', as a function of applied stress intensity range for LF condition of steel at different R ratios. ....	177
Fig. 4.70	Ratio of stress fractions, U/U', as a function of applied stress intensity range for HF condition of steel at different R ratios. ....	178
Fig. 4.71	Ratio of stress fractions, U/U', as a function of applied stress intensity range for LC condition of steel at different R ratios. ....	179
Fig. 4.72	Ratio of stress fractions, U/U', as a function of applied stress intensity range for HC condition of steel at different R ratios. ....	180
Fig. 4.73	Growth rate of short cracks at low and high stress levels as a function of effective stress intensity range in LF condition of steel at R ratio of 0.1 .....	181
Fig. 4.74	Growth rate of short cracks at low and high stress levels as a function of effective stress intensity range in HF condition of steel at R ratio of 0.1 .....	182
Fig. 4.75	Growth rate of short cracks at low and high stress levels as a function of effective stress intensity range in LC condition of steel at R ratio of 0.1. ....	183
Fig. 4.76	Growth rate of short cracks at low and high stress levels as a function of effective stress intensity range in HC condition of steel at R ratio of 0.1. ....	184
Fig. 4.77	Growth rate of short cracks at low and high stress levels as a function of effective stress intensity range in aluminum at R ratio of 0.1. ....	185

Fig. 4.78	Growth rate of short cracks at low and high stress levels as a function of effective stress intensity range in LF condition of steel at R ratio of 0.4. ....	186
Fig. 4.79	Growth rate of short cracks at low and high stress levels as a function of effective stress intensity range in HF condition of steel at R ratio of 0.4. ....	187
Fig. 4.80	Growth rate of short cracks at low and high stress levels as a function of effective stress intensity range in LC condition of steel at R ratio of 0.4. ....	188
Fig. 4.81	Growth rate of short cracks at low and high stress levels as a function of effective stress intensity range in HC condition of steel at R ratio of 0.4. ....	189
Fig. 4.82	Growth rate of short cracks at low and high stress levels as a function of effective stress intensity range in aluminum at R ratio of 0.4. ....	190
Fig. 4.83	Growth rate of short cracks at low and high stress levels as a function of effective stress intensity range in LF condition of steel at R ratio of 0.7. ....	191
Fig. 4.84	Growth rate of short cracks at low and high stress levels as a function of effective stress intensity range in HF condition of steel at R ratio of 0.7. ....	192
Fig. 4.85	Growth rate, $da/dn$ , of short cracks at low stress level as a function of effective stress intensity range in LC condition of steel at R ratio of 0.7. ....	193
Fig. 4.86	Growth rate, $da/dn$ , of short cracks at low stress level as a function of effective stress intensity range in HC condition of steel at R ratio of 0.7. ....	194
Fig. 4.87	Growth rate, $da/dn$ , of short cracks at low and high stress levels as a function of effective stress intensity range in aluminum at R ratio of 0.7. ....	195
Fig. 4.88	Growth rate of short cracks at low and high stress levels as a function of effective stress intensity range in LF condition of steel at R ratio of -1.0. ....	196
Fig. 4.89	Growth rate of short cracks at low and high stress levels as a function of effective stress intensity range in HF condition of steel at R ratio of -1.0. ....	197
Fig. 4.90	Growth rate of short cracks at low and high stress levels as a function of effective stress intensity range in LC condition of steel at R ratio of -1.0. ....	198

Fig. 4.91	Growth rate, $da/dn$ , of short cracks at low stress level as a function of effective stress intensity range in HC condition of steel at R ratio of -1.0. ....	199
Fig. 4.92	Growth rate of short cracks at different R ratios as a function of effective stress intensity range in LF condition of steel. ....	200
Fig. 4.93	Growth rate of short cracks at different R ratios as a function of effective stress intensity range in HF condition of steel. ....	201
Fig. 4.94	Growth rate of short cracks at different R ratios as a function of effective stress intensity range in LC condition of steel. ....	202
Fig. 4.95	Growth rate of short cracks at different R ratios as a function of effective stress intensity range in HC condition of steel. ....	203
Fig. 4.96	Growth rate of short cracks at different R ratios as a function of effective stress intensity range in aluminum. ....	204
Fig. 4.97	Relative in-plane displacements in the direction perpendicular to the crack axis at R = 0.1 in LF condition of steel. ....	205
Fig. 4.98	Relative in-plane displacements in the direction perpendicular to the crack axis at R = -1.0 in LF condition of steel. ....	206
Fig. 4.99	Relative in-plane displacements in the direction perpendicular to the crack axis at R = 0.1 in HF condition of steel. ....	207
Fig. 4.100	Relative in-plane displacements in the direction perpendicular to the crack axis at R = 0.1 in HF condition of steel. ....	208
Fig. 4.101	Relative in-plane displacements in the direction perpendicular to the crack axis at R = 0.1 in LC condition of steel. ....	209
Fig. 4.102	Relative in-plane displacements in the direction perpendicular to the crack axis at R = 0.4 in LC condition of steel. ....	210
Fig. 4.103	Relative in-plane displacements in the direction perpendicular to the crack axis at R = 0.1 in HC condition of steel. ....	211
Fig. 4.104	Relative in-plane displacements in the direction perpendicular to the crack axis at R = 0.4 in HC condition of steel. ....	212
Fig. 4.105	Relative in-plane displacements in the direction perpendicular to the crack axis at R = 0.1 in aluminum. ....	213
Fig. 4.106	Relative in-plane displacements in the direction perpendicular to the crack axis at R = 0.4 in aluminum. ....	214

Fig. 4.107	Crack opening displacements corresponding to Fig. 4.97 at maximum and opening points of the loading cycle. ....	215
Fig. 4.108	Crack opening displacements corresponding to Fig. 4.98 at maximum and opening points of the loading cycle. ....	216
Fig. 4.109	Crack opening displacements corresponding to Fig. 4.99 at maximum and opening points of the loading cycle. ....	217
Fig. 4.110	Crack opening displacements corresponding to Fig. 4.100 at maximum and opening points of the loading cycle. ....	218
Fig. 4.111	Crack opening displacements corresponding to Fig. 4.101 at maximum and opening points of the loading cycle. ....	219
Fig. 4.112	Crack opening displacements corresponding to Fig. 4.102 at maximum and opening points of the loading cycle. ....	220
Fig. 4.113	Crack opening displacements corresponding to Fig. 4.103 at maximum and opening points of the loading cycle. ....	221
Fig. 4.114	Crack opening displacements corresponding to Fig. 4.97 at maximum and opening points of the loading cycle. ....	222
Fig. 4.115	Crack opening displacements corresponding to Fig. 4.105 at maximum and opening points of the loading cycle. ....	223
Fig. 4.116	Crack opening displacements corresponding to Fig. 4.106 at maximum and opening points of the loading cycle. ....	224
Fig. 4.117	Crack growth rate, $da/dn$ , versus stress intensity range in notched specimens of aluminum at $R = 0.1$ under negligible notch plasticity effects. ....	225
Fig. 4.118	Crack growth rate, $da/dn$ , versus stress intensity range in notched specimens of aluminum at $R = 0.4$ under negligible notch plasticity effects. ....	226
Fig. 4.119	Crack growth rate, $da/dn$ , versus stress intensity range in notched specimens of aluminum at $R = 0.1$ under the influence of notch plasticity effects. ....	227
Fig. 4.120	Crack growth rate, $da/dn$ , versus stress intensity range in notched specimens of aluminum at $R = 0.7$ under the influence of notch plasticity effects. ....	228
Fig. 4.121	Crack growth rate, $da/dn$ , as a function of effective stress intensity range corresponding to Fig. 4.117. ....	229
Fig. 4.122	Crack growth rate, $da/dn$ , as a function of effective stress intensity range corresponding to Fig. 4.118. ....	230

Fig. 4.123	Combined plot showing growth rate of short cracks in front of notches under different conditions. ....	231
Fig. 5.1	Schematic illustration of the method of back extrapolation .....	246
Fig. 5.2	Typical method of back extrapolation adopted. ....	247
Fig. 5.3	Estimated initial crack length versus initial crack length in LF condition of steel at different R ratios using C and m. ....	248
Fig. 5.4	Estimated initial crack length versus initial crack length in HF condition of steel at different R ratios using C and m. ....	249
Fig. 5.5	Estimated initial crack length versus initial crack length in LC condition of steel at different R ratios using C and m. ....	250
Fig. 5.6	Estimated initial crack length versus initial crack length in HC condition of steel at different R ratios using C and m. ....	251
Fig. 5.7	Estimated initial crack length versus initial crack length in LF condition of steel at different R ratios using C' and m'. ....	252
Fig. 5.8	Estimated initial crack length versus initial crack length in HF condition of steel at different R ratios using C' and m'. ....	253
Fig. 5.9	Estimated initial crack length versus initial crack length in LC condition of steel at different R ratios using C' and m'. ....	254
Fig. 5.10	Estimated initial crack length versus initial crack length in HC condition of steel at different R ratios using C' and m'. ....	255
Fig. 5.11	Schematic diagram indicating back extrapolation based on C and m and C' and m'. ....	256
Fig. 5.12	Crack opening and closing at high strain cycling. ....	257
Fig. 5.13	Closure data for LF condition of steel at high strains. ....	258
Fig. 5.14	Crack growth rate as a function of stress intensity range without correction for closure and plasticity. ....	259
Fig. 5.15	Crack growth rate as a function of effective stress intensity range based on J with correction for closure and plasticity. ....	260
Fig. 5.16	Estimated initial crack length versus initial crack length for data of Fig. 5.14 using C and m .....	261
Fig. 5.17	Estimated initial crack length versus initial crack length for data of Fig. 5.14 using J. ....	262

Fig. 5.18	Ratios of estimated initial crack length to the actual initial crack length based on K and J. ....	263
Fig. 5.19	Combined plot showing crack growth rates of long cracks for all conditions of steel as a function of effective stress intensity range ...	264
Fig. 5.20	da/dn versus effective stress intensity range for short cracks at positive R ratios in LF condition of steel .....	265
Fig. 5.21	da/dn versus effective stress intensity range for short cracks at positive R ratios in HF condition of steel .....	266
Fig. 5.22	da/dn versus effective stress intensity range for short cracks at positive R ratios in LC condition of steel .....	267
Fig. 5.23	da/dn versus effective stress intensity range for short cracks at positive R ratios in HC condition of steel .....	268
Fig. 5.24	da/dn versus effective stress intensity range for all conditions of steel at R = -1 .....	269
Fig. 5.25	da/dn versus effective stress intensity range for short cracks at positive R ratios for all conditions of steel. ....	270

## **1.0 List of Tables**

<b>Table 2.1</b>	<b>Chemical composition of 4340 Steel</b>	<b>33</b>
<b>Table 2.2</b>	<b>Chemical composition of 2024-T351 aluminum alloy</b>	<b>34</b>
<b>Table 2.3</b>	<b>Heat Treatment of 4340 Steel</b>	<b>35</b>
<b>Table 2.4</b>	<b>Matrix of long crack tests</b>	<b>36</b>
<b>Table 2.5</b>	<b>Matrix of short crack tests</b>	<b>37</b>
<b>Table 2.6</b>	<b>Matrix of notched specimen tests</b>	<b>38</b>
<b>Table 4.1</b>	<b>Mechanical properties of different conditions of 4340 steel</b>	<b>105</b>
<b>Table 4.2</b>	<b>Mechanical properties of 2024-T351 aluminum alloy</b>	<b>106</b>
<b>Table 4.3</b>	<b>Linear elastic crack growth paramters C and m</b>	<b>107</b>
<b>Table 4.4</b>	<b>Linear elastic crack growth paramters C' and m'</b>	<b>108</b>

## **Section 1**

# **INTRODUCTION AND LITERATURE REVIEW**

A reasonable and an improved estimate of the life of a component can be made by the study of short crack initiation and growth. Since most service failures are caused by cyclically varying stresses which cause progressive failure of a component, short crack problems in fatigue are a major concern today.

Many investigators have studied the anomalous behavior of short cracks. Advances in small crack growth have enabled increasingly quantitative studies that affect initiation and growth at structural details. Manufacturing problems that limit structural lives and which involve growth of short cracks have been identified. References [1,2,3] list the importance of the short crack problem.

## 1.1 RATIONALIZATION OF SHORT CRACK GROWTH

The behavior of short cracks has been described as being 'anomalous' because short cracks show a higher crack growth rate compared to that of long cracks. In the case of long cracks, crack growth rates show a single relation of the applied stress intensity range,  $\Delta K$ . This simple relation ceases to exist when the short crack growth rates are considered. The apparent threshold stress intensity level  $\Delta K_{th}$ , manifest in long cracks, seems to disappear for short cracks. This behavior of short cracks raises the question whether Linear Elastic Fracture Mechanics, LEFM, is applicable to short fatigue crack analysis or not. Linear Elastic Fracture Mechanics, LEFM, implies the study of crack problem for which the structural material is considered linear elastic. In LEFM, the magnitude of the strength of singularity at the crack tip is expressed by the stress intensity factor,  $K$ , which depends on the applied load and geometry. Resistance of the metal to fracture, under static and cyclic conditions, are also described by the same parameter,  $K$ . A typical crack growth rate versus  $\Delta K$  for long cracks, which are characterized by LEFM conditions, is shown in Fig. 1.1. The three distinct regions of this curve are quite apparent: a threshold region in the beginning, a linear region, and a fast fracture region at the extreme.

Figure 1.2 shows the view of LEFM [4], with a small region of small inelastic process zone, embedded in a larger  $K$  dominant region, where the stress field is described by

$$\sigma_{ij} = \frac{K}{\sqrt{(2\pi r)}} f_{ij}(\theta)$$

Note that this equation is not unique because of invoking similitude. It is important to note that the plastic zone in front of the crack tip should be relatively small compared with the crack length and should be embedded inside the larger elastic zone in order to use this equation effectively. These two conditions are met in the case of long cracks and hence LEFM is applicable to long cracks. Note that the small scale yielding approximations used in LEFM, employing elastic stress intensity approaches are based on the fact that plastic deformation is entirely determined by the history of variation of  $K$ .

Figure 1.3 shows the crack growth rate versus  $\Delta K$  for short and long cracks.[5] Starting with a high growth rate, a deceleration is observed first. Note that there exists a transition region before the growth rate of short cracks merges with the long crack growth data. Figure 1.3 also shows some cracks getting completely arrested when the cracks encounter grain boundaries. This figure is shown only as an indicator of the nature of growth behavior of short cracks in comparison to long cracks. The main problem of short fatigue crack growth is the lack of mechanics formulation to describe the variety of short crack conditions. The crack lengths may vary from cracks contained within one grain (where plastic flow may or may not be isotropic) to cracks under gross plastic deformation in high strain fatigue, where local effects are important [6]. Short crack growth is also greatly influenced by local strain field gradients. All these attributes that are associated with short cracks stem from the violation of the continuum mechanics assumption and the violation of the linear elasticity assumption [7]. The inappropriate use of LEFM analysis, as discussed in reference [8] also leads to the anomalies observed in short cracks.

Material inhomogeneities, crack front irregularities, second phase particles and inclusions, play a vital role in affecting the local stress field in front of the crack tip, and hence in the breakdown of similitude conditions assumed in LEFM. In the case of long cracks, all these effects are integrated and averaged over many grains. However, in short cracks, these effects do play a prominent role in their growth behavior. Besides the factors mentioned above, contributions from stress level, mechanical properties, microstructural unit sizes and distribution of different phases, mean stress level, prior deformation, environment, local effects etc. affect the growth of short fatigue cracks significantly.

Thus, the analysis of short cracks in fatigue can be from fracture mechanics characterization, involving elastic-plastic fracture mechanics, and/or the physics of crack propagation involving microstructure, plasticity, closure effects, crack size and shape.

The efforts in identifying crack length above which LEFM concepts could be utilized can be traced to the works of Kitagawa [9], where a critical crack length has been defined. Several attempts in correlating short crack and long crack data have been made in studies by Dowling [8], El Haddad [10], and Ohuchida [11]. Fatigue crack growth rate has been analyzed by using J-integral in reference [8]. El Haddad [10] suggested an empirical model involving a parameter  $\ell_0$  to predict the behavior of cracks. Parameter  $\ell_0$  which has the same significance of the critical crack size defined in the earlier study, is valid only in some conditions and does not work in all situations [12]. Parameter  $\ell_0$  may be a useful tool for correlating data from comparable geometries. A closer correspondence was obtained between long and short cracks using the J-integral and  $\ell_0$  concept [13].

Besides the short crack problem, crack propagation under repeated plastic straining (as in low cycle fatigue) has not been fully analyzed because of mathematical complexities involved.

## 1.2 PLASTICITY AND CRACK CLOSURE

It was first observed that cracks growing from notches exhibit a non-LEFM behavior. In other words, the crack growth rate of cracks at notches did not show the behavior of long cracks. The problems encountered with cracks from notches are stress and strain fields with high gradients and plasticity effects. Elastic Plastic analysis for the growth rates have been done using shear displacement [14] and J-integral (J) based on elastic plastic analysis. All these indicate that cracks from notches decelerate first, (and in some cases get completely arrested, NPCs) before growing any further. The deceleration of the crack in front of the notch is mainly due to a decrease of crack driving force, (  $K$  or  $J$  ) with the increase of crack length and limited lateral extent of the notch stress-strain field relative to crack size. There are several estimates of this transition region. The transition crack length has been interpreted as the extent of the local notch field which extends to small fractions of the notch radius [8]. This correspondence between the notch plastic zone size and the transition crack length is limited to the case of stress ratio of -1.

The numerical analyses of Newman [15] and Ohji [16] for growth behavior of cracks at notches also revealed the initial deceleration of the crack. Qualitatively, even though  $K_{max}$  increases with the crack length, the  $\Delta K_{eff}$  decreases because of the in-

crease in the opening level of the crack. All these analyses show that plasticity induced effects near notches can explain short crack growth behavior. However, there is no definite conclusion on whether notch plasticity is solely instrumental for the observed behavior of short crack growth.

In general, growth of short cracks can be attributed to plasticity and plasticity-induced mechanisms. These are notch tip plasticity, micro and macroplasticity, grain boundary blocking of slip bands and crack closure.

### ***Crack Closure***

Since Elber [17] showed that fatigue crack is partially closed even under tensile loading, crack closure is widely investigated and recognized as an important factor in correlating the fatigue crack growth rates. Crack closure is one of the mechanisms of crack tip shielding, as discussed by Ritchie et al [18] To a great extent, crack closure explains the decreased driving force in front of the fatigue crack tip of long cracks.

Briefly, the closure can be plasticity induced, oxide induced and roughness induced. A schematic illustration showing these types are shown in Fig.1.4. Although, oxide induced crack closure plays a major role in explaining the near threshold growth of small cracks, for the case of physically short cracks at stress intensities greater than the threshold level, the oxide and roughness induced closure are less significant in comparison to the plasticity induced closure.

Plasticity induced crack closure is due to the contained plasticity and the residual tensile strains left behind the crack tip. It is apparent that, as the load is applied, the material ahead of the crack tip yields due to stress concentration, even if the applied stress on the specimen is below the yield stress. The size of the plastic zone is related to the crack length and applied stress [19]. The material surrounding the plastic zone remains elastic and as the load is decreased, compressive stresses build up near the crack tip. These compressive stresses must be overcome before the crack tip can open upon reloading.

The other mechanism which causes crack closure behavior is the residual strains that exist in the wake of the moving crack tip. There exists a region of residual tensile strains (deformations) which are left in the material behind the crack tip. This is illustrated schematically in Fig. 1.5. The residual tensile strains (existing inside all the envelopes of the plastic zone) are also responsible for crack closure, since these cause the crack faces to come into contact before the minimum cycle is reached. Once the crack surfaces contact, compressive residual stresses develop behind the crack tip. Upon loading, the crack will open only when the applied stresses overcome the residual stresses. The stress intensity at which the crack opens is denoted by  $K_{op}$ .

Assuming that there is no further cyclic straining of material, for loads less than the crack opening load, an effective stress intensity,  $\Delta K_{eff}$  is written as

$$\Delta K_{eff} = K_{max} - K_{op}$$

and effective stress fraction,  $U$ , as

$$U = \left[ \frac{\Delta K_{eff}}{\Delta K} \right] = \left[ \frac{K_{max} - K_{op}}{K_{max} - K_{min}} \right]$$

Using effective stress intensity, crack growth correlations have been made [20,21] by using a relation such as

$$\frac{da}{dn} = C[\Delta K_{eff}]^m$$

Thus, by changing the focus on  $\Delta K_{eff}$ , investigations have determined the various factors that affect  $K_{op}$ . Several empirical relations exist to provide information on the closure response by such factors as  $K$  and stress ratios. It is observed that closure response is also material dependent, since in some steels closure response is independent of stress ratios. Increasing mean opening displacement with increasing  $R$  ratios have led to the conclusions that  $\Delta K_{eff}$  near threshold is independent of  $R$  ratios [22].

From the various reported works, the following observation has been made.

1.  $U = f(R)$  for a material is independent of other parameters. [23,24].
2.  $U$  increases with increase in  $R$  in all cases, whereas the relationship of  $U$  with  $K_{max}$  is not usually the same
3. No crack closure is observed at higher values of  $R$ . In other words,  $U$  becomes more than unity [25].
4. The crack closure measurement technique influences the results of  $U$ .

Generalizing, the effective stress intensity level can be written as:

$$\Delta K_{eff} = \Delta K_{eff}[R, \Delta K, \text{material, crack length, stress state, constraint, environment,...}]$$

The closure behavior is strongly influenced by the material and prior deformation [26]. Although, for a variety of materials and alloys, crack growth rate when plotted against  $\Delta K/E$  results in a fairly narrow scatterband in the linear region of crack growth rate [27], no conclusions can be drawn from such behavior. Mechanical properties such as yield stress and strength, influence the closure response as well. Stewart [28] has found that increasing hardness reduced plasticity induced closure, and has shown that  $K_{op}$  remains almost the same for different yield strength.

The influence of the stress state on closure response is also important. It is observed that closure is more significant on the surface where plane stress prevails, and decreased closure at the interior. Constraint thus plays a major role in the closure response [29]. Reference [29] cites the influence of specimen thickness. This study revealed that crack closure is unable to account for the order of magnitude increase in growth rate when specimen thicknesses were increased.

Since the crack growth mechanics alters completely with the change in environment, no definite conclusions have been drawn from the closure response of materials in a changing environment [3,30,31]. Most studies of short crack growth with the change in environment consider corrosive environments [30,31,32], while a few studies consider inert environments [33,34]. Similar to the long crack growth behavior, these studies also rationalize the short crack growth in terms of  $\Delta K_{eff}$ . It has been found that

the effect of the environment is insignificant in some cases but significant in others [33]. In general, fatigue short crack growth in different environments is dependent on specific cases of material and environment interaction systems.

Crack closure has also been used to rationalize crack growth under variable amplitude loading. Crack growth retardation because of a single peak overload, has been attributed to the increase in the opening value of  $K$  as the crack grows through the overload of plastic zone. In addition to plasticity induced closure, other mechanisms such as the roughness and oxide induced closure have also been suggested [35] as the cause of crack growth retardation. References [36,37] report the characterization of the variable amplitude by closure response.

Corrosion products formed on the fracture surfaces influence crack growth. This mechanism has been observed by several investigators during the last decade. References [28], [35] and [38] reveal this line of research. The build-up of oxide layers results in yet another important mechanism of closure namely oxide induced closure. This phenomenon is significant at low load ratios, and at low growth rates near  $\Delta K_{th}$  level. This is because the total thickness of oxide deposits formed in this growth region is of the order of the crack tip opening displacement. Moist atmospheres lead to the formation of oxide layers, which in turn are enhanced by fretting mechanisms prevailing near the crack tip. Since fretting increases the effects of oxide induced closure, this mechanism is operative near the crack tip. Low strength materials tend to show a high degree of oxide induced closure mechanism because of their susceptibility to fretting damage. However, in some cases where fretting is non-existent, the effects of oxide induced closure is significant in the presence of oxidizing agents.

The existence of this mechanism in different materials such as ferritic-pearlitic, fully martensitic steels, and aluminum alloys, has been widely studied by researchers. It has been found that in the case of steels, oxide induced closure is found to be inversely related to the strength level [31].

The closure mechanisms described above are the result of mechanical and environmental effects. The microstructural effects induce another form of closure namely asperity induced closure. Shear (Mode II) displacements on the fracture surfaces cause the two faces of the crack to come into contact inducing closure of the crack. The fracture surface roughness depends upon the crystallographic slip and this has been shown to be related to continuous slip length of the microstructure [39]. Similar to the oxide induced closure, this form of closure is significant near low crack growth rates. References [40] and [41] describe efforts of modelling roughness induced closure.

#### ***Methods of Measuring Closing and Opening Levels***

The prediction of crack closure by accurate methods for short cracks is essential if the effective stress-intensity approach is to be applied for design purposes.

The different methods of measuring closure are thickness averaging and near-tip compliance, dc potential, ultrasonics, acoustics, interferometry, microscopic obser-

vation and vacuum infiltration techniques. Compliance techniques are based on the increase of compliance of a cracked specimen when the crack opens. Crack mouth gauge [42], back face strain gauge [43] and crack tip clip gauge [44] are mainly used to measure the change in compliance. The results obtained by these different techniques vary because of the geometry, loading and thickness effects. Compliance techniques are widely used because of simple instrumentation and easier methods of detecting closure.

The decrease in the ultrasonic impedance or the drop in the dc potential when the crack closes is used to detect the closure levels [45,46,47]. Instrumentation of the ultrasonic method is complex, and the measured value of the opening level tends to be higher, because of the transmission of sound waves through asperities which are in contact, but not load bearing. The interaction of waves with abrading fracture surfaces thus limits obtaining the actual closure point. In the dc potential method, the formation of oxide at the crack faces makes it difficult to monitor closure points accurately.

Microscopic observation methods such as the travelling microscope [48], the scanning electron microscope [49], and SEM in conjunction with stereoimaging provides a good measure of closure level and crack opening displacements by simple means. It is advantageous to use in situ fatigue testing facilities under a scanning electron microscope [49] since accurate measurements to the order of  $1\mu\text{m}$  can be made.

Laser interferometry [50] and photoelasticity [51] techniques also provide good information about closure levels. However, the changes in the stress and strain field

around the indentations used in laser interferometry may induce some changes in the closure level. The crack opening levels by interferometric studies are generally higher than those obtained by other techniques, since opening and closing levels are monitored very close to the tip. Most of the techniques used are nondestructive, except for the vacuum infiltration technique [52] where samples are broken to get closure level. We must consider the three-dimensional nature of crack closure when there are large effects of plasticity. Decreased closure, especially in thick specimens, exists in the center where plane strain conditions prevail. The interior measurement of closure is restricted to the pushrod compliance technique [53], the vacuum infiltration technique [52], and the optical interferometry techniques on transparent materials [54].

### **1.3 MICROSTRUCTURAL EFFECTS**

The process of crack initiation and the propagation of a fatigue crack in a component are significantly affected by chemical composition and the microstructural state of the material. One of the problems in evaluating the importance of microstructural features is the mutual interdependence of metallurgical quality on the mechanical properties such as strength, yield strength and fracture toughness.

The crack propagation is local and is affected by metallurgical features such as microstructure and inclusions. When the microstructure is uniformly distributed, it will play a major role in controlling the crack propagation. Literature on short cracks

contains many research papers which discuss the crack growth rate in terms of linear elastic fracture mechanics (LEFM) parameters such as  $\Delta K$ , neglecting the microstructural importance, apparently because of an averaging effect encountered in the study of long cracks. Many researchers [55,56,57] have concentrated on the effect of the microstructural unit sizes and have arrived at many different models, but all of these seem to be semi-empirical and have not been generalized to a great extent. It is important to note that in almost all materials, the near threshold crack growth rate is significantly influenced by the microstructural features. This microstructurally sensitive crack growth leads to complex modes of loading at the crack tip, and hence leads to different crack tip shielding mechanisms. One of the models suggested by Lankford [58] predicts the crack growth behavior based on crack tip strains. This model includes the effects of grain boundary retardation of short fatigue cracks. Tanaka's [59] model considers blockage of crack-tip slip band by a grain boundary and crack growth is controlled by a threshold value of the microscopic stress intensity factor ahead of a blocked crack-tip slip band. The models describing the crack growth rate by:

$$\frac{da}{dn} = C a^x [d - a]^{1-x}$$

where  $C$  and  $x$  are constants,

$d$  is the characteristic microstructural unit size, and

$a$  is the crack length,

explain the deceleration of crack at a grain boundary, but do not explain the growth of cracks into adjacent grains.

Thus, the form of functional relation between the mechanical properties (such as tensile and yield strengths), crack growth rate and characteristic microstructural dimensions hold the key to rigorous understanding of fatigue crack growth.

Besides the characteristic microstructural dimensions, the different phases present in the microstructure are also important in predicting crack growth. This is clear because in most steels, large deposits of carbides near the grain boundary, act as crack initiators, and the crack has a different crack growth rate compared to a crack initiating inside a grain from the accumulation of dislocations at that region. Single phase materials would provide the key to isolate the importance of relative phases and grain size effects, but it is difficult to obtain different strength levels in a single phase material [60,61,62]. By varying the prior austenitic grain sizes, Daeubler and Thompson [63] found that in eutectoid steels, there was no appreciable influence in the change of small crack growth rates. However, they observed that the effects were significant with different cementite lamellar spacings.

#### **1.4 OTHER FACTORS CONTRIBUTING TO SHORT CRACK EFFECT**

Besides the major factors mentioned above, the other factors which have been suggested to explain the anomalous behavior of short cracks are crack deflection, crack shape, multiple crack interaction, and  $K$  estimation errors.

Short cracks do not possess many deflections in its path, and the number of deflections vary from one short crack to the other. This argument was utilized by Suresh

[64] to explain the variation of stress intensity from one short crack to the other. In the case of a long crack, these deflections or crookedness of the path averages out yielding uniform stress intensity.

If the  $K$  solutions are to be used effectively to describe the growth behavior of cracks, then the cracks need to possess definite shape required by  $K$ . The crack shapes of most small cracks are not known. Hence, the  $K$  solution used to describe the growth behavior of these cracks will be in error. Local variation near the crack tip will affect the crack shape. It has been found that the high stresses needed for the growth of small cracks in smooth specimens increase the influence of the plane stress on the surface [65] thereby changing the crack shape. It has also been suggested in reference [66] that surface cracks grow faster before showing a decelerated growth behavior.

Growth analysis in specimens where multiple cracks initiate is also subject to discussion because of the interaction of cracks with one another. Interaction of stress fields of one crack with the other changes the history of variation of  $K$  at crack tips. Reference [67] reports magnification of the stress intensity values when two cracks approach each other.

The influence of higher order terms has been shown to be significant for microstructurally short cracks [68]. Stress distribution near microstructurally short crack has been shown to be different when a more complete form of Westergaard equation is adapted [69]. However, it is difficult to define  $K$  value in these cases because of the lack of a simple singularity [70].

## **1.5 IMPORTANCE OF SHORT CRACKS IN AIRCRAFT INDUSTRY**

Short cracks are important to the aircraft industry only when the assumed initial flaw sizes are in the short crack regime. Although the assumed initial flaw size considered for damage tolerant studies is 1.27mm, cracks of length shorter than this are considered for durability analysis. In these cases, short cracks are important for the durability of airframe components. As an example, if the threshold stress intensity values are used as a criterion to prevent high cycle fatigue failure, the use of  $\Delta K_{th}$  from long crack data could be unconservative in cases where short cracks are present. In some components such as engine discs, where low cycle high amplitude loadings exist, critical crack lengths may be in the short crack regime [71]. In these cases, short crack growth behavior is important for the application of damage tolerant principles to reduce the risk of failure of components. Life calculations based on the linear long crack data may lead to unconservative predictions because of the short crack effects in these situations.

## **1.6 DISCUSSION AND SIGNIFICANCE OF THE PRESENT STUDY**

Many aspects of the short crack growth and behavior are still not clear even after a decade of research effort by many investigators. Several aspects concerning the short crack growth are still controversial such as the interactions with the micro-

structural unit sizes. In general, there is no adequate definition and description of the growth of short cracks. Although the limitations of the applicability of LEFM to short cracks is well understood, many researchers find it convenient to present the short crack growth data in terms of the applied stress intensity range, as there is no definite characteristic fracture mechanics driving force derived for the cases beyond the limits of LEFM. J-integral seems to provide [72] a key to handle situations where gross plastic deformation exists. Many hypotheses have been proposed to quantify the transition from short crack to long cracks. These research efforts [55,56,75] provide a general description of the short crack behavior.

From the various reported works, the following observations can be made for constant amplitude tests:

- The short crack definition is not completely clear. However, there is a general consensus among researchers about considering cracks as 'short' when the crack length is smaller than the characteristic crack length such as plastic zone size.
- Growth rates of short cracks are substantially greater than predicted by conventional linear elastic long cracks.
- Short cracks do grow below the long crack threshold,  $\Delta K_{th}$ .
- Transition from short to long cracks is in the regime of 0.5 - 1.0mm depending upon the material system.
- Growth rate of short cracks depends upon the individual orientation of grains.
- Crack closure is found to increase with crack length.

- A stress level effect is seen in the growth of short cracks at negative R ratio tests. Little information is available about the stress level effects at positive R ratios.
- Most of the reported work on short crack growth and behavior are for constant amplitude loading cases.
- Closure measurements vary from technique to technique because of the geometry and loading effects on short cracks.
- Roughness and oxide induced closure play important roles near the threshold region.

As mentioned earlier, research studies concentrate on two different types of cracks namely, microstructurally short cracks and physically short cracks. There is of confusion regarding this issue. The nature of physically short cracks is still not well understood because of the difference in the crack tip conditions between the long and short cracks such as plasticity, crack closure etc.

The objective of the present study is to understand the growth behavior of short cracks and to compare this with long cracks in aluminum and four different conditions of 4340 steel. Note that very few investigations have been carried out in this area, especially in steel since their point of focus is on the alloys of aluminum and titanium. The closure response of short cracks is studied in detail here. The crack opening levels were determined by the stereoimaging technique developed and adapted in this investigation using a low power microscope. This technique, in contrast to other techniques of measuring crack opening levels is simple and inexpensive. Crack opening levels determined by stereoimaging are utilized here to rationalize the growth behavior of long and short cracks on the basis of effective stress intensity

approaches. This is done by conducting experiments at different stress ratios and stress levels. This study also investigates the prediction of initial fatigue quality in components involving short crack growth by means of long crack data as practiced in durability design methods.

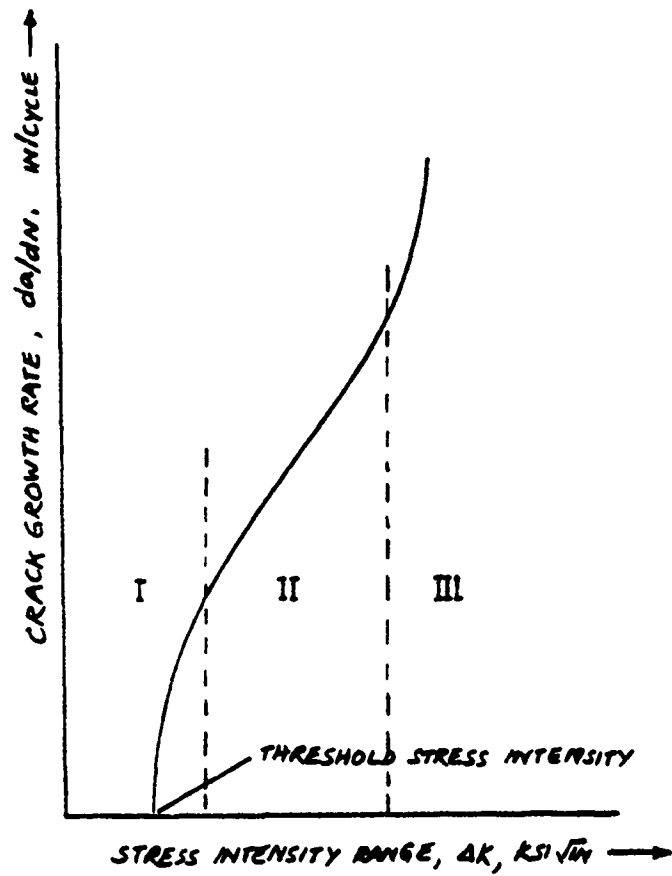


Fig 1.1 Typical crack growth rate versus stress intensity range

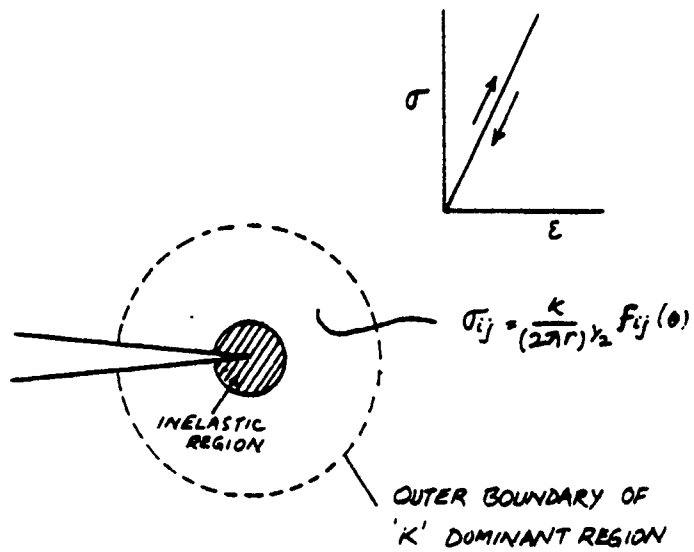


Fig 1.2 Basis of Linear Elastic Fracture Mechanics, LEFM [4].

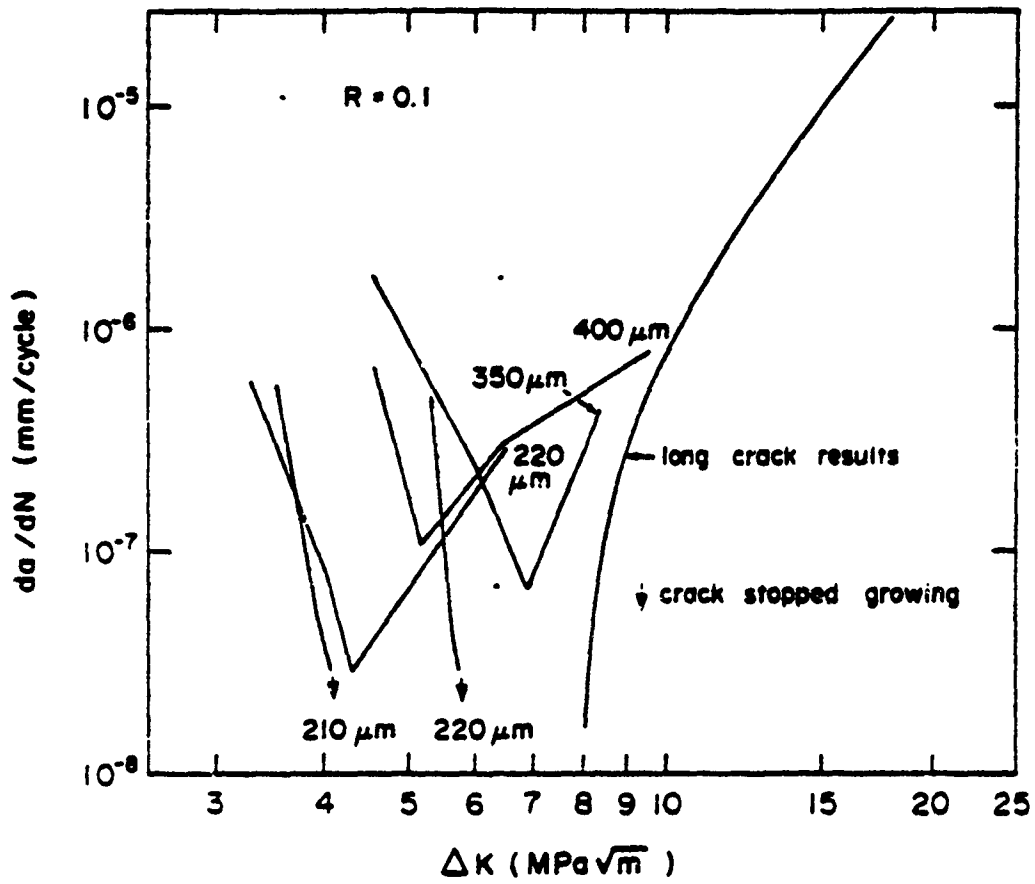


Fig 1.3 Crack growth rate versus stress intensity range for short cracks [5].



plastic  
zone

Plasticity-Induced  
Closure



oxide debris

Oxide-Induced  
Closure



Roughness-Induced  
Closure

Fig 1.4 Schematic diagram illustrating different mechanisms of closure

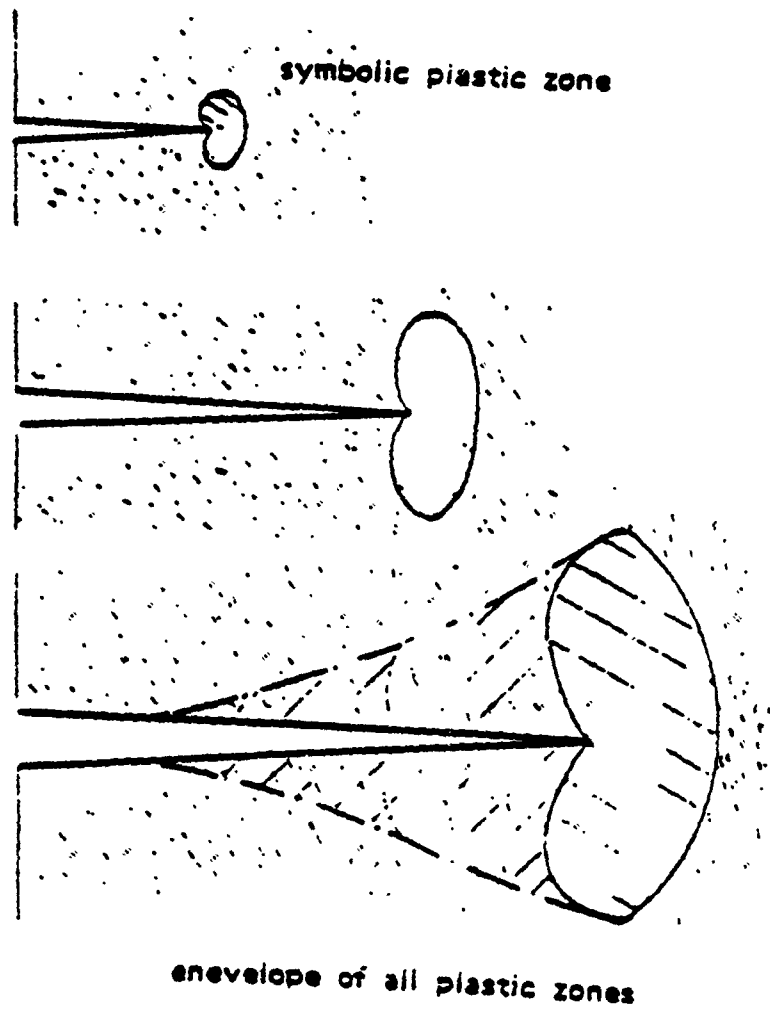


Fig 1.5 Schematic diagram illustrating the residual strains in the wake of crack.

## **Section 2**

### **EXPERIMENTAL PROGRAM**

The experiments were designed to study the growth behavior and closure of short cracks growing from a known initial state in ferrous and nonferrous materials. The initial state of these short cracks corresponds to a definite crack length and shape produced by machining material from specimens containing long cracks. Specifically, the materials chosen were 2024-T351 aluminum alloy and 4340 alloy steel. A matrix of tests were carried out in order to study growth of cracks at different stress levels, R ratios, prior austenitic grain size, yield strength. The stereomaging technique was adapted to obtain crack opening and closing points, and displacement field around the crack tip.

## 2.1 MATERIALS AND HEAT TREATMENT

The materials chosen were 2024-T351 aluminum alloy and 4340 steel. The chemical compositions of these are given in Tables 2.1 and 2.2 respectively. The aluminum specimens were machined from plates of size 2.3 by 304.8 by 50.8 mm, supplied by NASA Langley. The yield and the ultimate tensile strength of this aluminum alloy are 359 MPa and 496 MPa respectively. The typical grain dimension in the rolling direction is 55  $\mu\text{m}$  for this aluminum alloy. The aluminum alloy used in this study is the same as the one used in the AGARD (Advisory Group for Aerospace Research and Development) collaborative program on short cracks.

The 4340 steel specimens were cut from a bar of 190.5mm diameter. The longitudinal axis of the steel specimens were parallel to the axis of the circular bar and was in the rolling direction. It was possible to obtain different strengths and widely varying prior austenitic grain sizes in this steel by varying the austenitizing and tempering temperatures. The heat treatments which were carried out on 4340 steel were designed to get both high and low strength levels of the material, at two widely differing prior austenitic grain sizes. After establishing proper heat treatment procedures, specimen blanks of 6.35 by 25.4 by 127 mm were heat treated, taking care to allow enough time for the specimens to reach the austenitizing temperatures in order to avoid any through thickness temperature gradients. The final heat treatments schedule is shown in Table 2.3. Austenitizing at temperatures of 815° C and 843°C resulted in fine prior austenitic grain sizes. An austenitizing temperature of 1204°C resulted in coarse prior austenitic grain sizes. The fine grain sizes correspond to 20 to 25  $\mu\text{m}$  and

coarse grain sizes correspond to 275 to 300  $\mu\text{m}$ . Different strength levels in the steel were obtained by varying the temperatures. The tempering temperatures selected for this study were 316°C and 663°C. Lower tempering temperature resulted in increased strength. The details of heat treatment and discussion on heat treatment of 4340 steel is discussed separately in Section 3. Notably, these heat treatments resulted in uniform microstructure refinement.

The four different heat treatments resulted in four different conditions of steel. Specifically, low strength with fine grain size (LF), high strength with fine grain size (HF), low strength with coarse grain size (LC) and high strength with coarse grain size (HC).

## 2.2 SPECIMENS

The specimens were designed for long and short crack fatigue tests. They were of three types namely, (1) compact tension specimens, (2) short crack test (SCT) specimens and (3) notched specimens. Only short crack test specimens were machined from 4340 steel while all three types of specimens were machined from aluminum. The three types of specimens are shown in Figs. 2.1 through 2.3. The  $K_t$  of the notched specimens was 3.06 to 3.10.

### ***Specimen Preparation***

To introduce cracks of known initial length and shape in the short crack test specimens and notched specimens, the material was machined from specimens containing long cracks. The following paragraph describes the production of short cracks in test specimens.

Double edge notched (DEN) specimens of aluminum and 4340 steel (all heat treated) were precracked to obtain a crack of specific length. To avoid any possible history effects resulting from growing cracks in tension to tension loading, specimens were precracked in cyclic compression. Details of precracking are discussed in Section 3. This precracking procedure resulted in a sharp through thickness crack. After precracking, material from the sides of aluminum specimens and the material on both sides and faces of steel specimens was removed to retain a crack of length 0.1 to 0.25mm on both sides. The crack front of these short cracks were straight, being almost parallel to the through thickness direction. Short cracks in front of notches were introduced in a similar way. The notches were machined after removing the required amount of material on both sides.

The specimens were then checked for residual stresses using an X-ray diffractometer. The aluminum specimens were chemically polished and the steel specimens were electropolished to relieve the residual stresses on the surface. Details of chemical and electrochemical polishing procedures are given in Section 3.

## **2.3 FATIGUE TESTS**

The fatigue tests which were carried out in this study were (1) long crack tests, (2) short crack tests in unnotched specimens, and (3) short crack tests in notched specimens.

### ***Long Crack Tests***

To obtain the linear elastic crack growth parameters to describe the growth behavior of long cracks, these long tests were carried out on aluminum and steel. Compact tension specimens were used for long crack tests in aluminum. In the case of steel, short crack test specimens with initial crack lengths greater than 0.125mm, were utilized for long crack tests in the following way. The material on one side of the SCT specimens was machined to retain the longer crack on one side. 6.3mm diameter holes were drilled on the centerline of the specimen as shown in Fig. 2.4 to obtain single hole end configuration specimens.

Long crack tests at R ratios of 0.1, 0.4 and -1.0 were carried out on aluminum and four different conditions of steel. Test at R ratio of 0.7 was conducted only for aluminum specimens. Table 2.4 shows the matrix of long crack tests which were carried out.

### ***Short Crack Tests in Unnotched Specimens***

The short crack tests were carried out on short crack test specimens to study the growth behavior of short cracks growing from a known initial crack length in the ab-

sence of stress raisers. The short cracks which were introduced in the specimens ranged from 0.1 to 0.13mm. Short crack tests were conducted at R ratios of 0.1, 0.4 and 0.7 for aluminum and for four different conditions of steel at two different stress levels. Completely reversed cycling tests ( $R = -1$ ) were carried out only on steel at two different stress levels. Table 2.5 indicates the matrix of tests carried out under this case and that the stress amplitudes  $\Delta\sigma$  were small enough to avoid any gross plastic deformation. The thickness of the steel specimens used in short crack tests was 3.81mm while the thickness of aluminum specimens was 2.3mm.

#### ***Short Crack Tests in Notched Specimens***

Similar to the short crack tests in unnotched specimens, short fatigue tests were conducted in notched specimens of aluminum at R ratios of 0.1, 0.4, 0.7 at two different stress levels. Table 2.6 indicates the matrix of tests conducted in this case. Specifically, tests were carried out at low stress amplitudes at  $R = 0.1$  and  $0.4$  under negligible notch plasticity effects. Tests were also conducted at  $R = 0.1$  and  $R = 0.7$  when carried out at stress levels where notch plasticity effects were significant. Specifically, in these tests,  $K_t S / \sigma_y$  was greater than 1.

### **2.3 TESTING PROCEDURE AND METHODOLOGY**

All the fatigue tests described above were carried out in a closed loop hydraulic testing machine under load control. Constant amplitude sinusoidal wave form cycling, at test frequencies of 0.2 to 10 Hz, were employed in all cases. All the tests were

carried out at room temperature and laboratory environment. To avoid extraneous bending and to obtain high quality test results, special versatile hydraulic grips were used. Alignment of the testing machine was checked frequently to ensure proper loading of the specimens. The maximum bending strain which was allowed in the alignment procedure was  $20 \mu$  strain.

Chemically or electrochemically polished specimens were given a granular texture of fine resolution points by spraying chalk dust on the surface. Incremental crack lengths were monitored from the initial crack length using x120 stereozoom microscope which has a least reading of 0.005 mm. The precision with which the crack lengths could be measured was 0.01mm from multiple readings. Crack length and number of cycles was recorded for computing crack growth rates.

Crack opening and closing points were determined by the stereomaging technique. The principles and the techniques of the stereomaging technique are described in detail in Section 3. Pictures of good quality were taken at several points in the load cycle at three or four different crack lengths in the growth history of the crack. Several pictures were taken near the macroscopic opening and closing points. These pictures were then enlarged and used in stereomaging studies to obtain crack opening and closing points. The crack opening and closing points at each stress intensity level and crack length were thus obtained. The stereomaging procedure was also utilized to obtain the crack opening displacements along the length of the crack and in-plane displacements in the vicinity of the crack tip.

**TABLE 2.1**

**CHEMICAL COMPOSITION OF 4340 STEEL**

<b>NI</b>	<b>C</b>	<b>S</b>	<b>P</b>	<b>SI</b>	<b>Mn</b>	<b>Mo</b>	<b>Cr</b>
<b>1.89</b>	<b>0.38</b>	<b>0.052</b>	<b>0.012</b>	<b>0.29</b>	<b>0.77</b>	<b>0.21</b>	<b>0.83</b>

**TABLE 2.2**

**CHEMICAL COMPOSITION OF 2024-T351 ALUMINUM ALLOY**

<b>Cu</b>	<b>Mg</b>	<b>Mn</b>	<b>Si</b>	<b>Zn</b>	<b>Cr</b>	<b>Fe</b>	<b>Al</b>
<b>4.50</b>	<b>1.50</b>	<b>0.60</b>	<b>0.0</b>	<b>0.0</b>	<b>0.0</b>	<b>0.0</b>	<b>Rest</b>

**TABLE 2.3**

**HEAT TREATMENT OF 4340 STEEL**

No.	CONDITION	HEAT TREATMENT
1.	Low Fine (LF)	<p>Austenitize at 815°C; 5 hrs. to temperature. Hold 3 hrs.; Oil Quench.</p> <p>Temper at 663°C; 4 hrs. to temperature. Hold 8 hrs; Air Cool.</p>
2.	High Fine (HF)	<p>Austenitize at 843°C; 4 hrs. to temperature. Hold 1 hr; Oil Quench.</p> <p>Temper at 316°C; 2 hrs. to temperature. Hold 1½ hrs; Air Cool.</p>
3.	Low Coarse (LC)	<p>Austenitize at 1204°C; 4 hrs. to temperature. Hold 1 hr; Furnace cool slowly over 2 hrs. to 871°C; Hold ½hr; Oil Quench.</p> <p>Temper at 663°C; 2 hrs. to temperature. Hold 1½ hrs; Air Cool.</p>
4.	High Coarse (HC)	<p>Austenitize at 1204°C; 4 hrs. to temperature. Hold 1 hr; Furnace cool slowly over 2 hrs. to 871°C; Hold ½hr; Oil Quench.</p> <p>Temper at 316°C; 2 hrs. to temperature. Hold 1½ hrs; Air Cool.</p>

**TABLE 2.4**

**MATRIX OF LONG CRACK TESTS**

<b>R</b>	<b>LF</b>	<b>HF</b>	<b>LC</b>	<b>HC</b>	<b>AL<sup>1</sup></b>
<b>0.1</b>	•	•	•	•	•
<b>0.4</b>	•	•	•	•	•
<b>0.7</b>					•
<b>-1.0</b>	•	•	•	•	•

<sup>1</sup> 2024-T351 aluminum

TABLE 2.5

MATRIX OF SHORT CRACK TESTS

	LF	HF	LC	HC	ALUMINUM
Low R=.1	165.5 <sup>1</sup>	153.2	138.3	153.2	103.4
High	274.5	279.9	248.8	248.8	145.6
Low R=.4	184.2	149.3	184.3	165.9	114.9
High	245.8	276.5	258.1	276.5	142.4
Low R=.7	155.2	154.4	154.2	142.8	100.4
High	165.2	250.8	220.1	208.5	136.6
Low R=-1	245.9	399.5	245.8	307.2	
High	614.5	613.2	430.1	613.2	

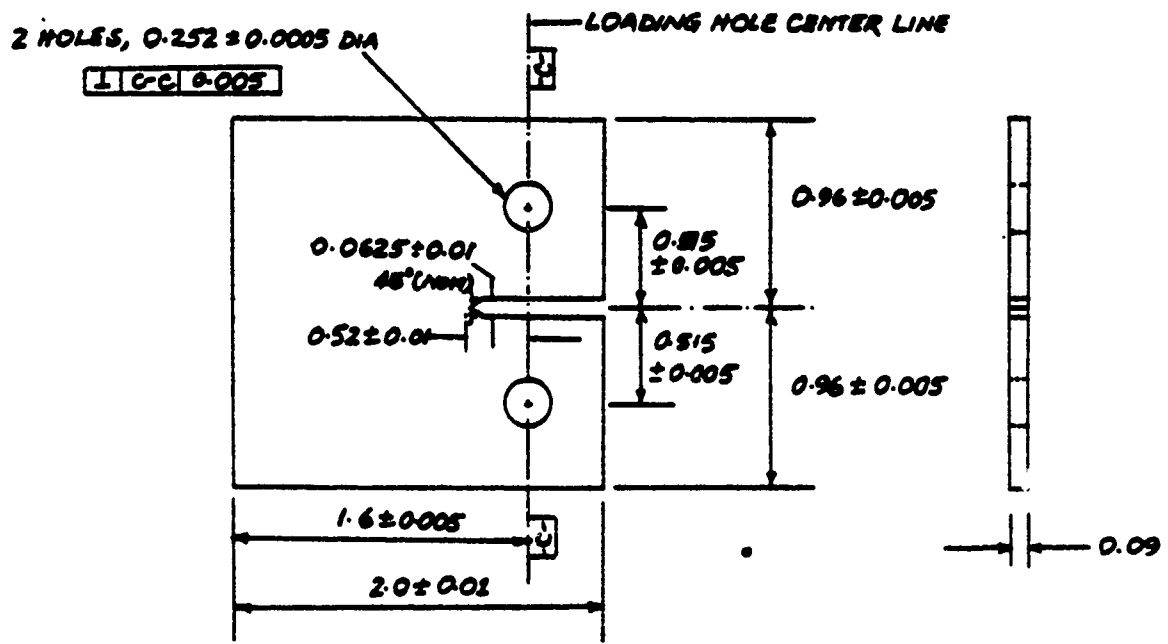
<sup>1</sup> These numbers indicate the stress ranges ( $P_{max} - P_{min}$ ), in MPa.

TABLE 2.6

MATRIX OF NOTCHED SPECIMEN TESTS

R = 0.1	R = 0.4	R = 0.7
0.428 <sup>1</sup>	0.592	1.219
0.740	0.912	2.106
1.253		
1.596		

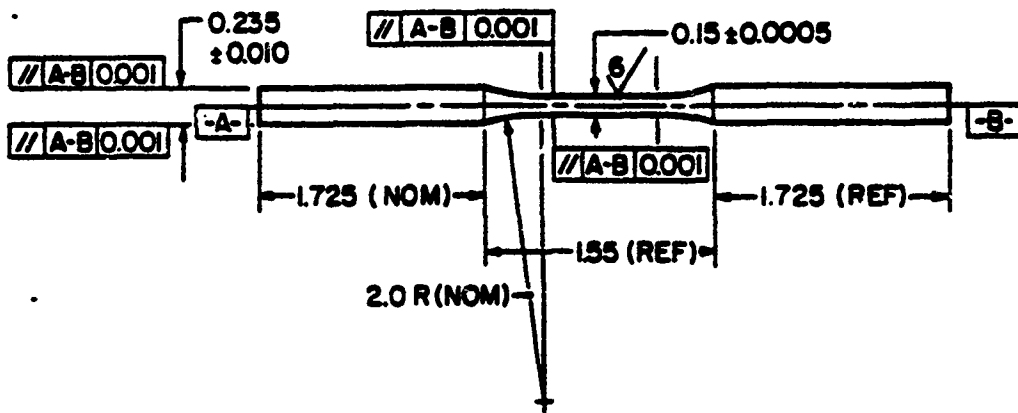
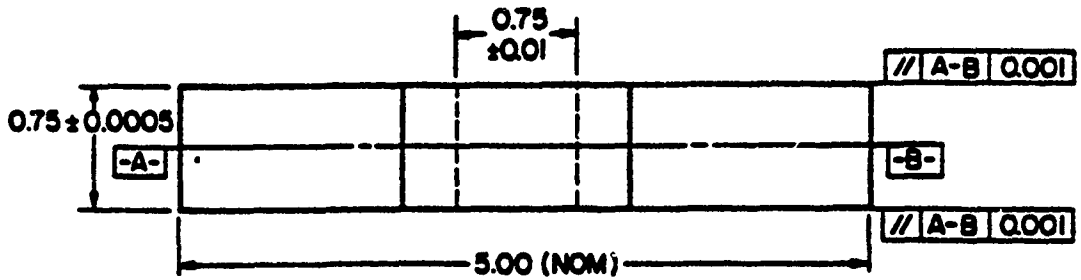
<sup>1</sup> These numbers refer to the values of  $K_t S_{nom}/\sigma_y$



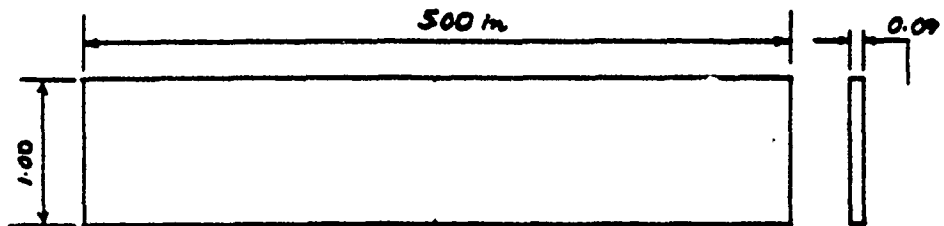
NOTE: ALL DIMENSIONS ARE IN INCHES

Fig 2.1 Geometry of compact tension specimen of 2024-T351 aluminum.

(a) 4340 STEEL

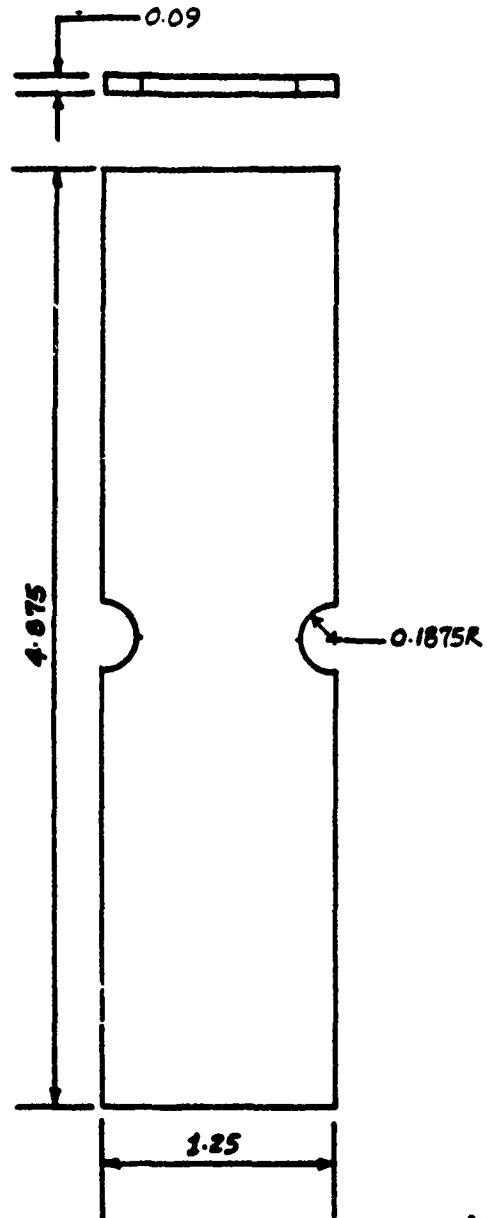


(b) 2024-T351 ALUMINUM



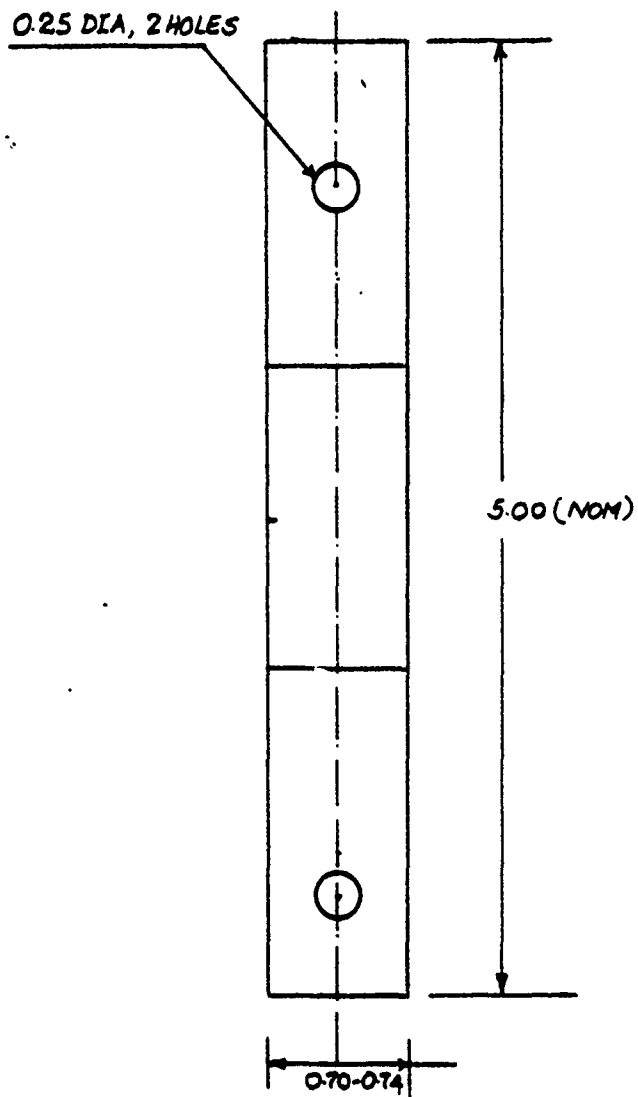
NOTE: ALL DIMENSIONS ARE  
IN INCHES

Fig 2.2 Specimen geometries of short crack test (SCT) specimens.



NOTE: ALL DIMENSIONS ARE  
IN INCHES

Fig 2.3 Specimen geometry of notched specimen of aluminum.



NOTE: ALL DIMENSIONS  
ARE IN INCHES

Fig 2.4 Geometry of single hole end configuration specimens of steel.

## **Section 3**

# **EXPERIMENTAL PROCEDURES**

Details of experimental procedures such as (1) heat treatment, (2) precracking, (3) electro and chemical polishing and (4) stereoinaging are described in this section.

### **3.1 HEAT TREATMENT**

Most commercial ultrahigh strength, low alloy steels, such as the AISI 43XX series steels, are conventionally austenitized at low temperatures ( 870°C) before quenching and tempering to produce fine prior austenitic grain sizes. This conventional heat treatment procedure of 43XX steel results in a good combination of strength and impact toughness [74]. However, several investigators [75,76,77] have reported that higher austenitizing temperatures (up to 1200°C) could be employed without reduction in strength and toughness.

Although the 4340 steel chosen in this study exhibits multiple phases, it is possible to get different strength levels at two widely differing prior austenitic grain sizes. The heat treatment procedure adopted was designed to achieve the same. The heat treatment schedule is shown in Table 2.3 after reviewing various reported works [75,76,77] on heat treatment of 4340 steel. The tempering temperatures of 315°C and 649°C were chosen to obtain low (689 MPa) and high (1550 MPa) strength levels. Before carrying out heat treatments on a large scale, sample materials were heat treated in the laboratory to establish proper schedules and procedures. The following paragraph describes such a laboratory procedure.

Sample sizes of the material in the form of 7.6 by 7.6 by 7.6 mm were normalized (870°C, 1 hour) before any heat treatment. The samples were then heat treated in a tubular furnace in an inert atmosphere of argon. The austenitizing temperatures of 843°C and 1204°C were obtained by small temperature increments. Since the sample sizes were small, it was easy to obtain the desired temperatures in less than 1.5 hours. Cooling was accomplished by oil quenching the samples in an agitated oil bath. Tempering times involved 1.5 to 2 hours at temperatures of 315°C and 649°C.

The hardness of the heat treated samples were then measured after each heat treatment to reflect the strength levels and also, proper heat treatment. The samples were then mounted in bakelite mounts and mechanically polished. A final polish was done with 1  $\mu$ m diamond paste. Micrographs were taken to observe the microstructural features. The etchant used was Vilella's. Longer etching time was necessary for in-

creased austenitizing temperatures of 1204°C to reveal prior austenitic grain boundaries. The heat treatments revealed uniform microstructure refinement, resulting in a coarse or a fine microstructure. Prior austenitic grain sizes were then determined by the comparative and planimetric techniques and an estimate was made of the ASTM grain size number.

#### ***Discussion on Heat Treatment of 4340 steel***

Increased austenitizing temperatures result in an increase in the value of fracture toughness,  $K_{Ic}$ . Charpy V-notch impact energy decreases with the increase of austenitizing temperatures. This is contrary to observed behavior in other steels. An explanation for the difference between the increase of fracture toughness to the decrease in Charpy energy has been provided by Ritchie et al [77] in terms of basic differences between the fracture toughness test and Charpy V-notch impact test, while relating to a marked reduction in critical fracture strain.

We have found that as the austenitizing temperature is increased, the strength remains unchanged while the toughness ( $K_{Ic}$ ) increases because of the larger proportions of retained austenite, around martensite plates and packets of lath. The microstructure is significantly coarsened with large austenitic grain sizes, increased martensitic packet diameter and increased particle spacing. It is believed that this uniform coarsening of the microstructure is also responsible for the increase of the sharp crack toughness with increased austenitizing temperatures. Also, increased austenitizing temperatures result in a small increase in the amount of segregated phosphorous. Thus the decrease of Charpy energy may also be the result of the

combined effects of grain size and concentration of segregated phosphorous in the microstructure. Note that increased strength in 4340 steel would cause transgranular cracking mode to intergranular separation along the prior austenitic grain boundaries. It has also been observed that for 4340 steels, there are no significant differences between the  $\Delta K_{th}$  values for different prior austenitic grain sizes [78,79].

We believed that enhancement of strength at increased austenitizing temperatures was due to the retained austenite between martensite laths [74], segregation and dissolution of carbides [75] and so forth. However, it has been reported in reference [77] that the presence of retained austenite is unimportant in contributing to the variation of toughness arising from changes in the austenitizing temperatures. The increase of toughness has been attributed to a large "effective" root radius, or a characteristic distance for fracture, resulting from dissolution of void-initiating particles at high austenitizing temperatures [77]. The increased austenitizing temperatures coarsens the microstructure significantly with increased particle spacing. This coarsening of the microstructure with increased particle spacing is believed to be responsible for the increase in sharp-crack toughness.

### **3.2 PRECRACKING**

Fatigue cracks can initiate and grow from regions of stress concentration under the influence of far field fully compressive loadings. Previous studies in this area are found in references [80,81,82]. This method of producing cracks under overall cyclic compression was utilized in our study for developing physically short cracks. In the

present study, cracks were grown from double edge notched (DEN) specimens of steel and aluminum under far field cyclic compression to obtain initial long cracks. As described in Subsection 2.2, the material was then removed to obtain short cracks.

The DEN specimens were fatigued in load control under constant amplitude cycling at an R ratio ( $P_{min}/P_{max}$ ) greater than 100. The specimens had notch lengths of 1.27 mm (steel) and 2.54mm (aluminum). The notch tip angle was 45°. The crack lengths on both the faces were monitored. A typical crack length versus cycles is shown in Fig. 3.1. Note that cracks get arrested after some length as they grow out of the region of tensile stresses. In general, it was observed that the crack length  $l_p$ , resulting from this method of precracking, ranged between the cyclic ( $r_{cy}$ ) and monotonic ( $r_m$ ) plastic zones. That is,

$$r_{cy} \leq l_p \leq r_m$$

where

$$r_{cy} = \frac{1}{2x\pi} \left[ \frac{\Delta K}{2\sigma_y} \right]^2$$

$$r_m = \frac{1}{2x\pi} \left[ \frac{K_{max}}{\sigma_y} \right]^2$$

$x = 1$  for plane stress, and  $x = 3$  for plane strain.

The crack growth rates are plotted as a function of crack length in Fig. 3.2 for the same tests at two different values of stress range. It was also observed that, for a

given value of stress range, the length of the arrested crack is longer in coarse grain size material than in the coarse grain size material of steel. Also, the lower the strength, the longer will the arrested crack length be. In a log-log plot of stress intensity range versus the arrested crack length, (this is not shown here), it was found that the slope of the fitted line was 2.104. This indicated that the arrested crack lengths were proportional to  $r_{cy}$ . In a few cases where the precracking resulted in shorter crack lengths than the desired length, the specimens were cycled in tension at low values of stress intensity by load shedding techniques.

#### ***Discussion on Precracking under Fully Compressive Loadings***

**Note** that tensile residual stresses ahead of the notch under overall cyclic compression start a crack. The region of the tensile residual stresses is pictured in Fig. 3.3 for an ideally elastic plastic material similar to the region of compressive stresses in overall tension loading. In this figure, the monotonic ( $r_m$ ) and cyclic ( $r_{cy}$ ) plastic zones are shown.

The growth and extent of cracks under far field cyclic compression depend upon the stress state, that is plane stress or plane strain, stress level, stress ratio, and microstructure. (In the context of the present investigation, the influence of the factors mentioned above were studied. However, the details are not reported here.)

The advantages of this method of precracking under far field cyclic compression are listed below :

- This produces a uniform crack front with a sharp crack tip.
- As the crack gets arrested after some growth, there is no need for load shedding to obtain low crack growth rates.
- The history effects of this procedure result in very insignificant plasticity effects for further testing.
- This procedure is suitable to produce "short cracks" which are being investigated for their characteristic behavior.

### **3.3 RESIDUAL STRESSES AND ELECTROCHEMICAL POLISHING**

The properties and characteristics of the surface layer are important for the usual nucleation of cracks on the surface. The residual stresses are a direct result of machining, (by cutting and grinding) in the production of the specimens. By grinding, the surface layer gets the characteristic residual tension stresses. The thermal processing or heat treatments carried out may also result in some residual stresses. As the crack length measurements made in this study were only on the surface, it was important to obtain a surface free of any residual stresses.

After the specimens were machined after precracking, they were checked for residual stresses. An X-ray diffractometer was used to measure residual stresses. The 2024-T351, aluminum specimens showed relatively low residual stresses such as 41-48 MPa whereas 4340 steel specimens showed unacceptably high compressive residual stresses to the order of 200-275 MPa. It was therefore necessary to relieve these residual stresses on the surface.

Aluminum specimens were chemically polished in a solution of 700ml of phosphoric acid, 30ml of nitric acid, 120 ml of acetic acid, and 150 ml of water. The solution was heated to 90 to 95°C and the specimens were immersed in this solution for 2 to 4 minutes. This was enough to remove about 50 to 100  $\mu\text{m}$ , and was also enough to relieve the stresses on the surface. It was necessary to prepare fresh solutions often since increased concentration of aluminum in the solution decreased the rate of the material removal and hence, of the quality of finish.

The 4340 steel specimens showed relatively high residual stresses. The residual stresses were observed to be present in the same order of magnitude on all four sides of the test section. It was necessary to determine the amount of material that was needed to be removed from the surface layer to get a stress free surface. In order to do this, selected samples of 4340 steel were chosen and chemically polished. The chemical polishing of steel involved a solution containing 252ml of oxalic acid (100gms/liter), 36ml of hydrogen peroxide, and 720 ml of distilled water. Specimens were immersed in this solution at room temperature. Since 4340 steel is an alloy steel, a passive film forms on the surface of steel, thus reducing the rate of material removed. Curve A in Fig.3.4 shows thickness removed as a function of time. The rate of material removed is greater in the beginning and reduces considerably to reach a limit. In order to remove more amounts of material, a method was adopted where, the specimens were removed from the solution after 1 hour, cleaned to remove the passive film, and immersed in a freshly prepared solution. This method aided in removing more amount of material in a given time. Curve B in Fig.3.4 corresponds to this method of metal removal.

At each step, the residual stresses were measured after removing the specimens from the solution. This resulted in residual stresses as a function of thickness removed. This is plotted in Fig.3.5. By removing 0.025 to 0.038 mm, the surfaces of the specimens become relatively stress free.

After establishing the necessary thickness to get a stress free surface, the specimens were electropolished on a large scale, to remove 0.051mm of material from all surfaces. Electropolishing of steel specimens was preferred to chemical polishing because the surface obtained by chemical polishing is inferior to that obtained by electropolishing.

### 3.4 STEREOIMAGING

The stereoimaging technique can be adapted to fatigue crack growth studies [83] and also offers a simple and easy method to detect crack closing and opening. This method additionally provides information on the displacement field around the crack tip. A notable feature of this method as adopted by Davidson et al [46,83,84] reveals that they were able to study microcracks of 7 to 10 $\mu$ m lengths at high resolution. Accurate measurements were obtained in their study with the aid of in situ testing facilities under a scanning electron microscope. High quality pictures at high magnifications (x10,000) were obtained to study details of microcracks at high resolution from a scanning electron microscope (SEM). It was thus possible in their study to quantify strains of the order of 100 percent within 1 $\mu$ m of the crack tip. This tech-

nique is perhaps the best high resolution method known for study of fracture processes.

The stereoimaging technique adapted in the present study utilizes a low power microscope and a single lens reflex camera to study the growth behavior of cracks of length greater than 0.15mm. The resolution is not as great as for the SEM technique, but equipment needed is more readily available. This technique therefore offers a viable tool to detect crack opening and closing points of physically short cracks. The displacements in front of the crack tip can also be quantified using the technique. In this section, the principles of stereoimaging and a detailed description of the method adopted are described.

### ***Principles of Stereoimaging***

Stereoscopic vision is a natural phenomenon associated with our vision and provides a "powerful and accurate means of locating objects in space" [85]. With the aid of stereoscopic vision, perception of three dimensional images is possible by looking simultaneously at two photographs (two dimensional) of the same scene, taken from two viewpoints, each with one eye. "This powerful eye-brain relationship resulting in the perception of three dimensional images is due to the horizontal disparity between the two retinal images of the eyes" [85].

The principle of stereoscopic viewing is explained with reference to Fig.3.6. If two dots (2 to 3mm diameter) of similar size are drawn on a sheet of paper, separated by a distance  $x$  (60-70mm), and held at a distance greater than 0.2 to 0.3m from the eyes,

then we will be able to perceive a single image of the two dots at some distance  $y_1$ . This is possible only if the left and right eye concentrate on the left and right dot respectively. If another pair of dots separated by a distance  $x + \delta x$  are also drawn, and the line joining these dots is parallel to the line joining the other pair, and if viewed stereoscopically, the viewer gains an impression that the second pair forms an image at a distance  $y_2$  from the eyes. The perception of depth,  $y_2 - y_1$ , is because of the difference between the parallax angles,  $\phi_2 - \phi_1$ . Detailed descriptions of photogrammetric techniques and stereoimaging are given in references [86,87,88].

Stereopairs of pictures are needed for stereoscopic viewing. The stereopair of pictures are essentially pictures of the same scene or the object taken from two viewpoints. It is possible to perceive a continuous uninterrupted stereoscopic image while stereoscopically viewing, by shifting the gaze continuously from point to point. This principle has been extensively used in aerial surveying to perceive height as a third dimension. The present study differs from the method utilized in aerial surveying in that, relative, highly localized, in-plane displacements of a cracked specimen are imaged as a third dimension.

To perceive in-plane displacements as a third dimension, a stereopair of pictures in our study comprises two pictures of the crack tip and its vicinity, taken from the same viewpoint but at two different loading conditions. This is in contrast to stereoimaging studies done in aerial surveying, where the stereopair of pictures comprises two pictures of the same scene taken from two different viewpoints. Thus, when the stereopair of pictures is viewed under a stereoviewer, such as a mirror stereoscope,

the relative in-plane displacements manifest themselves to the viewer as a third dimension, so that valleys and hills are seen in the stereoviewer.

### ***Principle of Stereoscope***

The ability of the observer to see a stereoscopic image while looking through a stereoscope, is based on the slight variation of parallax from point to point. Figure 3.7 shows a schematic diagram of the mirror stereoscope. The principle of mirror stereoscope which was used in the present study, consists of a pair of reflecting prisms  $a$  and  $a'$ , and a pair of wing mirrors,  $b$  and  $b'$ , each of which is oriented at  $45^\circ$  with the plane of photographs. The total optical path distance  $e - a - b - c$  and  $e' - a' - b' - c'$  varied from 200 to 450 mm. A pair of meniscus lenses are provided above the prisms  $a$  and  $a'$  to make viewing comfortable.

### ***Experimental Procedures***

The method used to take pictures of the specimen in the laboratory involves using a low power Bausch and Lomb Model Stereozoom 7 microscope (up to x120), a camera adapter, a trinocular tube, a connecting tube, a single lens reflex camera (Nikon F3) with an extension tube, eyepieces (x5 or x10), and a polarized light source. Figure 3.8 illustrates a schematic diagram of the experimental setup.

The camera adapter is mounted on the low power stereozoom microscope. This adapter provides a third opening for positioning the trinocular tube for photomicrography. The visual and the photomicrographic optical systems are

parfocal, that is an image seen visually will also be in focus when seen through the trinocular tube. A prism in the camera adapter is used to change the light path from the visual system to the photomicrographic system, making it impossible to see the field while the photograph is being taken.

The fatigue tests described in Subsection 2.3 are interrupted to make a detailed study of the growing crack in the specimen at different crack lengths by stopping the test and taking pictures. The following describes details of the technique. The microscope with the camera adapter mounted on it was hung from an attachment to the top grip. A rack and pinion attachment facilitated positioning the microscope at a proper distance from the specimen for best focus. The region of interest in the specimen, such as the crack tip vicinity, was illuminated by a polarized light source through one of the binocular openings of the microscope. Also, an external fiber-optic light source was used as an aid for better viewing. Since light scatter is very important to obtain good quality pictures, both light sources were properly adjusted so as to get a good image.

The single lens reflex camera is used in our study by removing the lens from the body and placing an extension tube in the lens position. A finely ground fresnel field focusing screen was used in the camera for better viewing at high magnification. A microscope adapter ring containing the proper eyepiece was fastened to the front of the extension tube. This assembly of the camera, extension tube and adapter ring was mounted on a tripod. This setup was then connected to the microscope by a connecting tube. This connecting tube helped in getting a proper image size and magnification of the area pictured. For images at low magnification, the connecting

tube and the eyepiece in front of the extension tube were removed and pictures taken.

A medium speed panchromatic 35mm film was selected after trying several other choices. Pictures of good quality were dependent on the film used, the maximum magnification possible through the microscope, and the optical quality of the system. Pictures of good quality up to magnification of x100 were possible with this setup. Since it was important to expose the film properly, several trial photographs were taken to get a good picture. Often, for good photographic focusing, several pictures were taken either way from the point of best focus, since best visual focus and the best photographic focus of this system did not always precisely coincide. Note that the distortion of the picture increases with higher magnification.

Pictures of the crack tip and its vicinity were taken while keeping vibrations to a minimum at magnifications of x30 to x70. Another set of pictures of the same region was taken at a different loading condition of the specimen without altering the position of the camera. In this way, many sets of pictures were taken to describe one fatigue cycle of the specimen. Usually two or three pictures were taken at each point to assure at least one of good quality. These pictures were then enlarged six to eight times before being viewed under a stereoviewer. It is advantageous to take pictures at low magnification and then enlarge them rather than to take pictures at high magnification, because of the difficulties encountered such as focusing, vibrations, less area of the specimen covered at high magnification. As it was important to have minimal distortion while enlarging, checks were made to measure distortions by

comparing squares and rectangles in original negatives with enlarged ones. These distortions were insignificant.

### ***Quantification of Displacements***

The stereopair of pictures obtained by the method described above were placed under a mirror type stereoscope sketched in Fig 3.8. Note that only enlarged negatives were used instead of positive prints because the glossy and uneven surface of positive prints made viewing under a stereoscope difficult. To permit viewing of the stereoscope image comfortably, several necessary adjustments were made, such as separating the photographs slightly, rotating either the photograph or the stereoscope slightly, or a combination of both.

The three-dimensional image seen is a consequence of the relative in-plane displacements between the two pictures in the direction along the axis of the eyes. Note that if the two pictures are switched left versus right, the image seen is inversed of the first. In other words, elevations would appear as depressions and depressions as elevations. In principle, it is possible to view the relative in-plane displacements in any direction by rotating the photographs to the desired direction relative to the axis of the eyes.

Quantification of the three-dimensional image seen is based on the principle of the "floating mark" (Fig.3.9). If two marks of the same size are placed in the corresponding position on each of the photographs of the stereopair and viewed stereoscopically, the two marks fuse into one image at some position in the image

space. The viewer will experience the sensation that the image of the mark is floating in space above the ground. When one of the marks is moved either way, the image appears to have been lowered or raised in position. This principle of the "floating mark" is utilized in making measurements using a parallax bar.

The parallax bar is schematically sketched in Fig.3.10. The parallax bar contains the bar proper, which holds a fixed platen of transparent material near the left end and a movable platen towards the right end. A measuring or a reference mark is located at the center of each platen and below the surface shown. The movable mark is moved by means of a micrometer screw. The micrometer can read to the nearest 0.05mm. Hence, the accuracy to which the displacements can be measured depends on this and the magnification of the pictures. Parallax measurements are made with reference to a known distance of separation,  $x$ , between the two pictures, such as a point which experiences no relative in-plane displacement. The points which appear elevated in the stereoscopic image will have a lower distance of separation,  $x - \delta x_1$ , and the points which appear to be sunk will have a larger distance of separation,  $x + \delta x_2$ , as quantified from the parallax bar. Figure 3.11 illustrates how the eye-brain visual system accomplishes this imaging. The parallax measurements are then transformed to displacements based on the magnification of the pictures. Crack opening displacements along the length of the crack are obtained in a similar way by making parallax measurements on corresponding points on each of the crack faces.

Crack opening and closing points are obtained by a set of pictures taken near the macroscopic closing and opening load levels, where we can observe the crack tip to

be either open or closed. Essentially, by comparing a picture with the crack closed at the tip, and a picture where the crack tip has just opened, we can see the projected edge extending right up to the tip. In a similar way, crack closing points are also measured with respect to a picture with the crack fully open. Figure 3.12 shows a schematic diagram describing the technique of detecting crack opening point. Note that crack opening and closing points determined by this system of measurement are directly related to the resolution of the pictures taken. A comparison was made between the crack opening points determined by this technique and the empirical relation of Elber [17], for crack opening levels of long cracks in 2024-T351 aluminum. This is shown in Fig 3.13. This demonstrates that reasonable crack opening points are being obtained using this technique.

The illustrations discussed below describe the technique. Figure 3.14 shows a crack 1.16mm in length in LF condition of steel at maximum, minimum and opening points of a fatigue cycle at a R ratio of 0.1. The stress intensity corresponding to the crack length and loading configuration was  $12.3 \text{ MPa}\sqrt{\text{m}}$ . The stereopair of pictures, taken at maximum and minimum points of the cycle, was used for quantifying the relative in-plane displacements in the direction perpendicular to the crack. The technique of quantifying the displacements is subject to human measurement errors. Since coordination and good perception is necessary at all times while quantifying the image, this technique of measurement is especially subject to errors. To minimize these errors, usually two or three sets of reading were taken at each point, while quantifying the image. The mean of the readings was taken at each point. The displacements were quantified by parallax measurements at 70 different points in the image space. Figure 3.15 shows such a displacement map. Because of the limitations on the ac-

curacy to which measurements can be made from the parallax bar, displacements in the direction of the crack could not be measured in the present study. Crack opening displacements along the length of the crack were quantified in a similar way by obtaining parallax measurements on the two faces of the crack. Fig. 3.16 shows the crack opening displacements as a function of the crack length at maximum and opening points.

### ***Discussion of the Stereoimaging Technique***

The technique of stereoimaging has already been shown [46,83,84] to provide a more qualitative and a mechanistic understanding of growth behavior of short cracks. The technique described in this section is relatively inexpensive and simple. Although the resolution limits the measurement of displacements very near the crack tip, crack opening and closing points of cracks of length greater than  $150\mu\text{m}$  can easily be obtained.

It is important to have high quality pictures for parallax measurements. Since image definition is critical, factors such as light scatter, granularity of the film, and the method of processing the film are important. More important are the optics of the system itself, such as the microscope and the lenses used and the type of camera. The quality of the image on the film may be degraded because of vibrations, inability to focus well, misalignment of focal plane position, or failure to keep the axis of the optics system perpendicular to the film plane. The single lens reflex camera used in our study does not have any fiducial marks by which the interior orientation can be measured. Thus, the interior orientation, including the radial distortion of the photo-

graphs, is unknown. Also, there is some ill conditioning of the light rays emerging from the specimen since the image does not cover the full portion of the photograph. Image quality depends, to a great extent, upon factors related directly to the lens itself such as focal length, spherical aberration, field curvature, distortion, and lateral chromatic aberration. If we wish to make a thorough evaluation of image quality over the whole area of the picture, we need many determination measurements. However, the image evaluation was made with a resolution test and distortion was checked by simple geometric considerations by using horizontal lines and vertical lines on the specimen. It was thus possible to use details on the specimen surface as control points for determining distortions. Surface preparation is important before taking pictures. A textured surface with distinct detail helps in getting pictures with suitable features to facilitate comfortable stereoscopic viewing and quantification of displacements. Various surface textures were successfully employed in our study, including inclined polishing marks, electropolished surfaces with microscopic pits, and surfaces sprayed with chalk dust.

Accurate measurements are possible only when the pictures are of a high resolution. Increasing magnification does not improve the resolution. The accuracy to which the parallax measurements can be made can be improved by using more sophisticated equipment, such as an "analytic plotter" or a "photogrammetric analyzer." Use of these also saves the laborious task of quantifying displacements from the parallax bar. Whatever method of measurement is used, interpretation of the stereoscopic image is more complex. Note that loading of the specimen sometimes induces certain changes in the through-thickness (out-of-plane) direction of the specimen. However, these changes were so small that it was not necessary to refocus the microscope.

Also, the specimens were firmly gripped so that they did not experience any significant tilt or rotation during loading. Thus, the contribution of any out-of-plane displacements in the stereoscopic image is minimal. The technique described in this study cannot be used to image out-of-plane displacements. Other methods, such as Moire interferometry, must be used to quantify out-of plane displacements.

High resolution of the pictures is needed for accurately determining the crack opening and closing events. These events can be determined accurately at high stress intensity levels with this simple technique. However, at very low stress intensity levels, crack opening and closing levels determined by this technique may not be accurate because of the low magnification and limited resolution of the pictures. Also note that this is a surface measurement technique. The results are therefore not representative of the behavior away from the surface except for plane stress cases where through-thickness effects are insignificant.

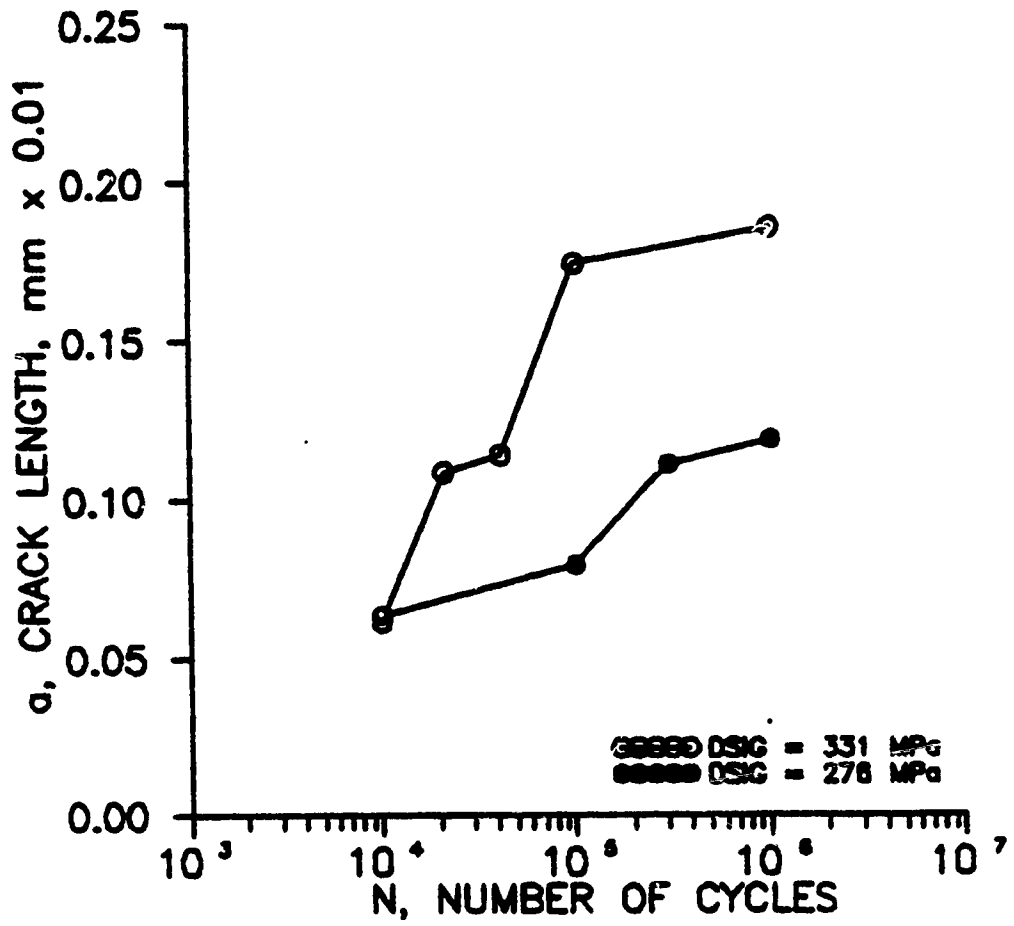


Fig. 3.1 Typical crack length versus cycles data for cracks growing under far field cyclic compression.

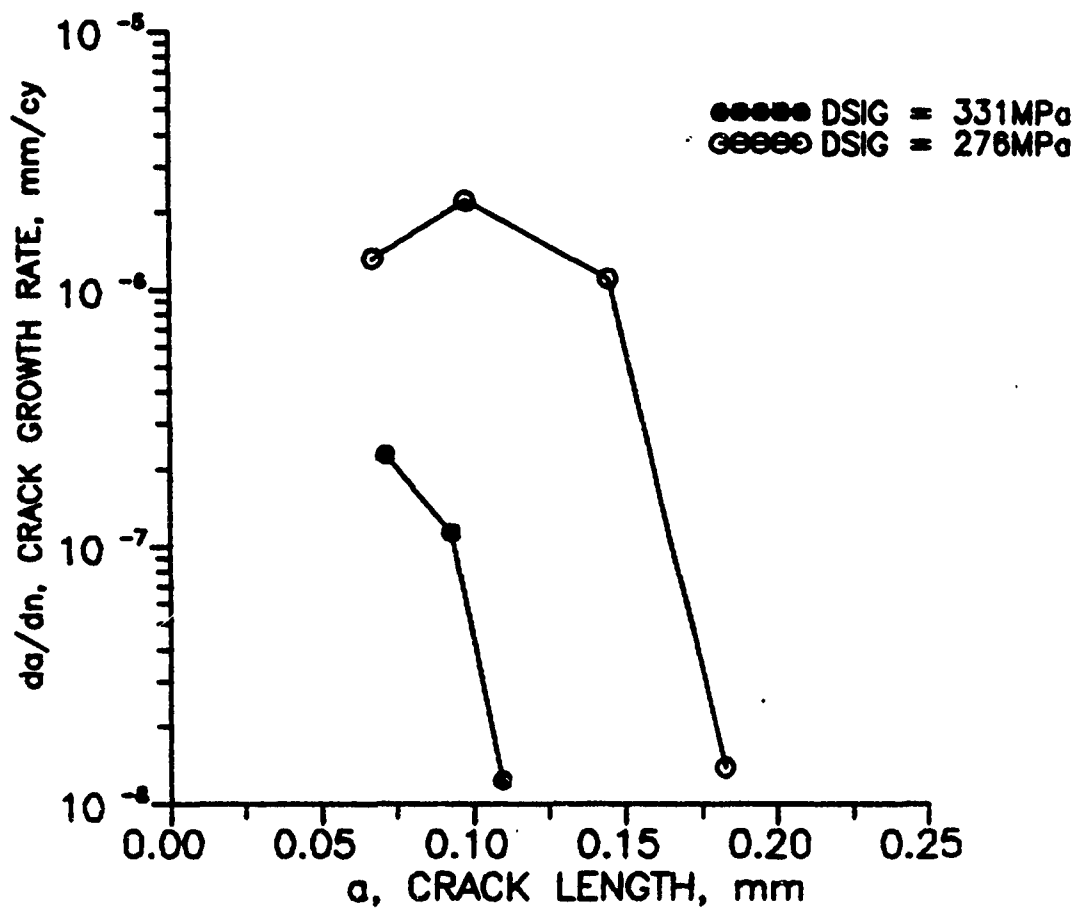


Fig. 3.2 Crack growth rate as a function of crack length.

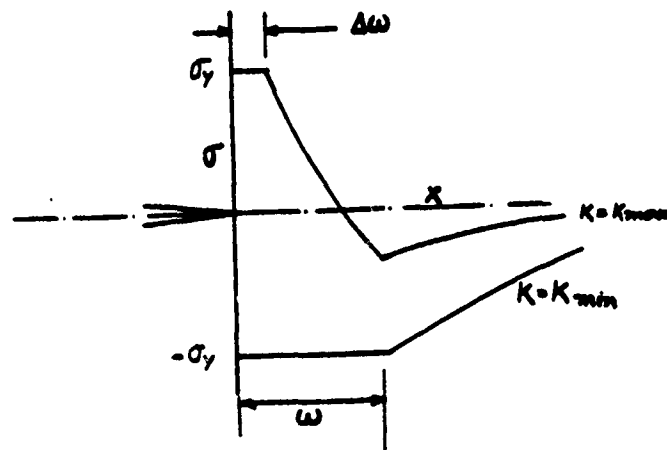


Fig. 3.3 Schematic diagram illustrating the region of residual strains in front of the notch under far field cyclic compression.

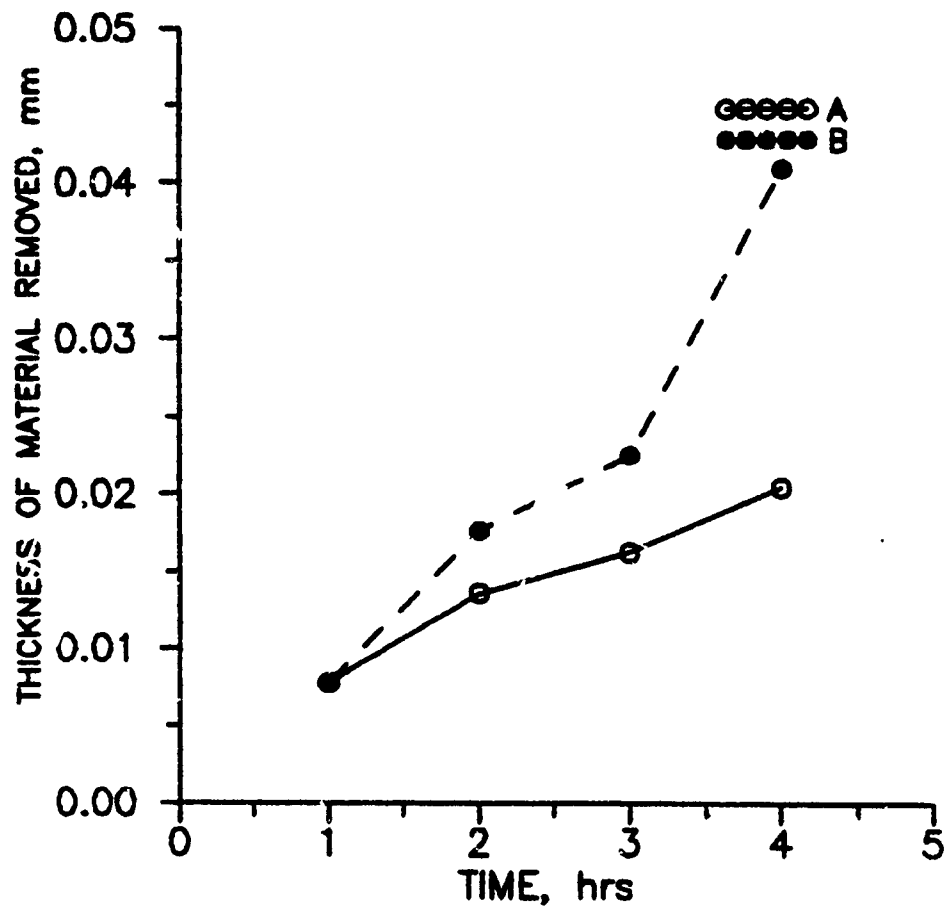


Fig. 3.4 Thickness of the material removed as a function of time.

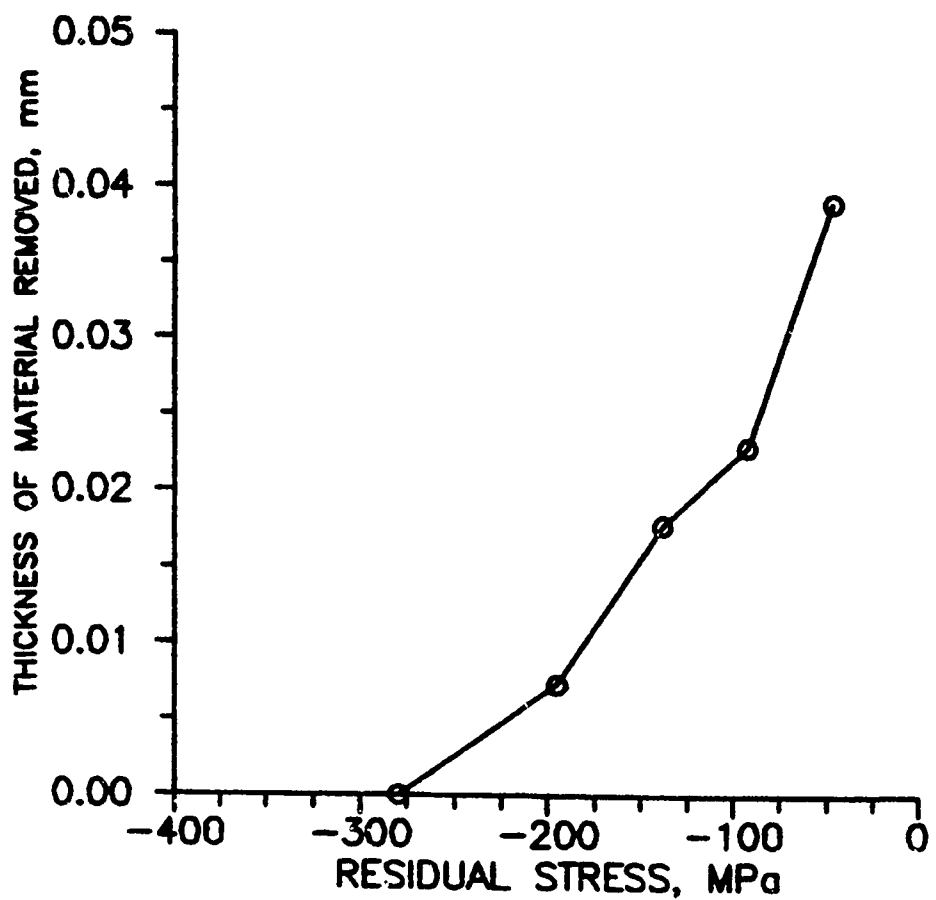


Fig. 3.5 Residual stresses on the surface as a function of the thickness of the material removed.

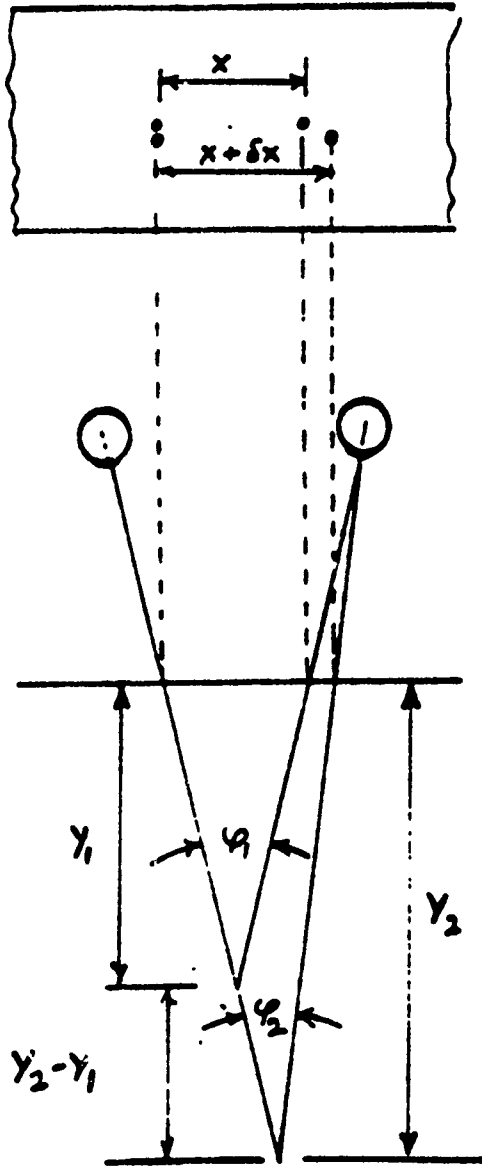


Fig. 3.6 Principle of stereoscopic viewing.

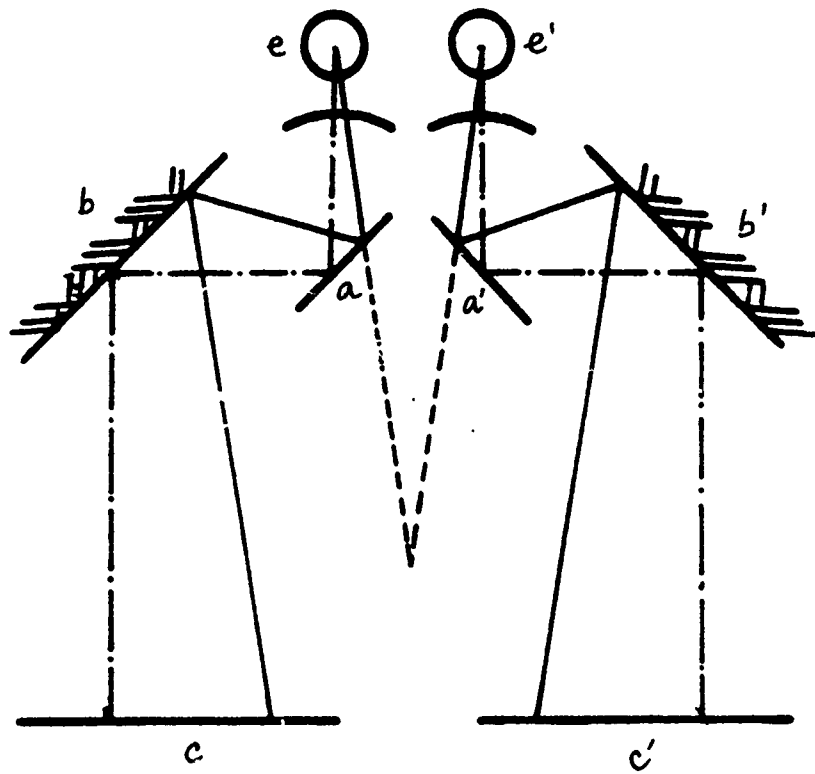


Fig. 3.7 Schematic diagram of a mirror stereoscope.

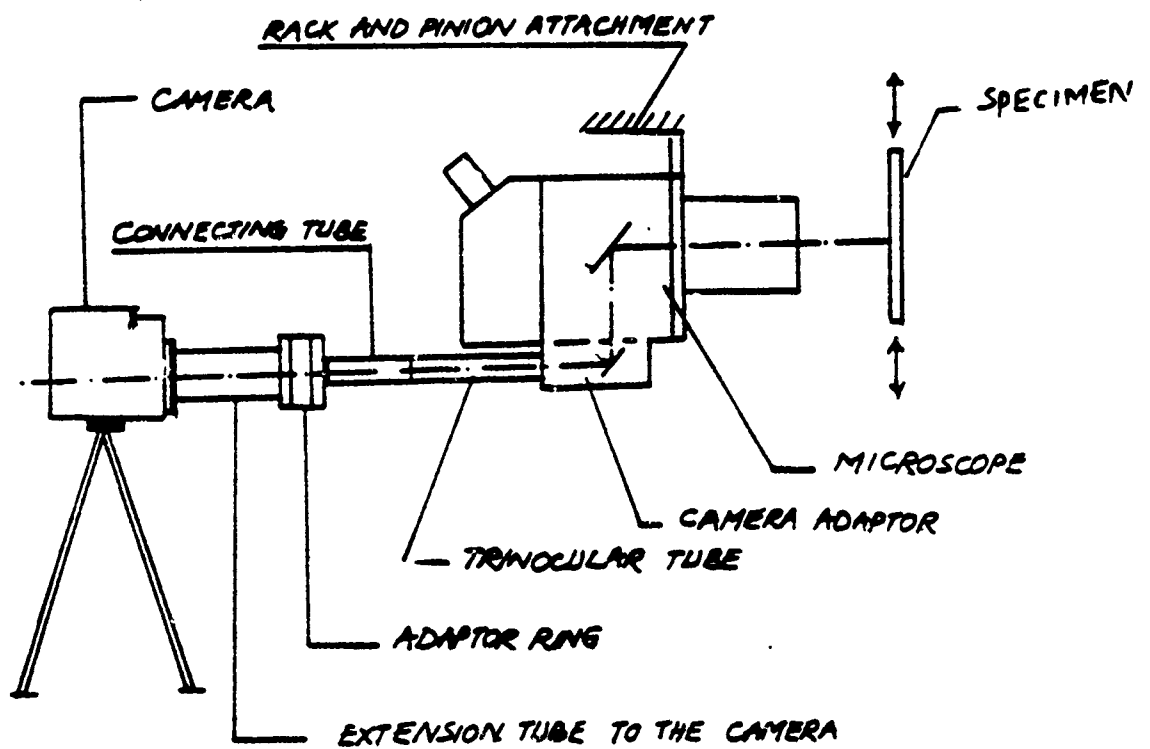


Fig. 3.8 Schematic diagram of the experimental set-up.

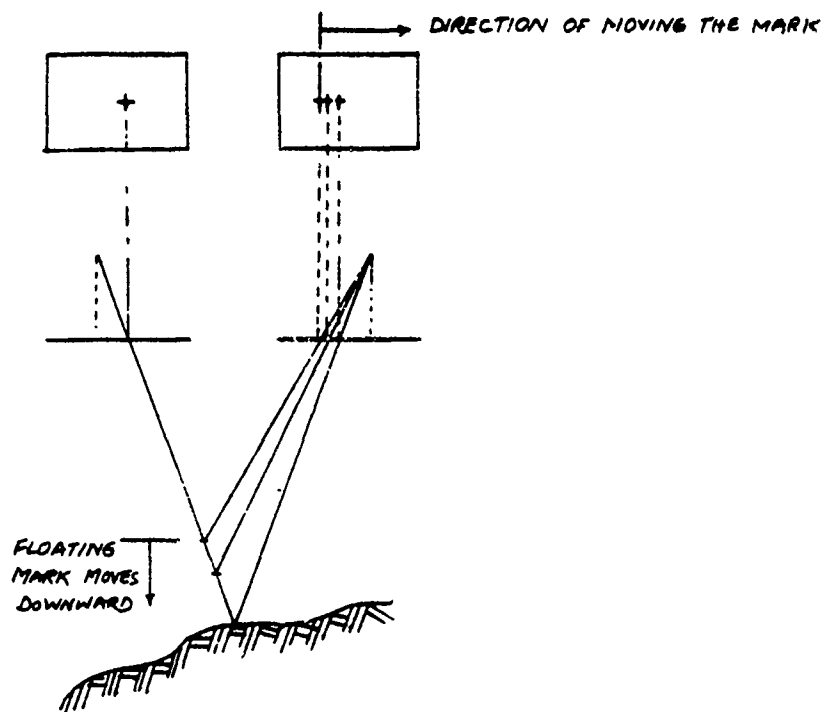


Fig. 3.9 Schematic diagram illustrating the principle of "floating mark."

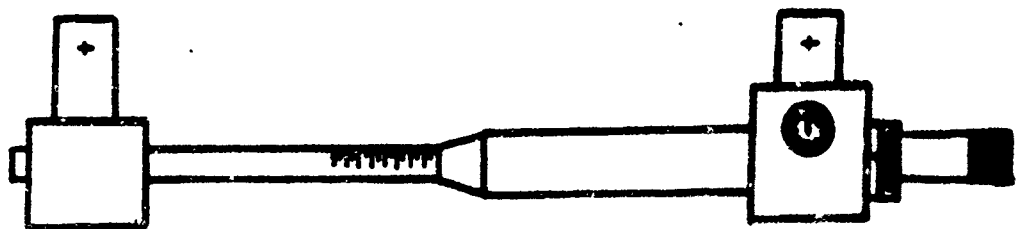


Fig. 3.10 Schematic diagram of the parallax bar.

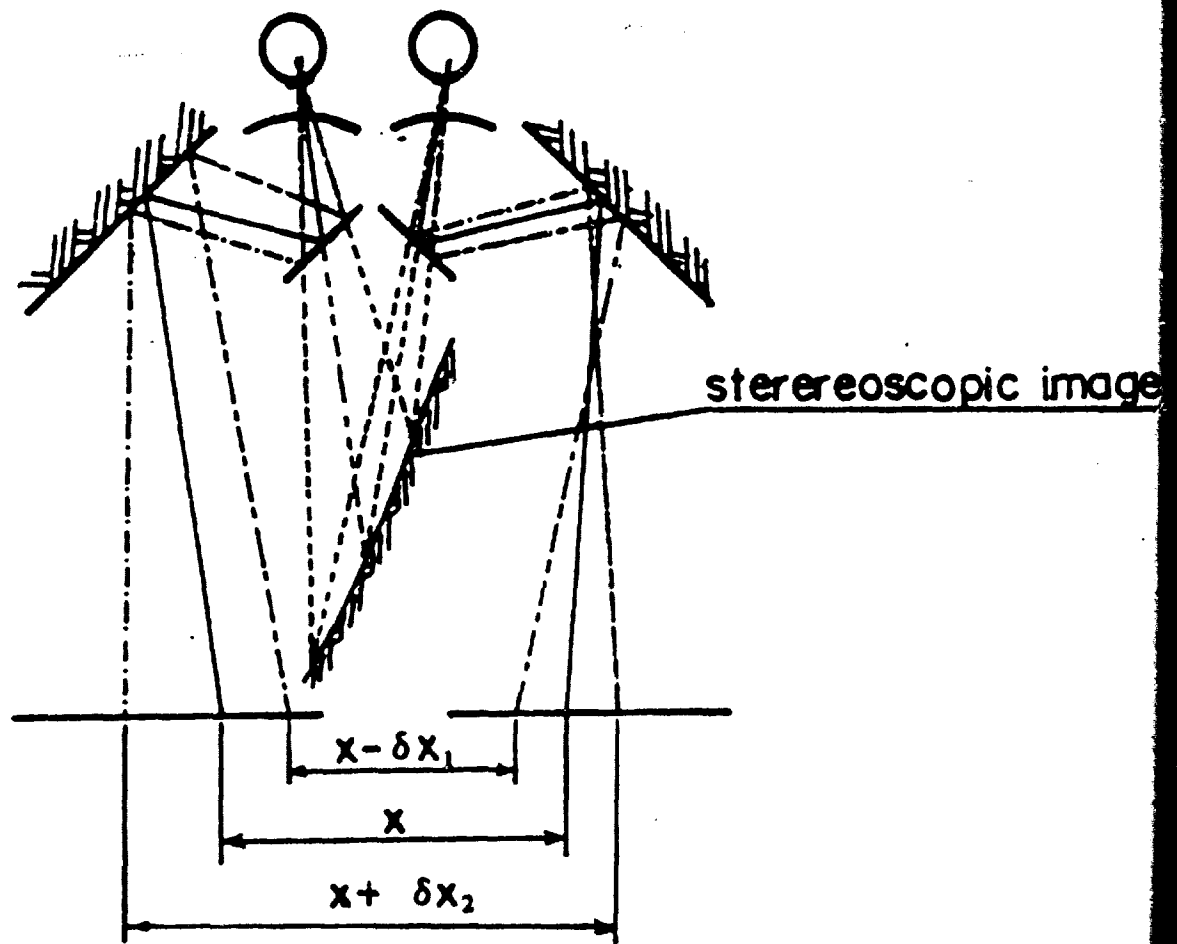
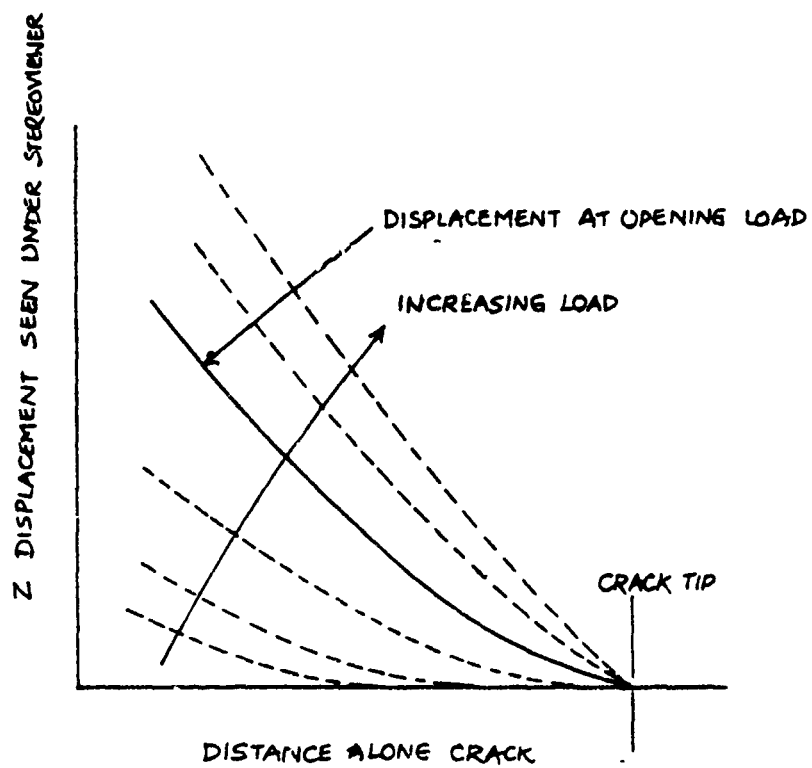


Fig. 3.11 Schematic diagram illustrating the eye-brain visual relationship.



NOTE : THE Z DISPLACEMENT SHOWN IS AT A SECTION THROUGH THE IMAGE SPACE TAKEN ALONG THE CRACK SITE

Fig. 3.12 Schematic diagram illustrating the technique of detecting crack opening point.

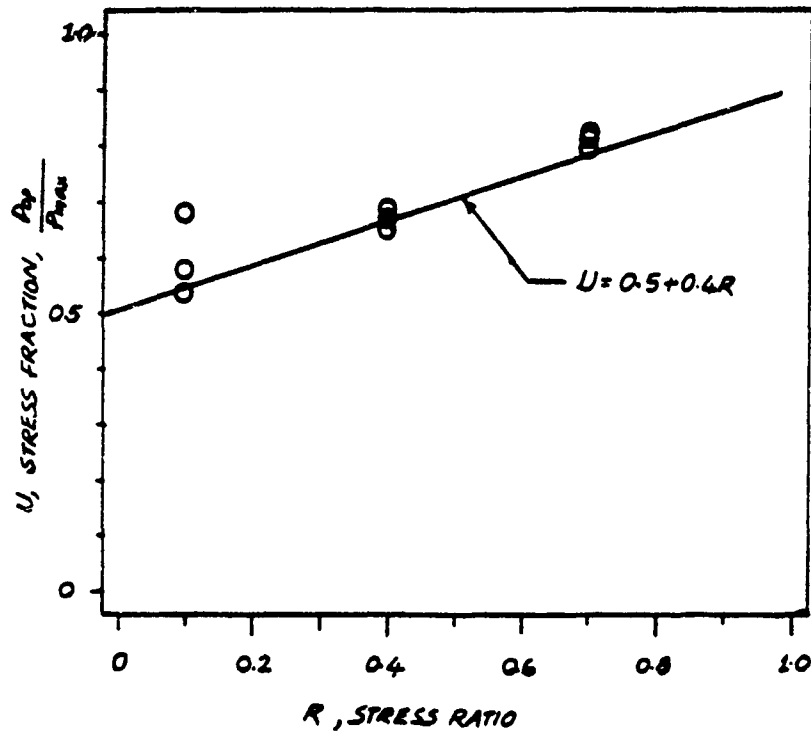


Fig. 3.13 Comparison of the opening levels determined by stereoinaging with Elber's [17] empirical relation in 2024-T351 aluminum alloy.

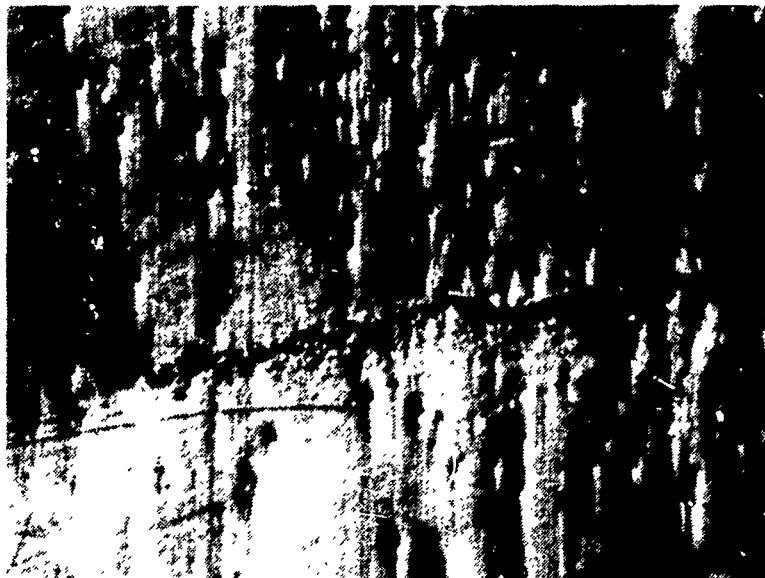
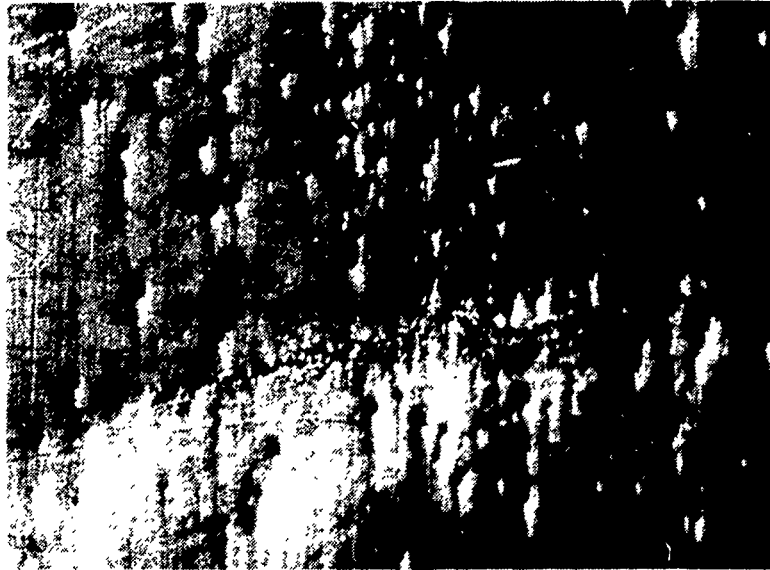


Fig. 3.14 Pictures (x86) of crack tip vicinity at minimum and maximum points of the loading cycle.

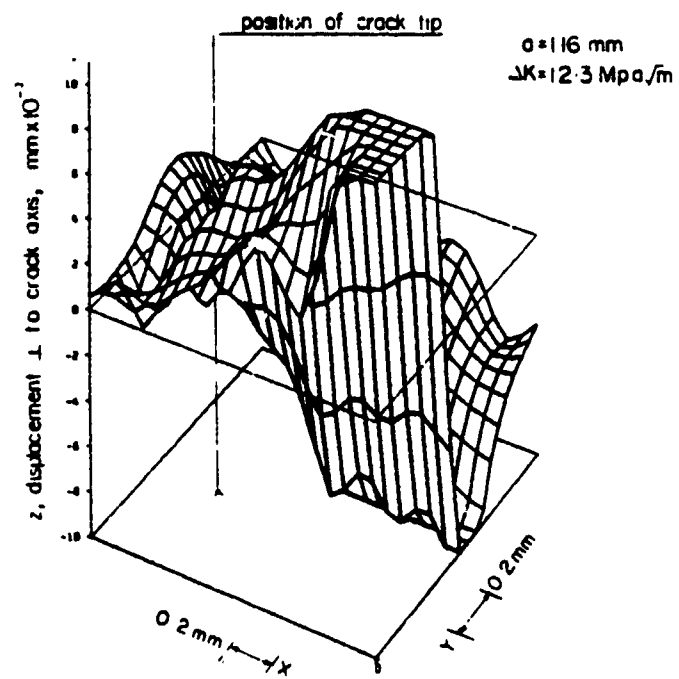


Fig. 3.15 Relative displacement in a direction perpendicular to the crack axis between the minimum and maximum points of the loading cycle corresponding to Fig. 3.14.

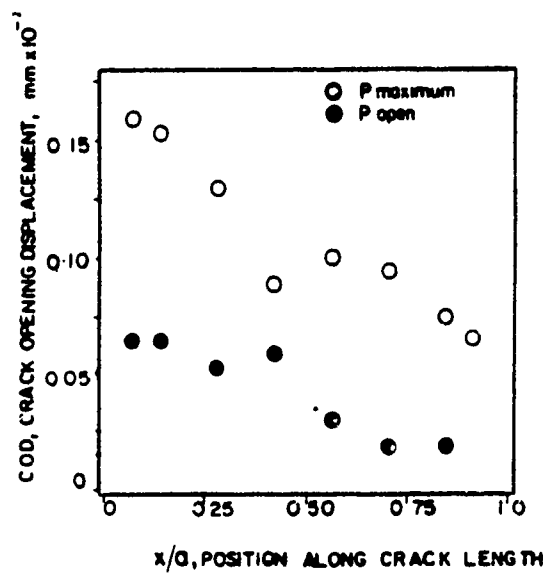


Fig. 3.16 Crack opening displacement as a function of crack length at maximum and opening points of the loading cycle corresponding to Fig. 3.14.

## **Section 4**

# **EXPERIMENTAL RESULTS**

### **4.1 MICROSTRUCTURAL CHARACTERIZATION**

The heat treatments which were carried out on 4340 steel resulted in four different conditions of 4340 steel - specifically, low strength fine grain size (LF), high strength fine grain size (HF), low strength coarse grain size (LC), and high strength coarse grain size (HC). Figures 4.1 through 4.4 reveal the microstructure of low strength fine grain size (LF), high strength fine grain size (HF), low strength coarse grain size (LC) and high strength coarse grain size (HC) respectively.

The prior austenitic grain sizes were determined from planimetric and comparative methods, in accordance with ASTM E112. A brief description of the planimetric (or Jeffries) and the comparative techniques of grain size determination is given below.

In the case of the planimetric technique, an inscription of known shape and area, such as a circle or a rectangle of  $5000\text{mm}^2$  area, is made on a photomicrograph of known magnification. The grains which are completely embedded inside the inscription are counted as one and the grains that are intercepted by the inscription are counted as half. The grain size is then determined by utilizing the Jeffries multiplier from ASTM E112. In the case of the comparative technique, grain sizes are determined by comparing the photomicrographs to the templates of known grain sizes.

The prior austenitic grain sizes determined by the above techniques for four different conditions of steel are given in Table 4.1. The grain sizes obtained from the present study were compared with the available data in the literature [75,77]. Figure 4.5 shows such a comparison. Note that there are differences in hold times and method of quenching from the austenitizing temperature between the present heat treatment procedure and the procedure adopted in reference [75].

#### **4.2 MECHANICAL PROPERTIES**

Uniaxial tension tests were carried out on tensile specimens shown in Fig. 4.6 for all four conditions of steel at ambient temperature and in a laboratory environment. The results of the tensile tests are shown in Table 4.1 along with the grain sizes. Note that these results are the average value of the two tensile tests carried out on the specimens in the direction of rolling. As expected, the fine grain conditions of steel showed a larger reduction in area and percentage elongation compared to the coarse grain conditions. The effect of tempering temperature on steel is evident from the fact

that when the tempering temperature is lower, the yield and ultimate strengths are higher.

The 2024-T351 aluminum was supplied by NASA Langley Research Center. This material is the same as used in the AGARD (Advisory Group for Aerospace Research Development) study. The microstructure and mechanical properties are widely reported in literature. The mechanical properties of the 2024-T351 aluminum are given in Table 4.2.

### **4.3 LONG CRACK FATIGUE TESTS**

In order to obtain long crack linear elastic data for 2024-T351 aluminum and four different conditions of steel at different R ratios, long crack tests were carried out on specimens discussed below. All tests were carried out under load control. Specifically, the long crack data were obtained for aluminum and all four conditions of steel at R ratios of 0.1, 0.4 and -1.0, and at R ratio of 0.7 for aluminum.

In the case of steel, specimens of single hole end configuration shown in Fig. 2.6 were tested to obtain long crack data. The specimen surfaces were polished at the site of the crack to facilitate better monitoring of the crack length. These specimens were pin-loaded and load controlled fatigue tests were carried out. Crack lengths were monitored using a x120 stereozoom microscope. The accuracy with which the crack lengths could be measured was 0.01mm. Frequencies that were used in testing were 10 to 15 Hz for positive R ratio tests, while frequencies less than 10 Hz were employed for completely reversed cycling tests. The alignment of the machine was

checked often with an alignment specimen to avoid any extraneous bending, and corrected when necessary.

Note that it is undesirable to conduct  $R = -1$  tests with a single hole end configuration specimens. However, tests were carried out with this configuration by checking the alignment of the machine at frequent intervals. Note that the thickness of the specimens used in these tests was 3.81mm.

In the case of steel specimens, a clip gauge of 12.5mm gauge length was mounted on one side where the crack was present and a trace of the crack mouth opening displacement versus the load was recorded to detect any global stiffness changes. It was observed that at longer crack lengths, that is, at high stress intensity ranges, the initial linear plot of crack mouth displacement versus the load showed a nonlinear behavior, indicating crack closure due to bulk plastic deformation.

Compact tension specimens of aluminum were precracked in tension-tension loading after applying an initial overload in compression. The long crack tests on 2024-T351 aluminum were carried out on compact tension specimens (shown in Fig. 2.1) in a similar way.

No threshold tests were carried out in these long crack tests as the objective of these tests was to get linear elastic long crack parameters. Thus, it is to be noted that the the results of the long crack tests, which will be presented subsequently, reflect only the linear region of the crack growth rate,  $\frac{da}{dn}$ , versus stress intensity range,  $\Delta K$ , plot. During these crack growth tests, the testing was frequently stopped and the

specimens were removed to check the crack lengths on the back face. The data points, where the difference between crack lengths on the front and back face exceeded 20%, were discarded for fine grain conditions of steel and aluminum. This difference was selected to be 40% for coarse grain conditions of steel.

The specimen surfaces were polished and distinctive features on the surfaces were provided for stereoimaging studies, as discussed in Section 3.4. Crack opening and closing points were detected at three or four different crack lengths by stereoimaging, as discussed in Section 3.4.

The crack growth rate,  $\frac{da}{dn}$ , was calculated from the crack length versus cycles data. The secant method, specifically point to point slope, was used in obtaining the crack growth rate. The applied stress intensity range was calculated using the following expression for single hole end configuration specimens of steel:

$$\Delta K = \frac{\Delta P}{wt} \sqrt{(\pi a)} [1.122 - 0.231\alpha + 10.550\alpha^2 - 21.710\alpha^3 + 30.382\alpha^4]$$

and using the following expression for compact tension specimens of 2024-T351 aluminum:

$$\Delta K = \frac{\Delta P}{t\sqrt{w}} \left[ \frac{2 + \alpha}{(1 - \alpha)^{3/2}} \right] [0.886 + 4.64\alpha - 13.32\alpha^2 + 14.72\alpha^3 - 5.6\alpha^4]$$

where,

$$\alpha = a/w,$$

$a$  = crack length, mm

$w$  = width of the specimen ( from the load line for CT specimens), mm

$t$  = thickness, mm

$\Delta P$  = applied load range, Newtons

$\Delta K$  = applied stress intensity range, MPa  $\sqrt{m}$

It is to be noted that the full range of stress was employed, namely  $K_{max} - K_{min}$ , for completely reversed cycling tests.

A regression analysis was carried out for the data of crack growth rate and stress intensity range, to obtain the linear elastic parameters,  $C$  and  $m$ , of the crack growth law:

$$\frac{da}{dn} = C[\Delta K]^m$$

The effective stress intensity fraction,  $U$ , was calculated at different stress intensity levels where the crack opening was detected by the stereoimaging technique. Note that  $U$  remained almost constant at these stress intensity levels. Effective stress intensity range was then calculated using the expression,

$$\Delta K_{eff} = U[\Delta K]$$

### **Long Crack Fatigue Test Results**

Figures 4.7 through 4.10 show the crack growth rate versus the applied stress intensity range for LF, HF, LC, and HC conditions of steel at R ratio of 0.1 respectively. Figure 4.11 shows a similar plot for aluminum. The constants C and m, which represent the intercept and the slope of the fitted line in the plot of the crack growth law, are also shown in these figures. Figures 4.7 through 4.10 show that there is no significant change in the crack growth rate for different conditions of steel for long cracks in the linear elastic regime (for crack growth rates  $\geq 1.5 \times 10^{-7}$ ). Figures 4.12 through 4.15 show the linear elastic long crack data for LF, HF, LC and HC conditions of steel at R ratio of 0.4 respectively. Similarly, Fig. 4.16 shows the long crack data for aluminum at R ratio of 0.4. R ratio effect is seen for aluminum where crack growth rates are higher at R = 0.4 than at R = 0.1. However, the effect of increased R is not that significant in the case of steel. The results of the long crack test at R ratio of 0.7 on aluminum is shown in Fig. 4.17. The growth rates at R = 0.7 are similar to the results of R = 0.4. In other words, there is no observable difference between growth rates at R = 0.4 and growth rates at R = 0.7. The long crack data from completely reversed cycling tests are shown in Figs. 4.18 through 4.21 for LF, HF, LC and HC conditions of steel respectively. Figure 4.22 depicts the data obtained for aluminum at R = -1.0.

In all these figures, the solid line shown is the least squares fit to the data. The parameters C and m of the crack growth law are shown at the right hand corner of the figure. Table 4.3 summarizes the results of the long crack tests for steel, where the

parameters C and m are given for each condition of steel. Table 4.3 also provides these parameters for aluminum.

The effective stress fraction determined, as described earlier, was utilized to obtain the effective stress intensity range. Figures 4.23 through 4.26 show the crack growth rate versus effective stress intensity range at R = 0.1 for LF, HF, LC and HC condition of steel. Similarly, Fig. 4.27 shows such a plot for aluminum at R = 0.1. Similar plots of crack growth rate versus the effective stress intensity range at R ratio of 0.4 are shown in Figs. 4.28 through 4.31 for LF, HF, LC and HC conditions of steel respectively. Figure 4.32 illustrates a similar plot for aluminum at R = 0.4. The crack growth rate at R ratio of 0.7, when plotted against effective stress intensity range is shown for aluminum in Fig.4.33.

Figures 4.34 through 4.37 depict the crack growth rate behavior when plotted against the effective stress intensity,  $\Delta K_{eff}$ , at R ratio of -1.0 for LF, HF, LC and HC conditions of steel respectively. Figure 4.38 shows a similar plot for aluminum at R ratio of -1. Note that in all these figures, the broken lines represent the least squares fit to the data. The constants C' and m' of the growth law of type:

$$\frac{da}{dn} = C'[\Delta K_{eff}]^{m'}$$

are shown in these figures. Table 4.4 summarizes the parameters thus obtained. A combined plot of crack growth rate data as a function of  $\Delta K_{eff}$ , under different R ratios is shown in Figs. 4.39 through 4.43 for LF, HF, LC, HC conditions of steel and aluminum respectively. Notice from these figures that effective stress intensity is able to

correlate the long crack data within a narrow scatter band. Also we can infer that including crack closure effects, the long crack growth rate data fall into a simple function of effective stress intensity range independent of the mean stress. The long crack data based on  $\Delta K_{eff}$ , for all four conditions of steel at all R ratios studied is shown in Fig. 4.44. The two solid lines in the Fig. 4.44 represent bounds for the data.

#### **4.4 SHORT CRACK FATIGUE TESTS**

The objective of the short crack tests was to carry out fatigue crack growth tests on specimens which have a known initial crack size of length less than 0.18mm under different R ratios and stress levels. Essentially, a matrix of tests under load control was carried out to establish the growth rate of short fatigue cracks at positive R ratios of 0.1, 0.4, and 0.7 on aluminum and all four different conditions of steel. Completely reversed cycling tests in load control were carried out only on steel specimens. Table 2.5 depicts the matrix of tests carried out on steel and aluminum specimens. Note that in the case of steel, the low stress level tests correspond to stress ranges of 138 to 185 MPa and the high stress level tests correspond to stress ranges of 248 to 307 MPa. In other words, the gross stress levels were still elastic. Similarly the low stress levels correspond to stress ranges of 100 to 115 MPa and high stress levels correspond to stress ranges of 135 to 146 MPa in the case of aluminum.

The short crack test (SCT) specimen design was discussed in Subsection 2.2. This allowed the SCT specimen to have an initial crack of known length and of straight crack front. The crack growth from a known initial point was thus well defined. The

initial crack length that was retained in these specimens varied from 0.12 to 0.18 mm, which is usually termed in most studies as a physically short crack.

The fatigue crack growth tests were similar to those of long crack tests. The propagation of these short cracks was monitored microscopically using the x120 stereozoom microscope. The crack lengths were measured by projecting the crack on to an axis perpendicular to the direction of loading. Crack length measurements were made up to a crack length of 1.85mm from the initial crack length. Note that crack length measurements of these short cracks are only surface measurements indicating that crack growth rate calculations are highly sensitive to local variations at the crack tip.

Some of the SCT specimens did not have an even crack length on both sides. These specimens were also utilized as single hole end configuration specimens which were discussed in Subsection 2.3. The applied stress intensity ranges were calculated using the following expression for SCT specimens:

$$\Delta K = \frac{\Delta P}{2wt} \sqrt{\pi a} \left[ \frac{1.122 - 0.561\alpha - 0.205\alpha^2 + 0.471\alpha^3 - 0.190\alpha^4}{\sqrt{(1-\alpha)}} \right]$$

where,

$$\alpha = a/w$$

a = the crack length, mm,

w = width of the specimen, mm,

t = thickness, mm,

$\Delta P$  = applied load range, Newtons

$\Delta K$  = applied stress intensity range, MPa  $\sqrt{m}$

The stress intensity range,  $\Delta K$ , was calculated for single hole end configuration specimens using the equation defined earlier in Subsection 3.3.

The specimen surfaces were prepared as discussed in Subsection 2.2. Pictures of the crack tip and its vicinity were taken at three or four crack lengths for stereoimaging studies. Crack opening and closing points at a crack length were determined from a set of pictures taken at different points in the load cycle. The description of the stereoimaging technique is discussed in Subsection 3.4.

Crack growth rate calculations were made using the crack length versus cycles data. The secant method of computing the slope (which is similar to the method adopted in long crack growth rate calculations) was adopted. In a few cases, during testing, the test was interrupted and the specimens removed to check the evenness of the crack on both the sides. During these checks, it was observed that the difference between the crack lengths on both sides did not exceed 20 percent of the average crack length.

The short crack tests on LC and HC conditions of steel at high stress levels at  $R = 0.7$ , and the test at high stress level at  $R = -1.0$  were not successful as the cracks grew very unevenly on both the sides limiting the stress intensity range calculations.

### **Short Crack Growth Rate Results**

The crack growth rate calculations will be presented in this section as a function of the applied  $\Delta K$ . The results are presented for the two stress levels for each condition of steel and aluminum. The solid line in these figures represent the linear long crack data fit.

Figures 4.45 through 4.48 show the crack growth rate as a function of  $\Delta K$  at  $R = 0.1$  for LF, HF, LC, and HC conditions of steel respectively. The short crack growth rate data is shown in Fig. 4.49 for aluminum at  $R = 0.1$ . The solid lines in these Figures represent long crack growth behavior.

In the case of LF condition of steel, short cracks show growth at a  $\Delta K$  of 5.2 MPa $\sqrt{m}$ . with initial crack growth rate of  $4.1 \times 10^{-6}$  mm/cycle. There is no significant difference between the growth rates at the two stress levels. In the case of HF condition of steel, the short crack growth rate data at both stress levels merge with the long crack data at  $\Delta K$  of 10-11 MPa $\sqrt{m}$ . Although there is scatter in the data points of Fig. 4.47, we can observe that for LC condition of steel, growth rates of short cracks are higher than the long cracks at low  $\Delta K$  levels. The low  $\Delta K$  levels correspond to cracks of length less than 0.392mm.. Note that the crack growth rate remains nearly the same at a value of  $1.2 \times 10^{-6}$  mm/cycle from 3-9 MPa $\sqrt{m}$ . High crack growth rates for short cracks in HC condition of steel are observed from Fig. 4.48. There is no discernible difference between the growth rates at two stress levels. In the case of aluminum, it is observed from Fig. 4.49 that the growth rates at high stress level are higher than the growth rates at low stress levels.

Figures 4.50 through 4.53 show the crack growth rate results at  $R = 0.4$  for LF, HF, LC and HC conditions of steel. Similar results for aluminum are shown in Fig. 4.54 at  $R = 0.4$ .

The initial high growth rates seen at both stress levels in LF condition at  $R = 0.4$  disappear at  $\Delta K$  value of about  $10.5 \text{ MPa}\sqrt{\text{m}}$ . Short crack growth data for HF condition of steel at  $R = 0.4$  follows the linear elastic data with no significant differences between the stress levels. Most of the data above  $\Delta K$  of  $11 \text{ MPa}\sqrt{\text{m}}$  for LC condition of steel at  $R = 0.4$  fall in the LEFM region. However, data points at very short crack lengths show a high crack growth rate. Even though there is scatter in the data points for HC condition of steel at  $R = 0.4$ , it can be observed from Fig. 4.53 that most data points fall above the the long crack data fit. The absence of stress level effect in the growth rates of short cracks is seen from Fig. 4.54 for aluminum at  $R$  ratio of 0.4.

Similar test results at  $R$  ratio of 0.7 are shown in Figs. 4.55 through 4.58 for LF, HF, LC and HC conditions of steel respectively, and in Fig. 4.59 for aluminum.

The results obtained for short cracks in LF and HF conditions of steel indicate the absence of stress level effects on growth rates. After a brief transient growth, the short crack data merges with the long crack data in LF condition of steel. The results at high stress level for LC and HC conditions of steel are not shown since only a few data points were obtained before the cracks started growing very unevenly. It is observed from Fig. 4.59 that in the case of aluminum, the growth rates at high stress levels are higher than growth rates at levels.

Completely reversed cycling test results at R ratio of -1.0 are shown in Figs. 4.60 through 4.63 for LF, HF, LC and HC conditions of steel.

In the case of LF condition of steel at  $R = -1$ , it is observed that short crack at low stress level shows a high growth rate ( $5.5 \times 10^{-7} \text{mm/cy}$ ) in the beginning, but decelerates to a growth rate of  $2.0 \times 10^{-7} \text{mm/cy}$  before joining the long crack data. The crack growth rate data ( $R = -1.0$ ) at high stress level shows a deviation from the long crack data in the beginning but merges with the long crack data as the applied  $\Delta K$  values increase with increase in crack length. In the case of HF condition of steel, no 'short crack effect' is seen at  $R = -1.0$ . In other words, the cracks show growth rates similar to those of long cracks at completely reversed cycling tests. In the case of LC condition of steel, the test results at  $R = -1.0$  reveal that growth rates decelerate from a high value before joining the long crack data at low stress level. Note that this deceleration of growth rates is absent at high stress levels.

In general, it is observed from short crack growth rate results presented for aluminum and different conditions of steel at different R ratios that, short cracks do not explicitly follow the long crack growth behavior. There exists a transition length below which the short cracks show a higher growth rate than the long crack growth rate. In most cases, the crack growth rates at high stress levels are slightly higher than a similar data at low stress levels. It can also be observed from these figures that the short crack growth rate data at both stress levels eventually merge with the long crack data.

The cracks in all these cases grew in a direction perpendicular to the loading axis as expected. In the case of fine grain conditions of steel and aluminum, the cracks maintained a smooth path. However, in the coarse conditions of steel, the crack followed a zig-zag path, but maintained an overall direction perpendicular to the loading axis.

### **Crack Opening Response**

The crack closing and opening points were determined by the stereomaging technique as described earlier in Subsection 3.4. The crack opening and closing points were determined at three or four selected crack lengths. The effective stress fraction,  $U$ , based on the crack opening load was calculated using the expression

$$U = \frac{K_{\max} - K_{op}}{K_{\max} - K_{\min}}$$

Similarly, the effective stress fraction,  $U'$ , based on the the crack closing point was determined using the expression

$$U' = \frac{K_{\max} - K_{cl}}{K_{\max} - K_{\min}}$$

The effective stress fraction,  $U$ , based on the crack opening load will be presented in the following discussion. In our experiments, continuous detection of crack opening

and closing points at each crack length was not carried out, as this involved laborious and time consuming effort in taking pictures and analyzing them by stereoimaging studies. To obtain the effective stress fraction at each crack length, the following procedure was adopted. Effective stress fractions obtained at each crack length was plotted against the crack length. An equation of the type,

$$U = \alpha[a]^\beta$$

where

$\alpha$  and  $\beta$  are constants and

$a$  is the crack length

was fitted to the data points. This equation was then used to calculate  $U$  at crack lengths less than 0.6mm.

Plots of effective stress fraction,  $U$ , versus crack length will be presented first for different  $R$  ratios at low stress levels in the following discussion. In these figures, lines which represent regression fits of the type mentioned earlier for the corresponding data points, are also shown.

Plots of  $U$  versus crack length for low stress level tests on steel are shown in Figs. 4.64 through 4.67 at  $R$  ratios of 0.1, 0.4, 0.7 and -1.0 respectively. Figure 4.68 shows similar results from low stress level tests on aluminum.

We can observe from Fig. 4.64 that the value of  $U$  is near unity in the beginning and decreases to a value near 0.6 for fine grain conditions of steel. Note that the values of  $U$  obtained from long crack tests were 0.62 and 0.64 for LF and HF conditions of steel respectively. It was observed for HF condition of steel that the value of  $U$  was higher than the value of  $U$  for LF condition at the same value of  $K_{max}$ . The crack opening levels for the coarse conditions of steel do not show any smooth behavior. In fact, the opening level for the LC condition of steel shows an increase with the crack length. This can be attributed to the discontinuous form of closure observed in the coarse conditions of steel.

The results obtained from tests at  $R = 0.4$  indicate that cracks exhibit less closure. This can be seen in Fig. 4.65 for different condition of steel and in Fig. 4.68 for aluminum. This was expected because of the increased mean opening displacement at increased  $R$  ratio.

The cracks remained open for the most part of the cycle in tests at  $R$  ratio of 0.7 in all conditions of steel as well as aluminum (Figs. 4.66 and 4.68). As mentioned earlier, the decreased closure behavior is apparent because of mean stress effects.

In the case of completely reversed cycling tests, the value of  $U$  decreased much faster than the value observed in positive  $R$  ratio tests (Fig. 4.67). At a crack length near 0.8mm, the value of  $U$  was 0.5 for all the four conditions of steel and aluminum. This indicated that for longer crack lengths, at  $R = -1.0$ , the cracks open only in the positive part of the load cycle. Note that the values of  $U$  obtained from long crack

tests at  $R = -1.0$  were 0.51, 0.524, 0.48 and 0.52 for LF, HF, LC and HC conditions of steel respectively.

The effect of increased stress level on the crack closure response was also studied. It was observed that increased stress level did not significantly change the value of  $U$  for all conditions of steel. However, in the case of aluminum, the values of  $U$  were higher than the values of  $U$  at low stress levels at the same value  $K_{max}$ . It was also observed that  $U$  at high stress levels stabilized more rapidly than that observed for lower stress levels.

In a normalized plot of  $K_{op}/K_{max}$  versus the monotonic plastic zone size,  $\left[ \frac{K_{max}}{\sigma_y} \right]^2$ , which is not shown here, it was observed that the normalized crack opening level increased rapidly in the beginning to stabilize at a value near 0.5 for fine grain conditions of steel at  $R = 0.1$ . It was also observed that the crack opens at a lower value of load for the same value of  $K_{max}$  for HF condition of steel. This is probably because of the fact that at the same value of  $K_{max}$ , plasticity effects near the tip and in the wake of the crack are lower in HF than in LF condition of steel.

From the crack opening response data obtained at different  $R$  ratios, it can be deduced that at higher  $R$  ratios, the cracks remain open for a larger portion of the loading cycle. It was observed that, following crack growth, the opening point moves up in the loading cycle in all cases. However, the rate at which the opening point moved up in the loading cycle was not the same for different  $R$  ratios. It was observed that there was less variation of the opening levels at increased  $R$  ratio tests.

In the case of completely reversed cycling tests on steel, cracks were observed to be open for the most part of the loading cycle during early growth stages, corresponding to crack lengths less than 0.3mm. However, at increasing crack lengths which is accompanied by increase of  $K_{max}$  the crack closure is significant. This can be observed from Fig. 4.67 where  $U$  decreases rapidly with an increase in crack length which corresponds to the rapid increase in the opening level with  $K_{max}$ . Note that for short cracks less than 0.50mm, the opening load level is still in the compressive part of the loading cycle.

### ***Crack Closing Response***

The stereoimaging technique was utilized to detect crack closing levels by a method similar to the detection of opening levels. The ratio of the effective stress fraction based on the opening level,  $U$ , to the effective stress fraction based on the closing level,  $U'$ , was calculated. Note that this ratio  $U/U'$  is

$$\frac{U}{U'} = \frac{K_{max} - K_{op}}{K_{max} - K_{cl}}$$

Figures 4.69 through 4.72 show the ratio  $U/U'$ , defined above, as a function of applied  $\Delta K$  for LF, HF, LC and HC conditions of steel respectively. It can be inferred from these figures that there exists a maximum of 10 percent difference between the opening and closing levels for LF condition of steel. In the case of HF condition, the difference is much smaller, being less than 5 percent. From the data of fine grain conditions of steel and aluminum, notice that the crack closing level is always less than the crack opening level. As mentioned previously, there is discontinuous closure

observed in coarse grain conditions of steel (Figs. 4.71 and 4.72). Observe from these figures that in a few cases, stress fraction based on the closing level,  $U'$ , is not less than the opening level.

### ***Effective Stress Intensity Approach***

The effective stress fraction based on the opening level,  $U$ , was utilized in computing the effective stress intensity range,  $\Delta K$ . As was pointed out in the previous section, the difference between stress fractions based on crack opening and closing was less than 10 percent in all cases. The  $\Delta K_{eff}$  based on the opening level will thus serve to indicate the utilization of effective stress intensity approaches for short cracks. Note that  $U$  was calculated at each crack length by fitting a regression fit to the data points at three or four crack lengths. The equation defined earlier for  $U$  as a function of crack length was utilized to obtain  $U$  for cracks of lengths less than 0.6mm. For cracks of lengths greater than 0.6mm,  $U$  from corresponding long crack test was utilized. In the following discussion, the crack growth rate data will be presented as a function of  $\Delta K_{eff}$ . In all these figures the broken line represents the regression fit to the corresponding long crack data.

The crack growth rate is plotted against the effective stress intensity range at  $R = 0.1$  in Figs. 4.73 through 4.76 for LF, HF, LC and HC conditions of steel respectively, and in Fig. 4.77 for aluminum at both stress levels. Notice from these figures that in HF condition of steel and aluminum, the utilization of  $\Delta K_{eff}$  yields a simple relation of crack growth rate as a function of  $\Delta K_{eff}$ . It can be observed from Figs. 4.75 and 4.76

that, no unique relation seems to exist for coarse conditions of steel because of the scatter seen in the data points.

The short crack test results utilizing  $\Delta K_{eff}$  at  $R = 0.4$  are shown in Figs. 4.78 through 4.81 for LF, HF, LC and HC conditions of steel and in Fig. 4.82 for aluminum. It can be noticed from these figures that the  $\Delta K_{eff}$  is able to consolidate the crack growth rates at two different stress levels in the cases of fine grain conditions of steel and aluminum. Again, no such good correlation is seen between growth rates at different stress levels in the cases of coarse conditions of steel.

Figures 4.83 through 4.86 show a similar plot of crack growth rate as a function of  $\Delta K_{eff}$  at  $R = 0.7$  for LF, HF, LC and HC conditions of steel. The growth rate data is shown in Fig. 4.87 for aluminum at  $R = 0.7$ . A similar behavior is observed for the cases of fine grain conditions of steel where  $\Delta K_{eff}$  is able to account for the difference in growth rates at different stress levels. Most of the data points in the case of aluminum, show a simple relation of  $\Delta K_{eff}$  except for a few data points during the early growth at high stress level test.

Crack growth rates are shown as a function  $\Delta K_{eff}$  in Figs. 4.88 through 4.91 for completely reversed cycling tests. The difference in growth rates at different stress levels tend to disappear when plotted against  $\Delta K_{eff}$  for fine grain and LC conditions of steel and aluminum.

Combined plots of growth rate as a function of  $\Delta K_{eff}$  at different R ratios are shown in Figs. 4.92 through 4.95 for LF, HF, LC and HC conditions of steel, and in Fig. 4.96 for

aluminum. These figures show that the crack growth rates at different positive R ratios seem to fall inside a narrow band. However, the results at  $R = -1$  differ significantly from the results at positive R ratios.

### ***Crack Surface Displacements***

Crack surface displacements were obtained by the stereoimaging technique at different crack lengths as described in Subsection 3.4. A few examples of crack surface displacements near the crack tip for different conditions of steel and aluminum will be presented in this section. Crack opening displacements along the length of the crack at maximum and opening levels of the loading cycle are also presented.

Figures 4.97 through 4.106 show the relative crack surface in-plane displacements in a direction perpendicular to the crack axis, between the maximum and minimum points of the loading cycle. The displacements were measured at discrete points in the photographs. These data points did not fall on the nodes of a rectangular grid. To create a three dimensional plot, it was necessary to generate the displacements at the grid nodes. This was done using the inverse distance method [89]. After generating grid nodal values of the displacements, a cubic spline was fitted to smooth the data. The figures shown above are the result of this smoothing. In these figures, the X-axis is in the direction parallel to the crack, the Y-axis in the direction perpendicular to the crack and the Z-axis represents the relative in-plane displacements between the maximum and minimum points of the loading cycle. The corresponding crack length  $a$ , applied  $\Delta K$ , value and the number of data points used in creating the three dimensional plots are indicated in these figures. A schematic sketch of the crack is

shown in the x-y plane of the base. Points which experienced no relative displacements between the stereopair of pictures were taken as the reference points for quantifying the displacements.

In general, it is observed from these figures that, the displacements increase towards the edge of the crack. The transition from one crack face to the other is evident in these figures from the steep jump in the displacement map.

The corresponding crack opening displacements for Figs. 4.97 through 4.106 along the length of the crack at maximum and opening points of the loading cycles are shown in Figs. 4.107 through 4.116. Note that in these figures the abscissa corresponds to the normalized distance along the crack length. In other words, distances along the crack length  $x$ , where the crack opening displacements were obtained, are normalized by the total crack length  $a$ , so that the value of 1 corresponds to the crack tip. Note that the crack opening displacements could not be measured accurately in the region very close to the crack tip because of the limitations of the measurement technique. Displacement gradients in the direction perpendicular to the crack axis, that is strains  $\epsilon_{yy}$ , which are not shown here, can be obtained by differentiating the displacements.

#### **4.5 SHORT CRACK FATIGUE TESTS IN NOTCHED SPECIMENS**

Short crack tests were carried out on notched specimens of aluminum shown in Fig. 2.3. Constant amplitude load control tests similar to short crack tests were carried out on these specimens. The tests were carried out at two stress levels at  $R = 0.1$  and

R = 0.4 under negligible plasticity effects. Tests at R ratios of 0.1 and 0.7 were also carried out where notch plasticity effects were significant. The  $K_t$  of the specimens were 3.06 to 3.10. The initial crack lengths in front of the notch were 0.15 to 0.28 mm. These lengths were less than the typical notch field of 0.42mm in all cases. Crack growth rates were computed in a similar way using the crack length versus cycles data by the point to point slope method. All the notched specimen tests were carried out at positive R ratios of 0.1, 0.4 and 0.7. Crack length data were recorded till the crack lengths reached a length of 1mm. The applied stress intensity values were calculated by using small crack solutions for short cracks of length less than 0.4mm and using long crack solutions for cracks greater than 0.4mm. Specifically, the following equations were used:

$$\Delta K = 1.12K_t \Delta \sigma \sqrt{(\pi \ell)}$$

for  $\ell \leq 0.4mm$  and

$$\Delta K = \Delta \sigma \sqrt{\pi a} \left[ \frac{1.122 - 0.561\alpha - 0.205\alpha^2 + 0.471\alpha^3 - 0.190\alpha^4}{\sqrt{(1 - \alpha)}} \right]$$

for  $\ell > 0.4mm$

where

$\ell$  = crack length measured from the notch root,

$\alpha = (r + \ell)/w$ ,

$r$  = radius of notch,  $2w$  = width of the specimen,

$\Delta \sigma$  = applied gross stress range.

### **Short Crack Growth Rate Results in Notched Specimens**

Figures 4.117 and 4.118 show the crack growth rate as a function of  $\Delta K$  at  $R=0.1$  and  $R=0.4$ . Note that the results are presented for two stress levels which are elastic. In other words,  $K_t\Delta\sigma/\sigma_y$  is less than 1 in these cases. The solid lines in these figures represent the corresponding long crack data obtained by testing the compact tension specimens. Note that in these cases, growth behavior of cracks in front of notches is similar to the growth behavior in plain specimens because of insignificant plasticity effects.

Figures 4.119 and 4.120 show the crack growth rates versus the  $\Delta K$  at  $R = 0.1$  and  $R=0.7$  at two different stress levels under conditions when  $K_t\Delta\sigma/\sigma_y$  is greater than 1. In these tests, there was no ratcheting phenomenon observed for cracks of lengths less than 0.75mm. Crack opening and closing points were obtained by the stereoimaging technique in the same way as they were obtained for long and short crack tests. Crack opening and closing levels were determined at three or four different crack lengths. Corresponding values of  $U$  were calculated. Values of  $U$  at different crack lengths were determined by fitting an equation mentioned earlier. The value of  $U$  for crack lengths greater than 0.6mm was chosen to be the value of  $U$  at 0.6mm crack length. Plots of crack growth rate as a function of  $\Delta K_{eff}$ , corresponding to Figs. 4.117 and 4.118 are shown in Figs. 4.121 and 4.122. It can be observed from these figures that the closure is able to account for the differences between the growth rates at high and low stress levels under elastic cases. The cracks were open in the tests at  $R=0.1$  and  $R=0.7$  (Figs. 4.121 and 4.122) and hence the value of  $U$  was

unity in these cases. A combined plot at different R ratios showing crack growth rate against  $\Delta K_{eff}$  can be seen in Fig. 4.123.

TABLE 4.1

MECHANICAL PROPERTIES OF DIFFERENT CONDITIONS OF 4340 STEEL

Condition	0.2 Pct yield stress (MPa)	Ultimate tensile strength (MPa)	Pct. elongation	Pct. Reduction in area	Hardness	Prior Austenite grain size ( $\mu\text{m}$ )
Low Fine (LF)	648.1	786.0	28.3	68.0	100 HRB	16-20
High Fine (HF)	1413.4	1627.2	14.0	35.7	48 HRC	20-25
Low Coarse (LC)	663.9	820.5	21.6	45.2	105 HRB	250-300
High Coarse (HC)	1282.5	1523.8	9.3	15.3	48 HRC	250-300

TABLE 4.2

MECHANICAL PROPERTIES OF 2024-T351 ALUMINUM ALLOY

Condition	0.2 Pct yield stress (MPa)	Ultimate tensile strength (MPa)	Pct. elongation	Pct. Reduction in area	Hardness	Prior Austenitic grain size ( $\mu\text{m}$ )
AL <sup>1</sup>	365	489	16.9	/		55

<sup>1</sup> Longitudinal direction of 2024-T351 aluminum alloy

TABLE 4.3

LINEAR ELASTIC CRACK GROWTH PARAMETERS C AND m

	0.1 <sup>1</sup>		0.4		0.7		-1.0	
	C	m	C	m	C	m	C	m
LF	1.011E-08	2.702	1.951E-09	3.398			1.118E-10	3.207
HF	1.518E-08	2.716	3.582E-09	2.484			7.781E-10	3.018
LC	6.352E-09	2.896	8.552E-09	2.746			5.911E-10	3.161
HC	8.475E-10	3.487	5.921E-09	2.976			6.021E-10	3.041
AL <sup>2</sup>	2.436E-07	2.337	1.109E-07	3.091	9.071E-08	3.128	1.927E-08	2.759

The values of C and m shown in this table correspond to the crack growth law of type:

$$\frac{da}{dn} = C[\Delta K]^m$$

where

da/dn = crack growth rate in mm/cycle

ΔK = stress intensity range in MPa√m

<sup>1</sup>The numbers in this row indicate R ratio

<sup>2</sup>2024-T351 aluminum

TABLE 4.4

LINEAR ELASTIC CRACK GROWTH PARAMETERS C' AND m'

	0.1 <sup>1</sup>		0.4		0.7		-1.0	
	C	m	C	m	C	m	C	m
LF	4.277E-08	2.686	5.061E-09	3.548			1.093E-09	3.185
HF	4.054E-08	2.818	6.811E-08	2.616			6.791E-09	3.009
LC	6.097E-09	3.388	2.407E-08	2.807			1.016E-08	2.941
HC	1.189E-08	3.224	3.276E-08	2.647			2.062E-08	2.626
AL <sup>2</sup>	9.837E-07	2.338	3.828E-07	3.089	1.908E-07	3.127	1.223E-07	2.759

The values of C and m shown in this table correspond to the crack growth law of type:

$$\frac{da}{dn} = C'[\Delta K_{eff}]^{m'}$$

where

da/dn = crack growth rate in mm/cycle

$\Delta K_{eff}$  = effective stress intensity range in MPa√m

<sup>1</sup>The numbers in this row indicate R ratio

<sup>2</sup>2024-T351 aluminum

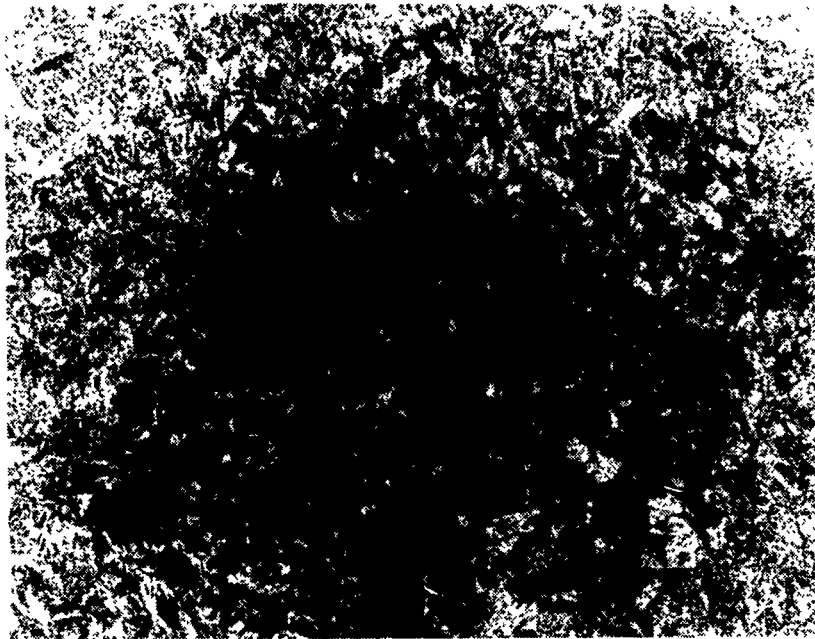


Fig. 4.1 Microstructure (x100) of low strength fine grain size condition of steel (LF).



Fig. 4.2 Microstructure (x100) of high strength fine grain size condition of steel (HF).



Fig. 4.3 Microstructure (x50) of low strength coarse grain size condition of steel (LC)



Fig. 4.4 Microstructure (x50) of high strength coarse grain size condition of steel (HC).

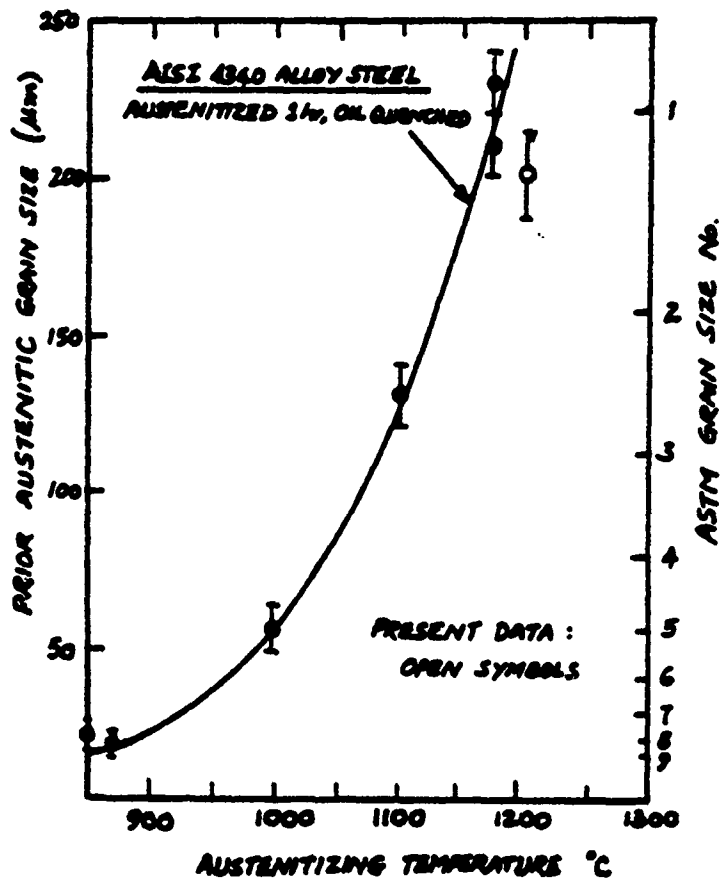


Fig. 4.5 Comparison of the prior austenitic grain sizes with the data reported in the literature [74].

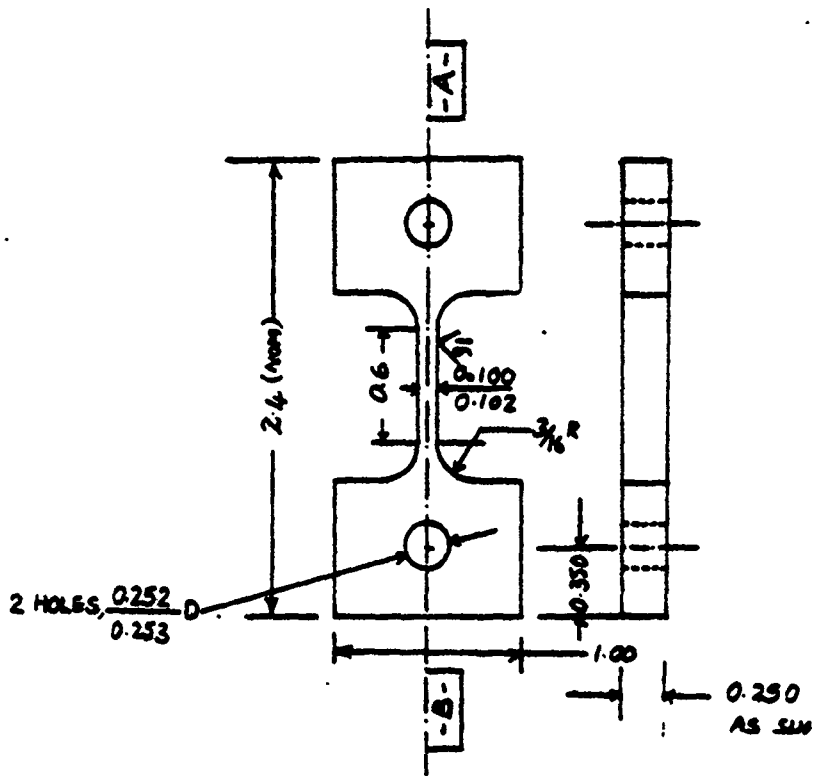


Fig. 4.6 Geometry of the tensile specimen.

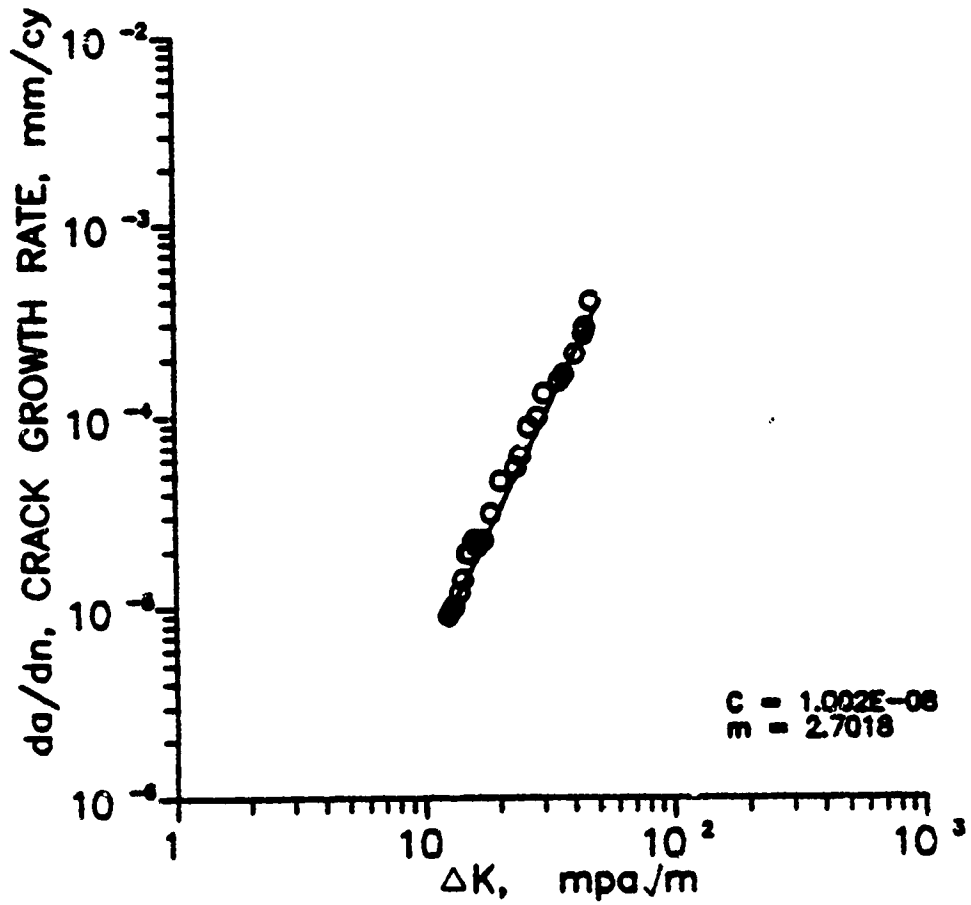


Fig. 4.7 Crack growth rate,  $da/dn$ , as a function of the applied stress intensity range,  $\Delta K$ , for LF condition of steel at  $R = 0.1$

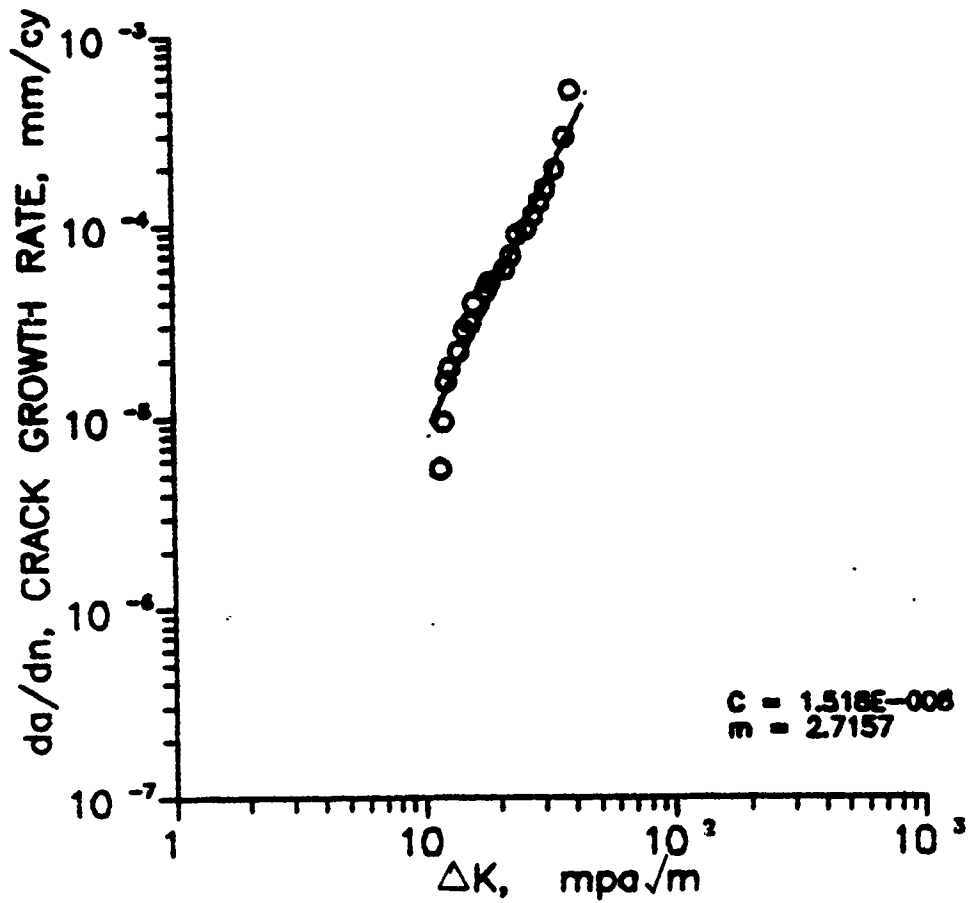


Fig. 4.8 Crack growth rate,  $da/dn$ , as a function of the applied stress intensity range,  $\Delta K$ , for HF condition of steel at  $R = 0.1$

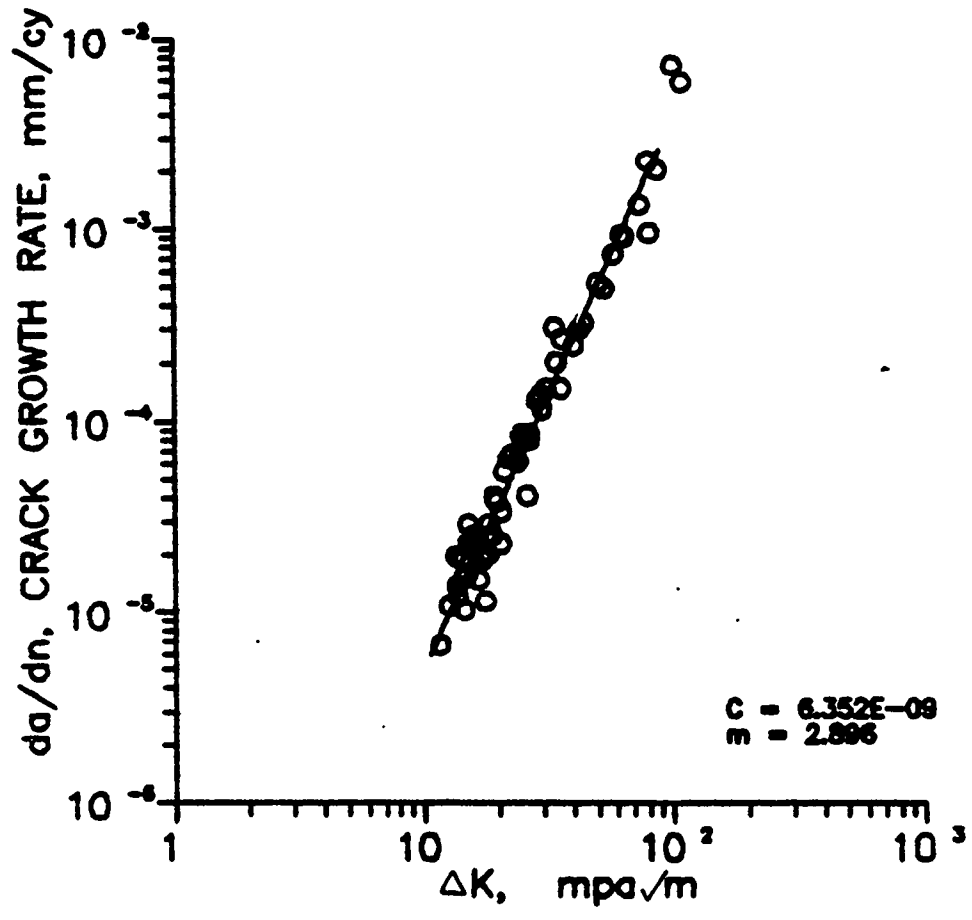


Fig. 4.9 Crack growth rate,  $da/dn$ , as a function of the applied stress intensity range,  $\Delta K$ , for LC condition of steel at  $R = 0.1$

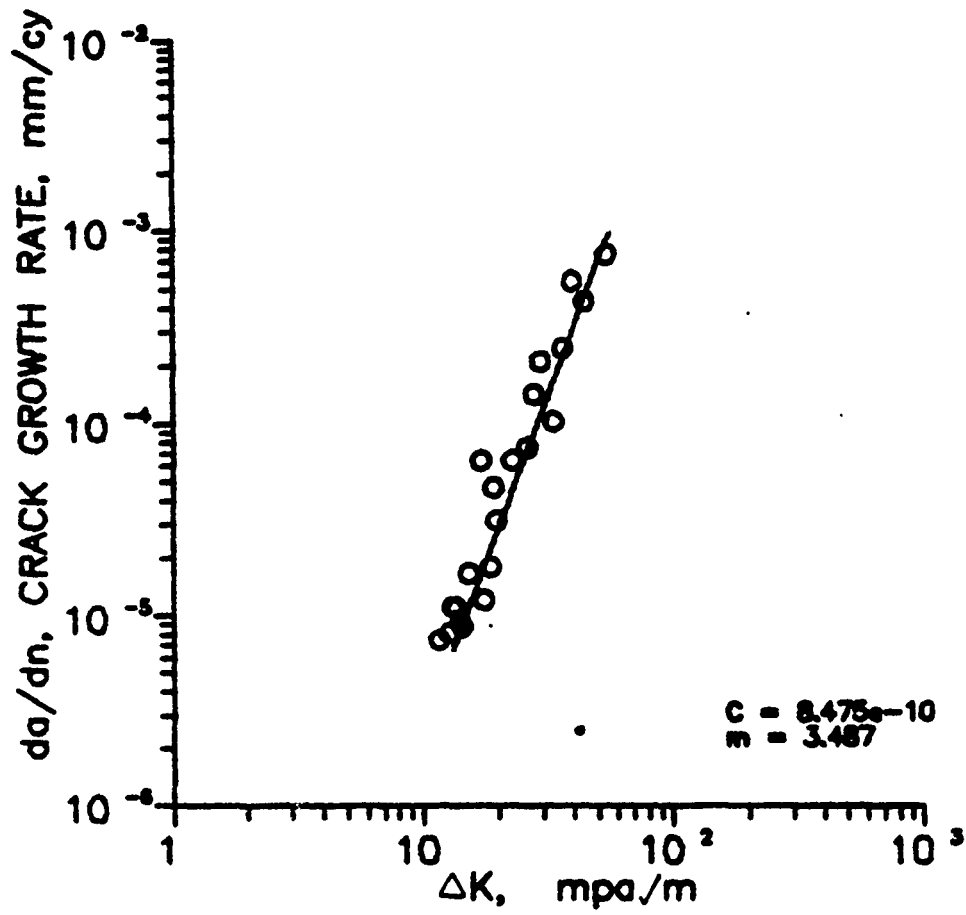


Fig. 4.10 Crack growth rate,  $da/dn$ , as a function of the applied stress intensity range,  $\Delta K$ , for HC condition of steel at  $R = 0.1$

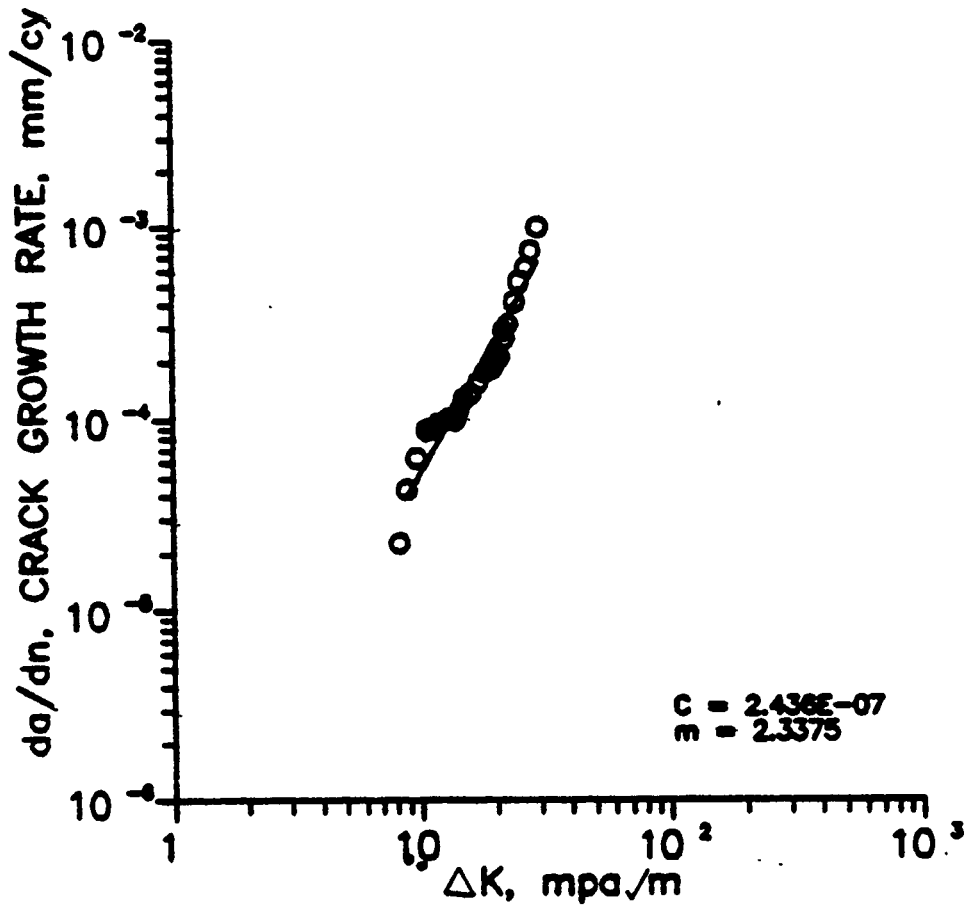


Fig. 4.11 Crack growth rate,  $da/dn$ , as a function of the applied stress intensity range,  $\Delta K$ , for aluminum at  $R = 0.1$

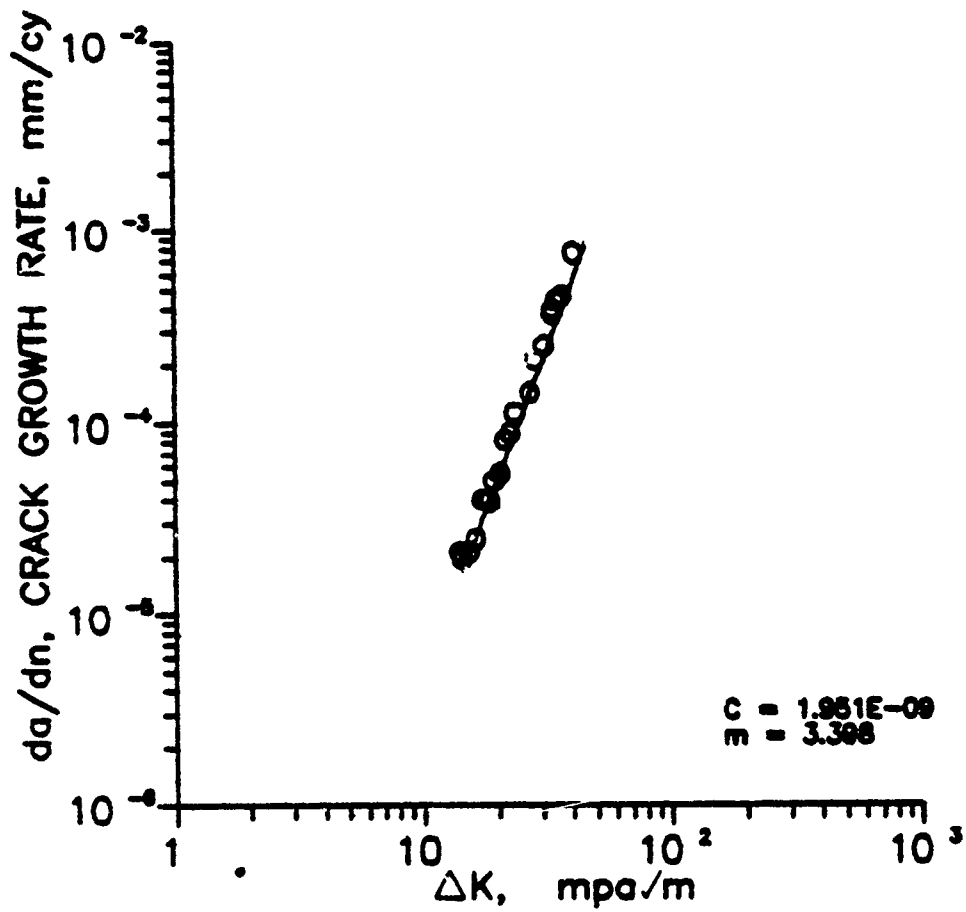


Fig. 4.12 Crack growth rate,  $da/dn$ , as a function of the applied stress intensity range,  $\Delta K$ , for LF condition of steel at  $R = 0.4$

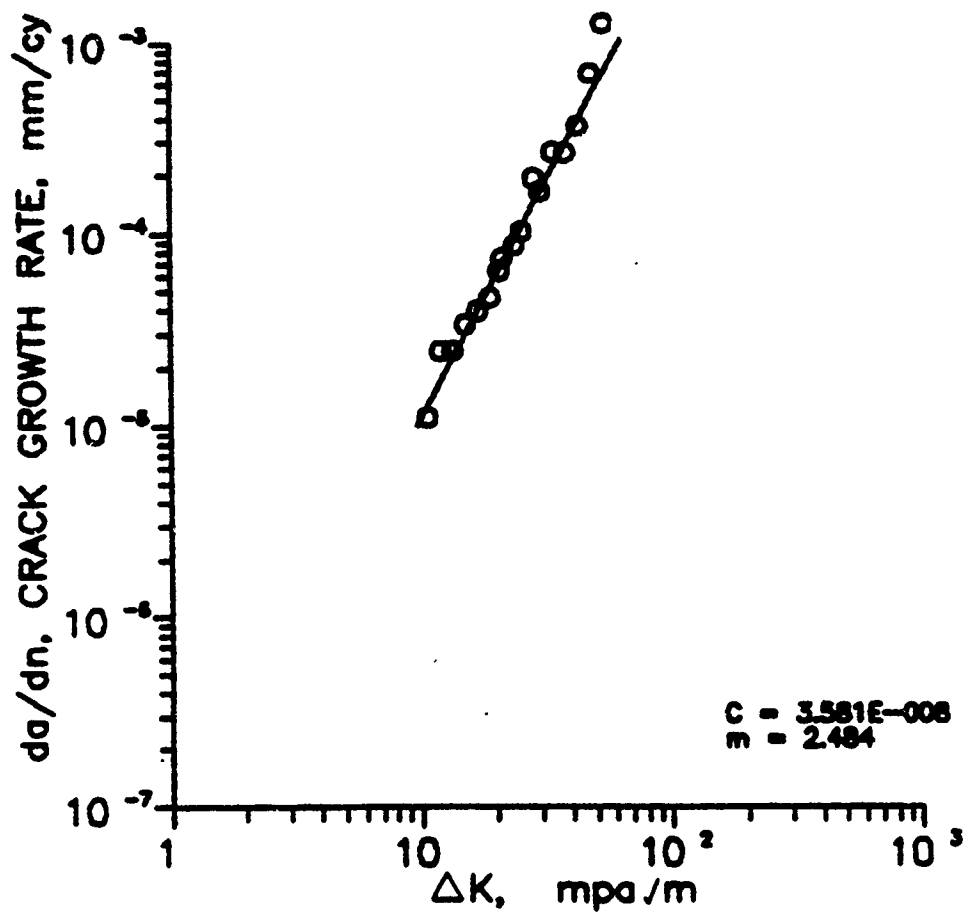


Fig. 4.13 Crack growth rate,  $da/dn$ , as a function of the applied stress intensity range,  $\Delta K$ , for HF condition of steel at  $R = 0.4$

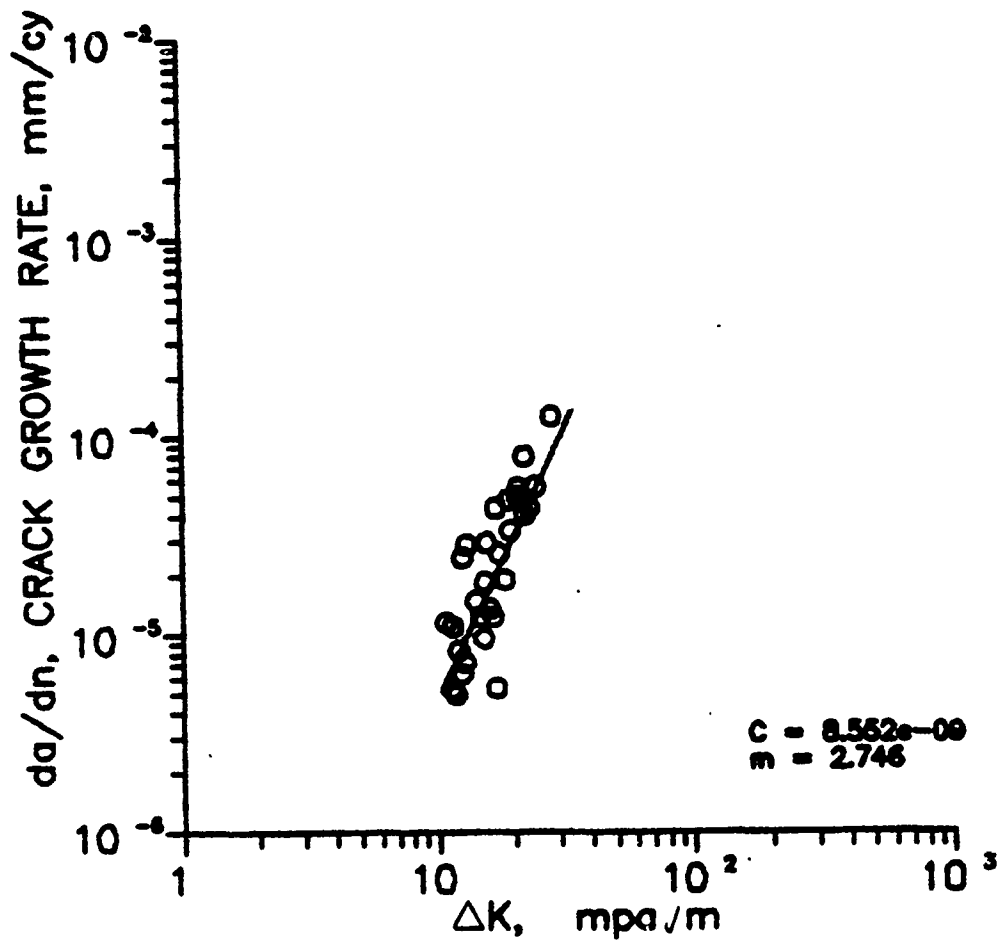


Fig. 4.14 Crack growth rate,  $da/dn$ , as a function of the applied stress intensity range,  $\Delta K$ , for LC condition of steel at  $R = 0.4$

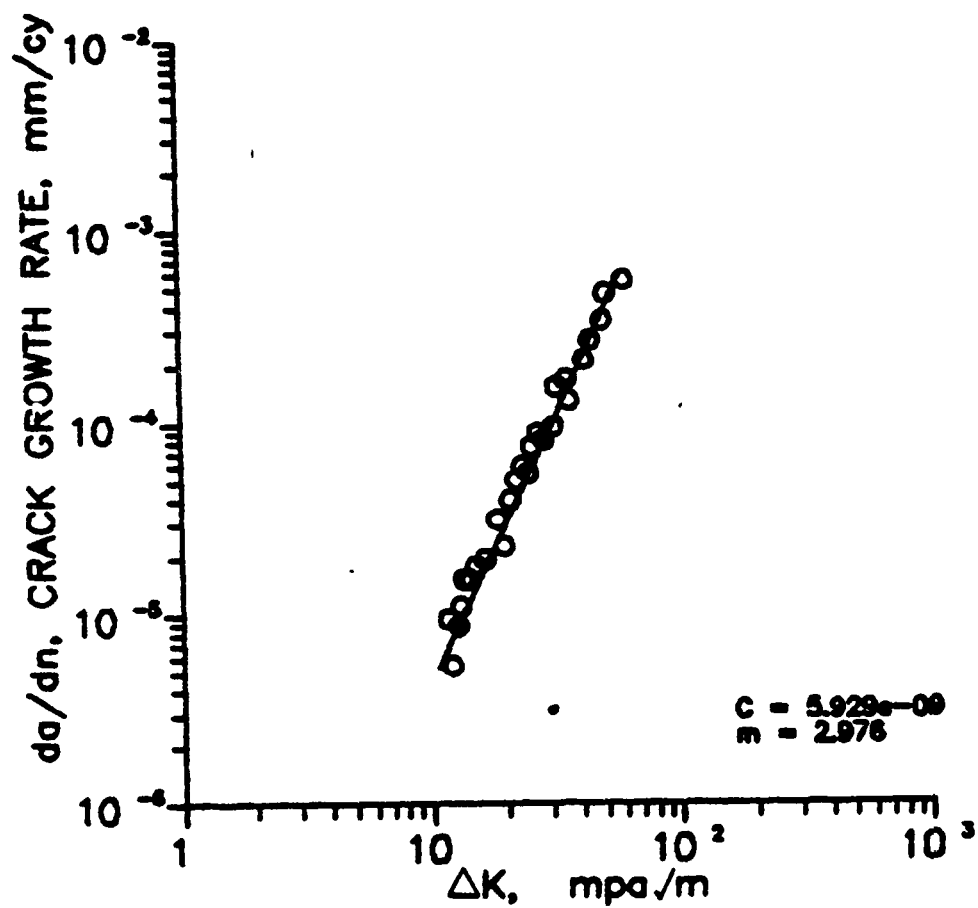


Fig. 4.15 Crack growth rate,  $da/dn$ , as a function of the applied stress intensity range,  $\Delta K$ , for HC condition of steel at  $R = 0.4$

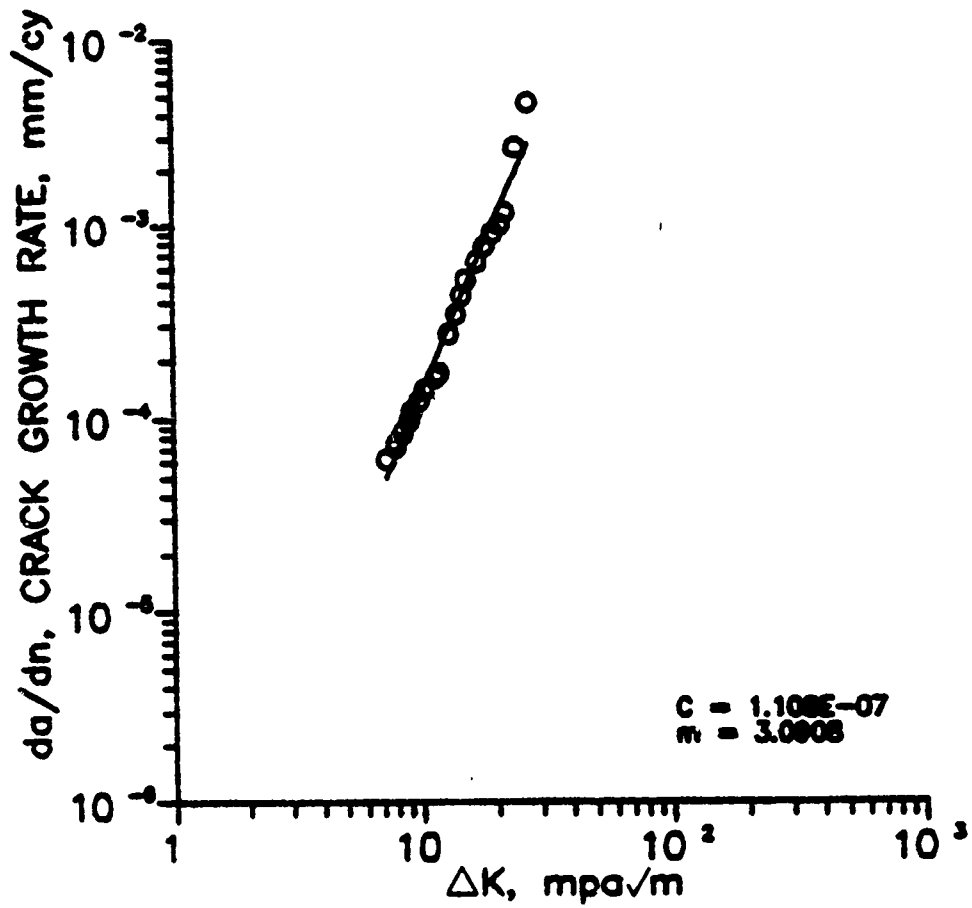


Fig. 4.16 Crack growth rate,  $da/dn$ , as a function of the applied stress intensity range,  $\Delta K$ , for aluminum at  $R = 0.4$

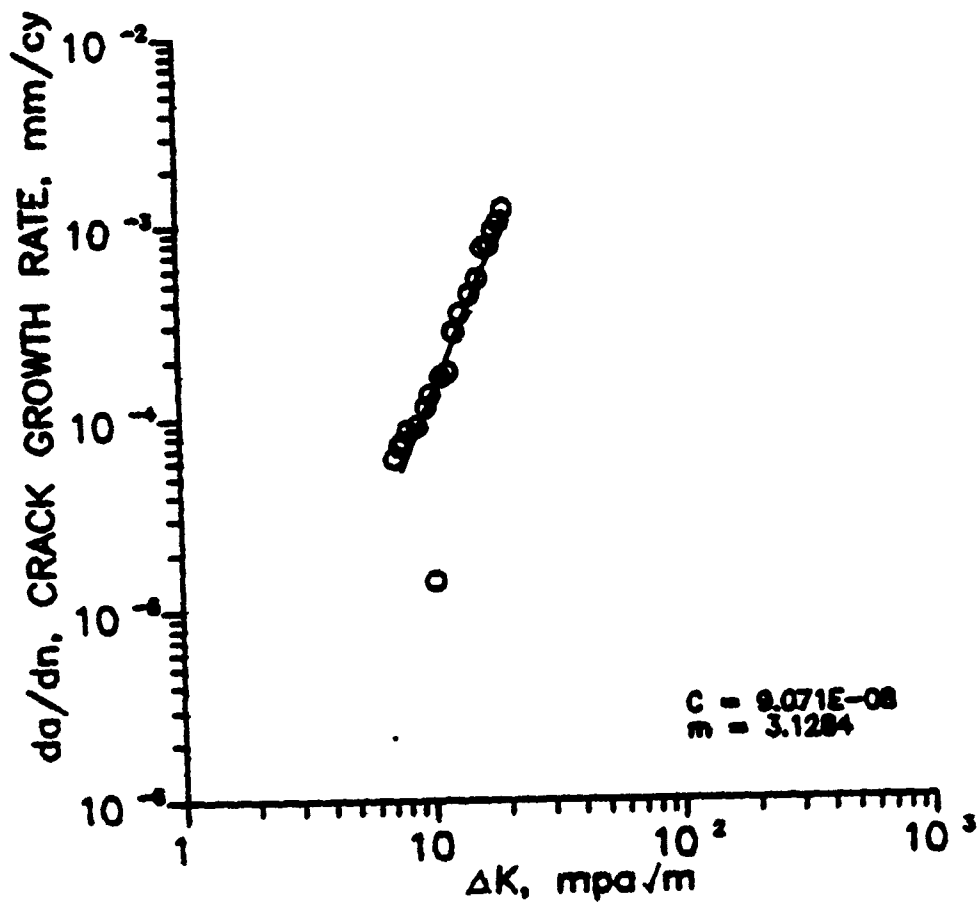


Fig. 4.17 Crack growth rate,  $da/dn$ , as a function of the applied stress intensity range,  $\Delta K$ , for aluminum at  $R = 0.7$

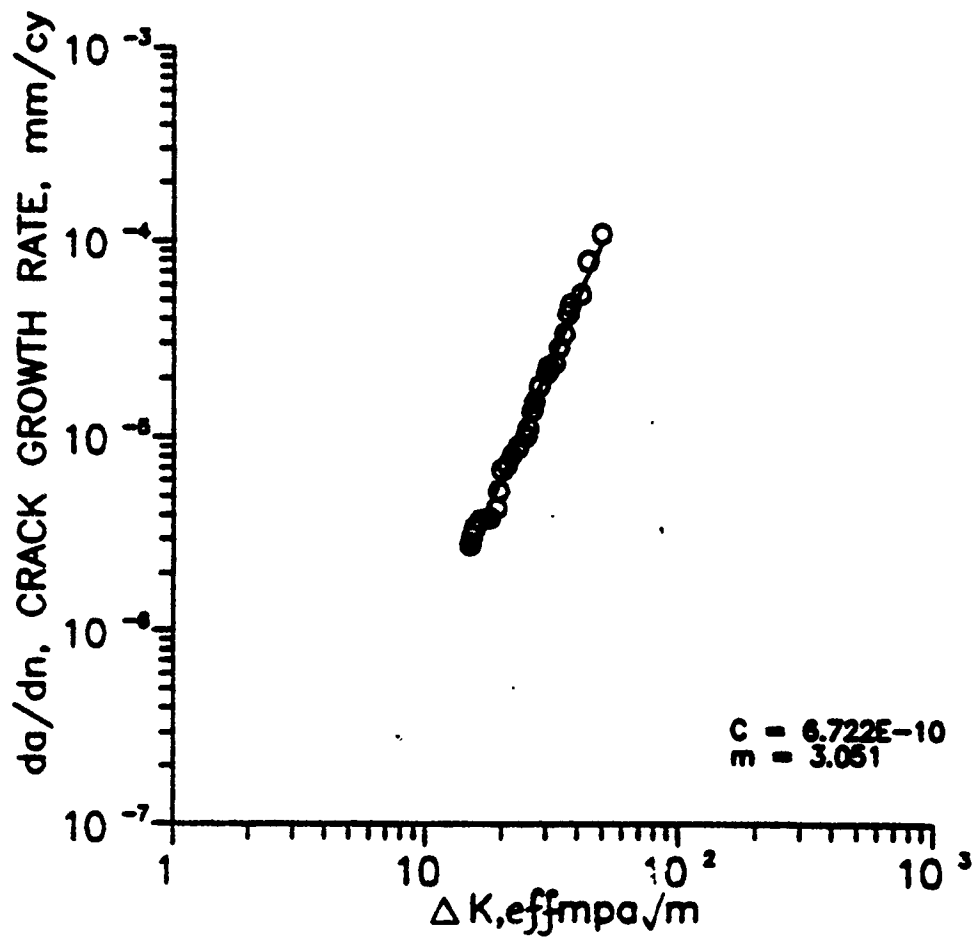


Fig. 4.18 Crack growth rate,  $da/dn$ , as a function of the applied stress intensity range,  $\Delta K$ , for LF condition of steel at  $R = -1.0$

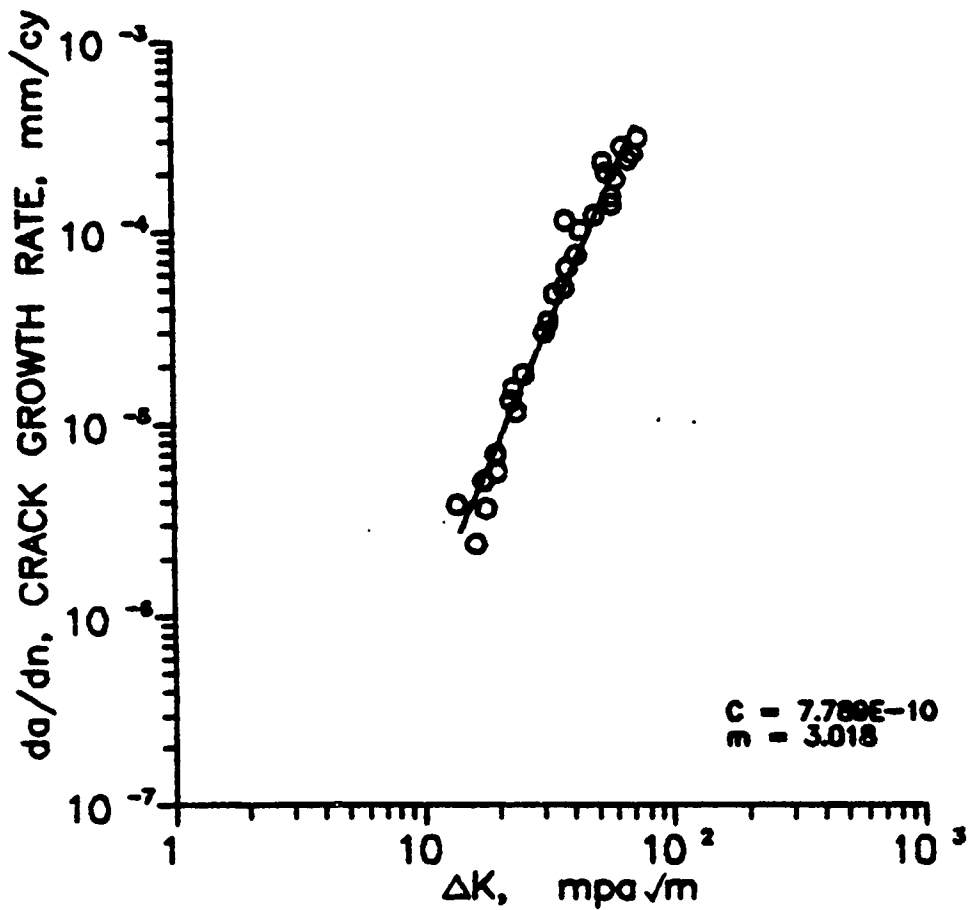


Fig. 4.19 Crack growth rate,  $da/dn$ , as a function of the applied stress intensity range,  $\Delta K$ , for HF condition of steel at  $R = -1.0$

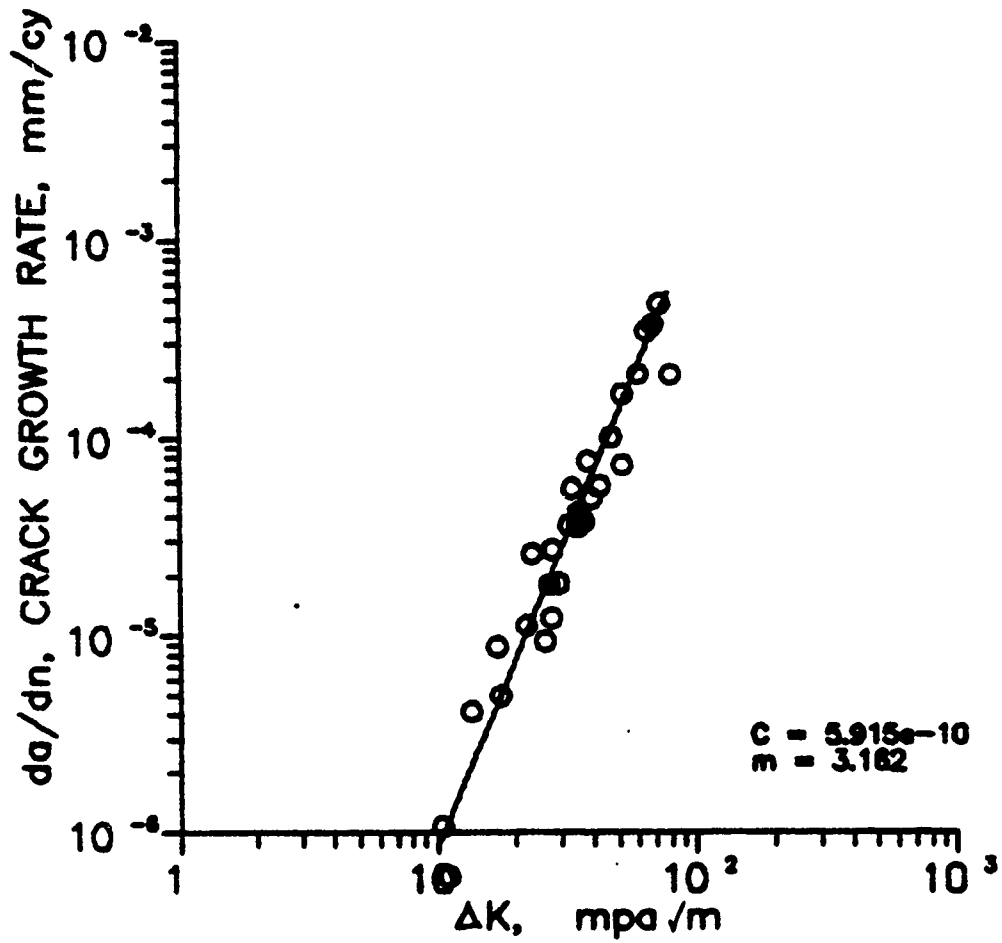


Fig. 4.20 Crack growth rate,  $da/dn$ , as a function of the applied Fig. 4. stress intensity range,  $\Delta K$ , for LC condition of steel at  $R = -1.0$

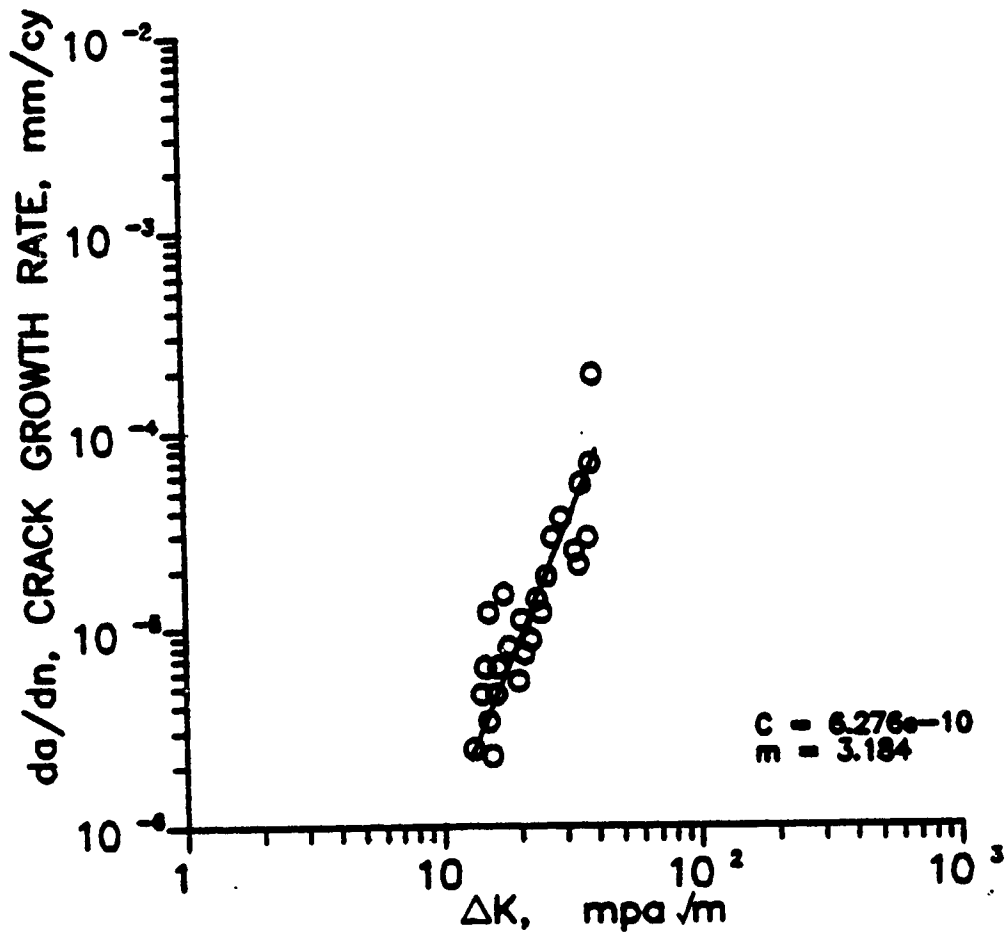


Fig. 4.21 Crack growth rate,  $da/dn$ , as a function of the applied stress intensity range,  $\Delta K$ , for HC condition of steel at  $R = -1.0$

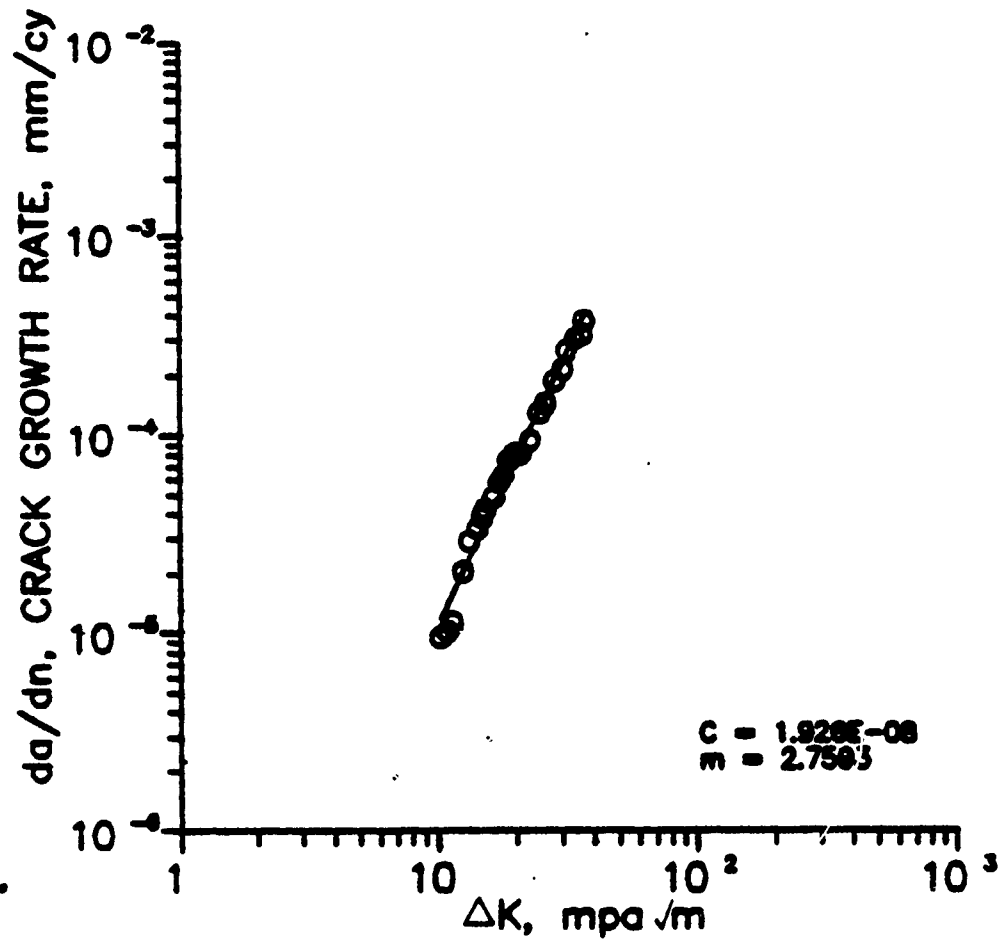


Fig. 4.22 Crack growth rate,  $da/dn$ , as a function of the applied stress intensity range,  $\Delta K$ , for aluminum at  $R = -1.0$ .

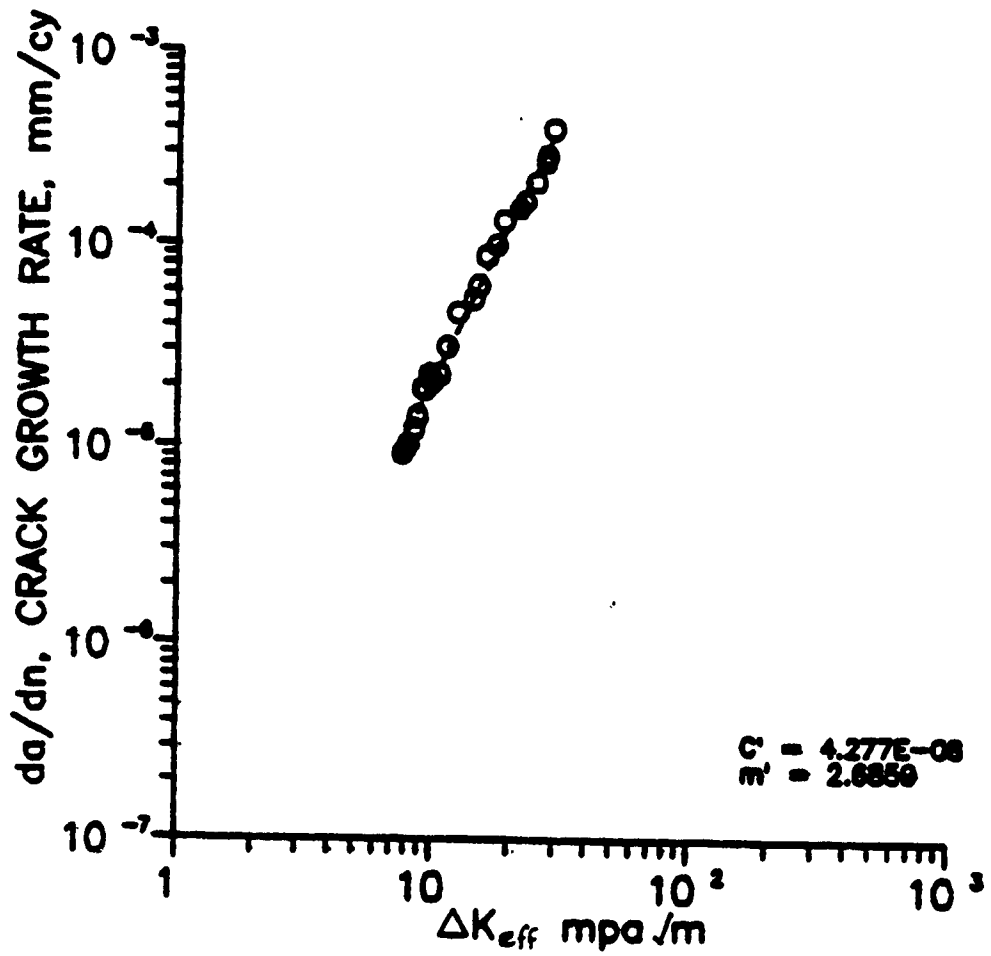
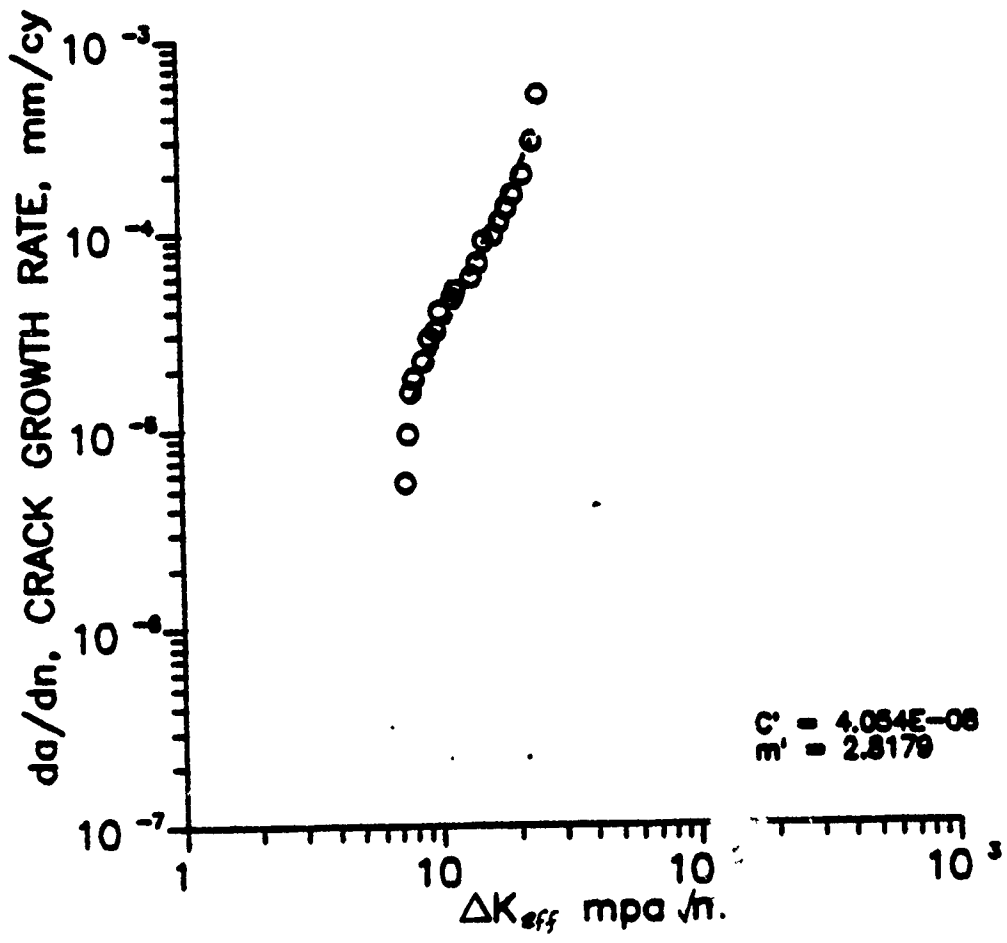


Fig. 4.23 Crack growth rate,  $da/dn$ , as a function of the applied stress intensity range,  $\Delta K_{eff}$ , for LF condition of steel at  $R = 0.1$



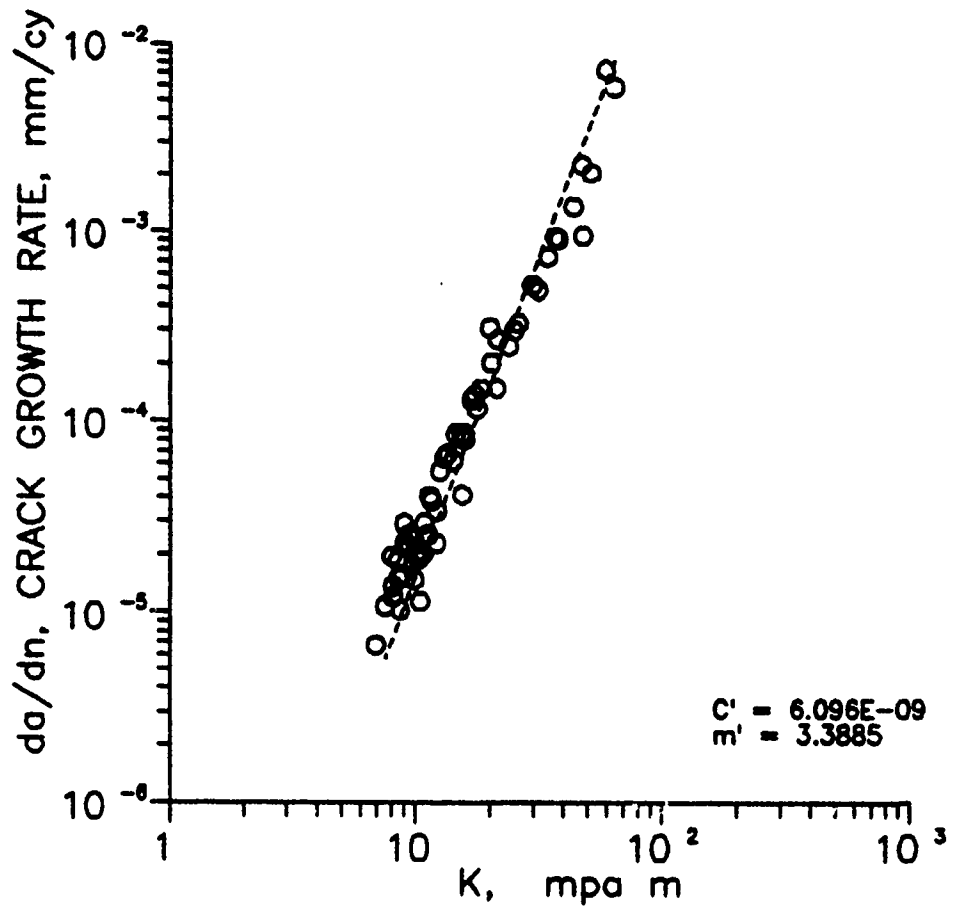


Fig. 4.25 Crack growth rate,  $da/dn$ , as a function of the applied stress intensity range,  $\Delta K_{em}$ , for LC condition of steel at  $R = 0.1$

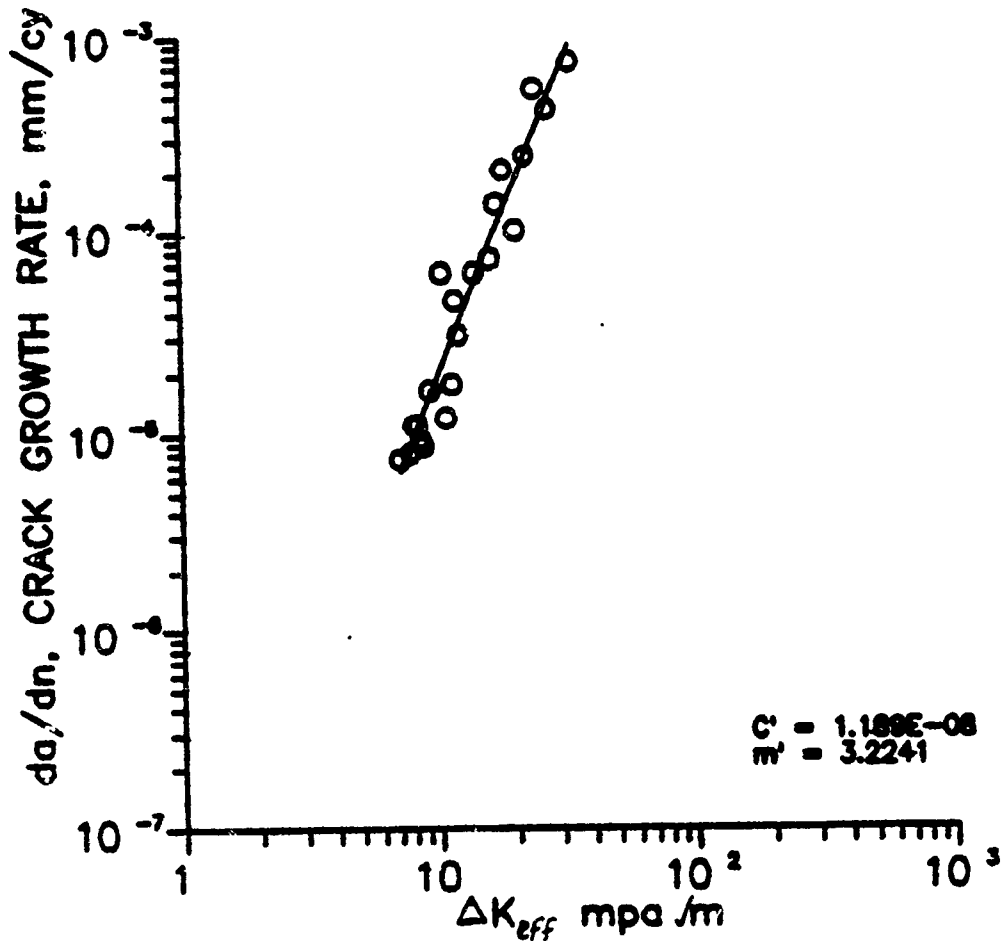


Fig. 4.26 Crack growth rate,  $da/dn$ , as a function of the applied stress intensity range,  $\Delta K_{eff}$ , for HC condition of steel at  $R = 0.1$

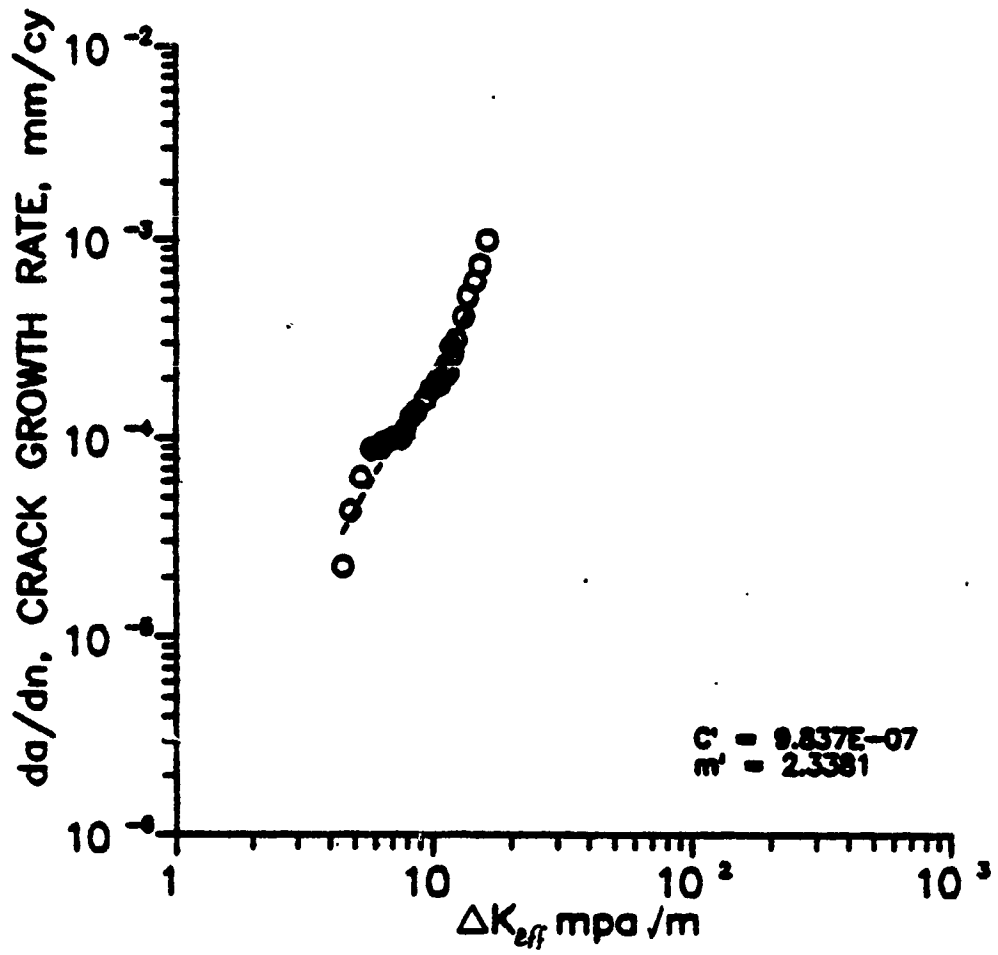


Fig. 4.27 Crack growth rate,  $da/dn$ , as a function of the applied stress intensity range,  $\Delta K_{eff}$  for aluminum at  $R = 0.1$

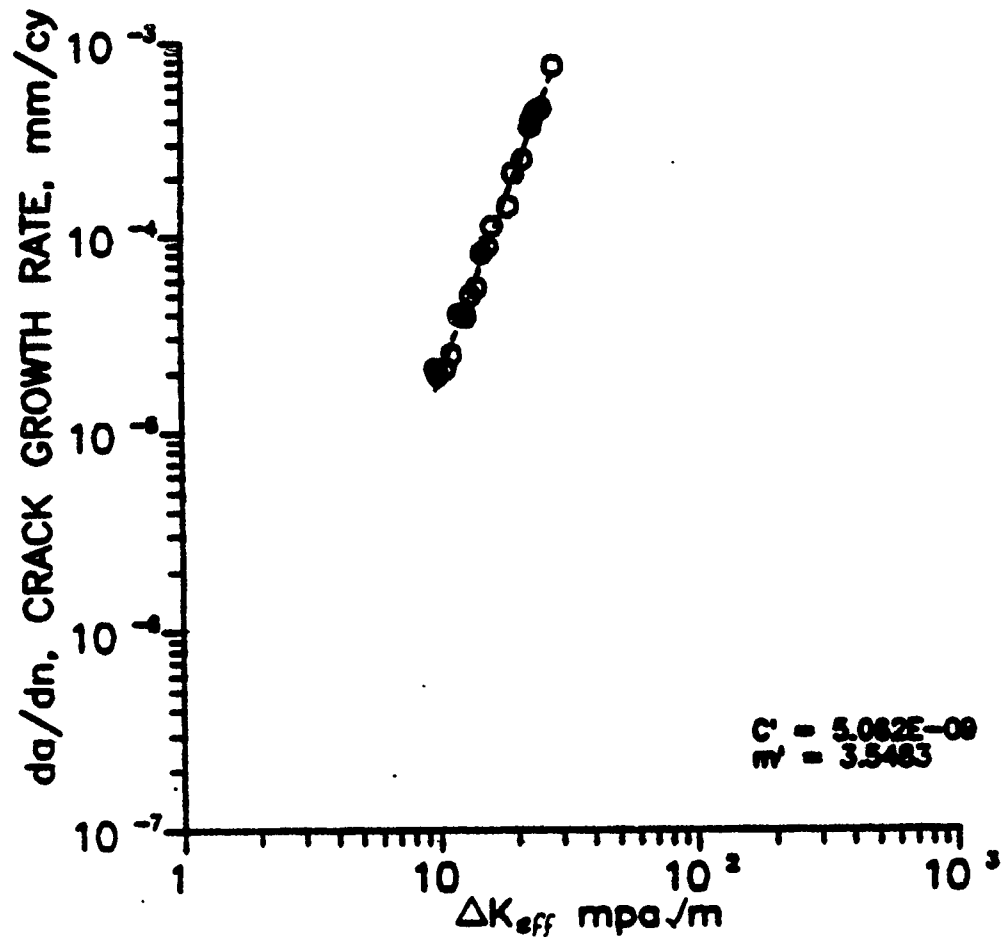


Fig. 4.28 Crack growth rate,  $da/dn$ , as a function of the applied stress intensity range,  $\Delta K_{eff}$ , for LF condition of steel at  $R = 0.4$

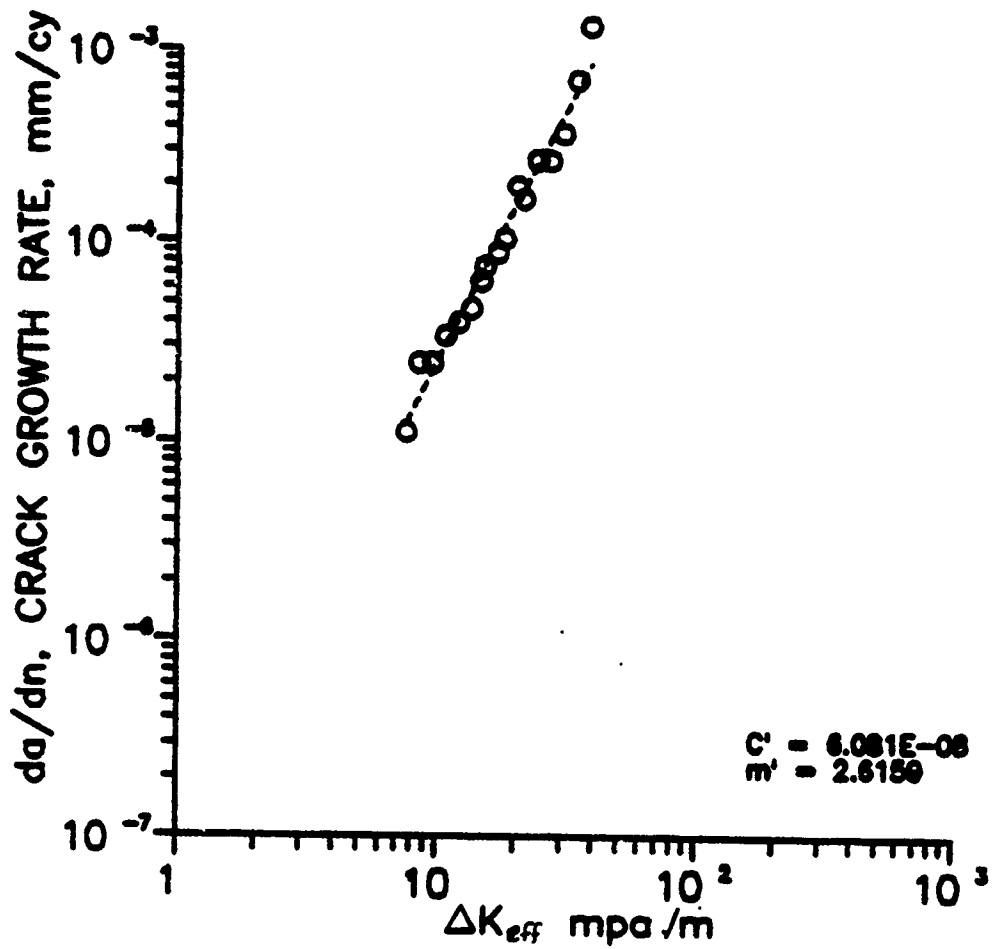


Fig. 4.29 Crack growth rate,  $da/dn$ , as a function of the applied stress intensity range,  $\Delta K_{eff}$ , for HF condition of steel at  $R = 0.4$

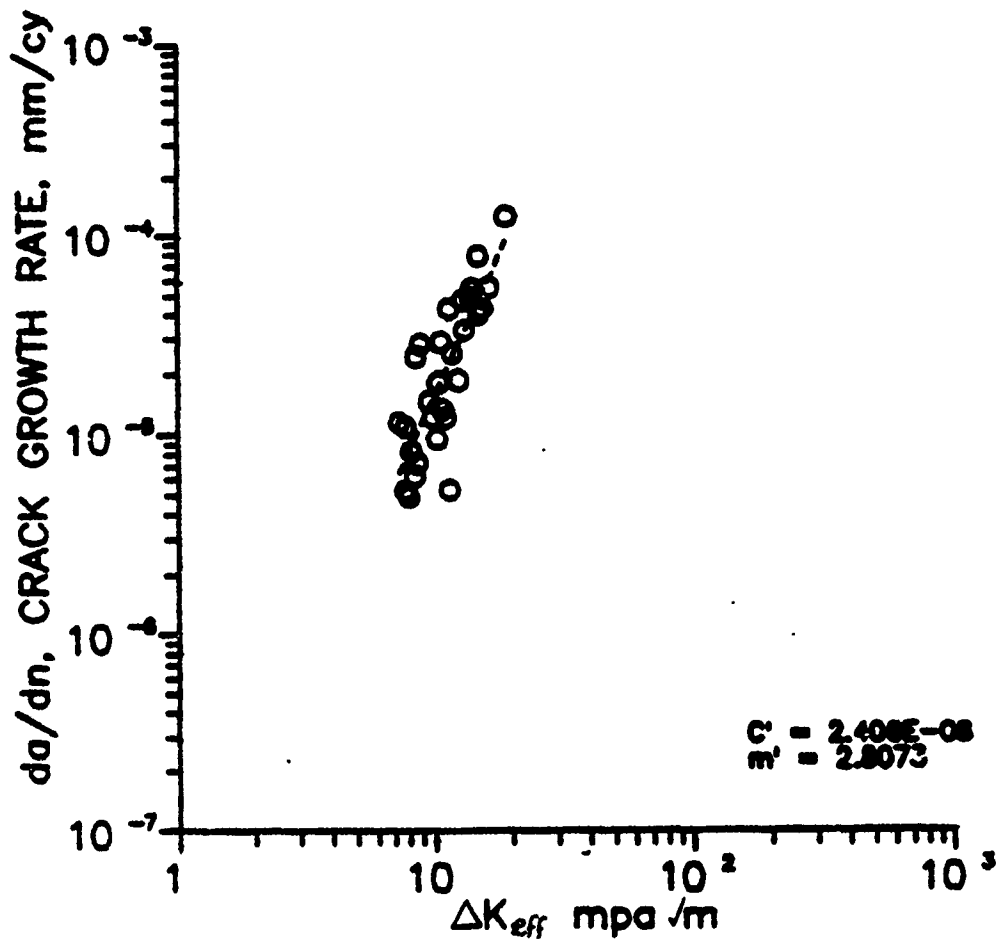


Fig. 4.30 Crack growth rate,  $da/dn$ , as a function of the applied stress intensity range,  $\Delta K_{eff}$ , for LC condition of steel at  $R = 0.4$

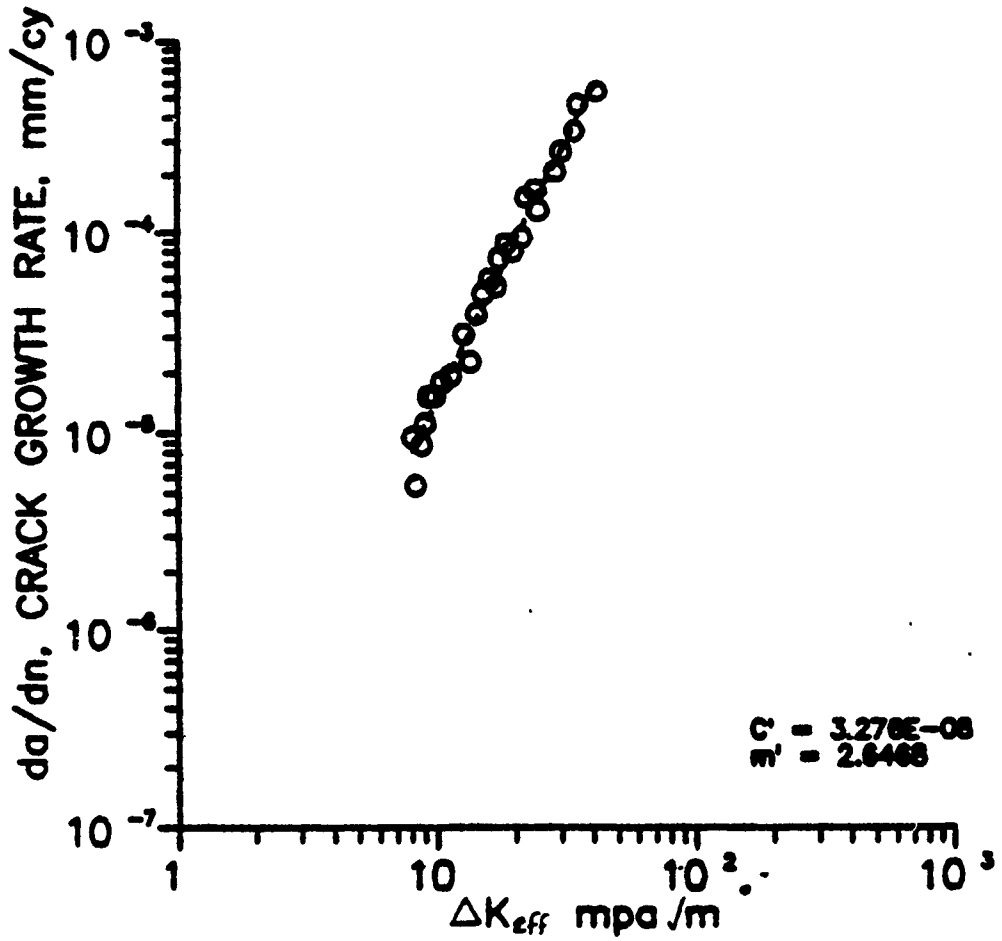


Fig. 4.31 Crack growth rate,  $da/dn$ , as a function of the applied stress intensity range,  $\Delta K_{eff}$ , for HC condition of steel at  $R = 0.4$

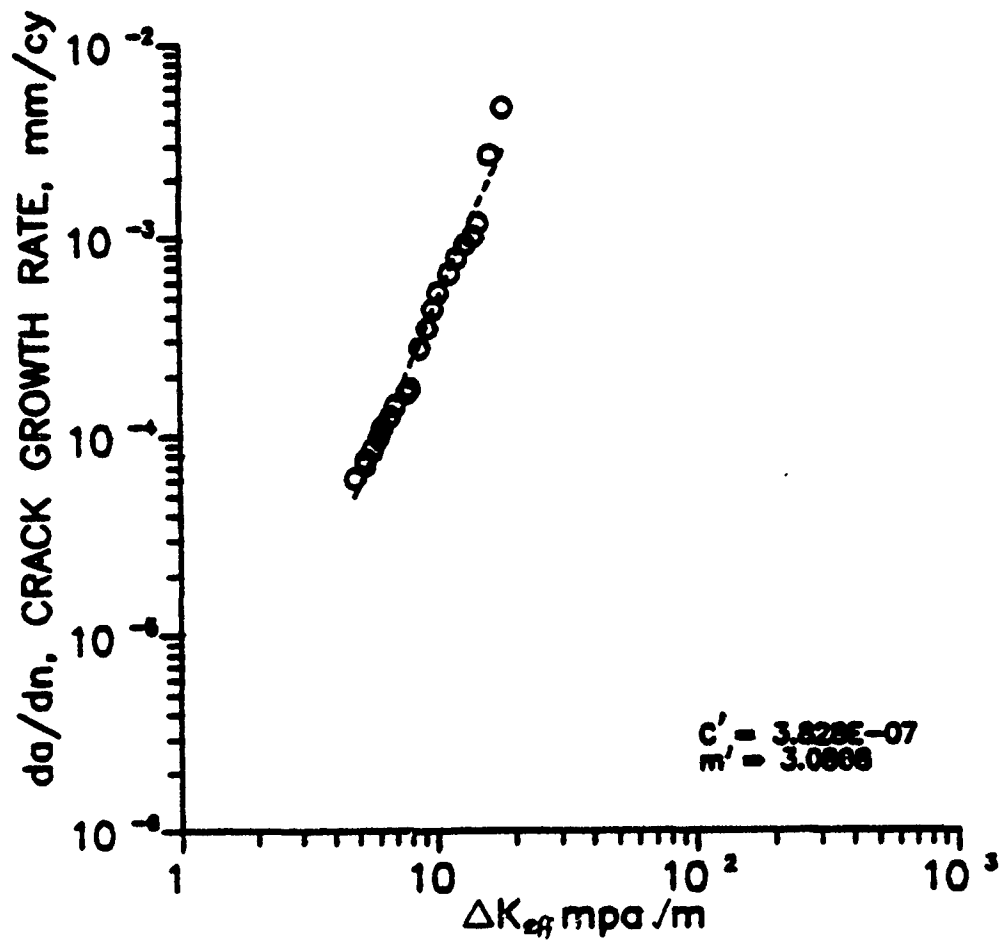
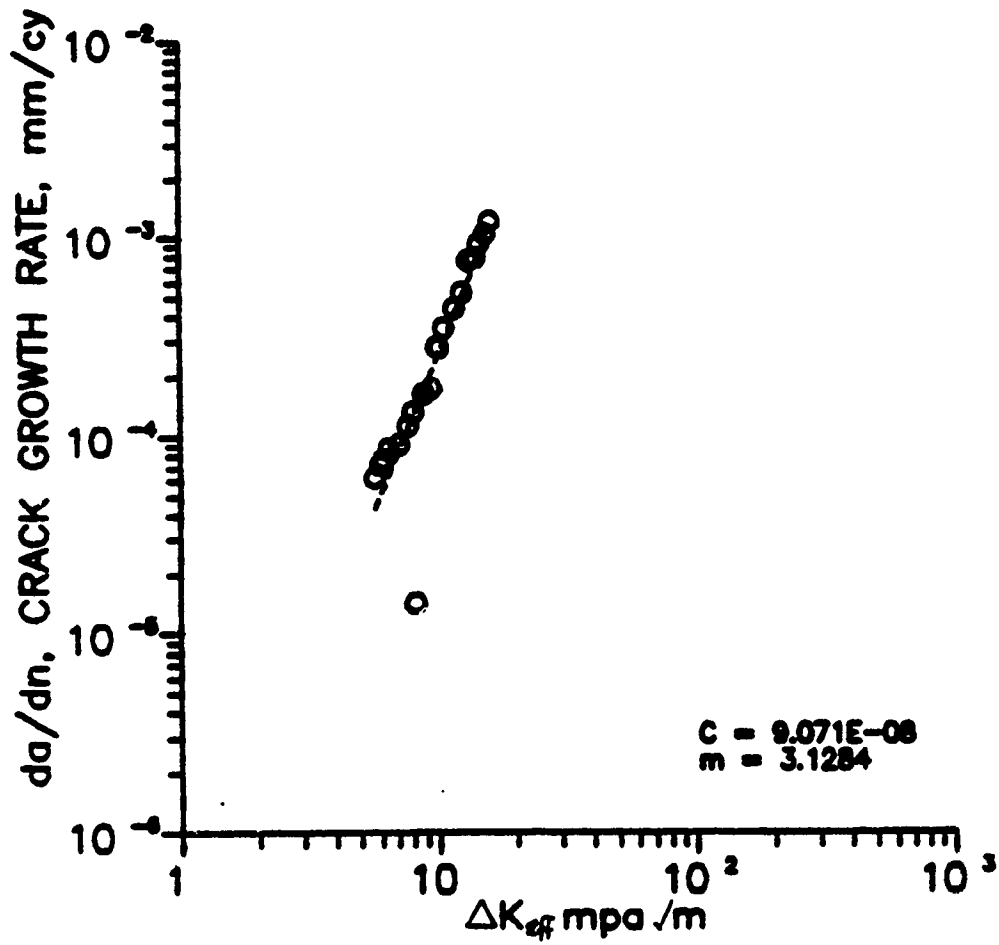


Fig. 4.32 Crack growth rate,  $da/dn$ , as a function of the applied stress intensity range,  $\Delta K_{eff}$ , for aluminum at  $R = 0.4$



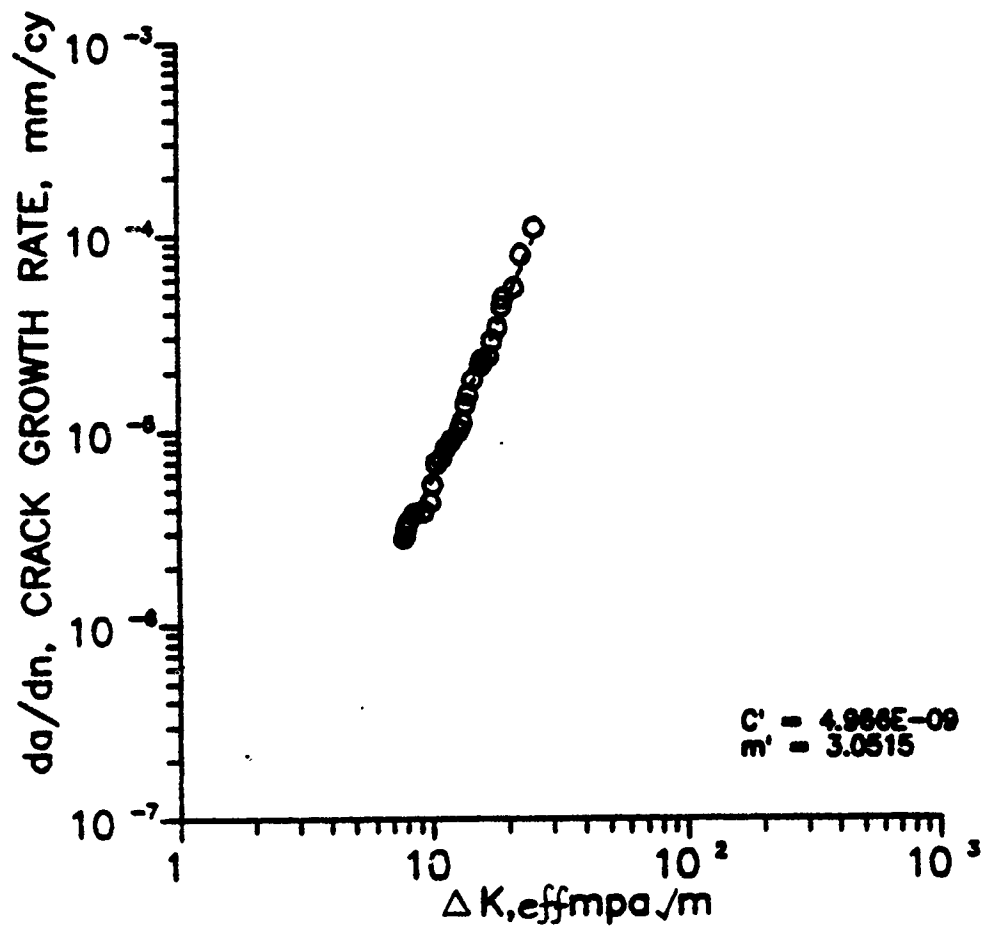


Fig. 4.34 Crack growth rate,  $da/dn$ , as a function of the applied stress intensity range,  $\Delta K_{eff}$ , for LF condition of steel at  $R = -1.0$

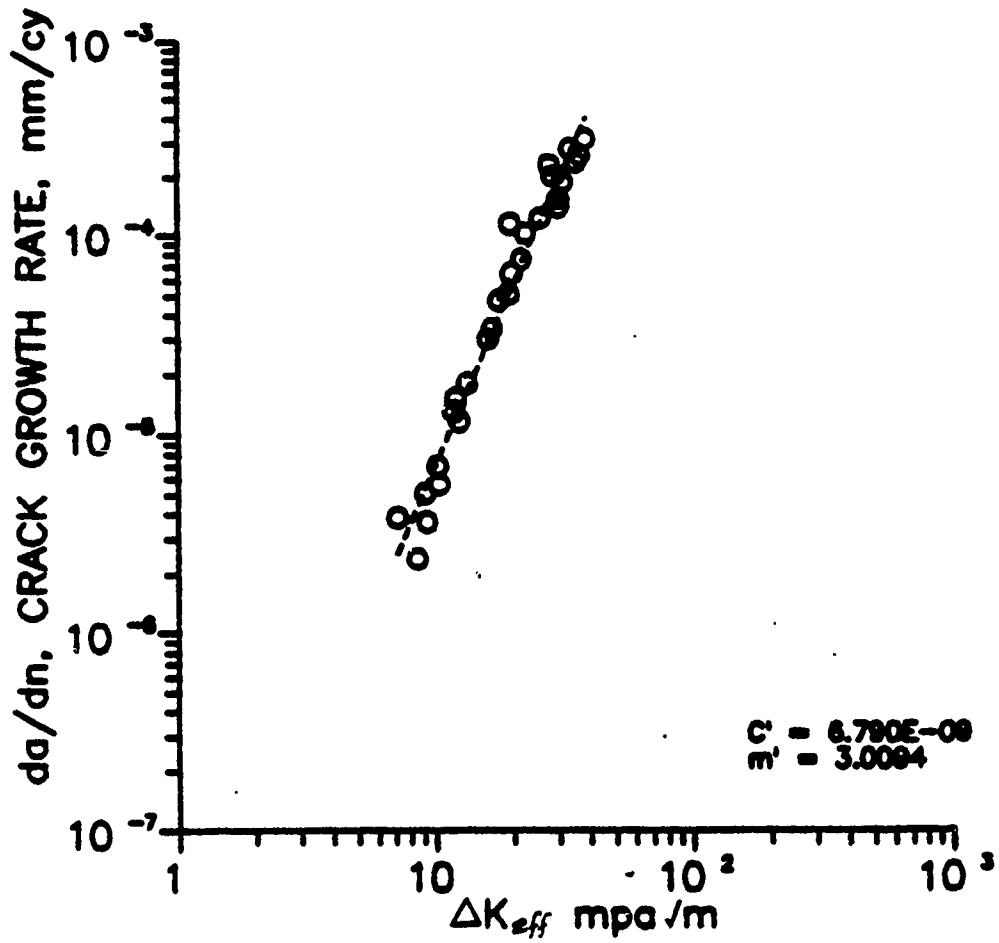


Fig. 4.35 Crack growth rate,  $da/dn$ , as a function of the applied stress intensity range,  $\Delta K_{eff}$ , for HF condition of steel at  $R = -1.0$

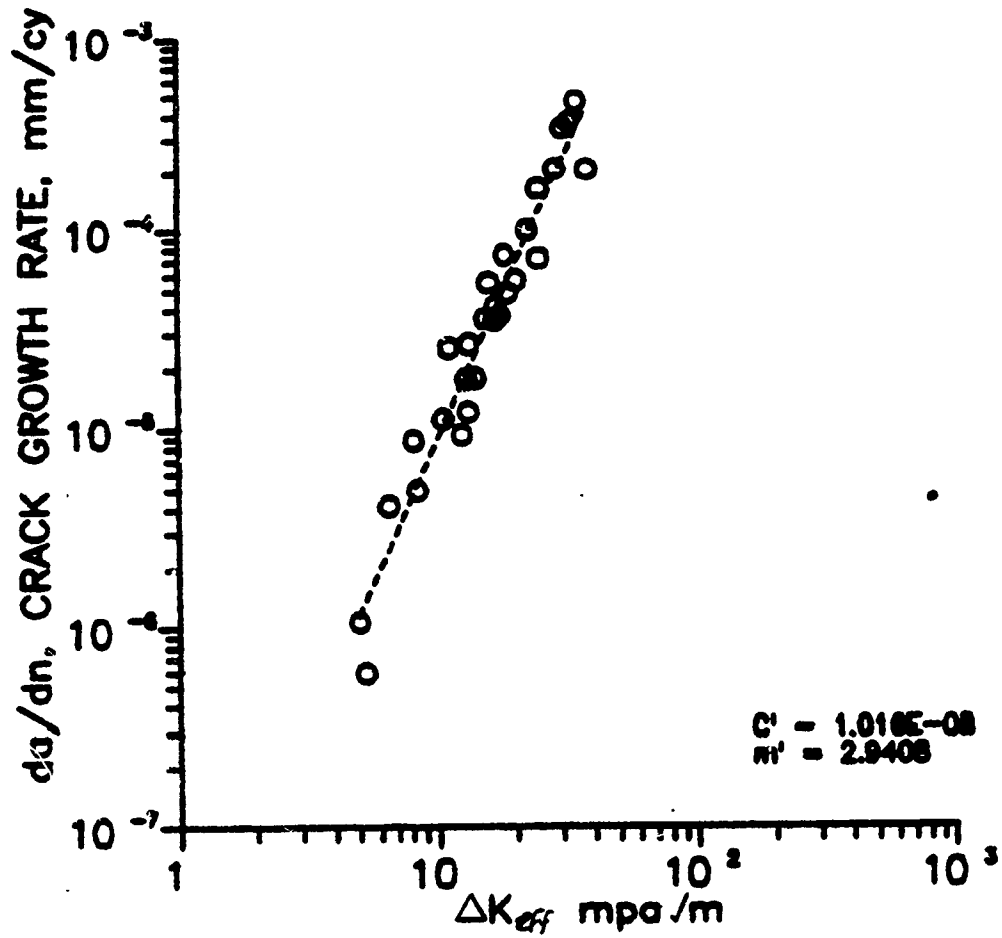


Fig. 4.36 Crack growth rate,  $da/dn$ , as a function of the applied stress intensity range,  $\Delta K_{eff}$ , for LC condition of steel at  $R = -1.0$

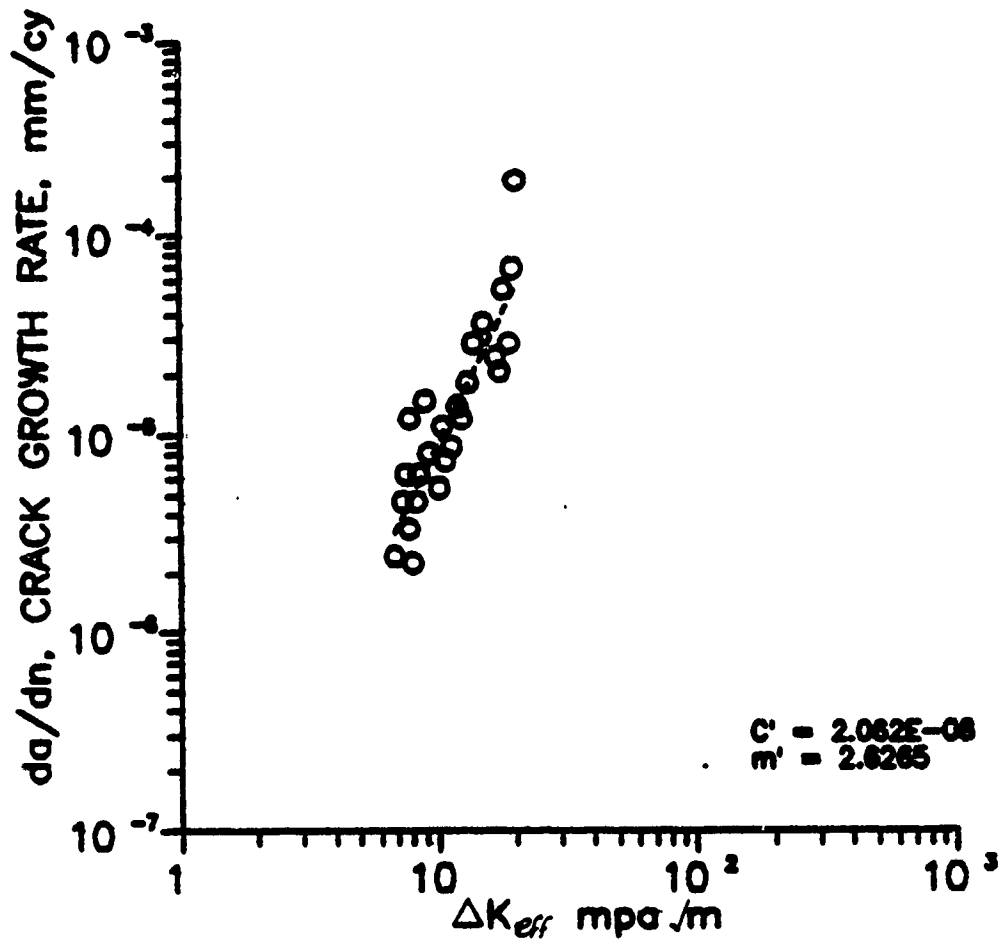


Fig. 4.37 Crack growth rate,  $da/dn$ , as a function of the applied stress intensity range,  $\Delta K_{eff}$ , for HC condition of steel at  $R = -1.0$

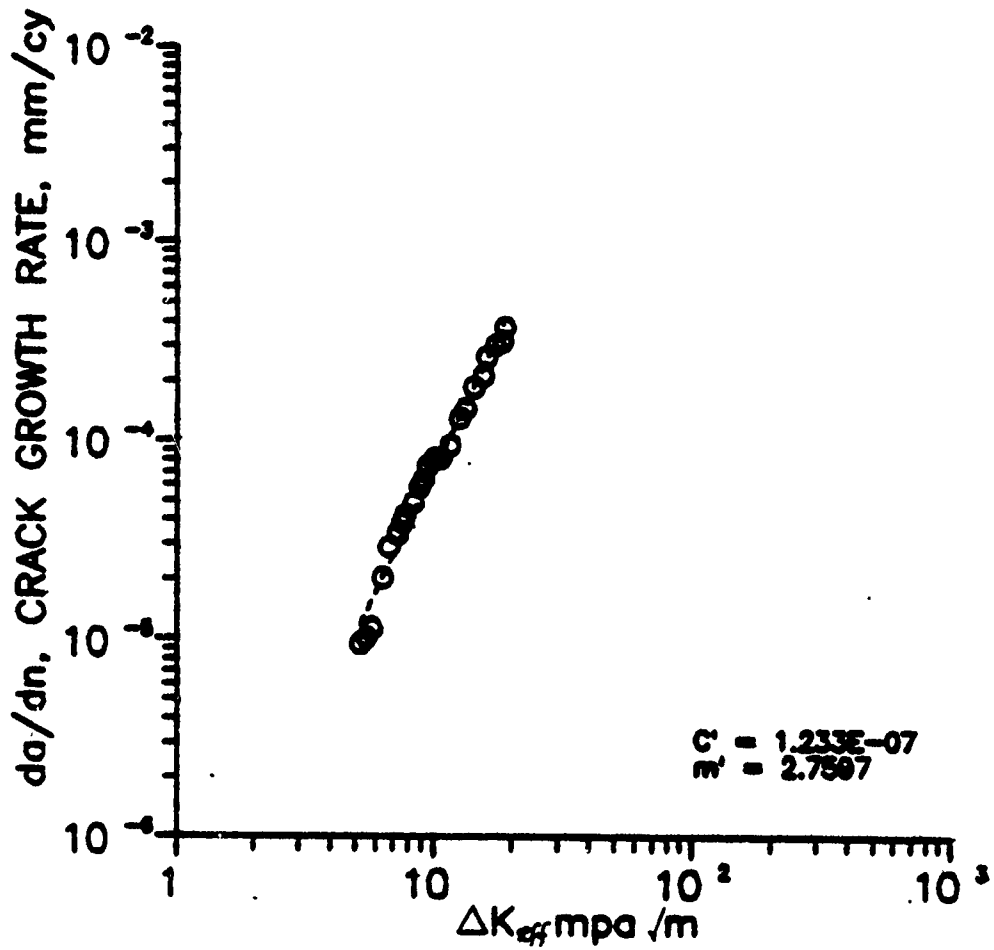


Fig. 4.38 Crack growth rate,  $da/dn$ , as a function of the applied stress intensity range,  $\Delta K_{eff}$ , for aluminum at  $R = -1.0$

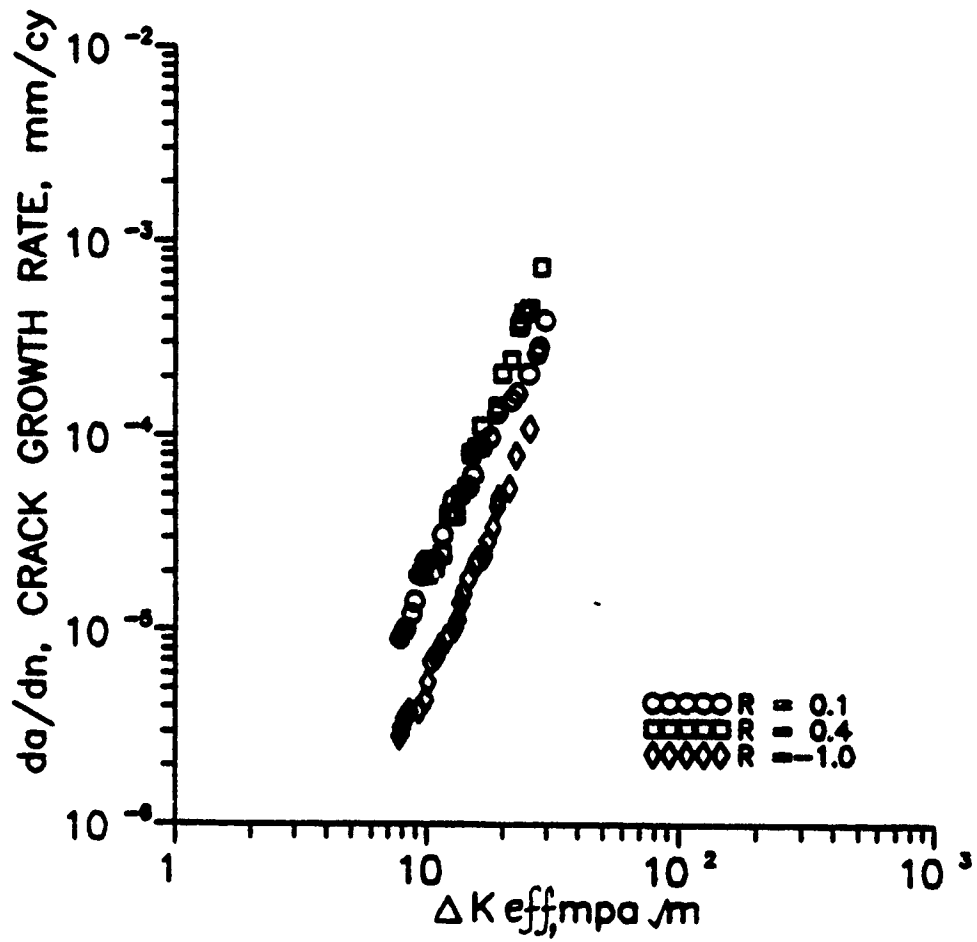


Fig. 4.39  $da/dn$  as a function of  $\Delta K_{eff}$  for LF condition of steel at all R ratios.

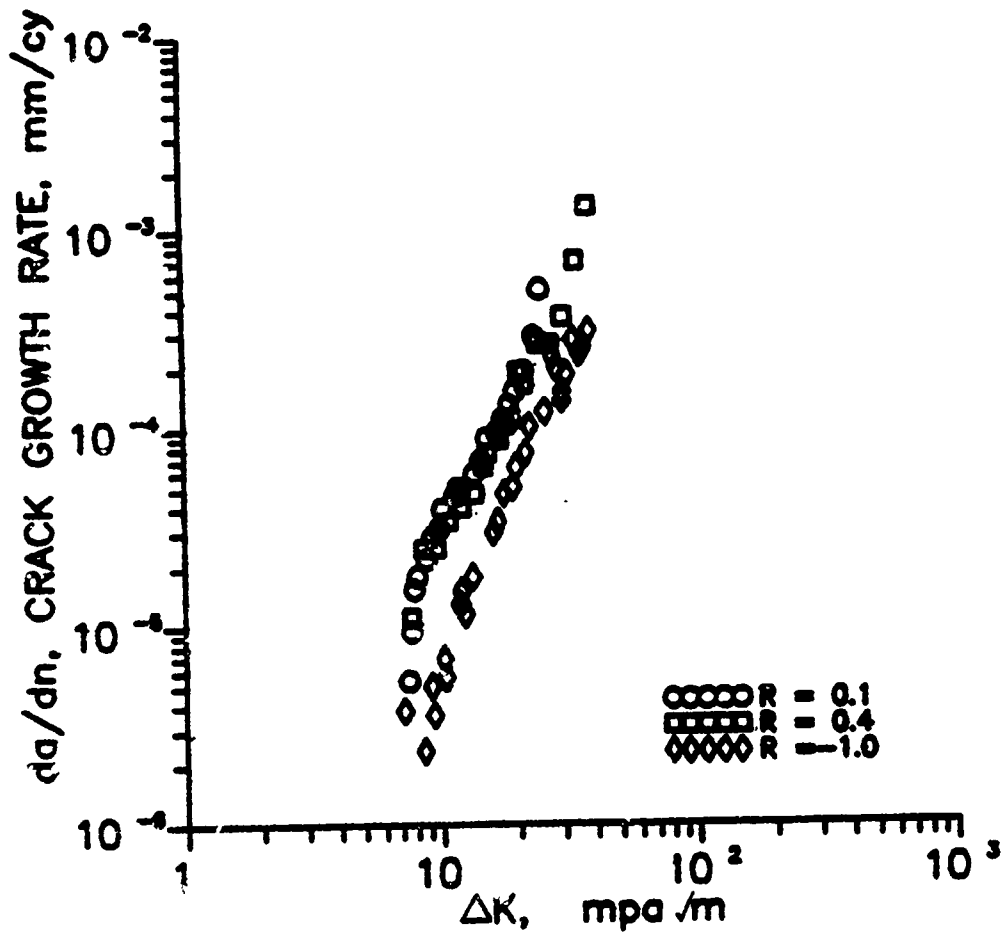


Fig. 4.40  $da/dn$  as a function of  $\Delta K_{eff}$  for HF condition of steel at all R ratios.

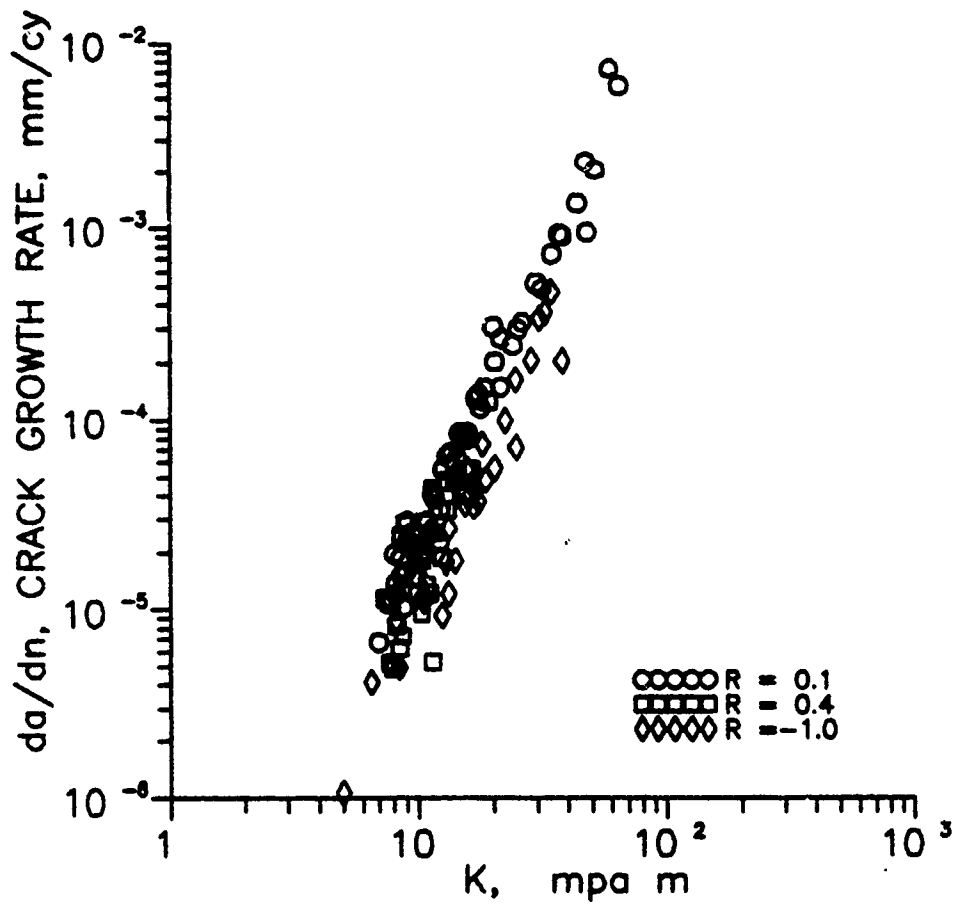


Fig. 4.41  $da/dn$  as a function of  $\Delta K_{eff}$  for LC condition of steel at all R ratios

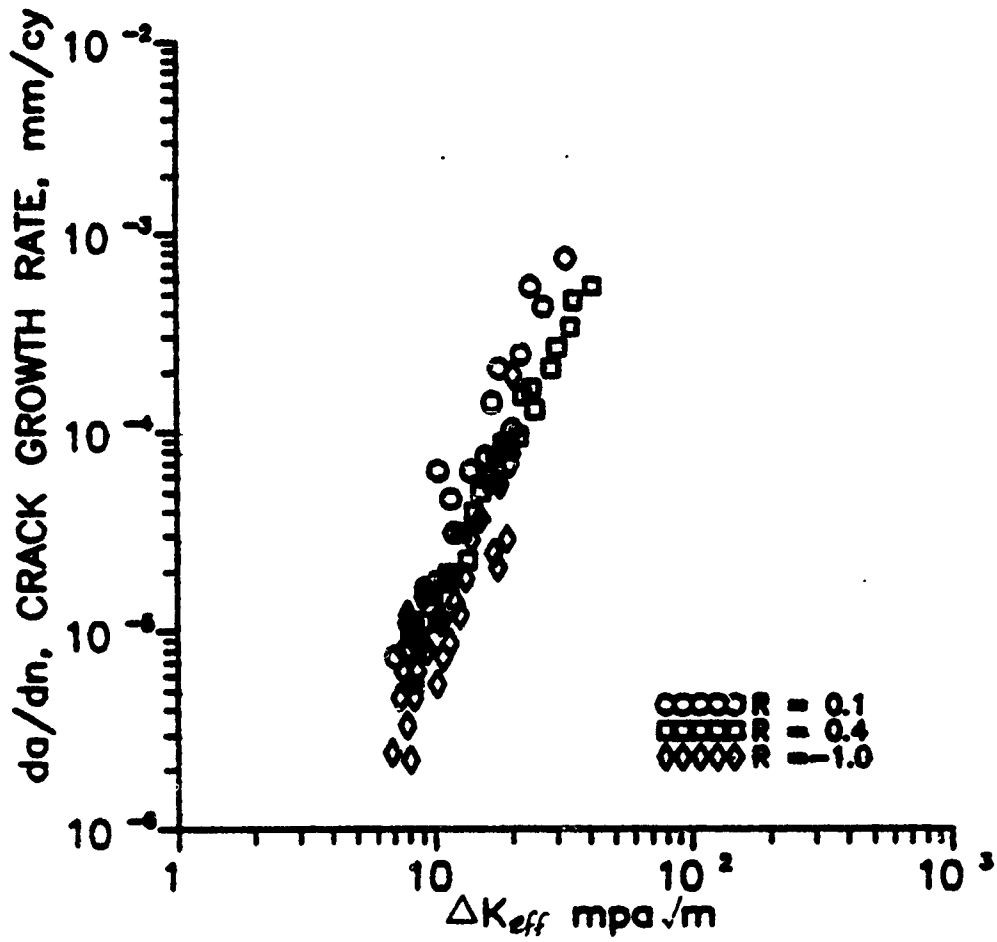


Fig. 4.42  $da/dn$  as a function of  $\Delta K_{eff}$  for HC condition of steel at all R ratios

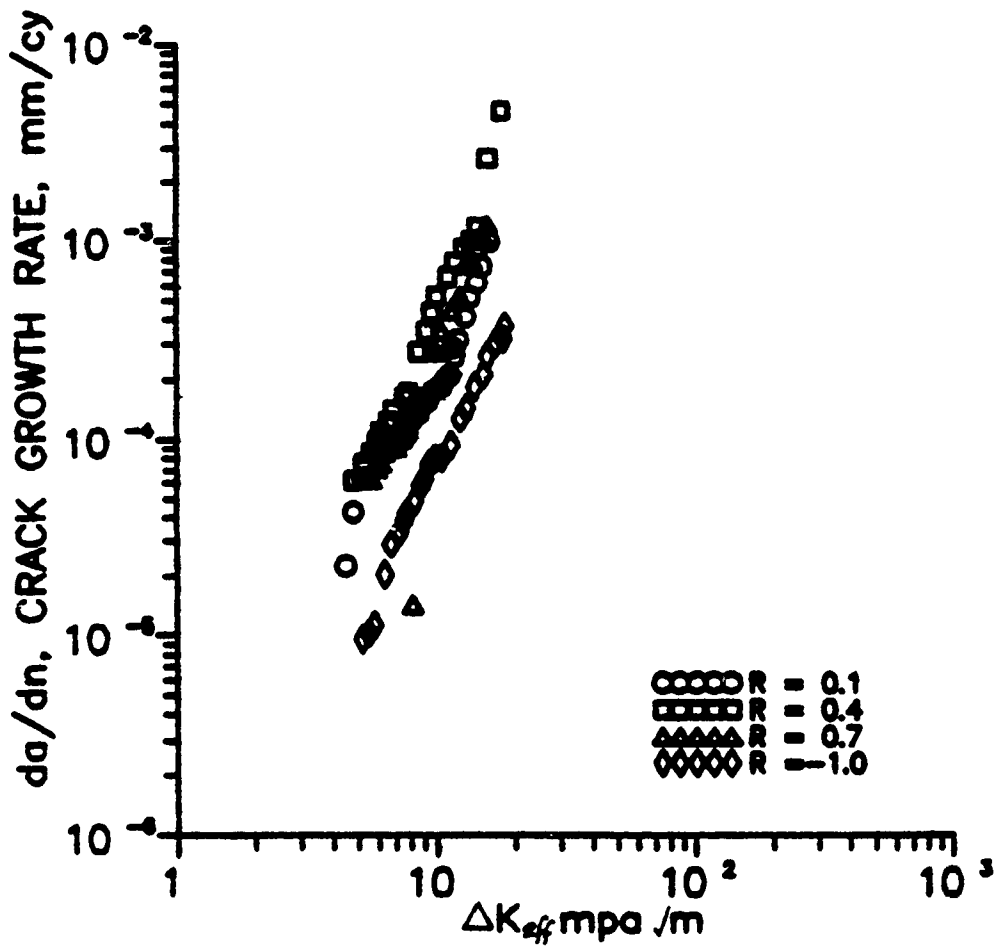


Fig. 4.43  $da/dn$  as a function of  $\Delta K_m$  for aluminum at all R ratios

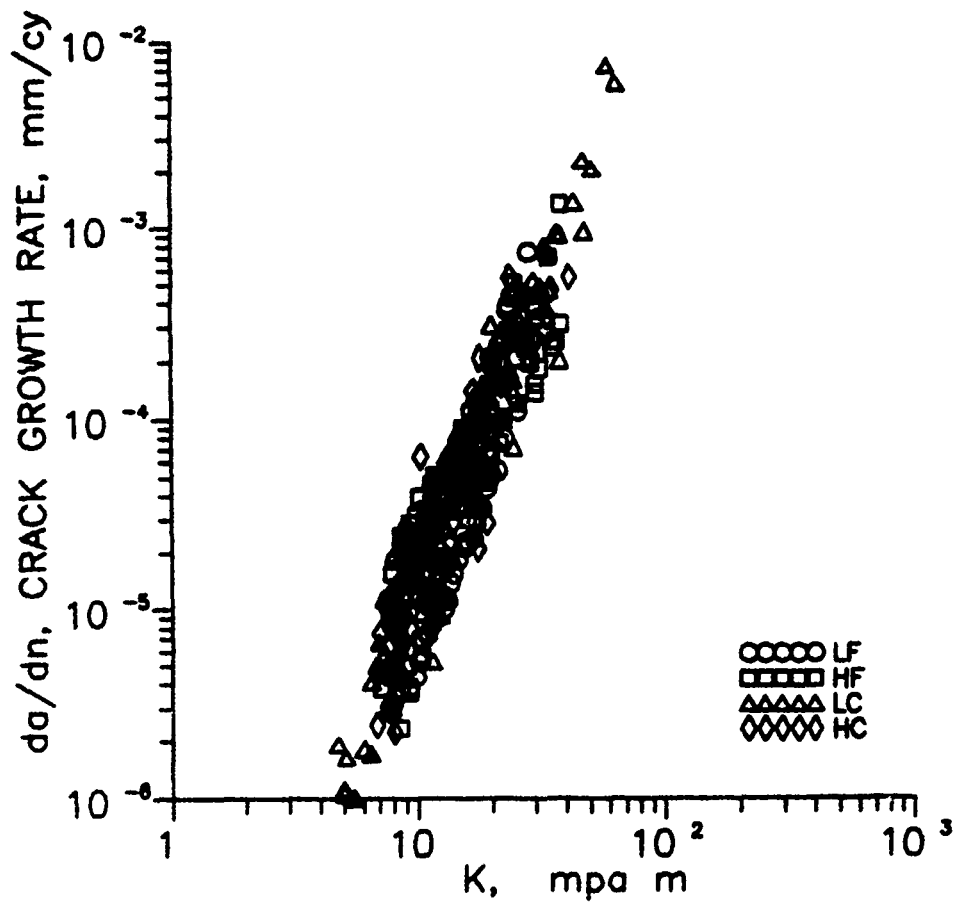


Fig. 4.44  $da/dn$  as a function of  $\Delta K_m$  for all four conditions of steel at different R ratios.

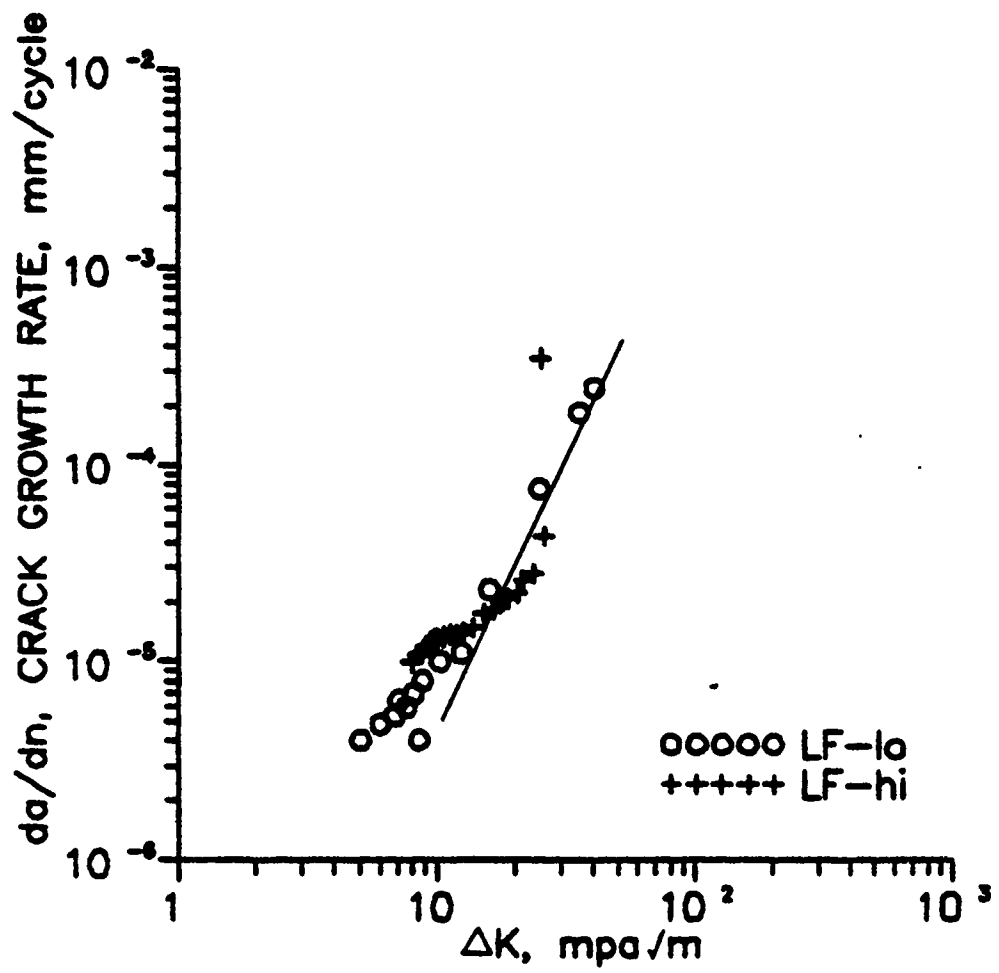


Fig. 4.45 Growth rate of short cracks in LF condition of steel at low and high stress levels at R ratio of 0.1

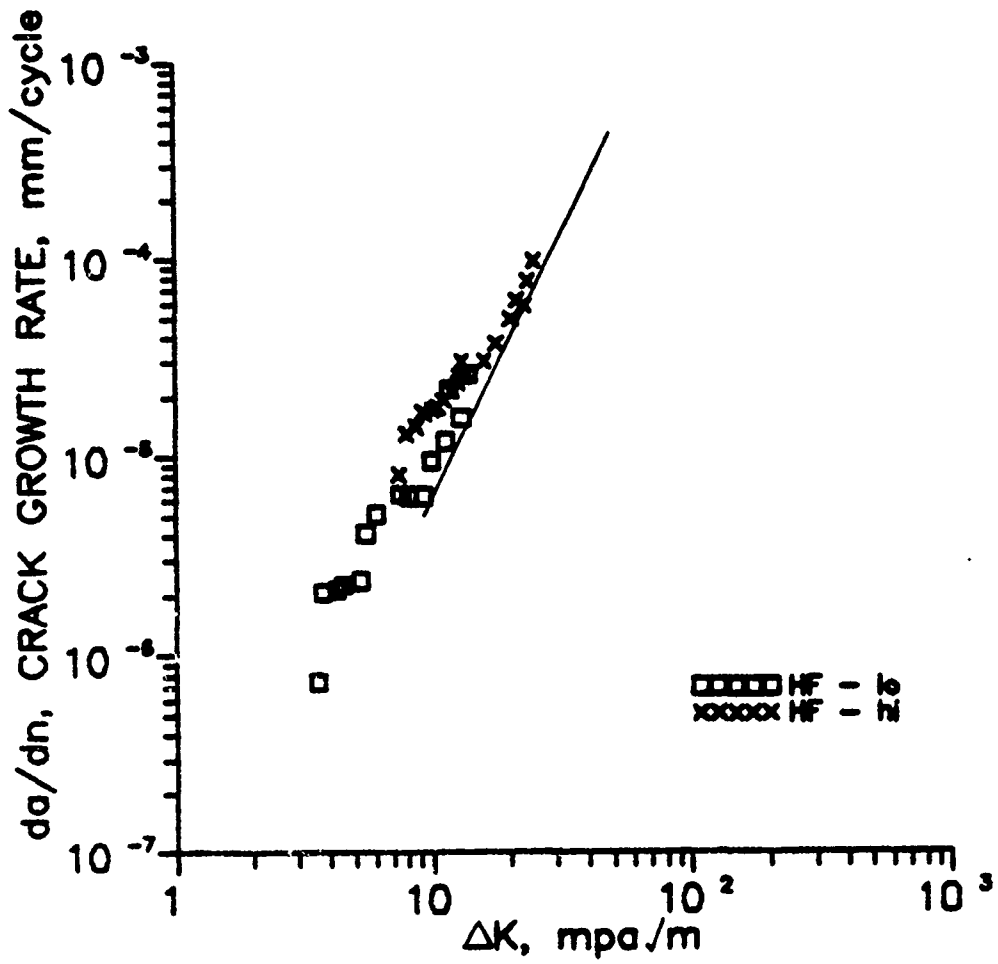


Fig. 4.46 Growth rate of short cracks in HF condition of steel at low and high stress levels at R ratio of 0.1

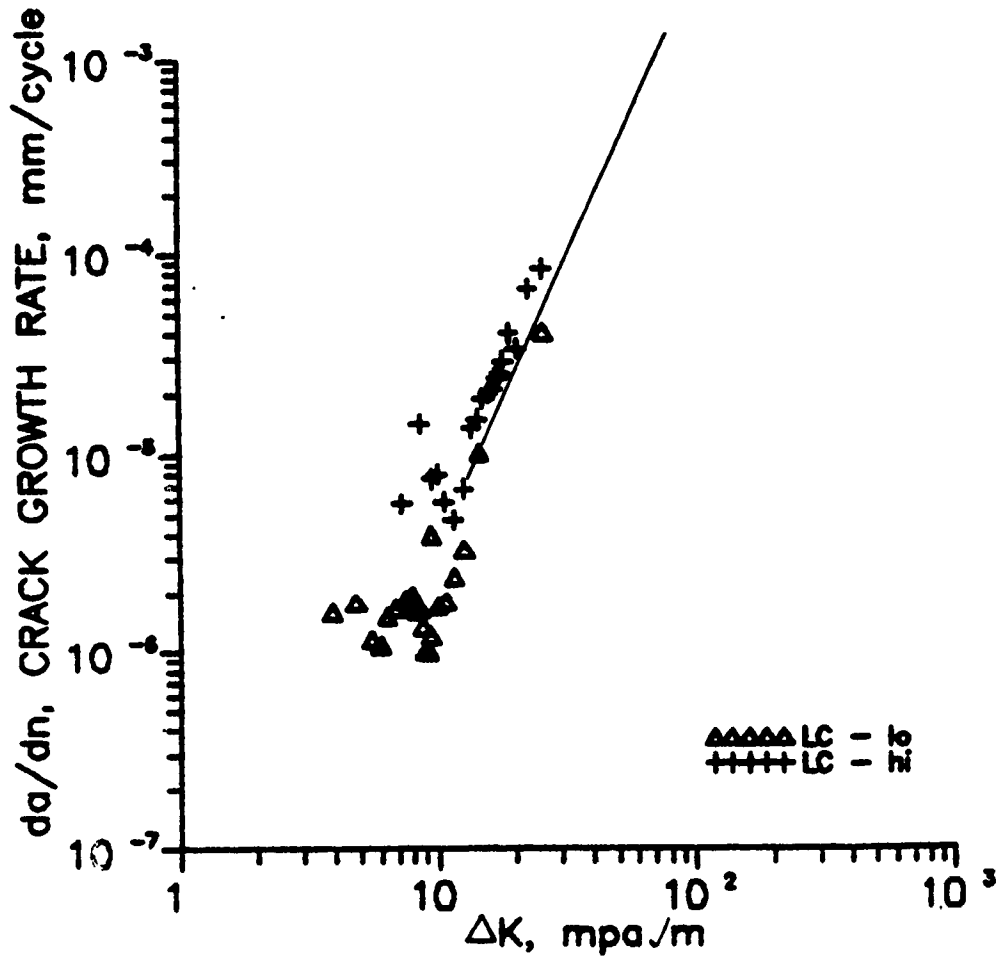


Fig. 4.47 Growth rate of short cracks in LC condition of steel at low and high stress levels at R ratio of 0.1

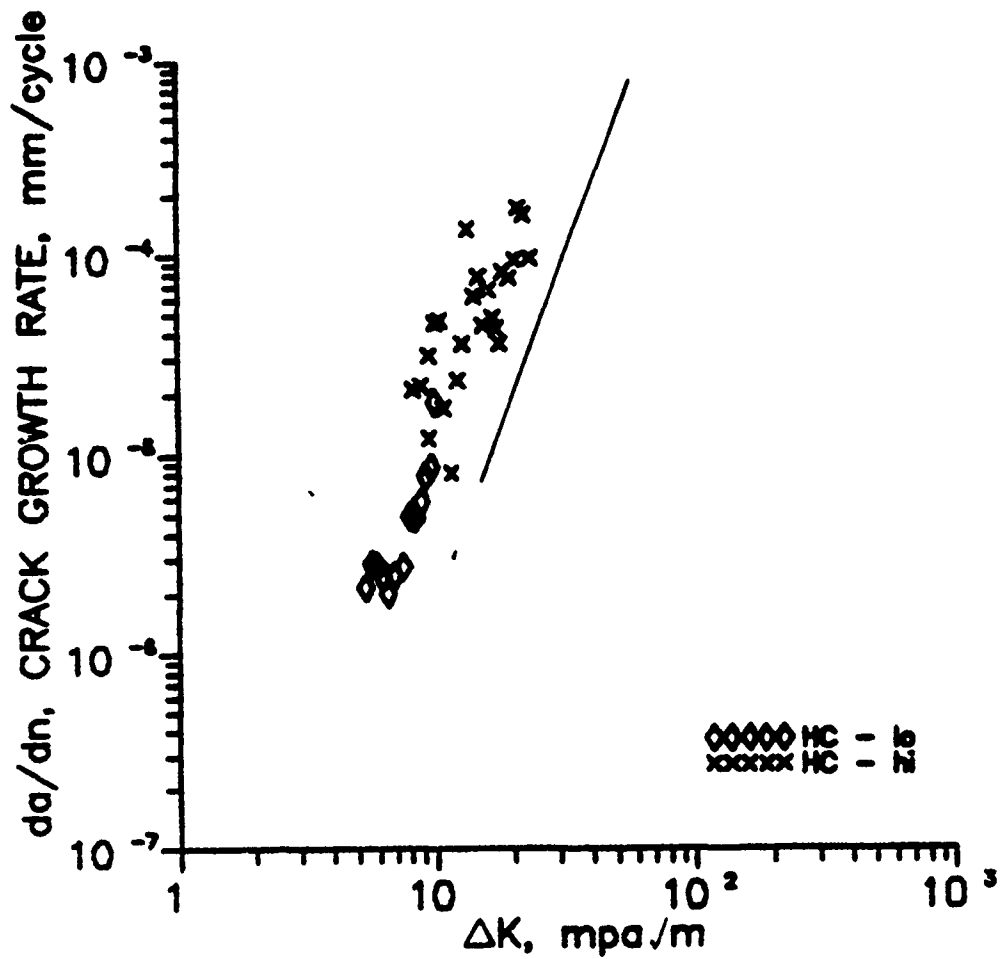


Fig. 4.48 Growth rate of short cracks in HC condition of steel at low and high stress levels at R ratio of 0.1

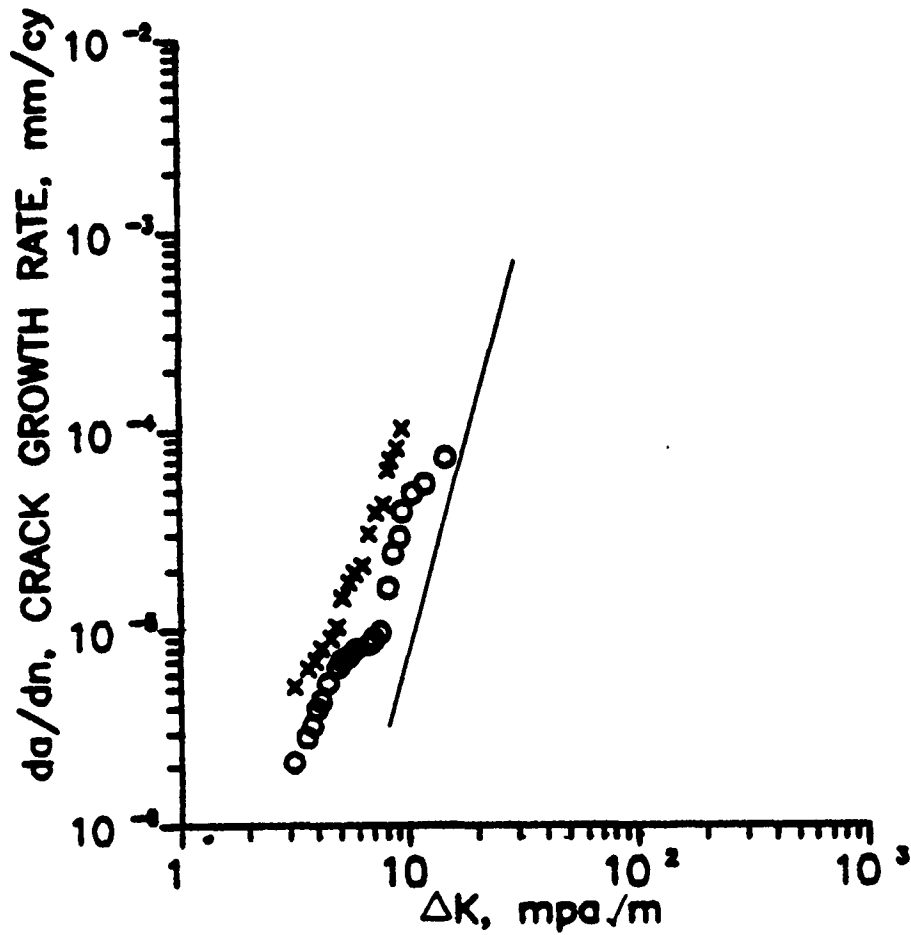


Fig. 4.49 Growth rate of short cracks in aluminum at low and high stress levels at R ratio of 0.1

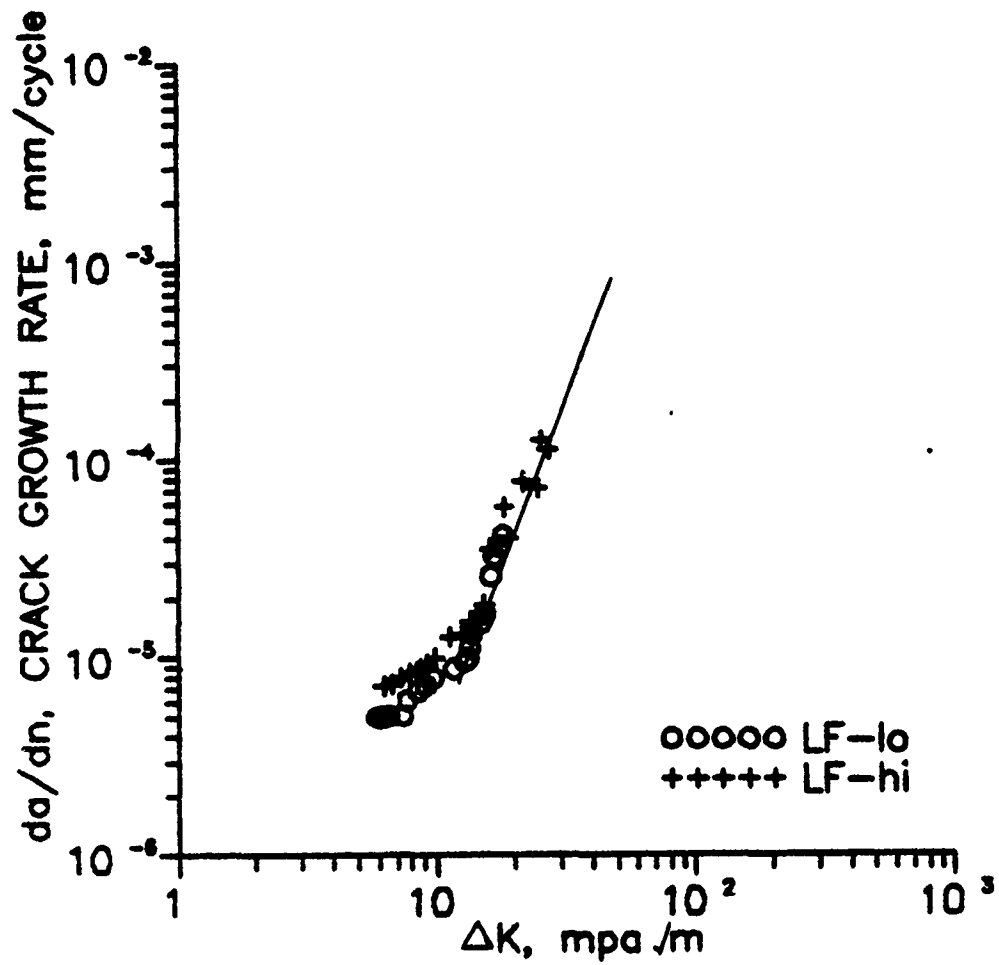


Fig. 4.50 Growth rate of short cracks in LF condition of steel at low and high stress levels at R ratio of 0.4

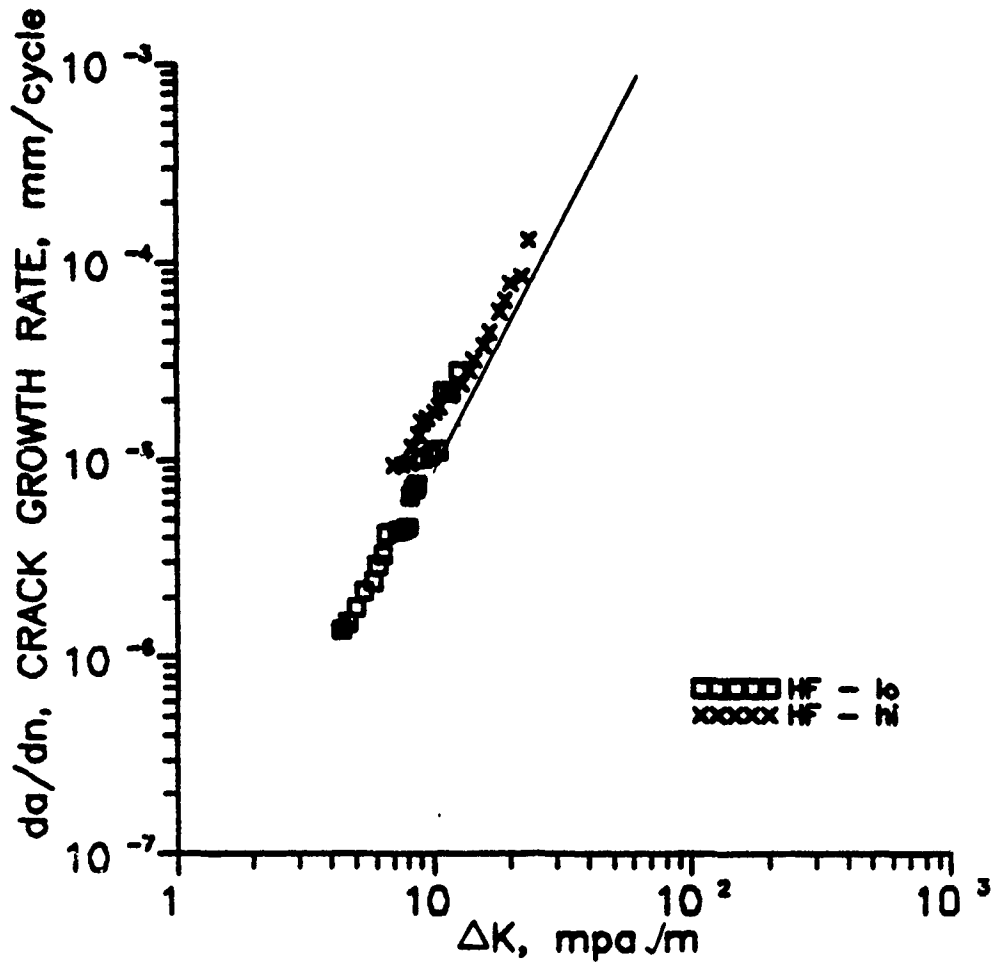


Fig. 4.51 Growth rate of short cracks in HF condition of steel at low and high stress levels at R ratio of 0.4

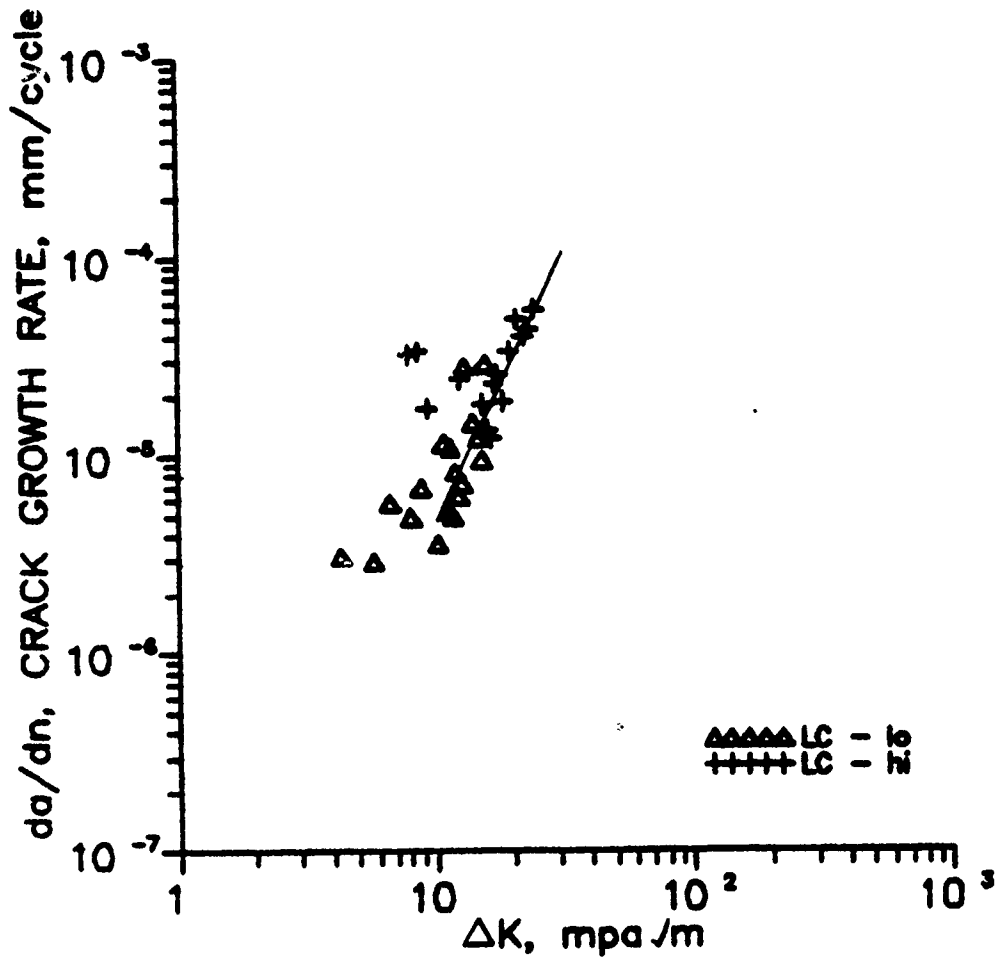


Fig. 4.52 Growth rate of short cracks in LC condition of steel at low and high stress levels at R ratio of 0.4

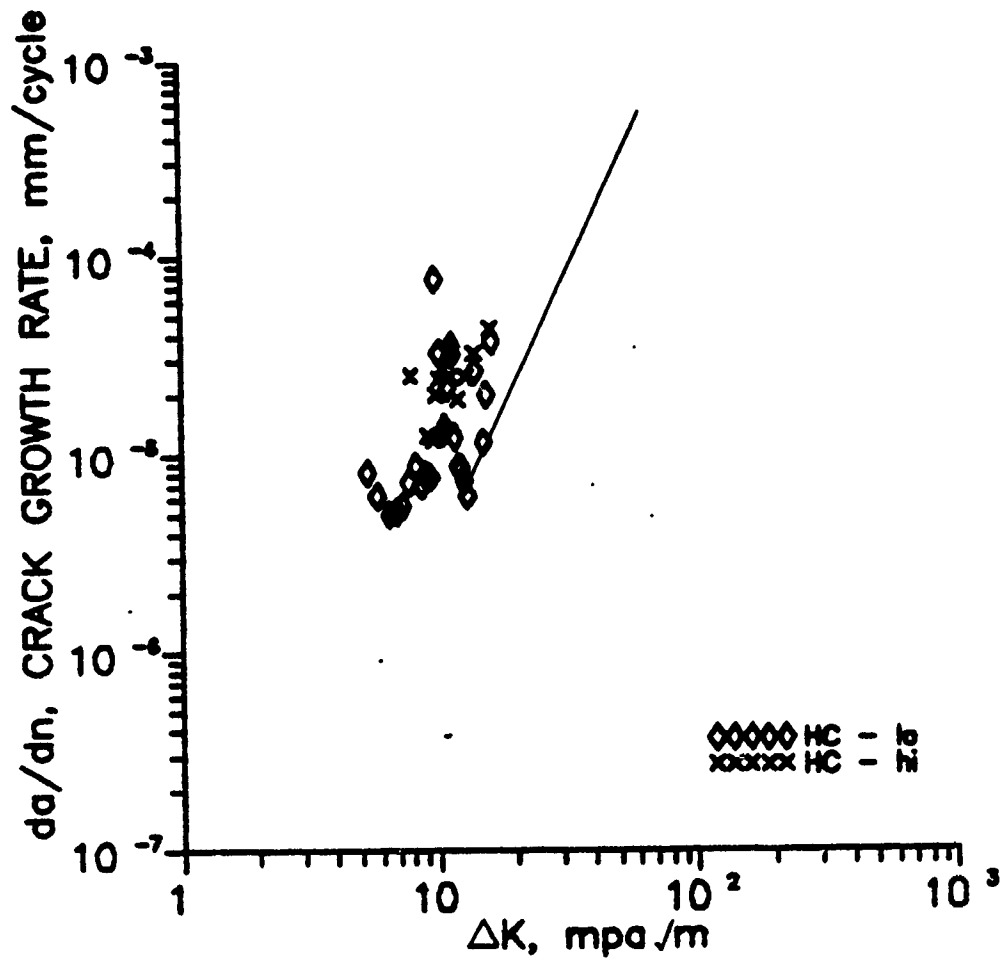


Fig. 4.53 Growth rate of short cracks in HC condition of steel at low and high stress levels at R ratio of 0.4

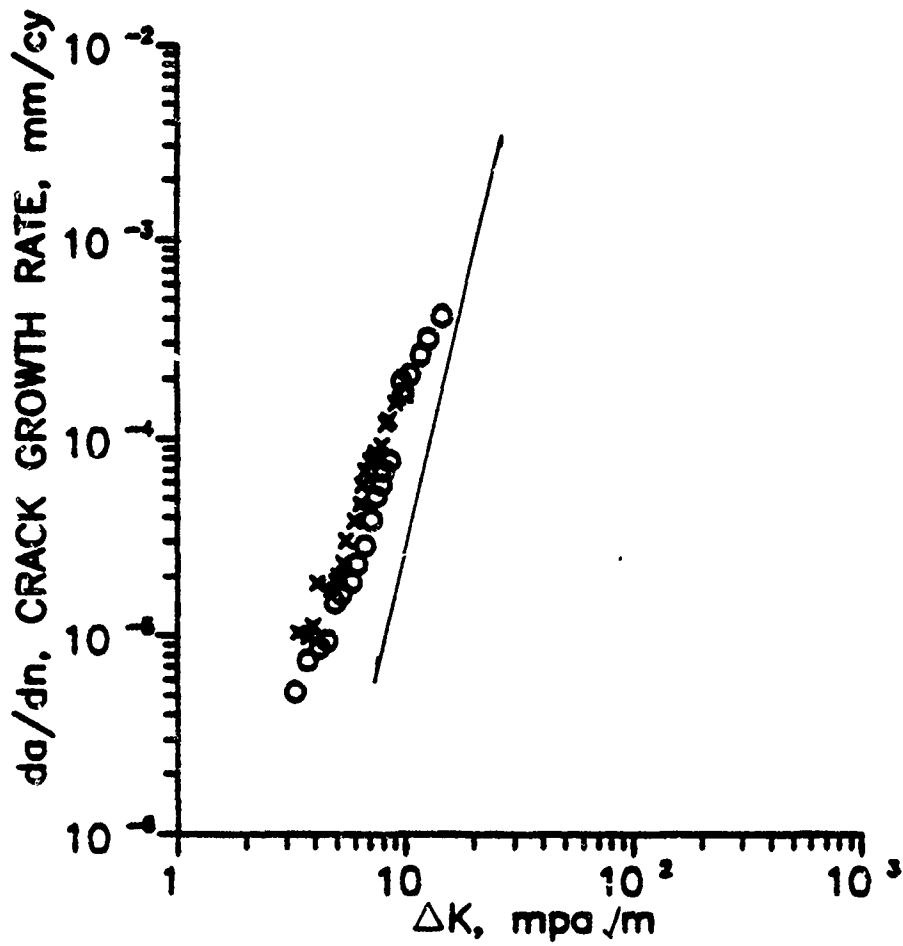


Fig. 4.54 Growth rate of short cracks in aluminum at low and high stress levels at R ratio of 0.4

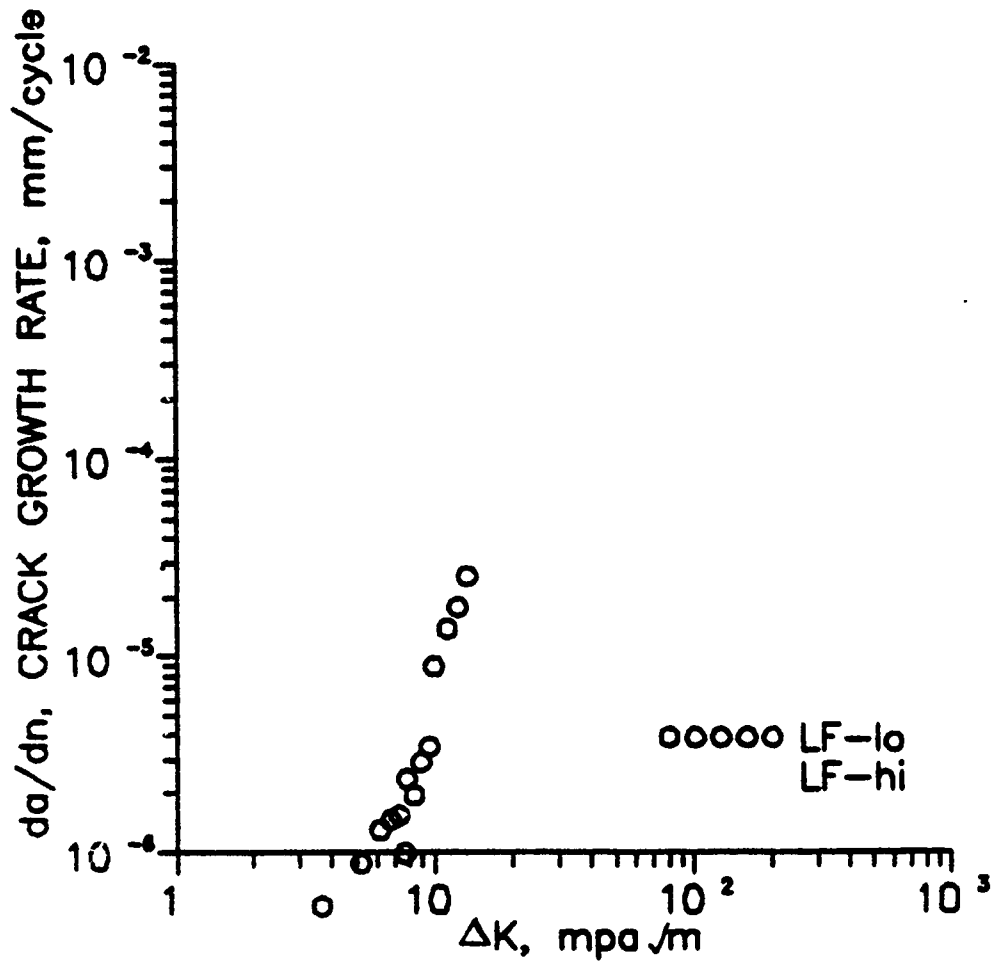


Fig. 4.55 Growth rate of short cracks in LF condition of steel at low and high stress levels at R ratio of 0.7

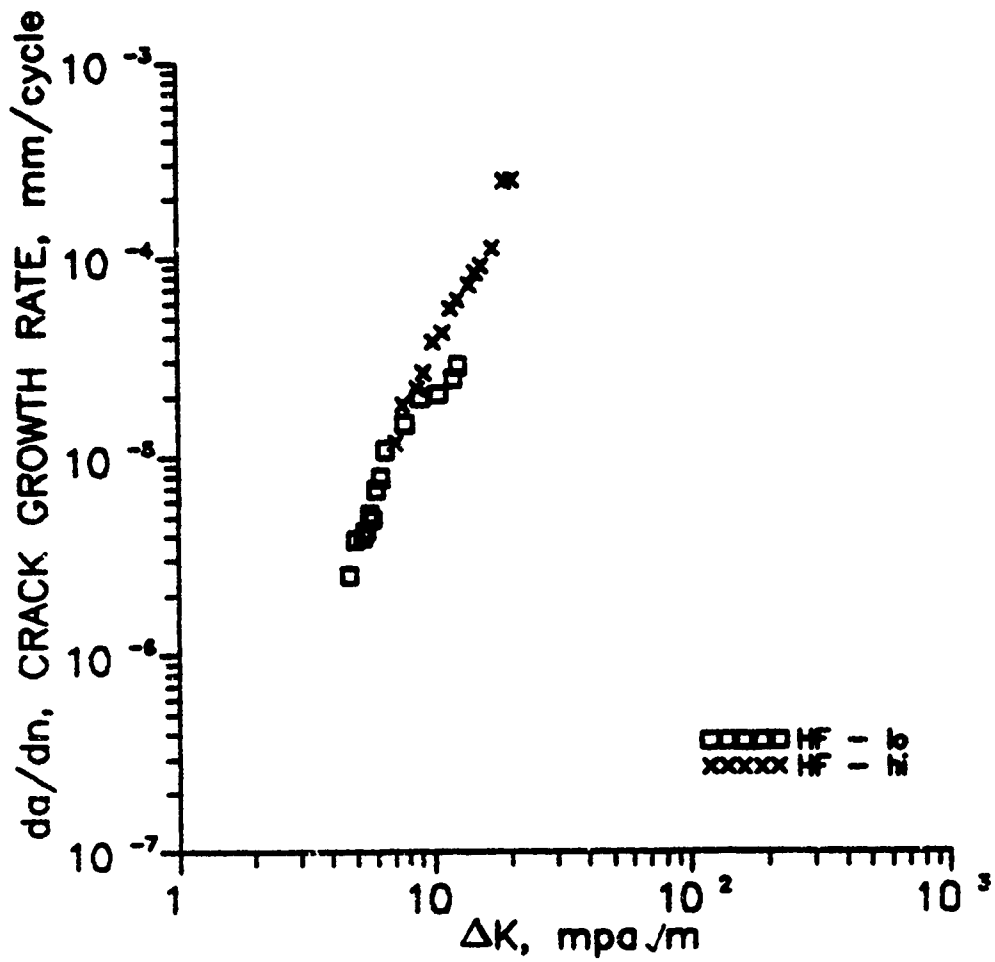


Fig. 4.56 Growth rate of short cracks in HF condition of steel at low and high stress levels at R ratio of 0.7

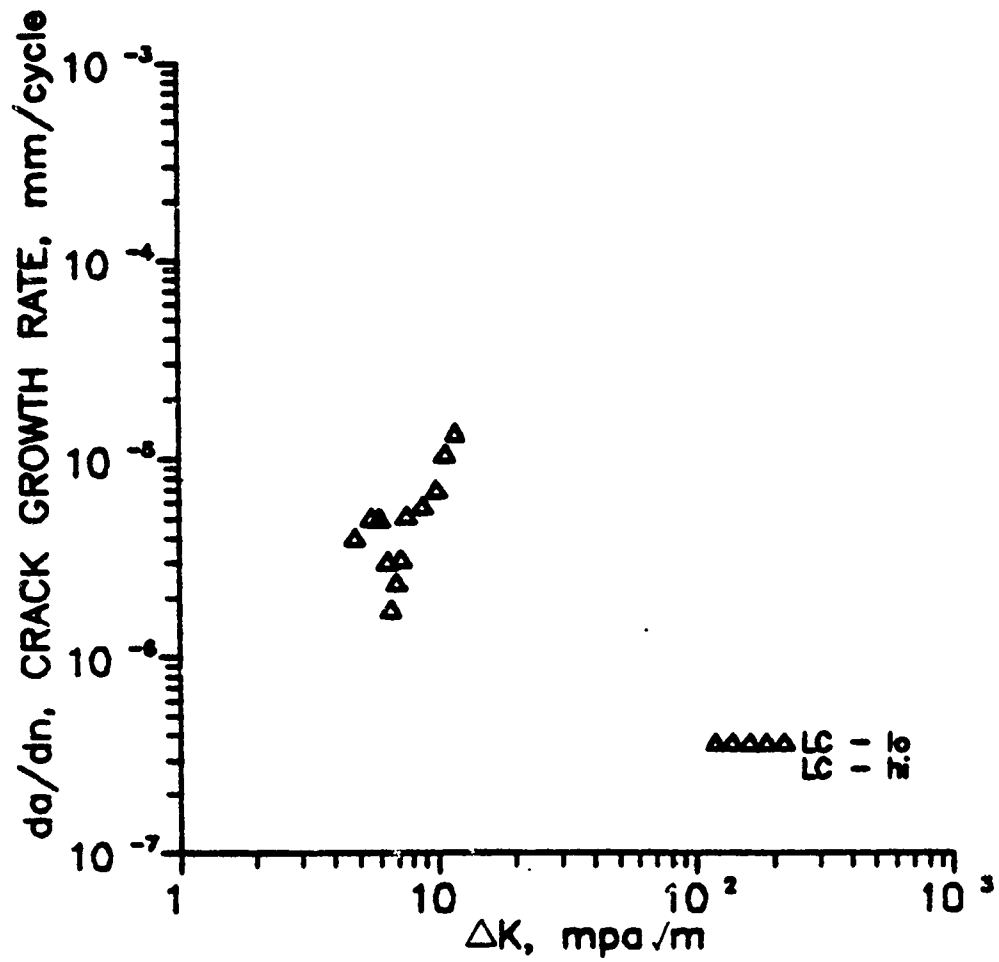


Fig. 4.57 Growth rate of short cracks in LC condition of steel at low and high stress level at R ratio of 0.7

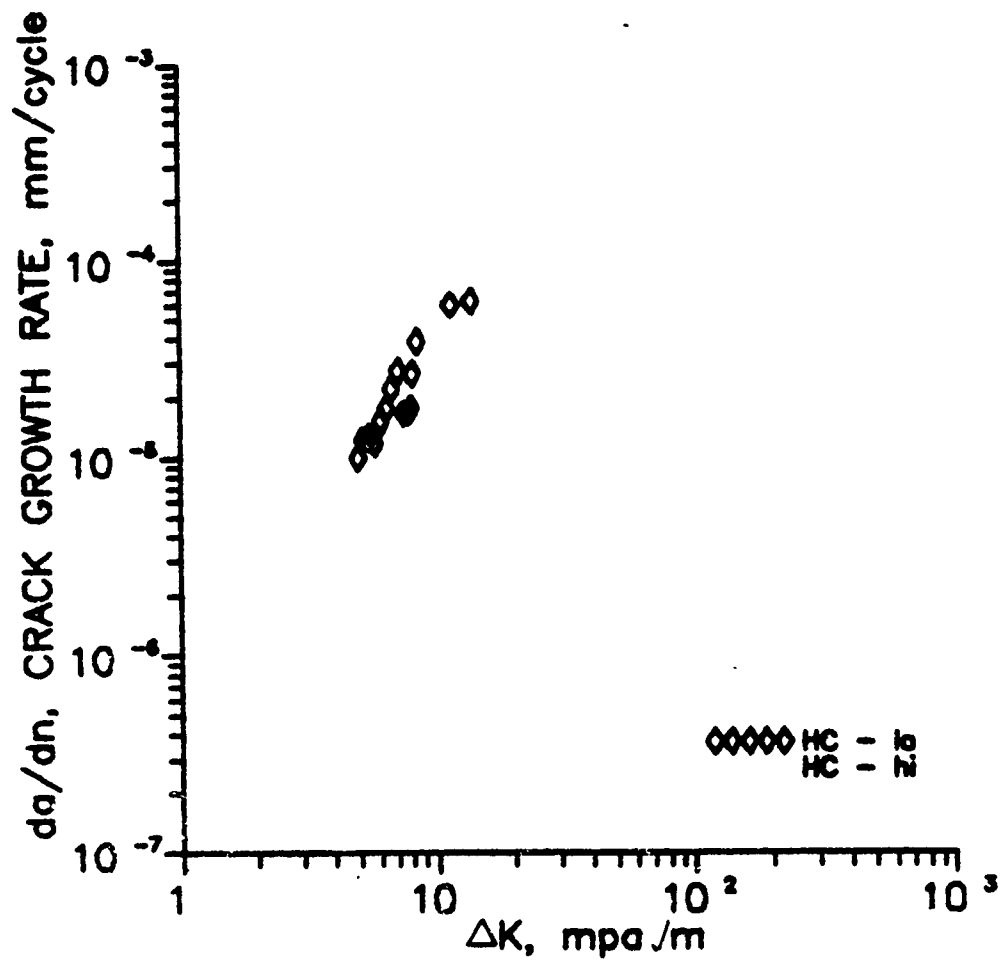


Fig. 4.58 Growth rate of short cracks in HC condition of steel at low and high stress levels at R ratio of 0.7

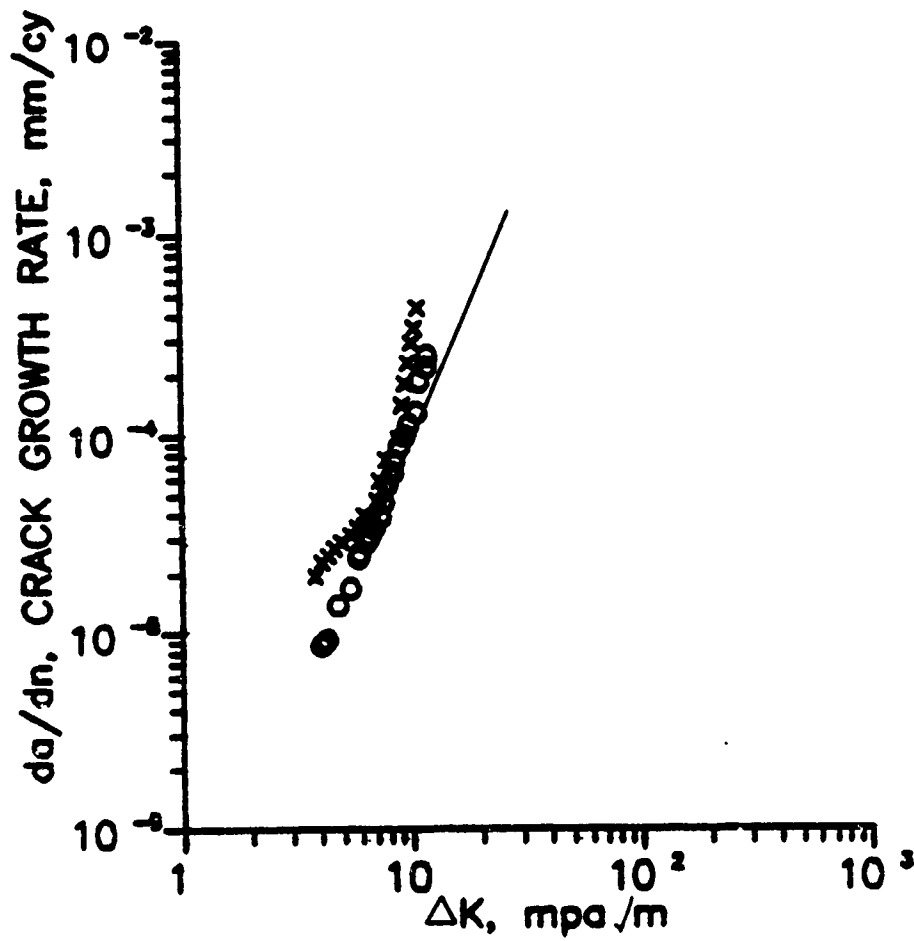


Fig. 4.59 Growth rate of short cracks in aluminum at low and high stress levels at R ratio of 0.7

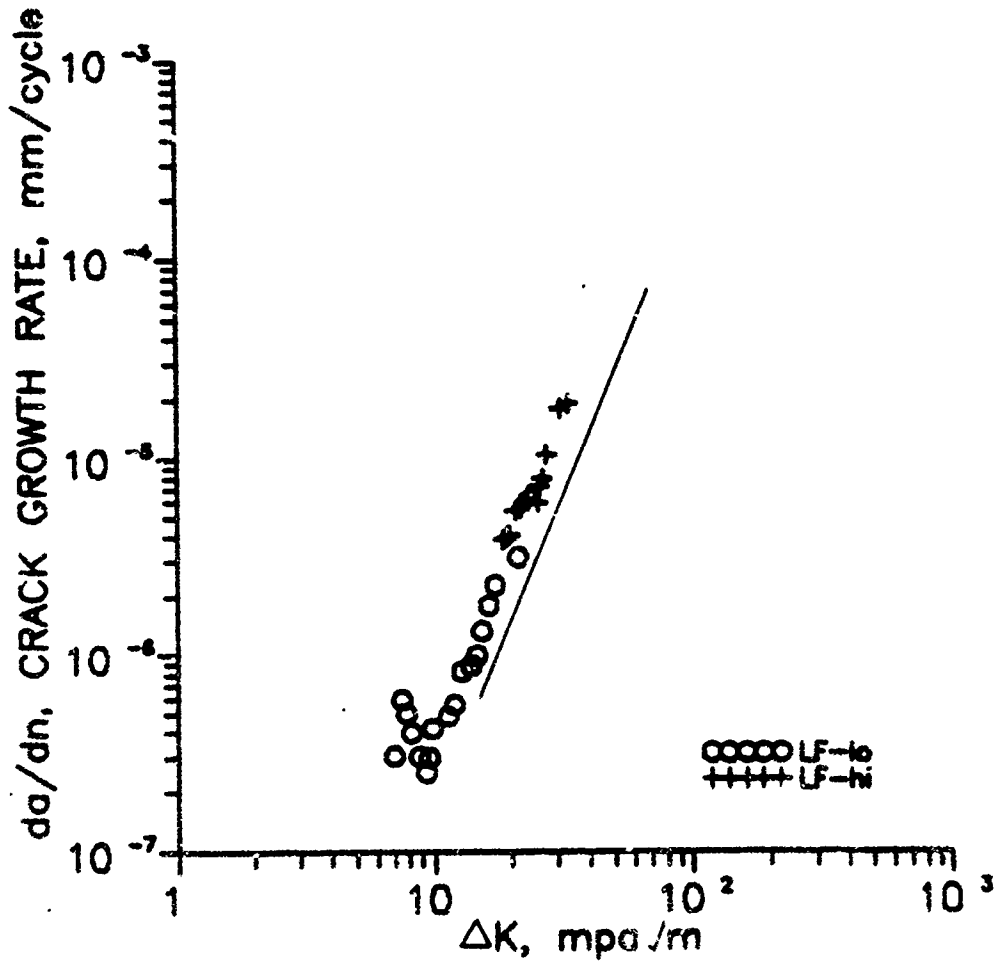


Fig. 4.60 Growth rate of short cracks in LF condition of steel at low and high stress levels at R ratio of -1.0

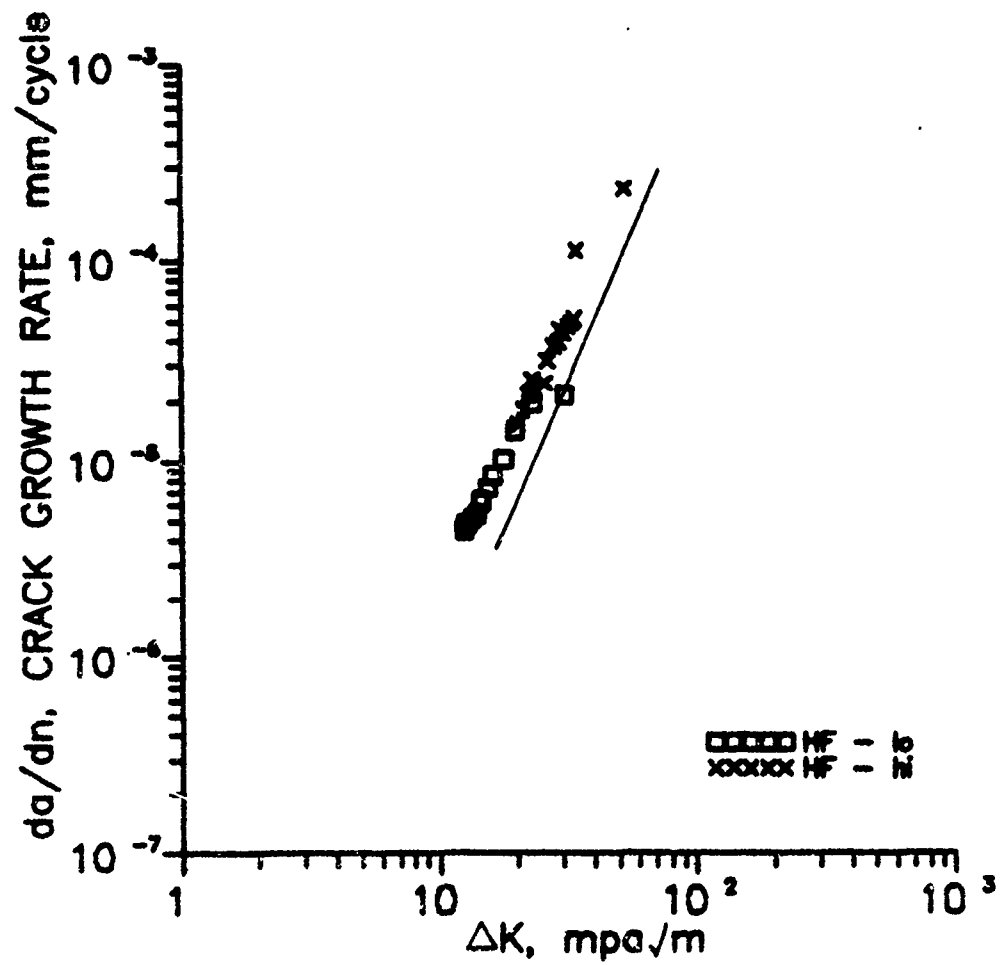


Fig. 4.61 Growth rate of short cracks in HF condition of steel at low and high stress levels at R ratio of -1.0

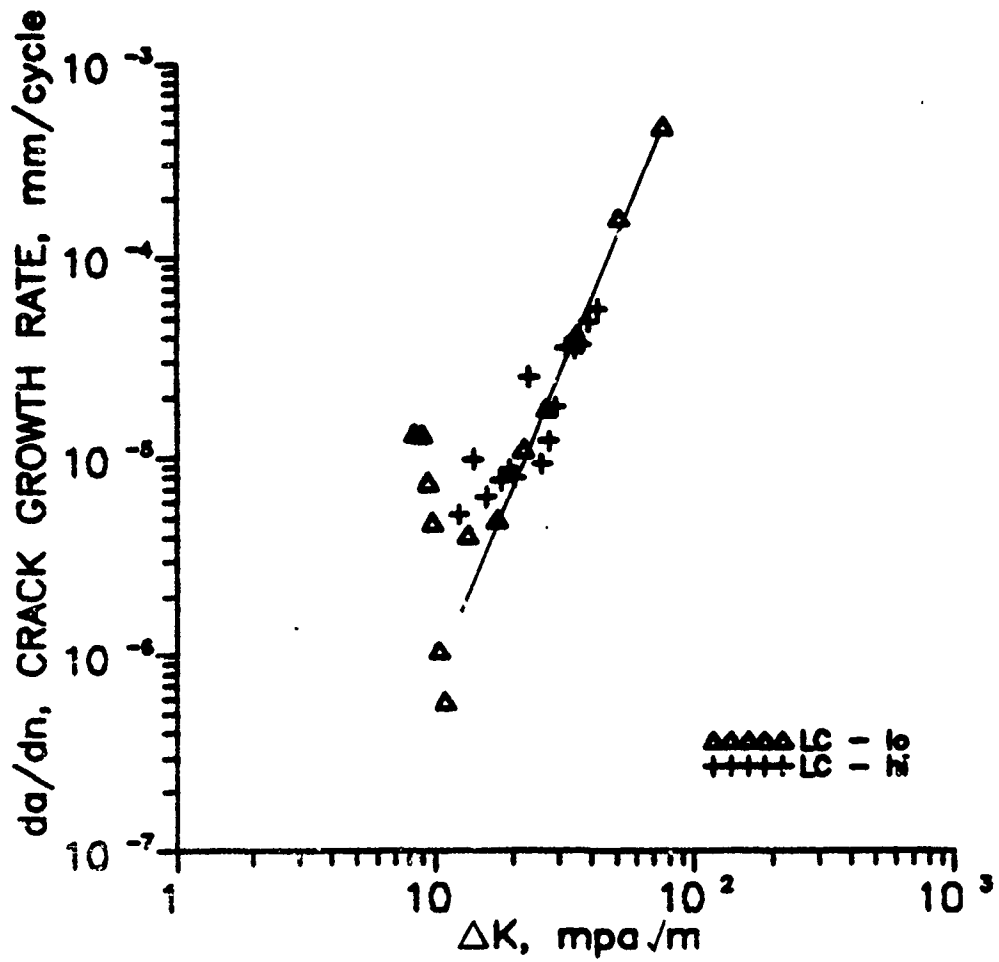


Fig. 4.62 Growth rate of short cracks in LC condition of steel at low and high stress level at R ratio of -1.0



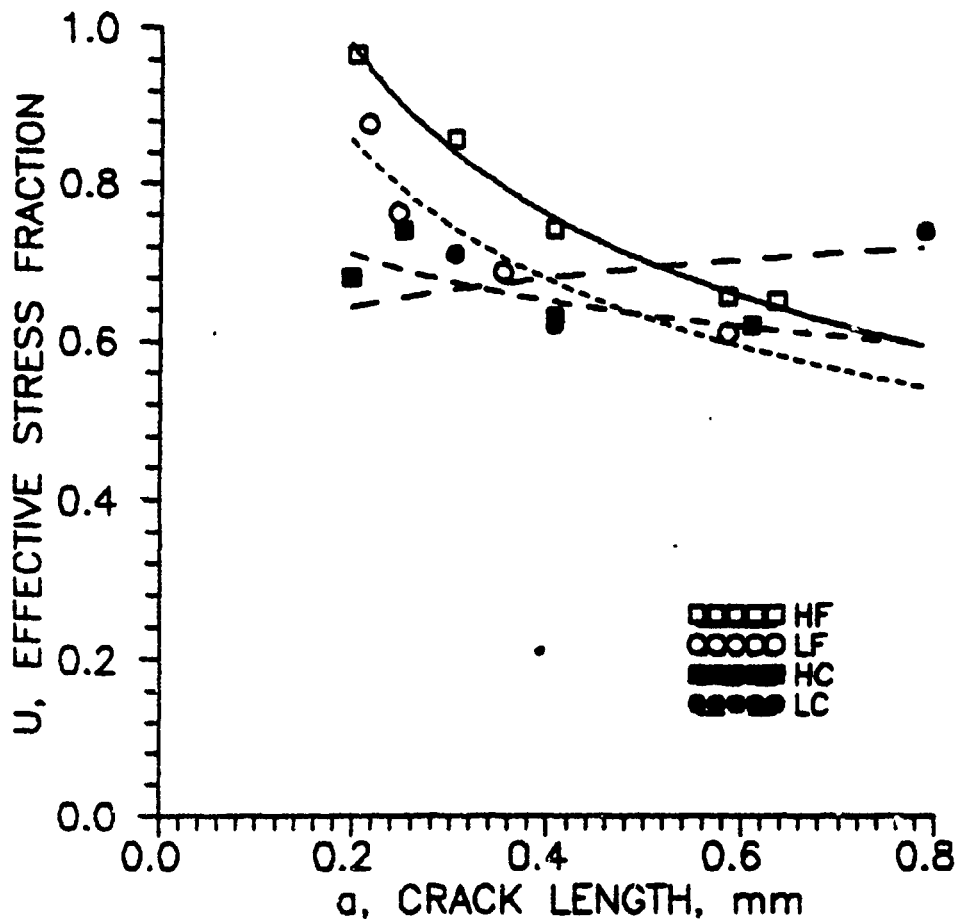


Fig. 4.64 Effective stress fraction, U, as a function of crack length, a, in LF, HF, LC, and HC conditions of steel at R = 0.1 (low stress level)

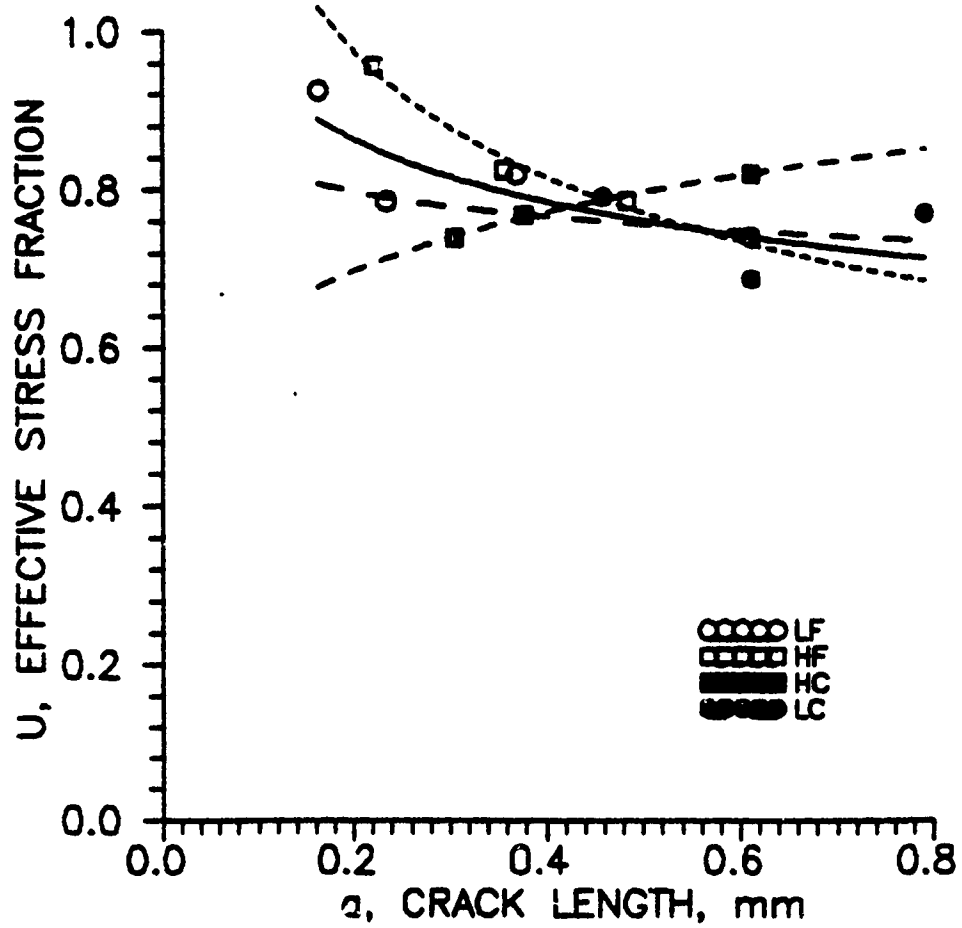


Fig. 4.65 Effective stress fraction, U, as a function of crack length, a, in LF, HF, LC and HC conditions of steel at R = 0.4 (low stress level)

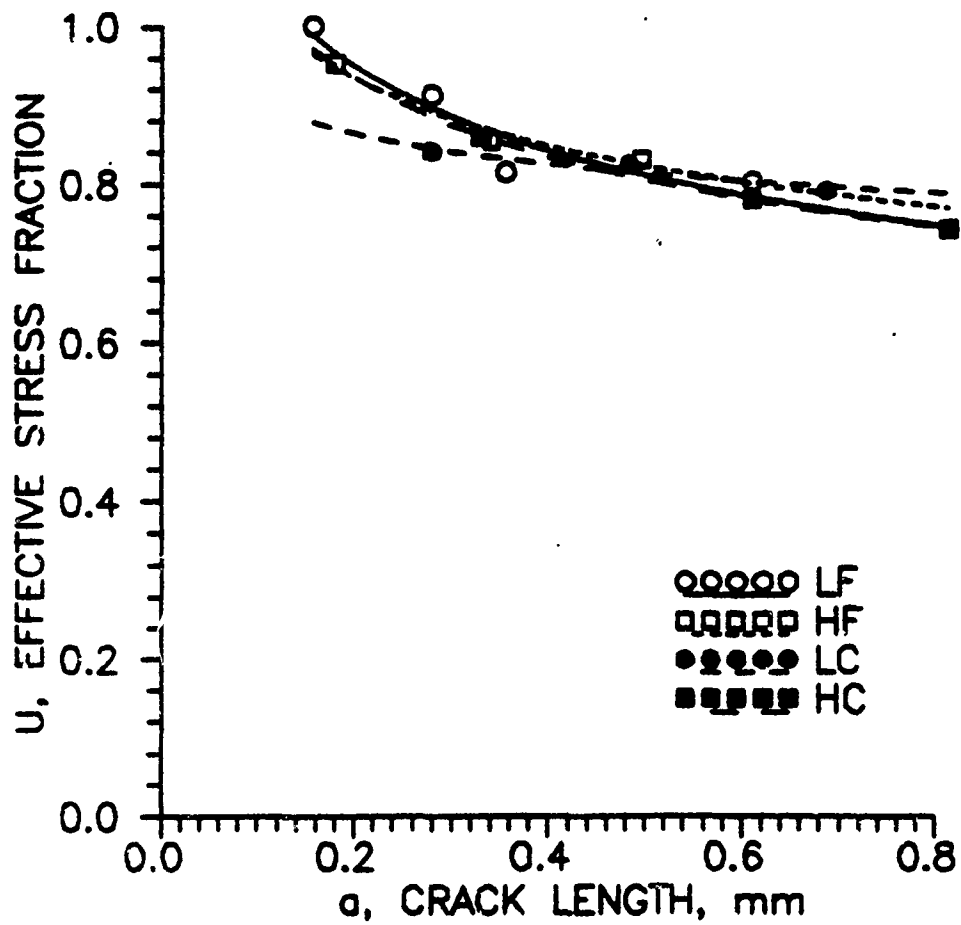


Fig. 4.66 Effective stress fraction, U, as a function of crack length, a, in LF, HF, LC and HC conditions of steel at R = 0.7 (low stress level)

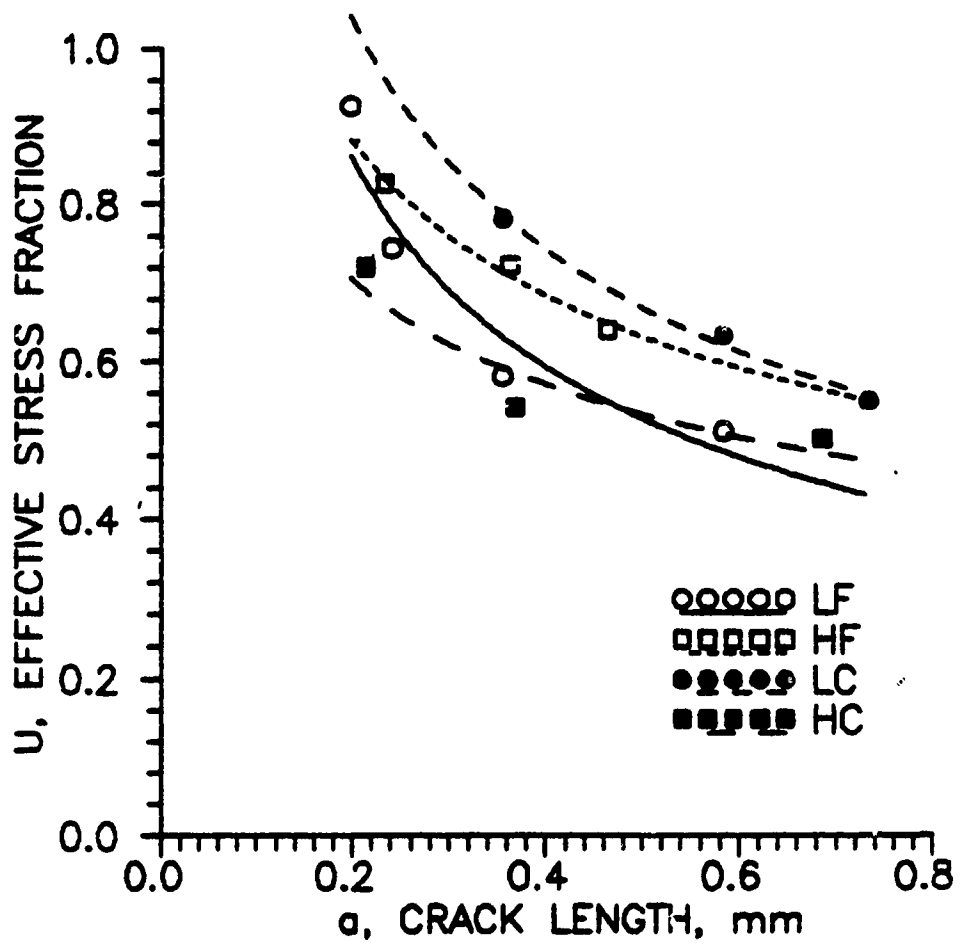


Fig. 4.67 Effective stress fraction, U, as a function of crack length, a, in LF, HF, LC and HC conditions of steel at  $R = -1.0$  (low stress level)

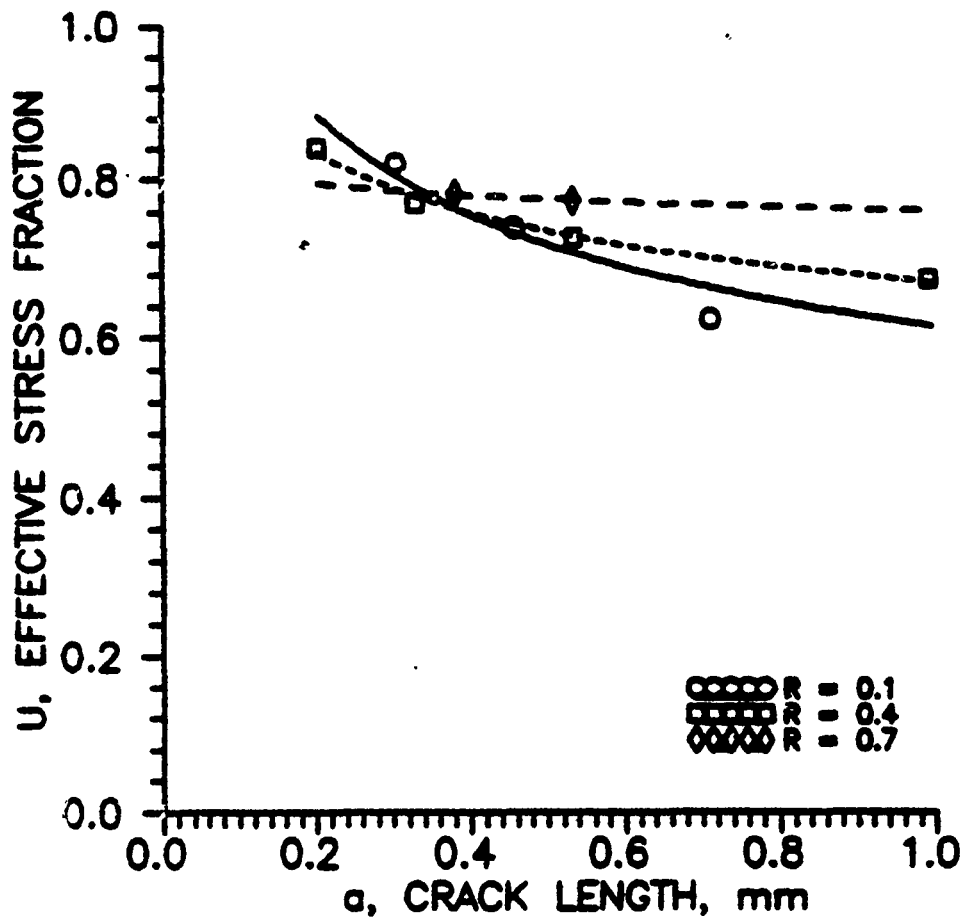


Fig. 4.68 Effective stress fraction,  $U$ , as a function of crack length,  $a$ , in aluminum at different  $R$  ratios (low stress level).

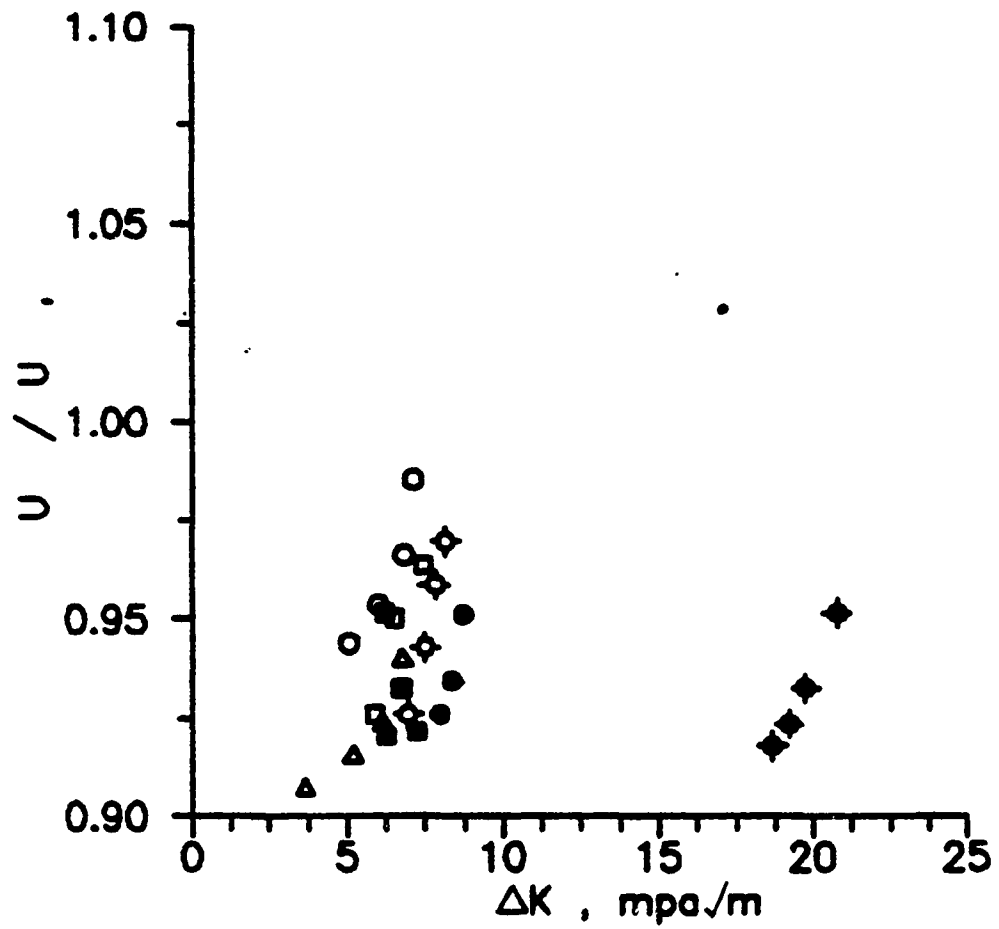


Fig. 4.59 Ratio of stress functions,  $U/U'$ , as a function of applied  $\Delta K$  for LF condition of steel at different R ratios.

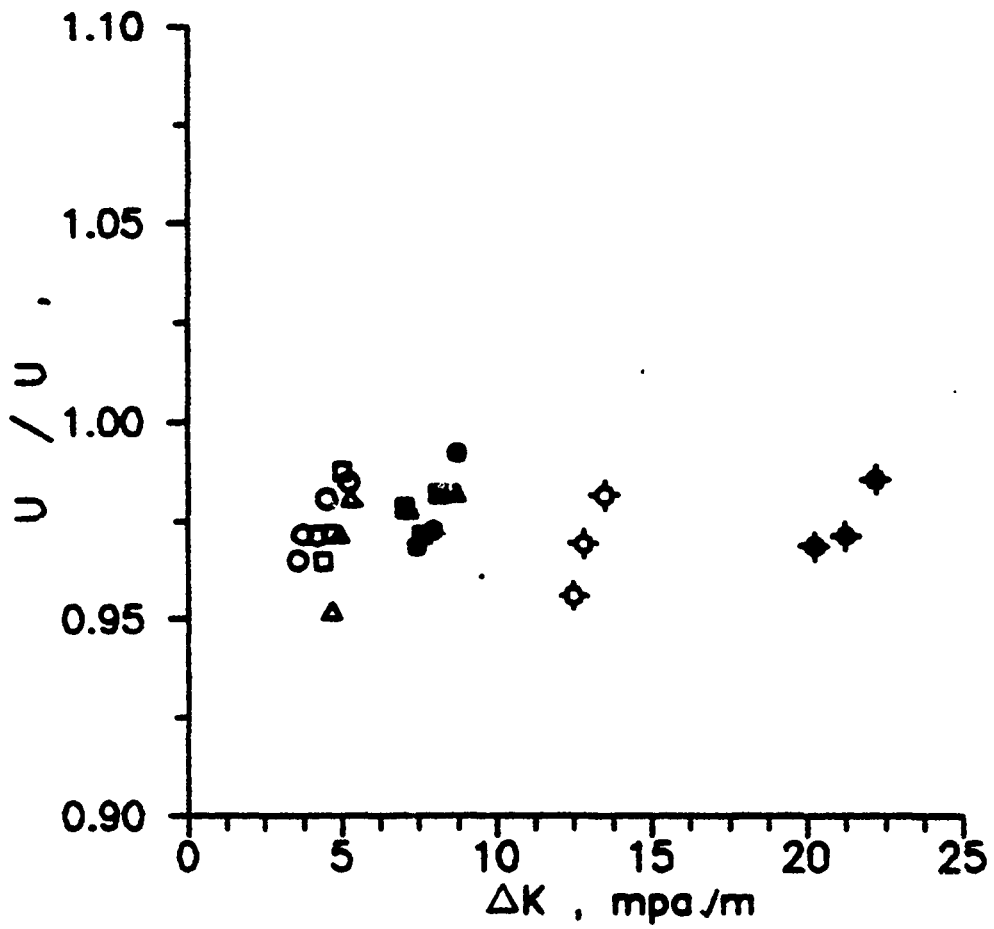


Fig. 4.70 Ratio of stress fractions,  $U/U'$ , as a function of applied  $\Delta K$  for HF condition of steel at different R ratios.

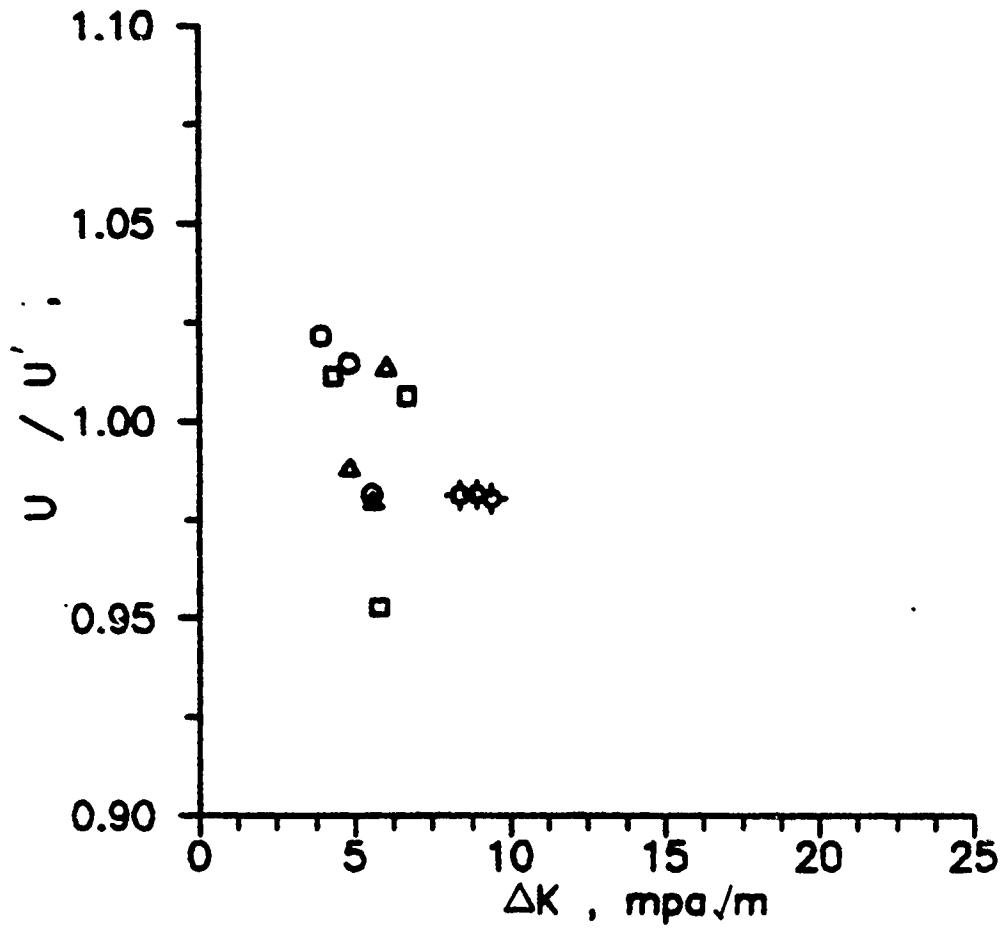


Fig. 4.71 Ratio of stress fractions,  $U/U'$ , as a function of applied  $\Delta K$  for LC condition of steel at different R ratios.

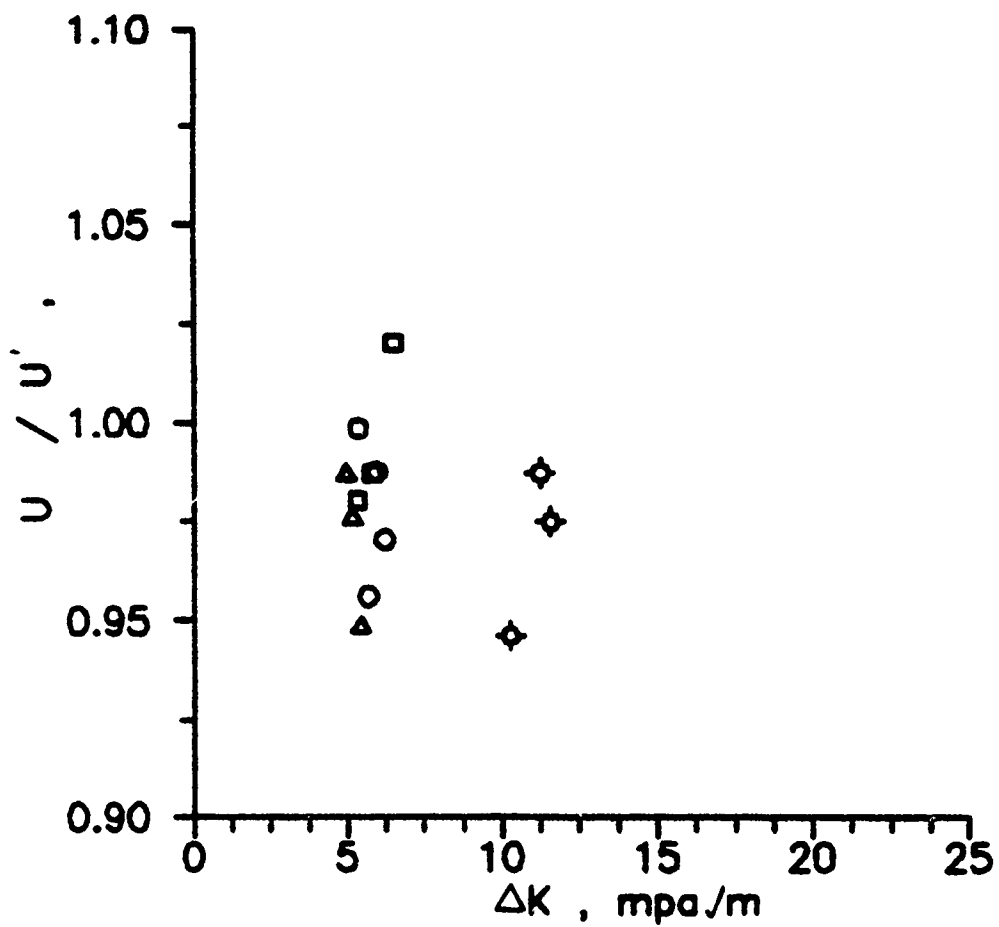


Fig. 4.72 Ratio of stress fractions,  $U/U'$ , as a function of applied  $\Delta K$  for HC condition of steel at different R ratios.

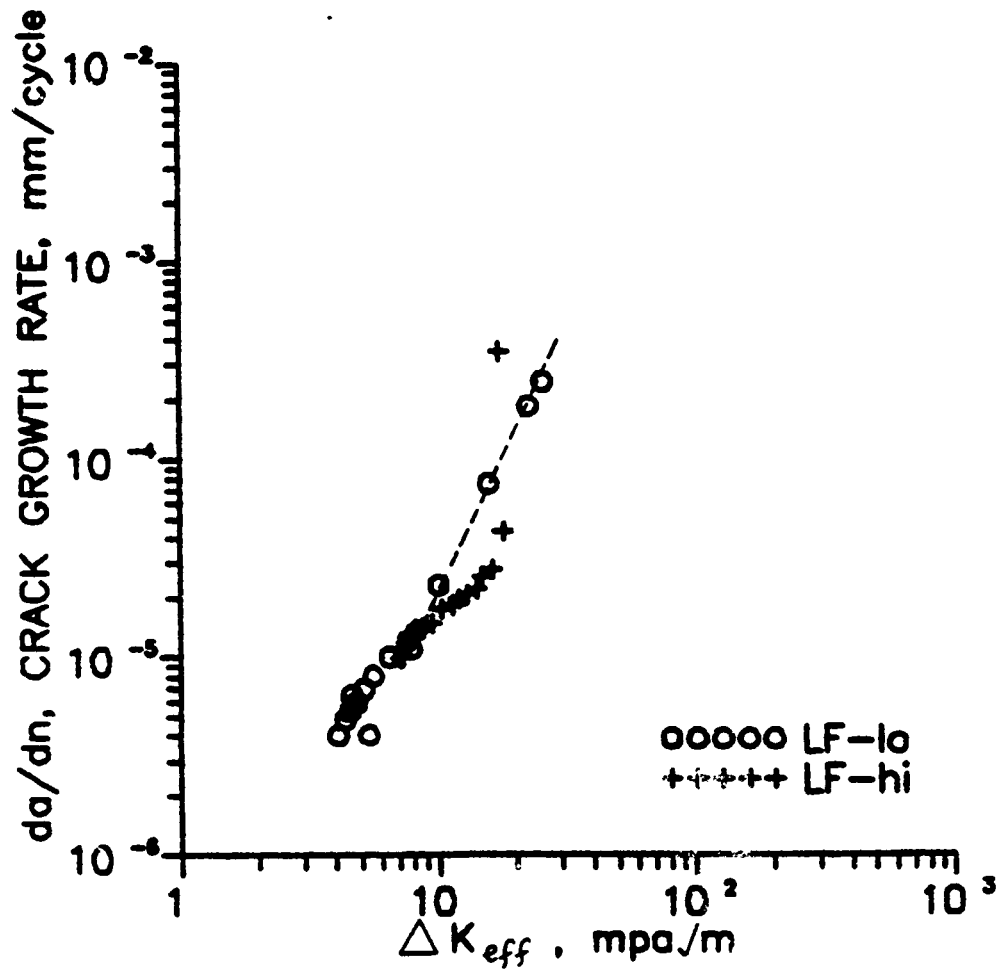


Fig. 4.73 Growth rate,  $da/dn$ , of short cracks at low and high stress levels as a function of  $\Delta K_{eff}$  in LF condition of steel at R ratio of 0.1.

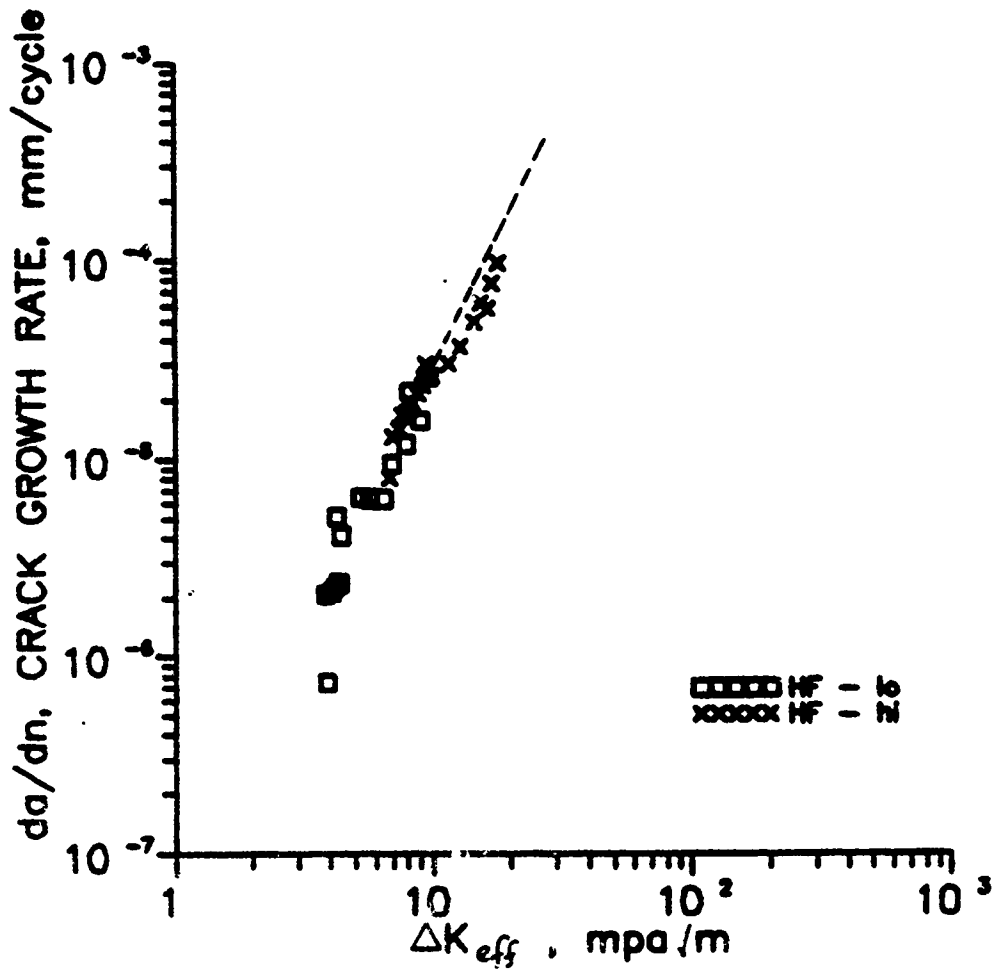


Fig. 4.74 Growth rate,  $da/dn$ , of short cracks at low and high stress levels as a function of  $\Delta K_{eff}$  in HF condition of steel at R ratio of 0.1.

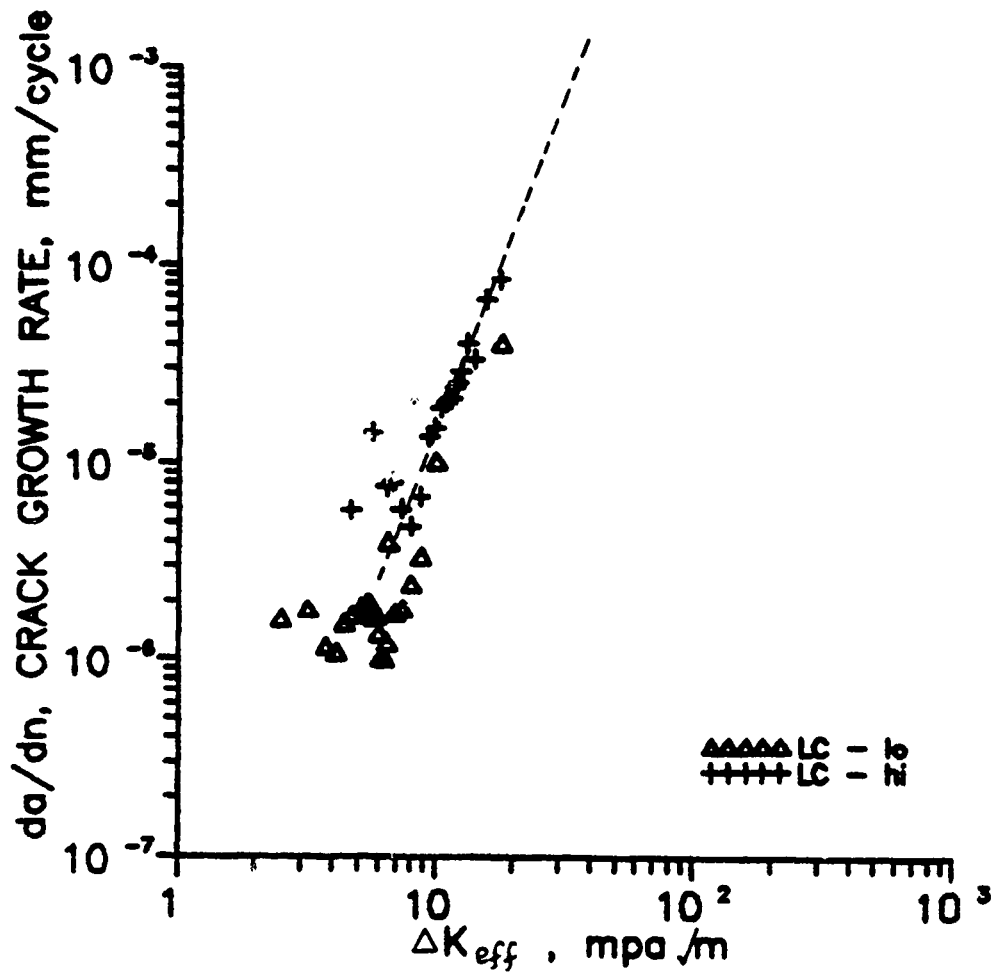


Fig. 4.75 Growth rate,  $da/dn$ , of short cracks at low and high stress levels as a function of  $\Delta K_{eff}$  in LC condition of steel at R ratio of 0.1.

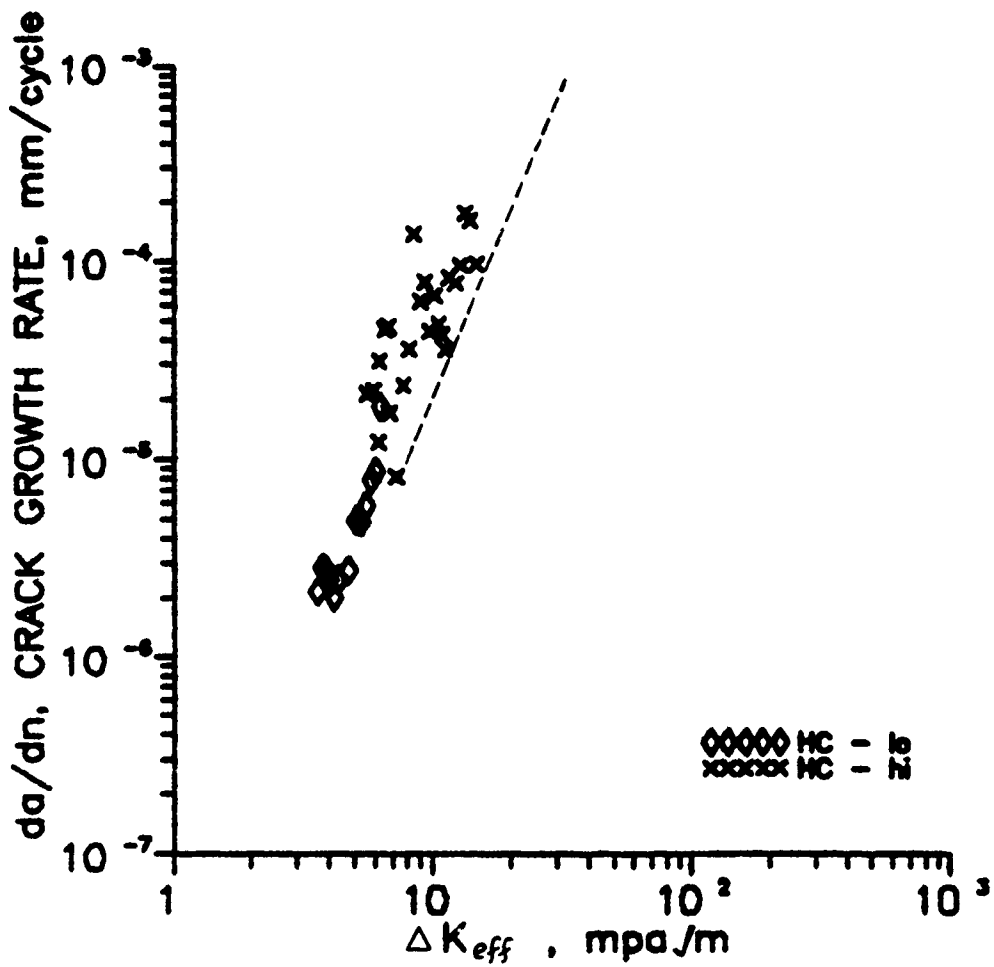


Fig. 4.76 Growth rate,  $da/dn$ , of short cracks at low and high stress levels as a function of  $\Delta K_{eff}$  in HC condition of steel at R ratio of 0.1.

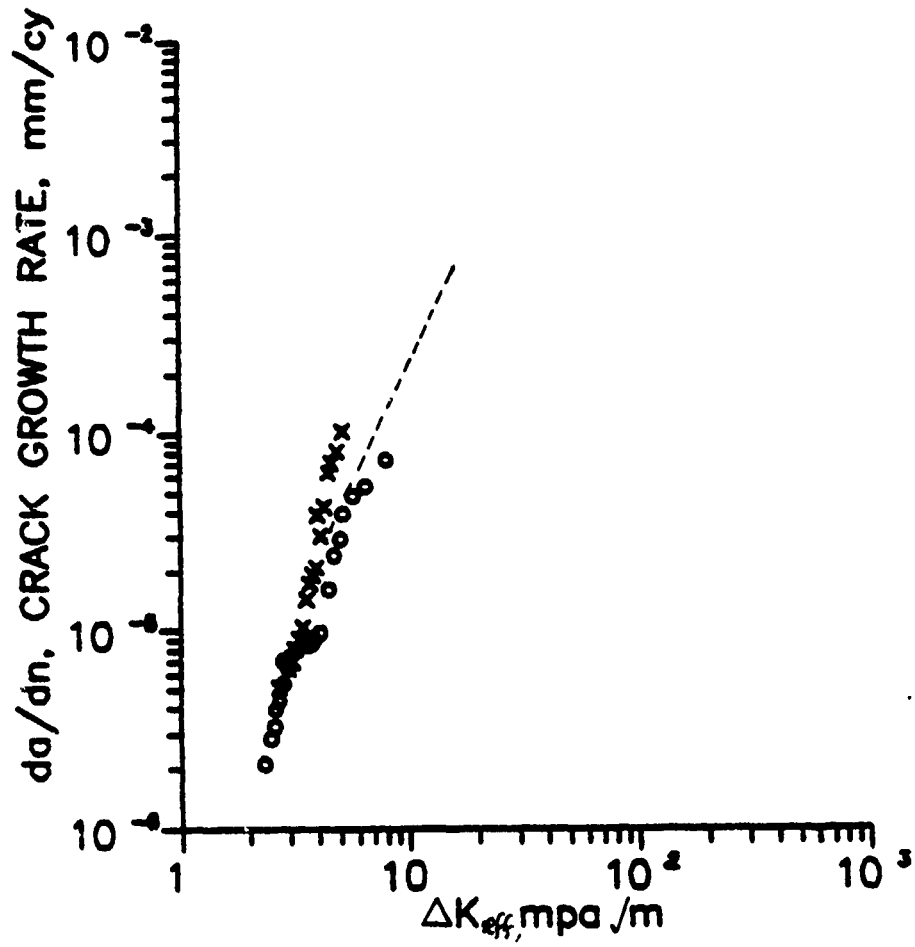


Fig. 4.77 Growth rate,  $da/dn$ , of short cracks at low and high stress levels as a function of  $\Delta K_{eff}$  in aluminum at R ratio of 0.1.

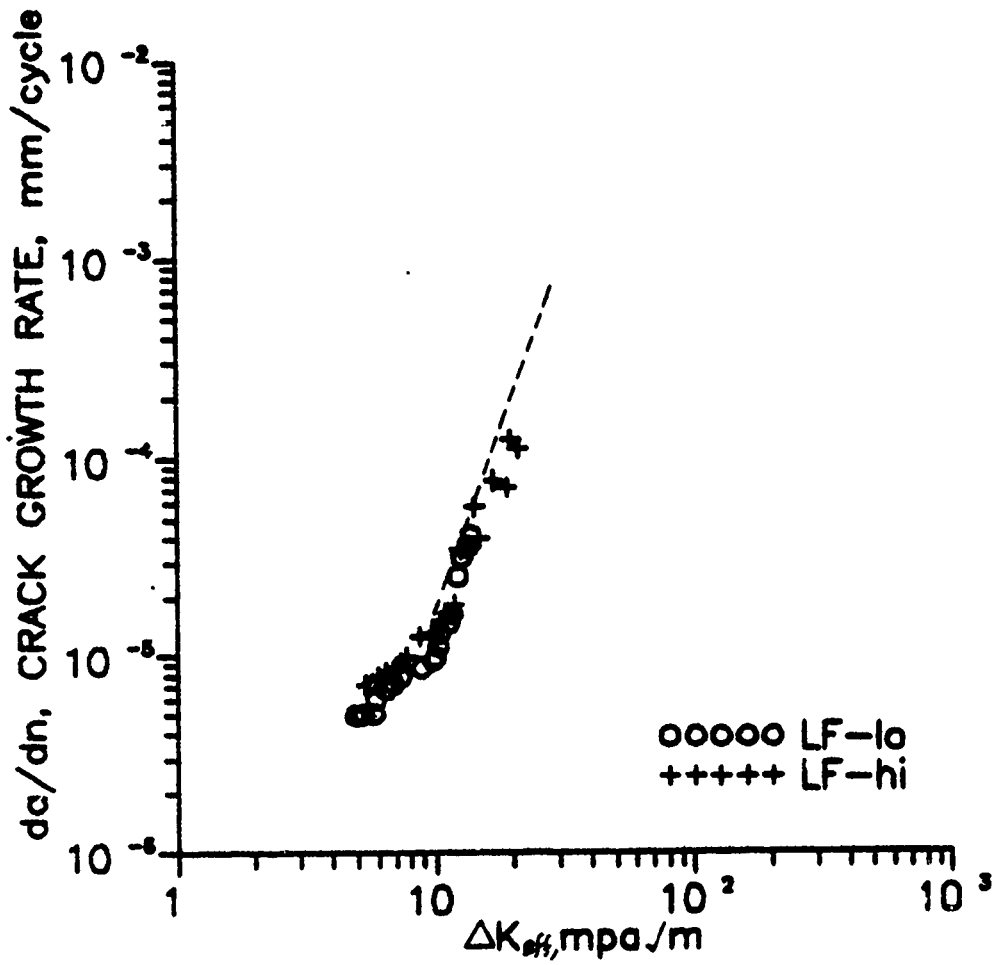


Fig. 4.78 Growth rate,  $da/dn$ , of short cracks at low and high stress levels as a function of  $\Delta K_{eff}$  in LF condition of steel at R ratio of 0.4.

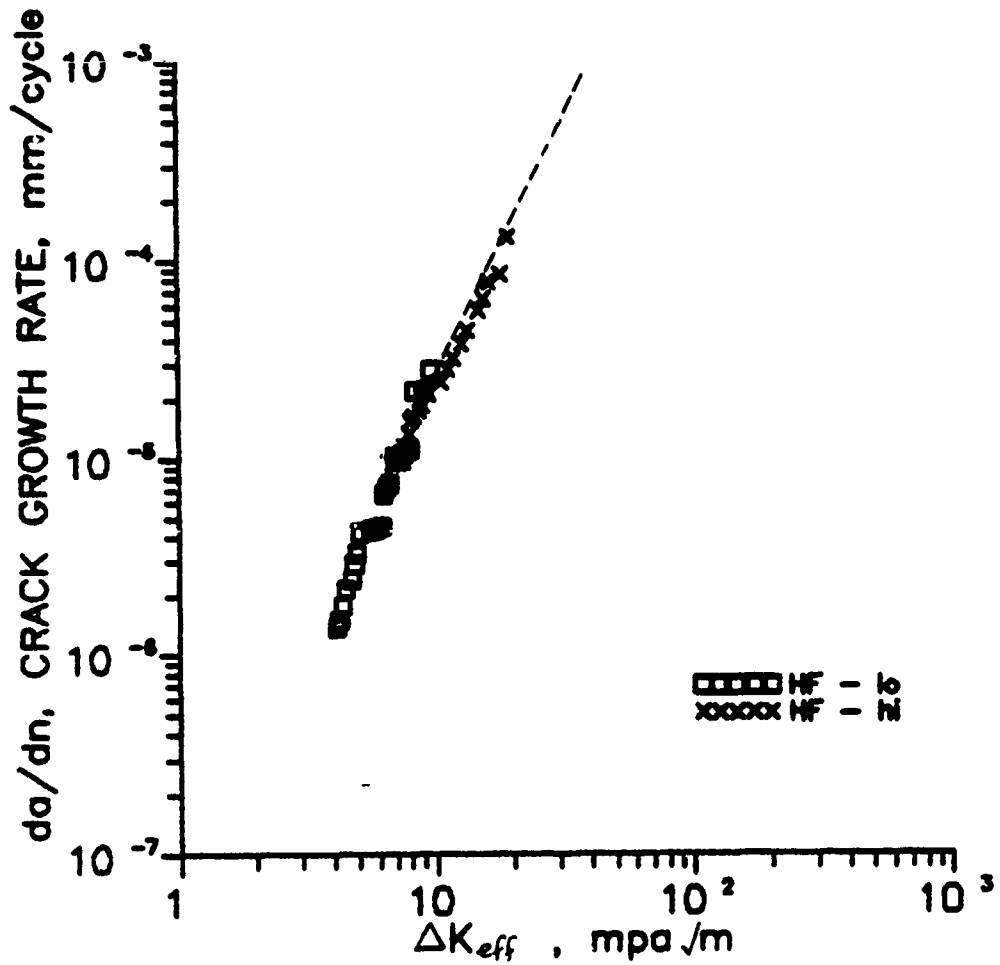


Fig. 4.79 Growth rate,  $da/dn$ , of short cracks at low and high stress levels as a function of  $\Delta K_{eff}$  in HF condition of steel at R ratio of 0.4.

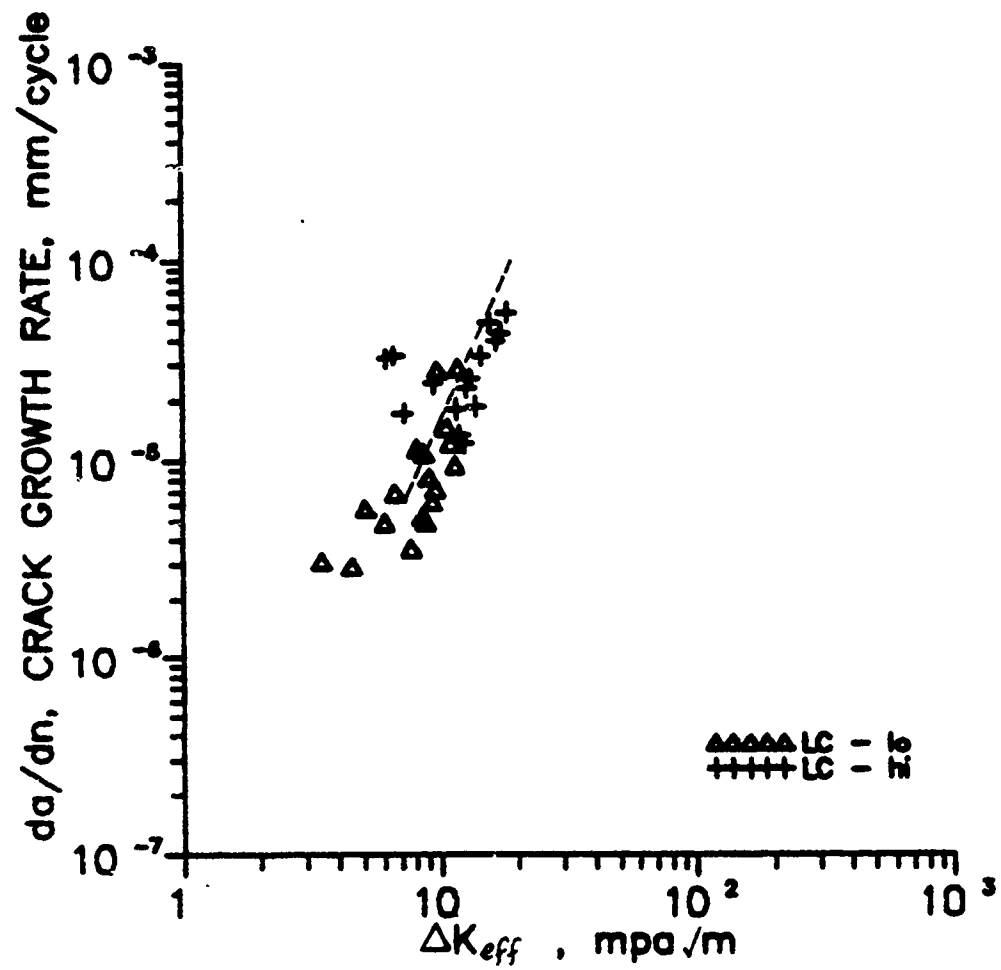


Fig. 4.80 Growth rate,  $da/dn$ , of short cracks at low and high stress levels as a function of  $\Delta K_{eff}$  in LC condition of steel at R ratio of 0.4.

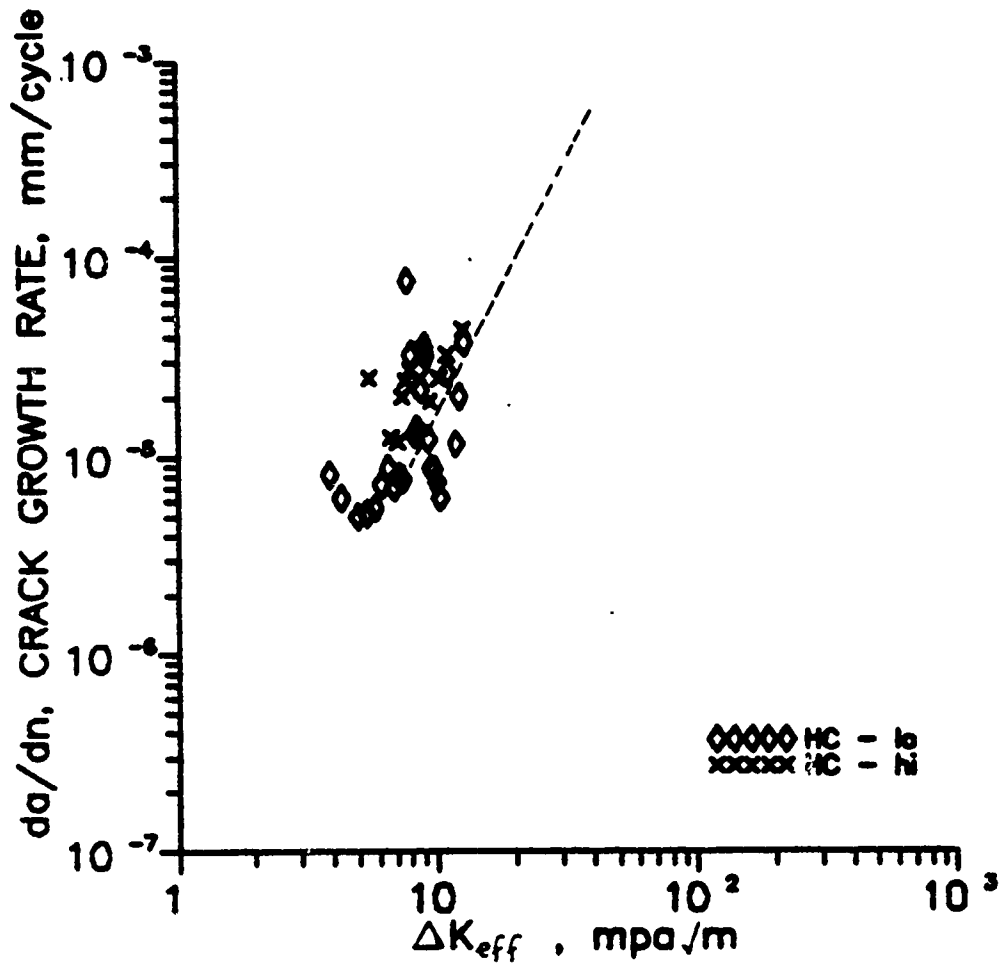


Fig. 4.81 Growth rate,  $da/dn$ , of short cracks at low and high stress levels as a function of  $\Delta K_{eff}$  in HC condition of steel at R ratio of 0.4.

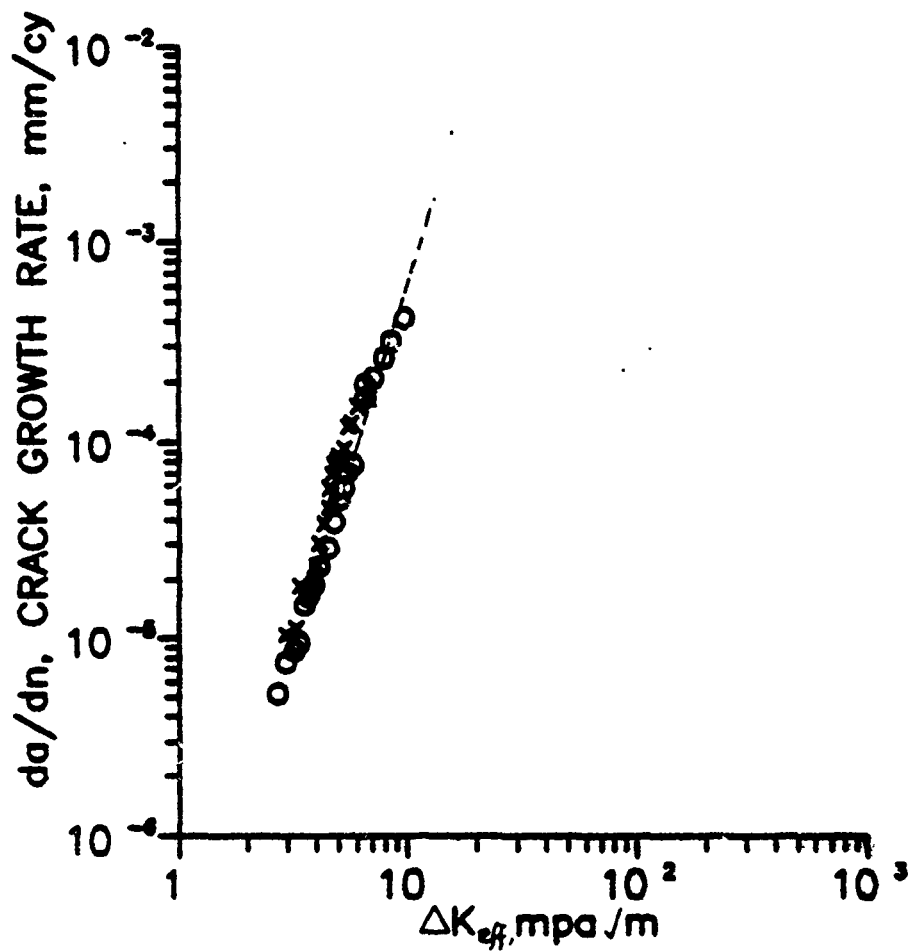


Fig. 4.82 Growth rate,  $da/dn$ , of short cracks at low and high stress levels as a function of  $\Delta K_{eff}$  in aluminum at R ratio of 0.4.

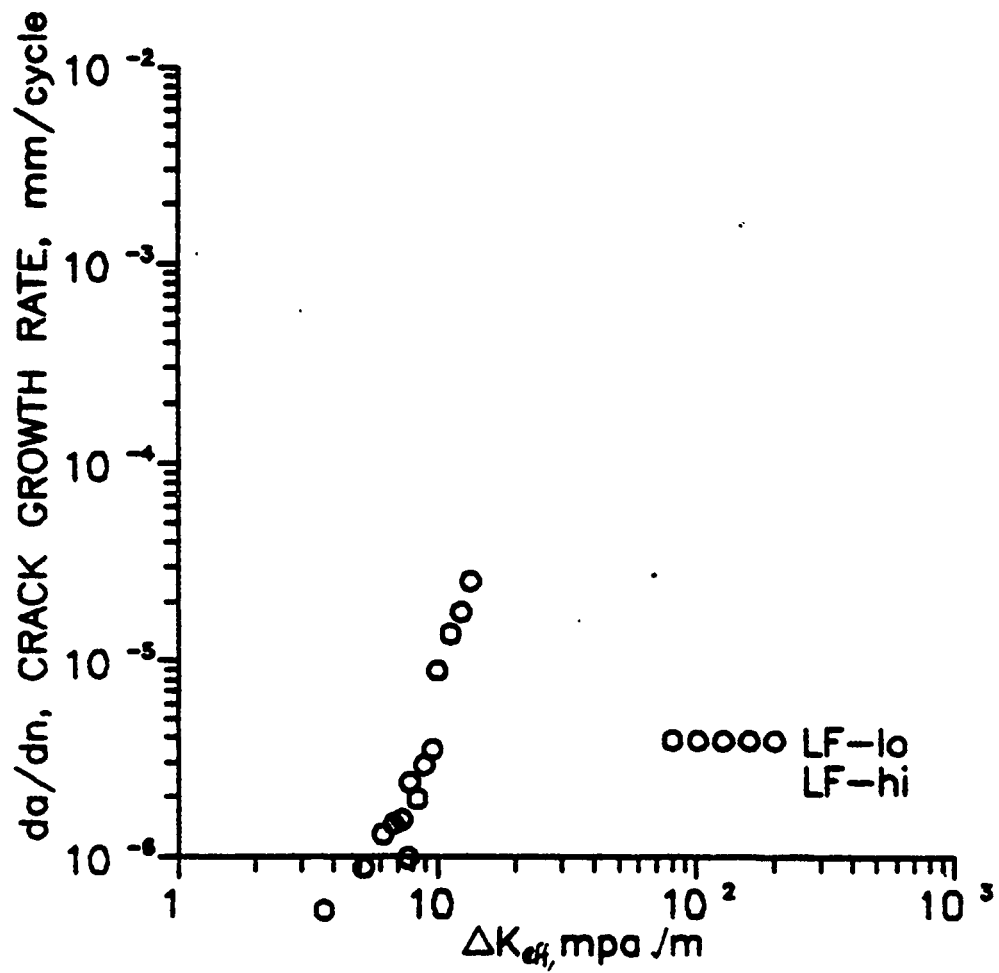


Fig. 4.83 Growth rate,  $da/dn$ , of short cracks at low and high stress levels as a function of  $\Delta K_{eff}$  in LF condition of steel at R ratio of 0.7.

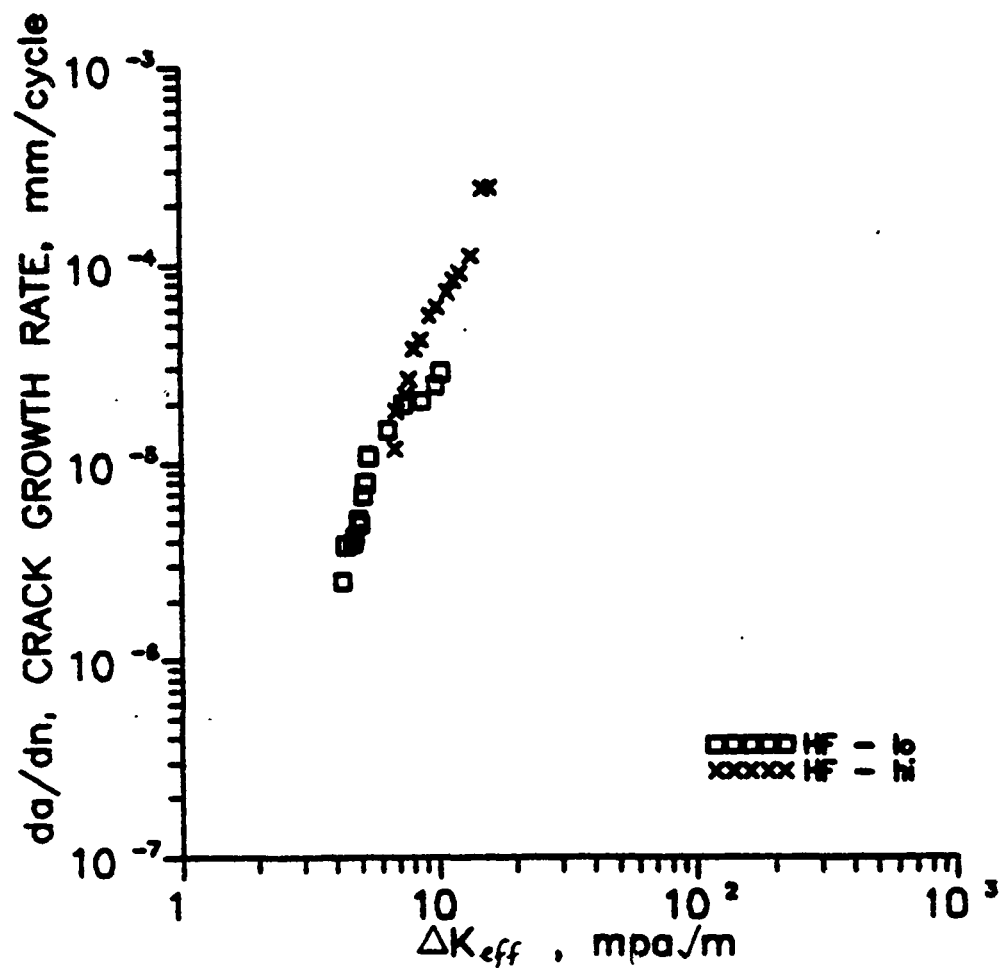


Fig. 4.84 Growth rate,  $da/dn$ , of short cracks at low and high stress levels as a function of  $\Delta K_{eff}$  in HF condition of steel at R ratio of 0.7.

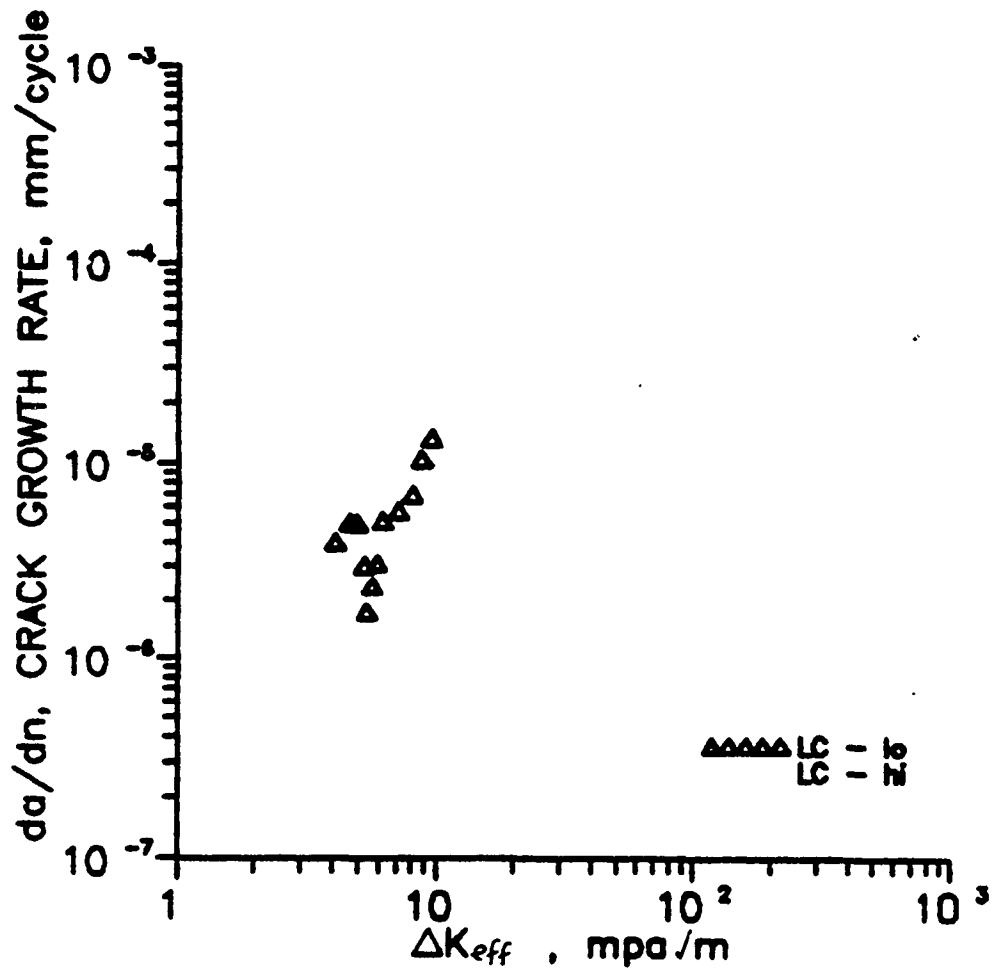


Fig. 4.85 Growth rate,  $da/dn$ , of short cracks at low stress level as a function of  $\Delta K_{eff}$  in LC condition of steel at R ratio of 0.7.

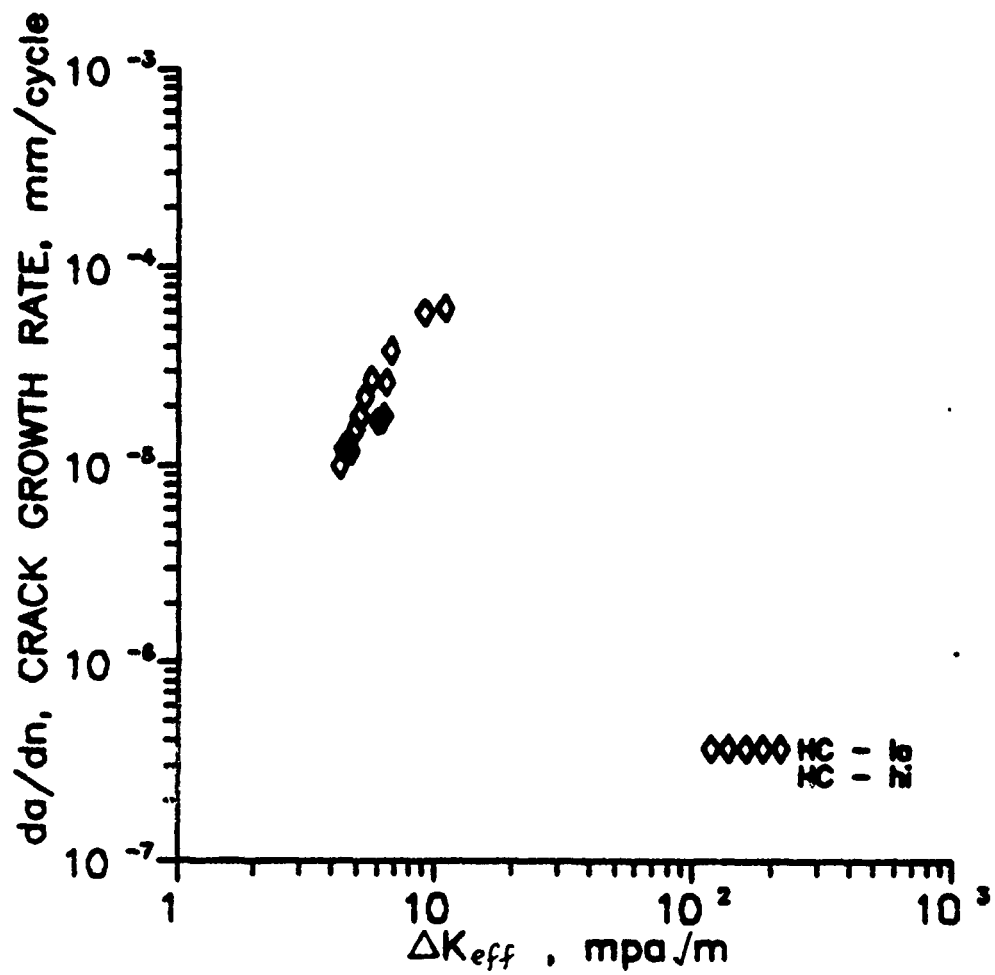


Fig. 4.86 Growth rate,  $da/dn$ , of short cracks at low stress level as a function of  $\Delta K_{eff}$  in HC condition of steel at R ratio of 0.7.

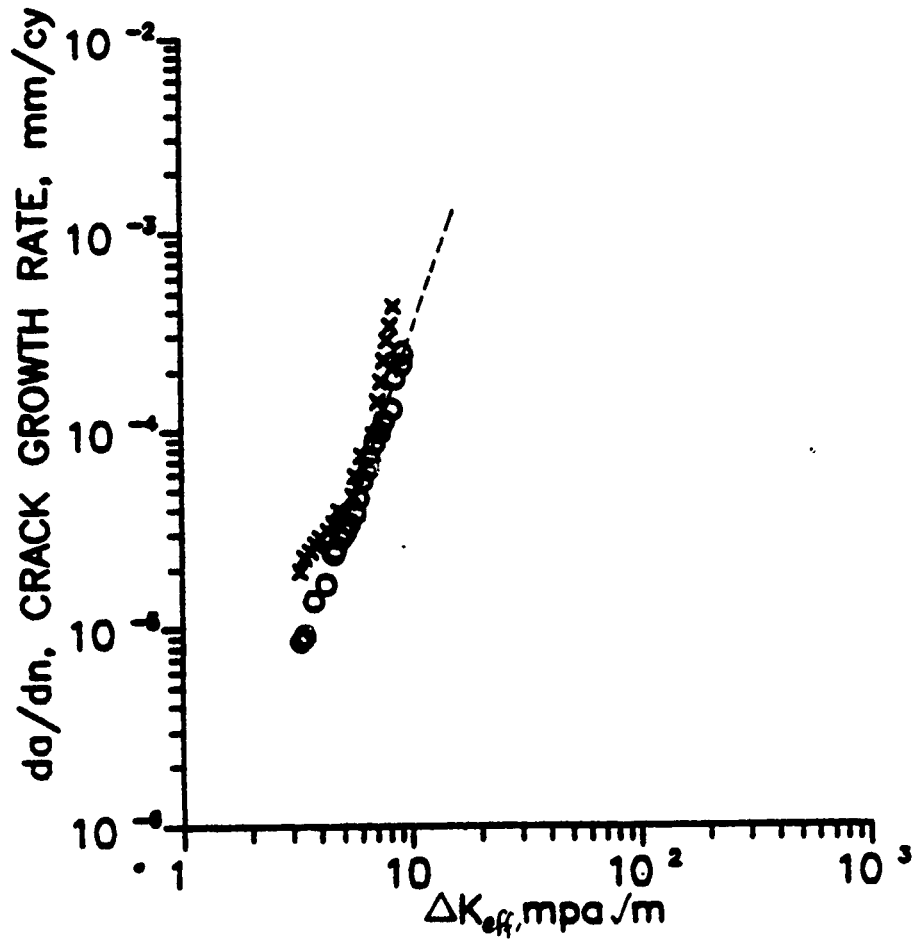


Fig. 4.87 Growth rate,  $da/dn$ , of short cracks at low and high stress levels as a function of  $\Delta K_{eff}$  in aluminum at R ratio of 0.7.

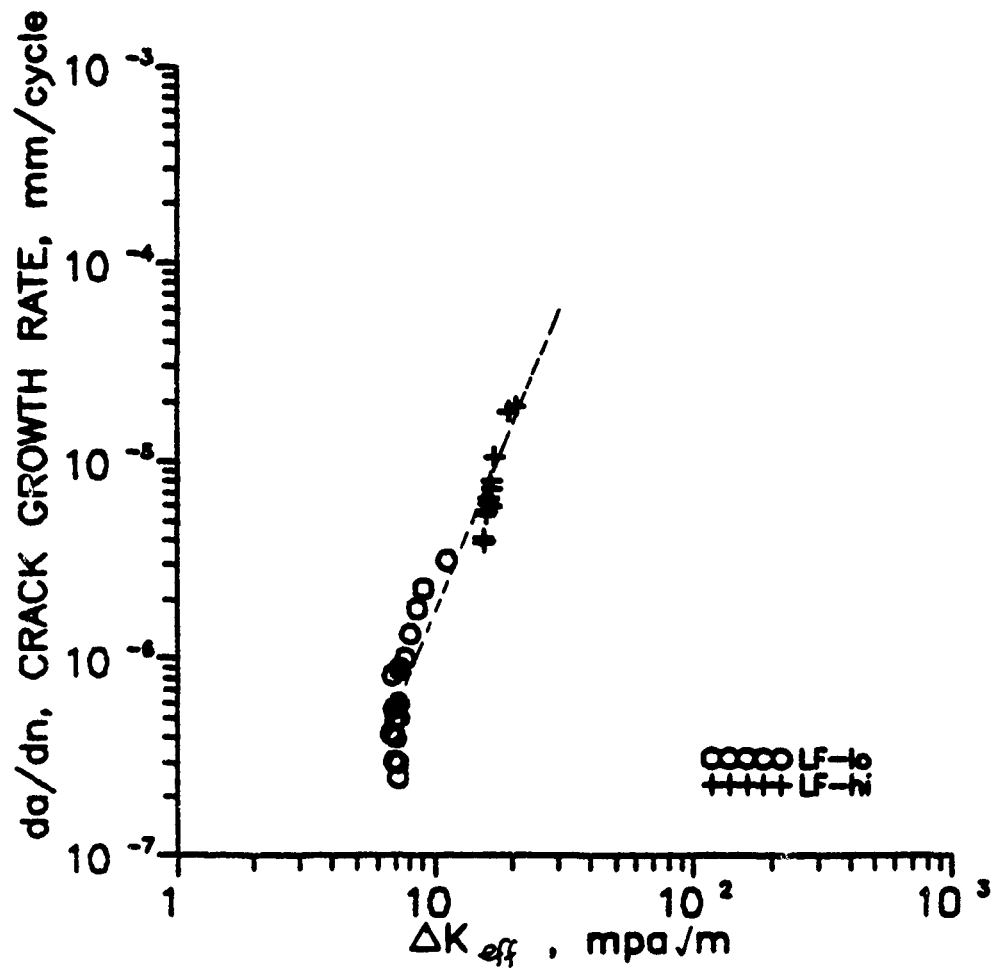


Fig. 4.88 Growth rate,  $da/dn$ , of short cracks at low and high stress levels as a function of  $\Delta K_{eff}$  in LF condition of steel at R ratio of -1.0.

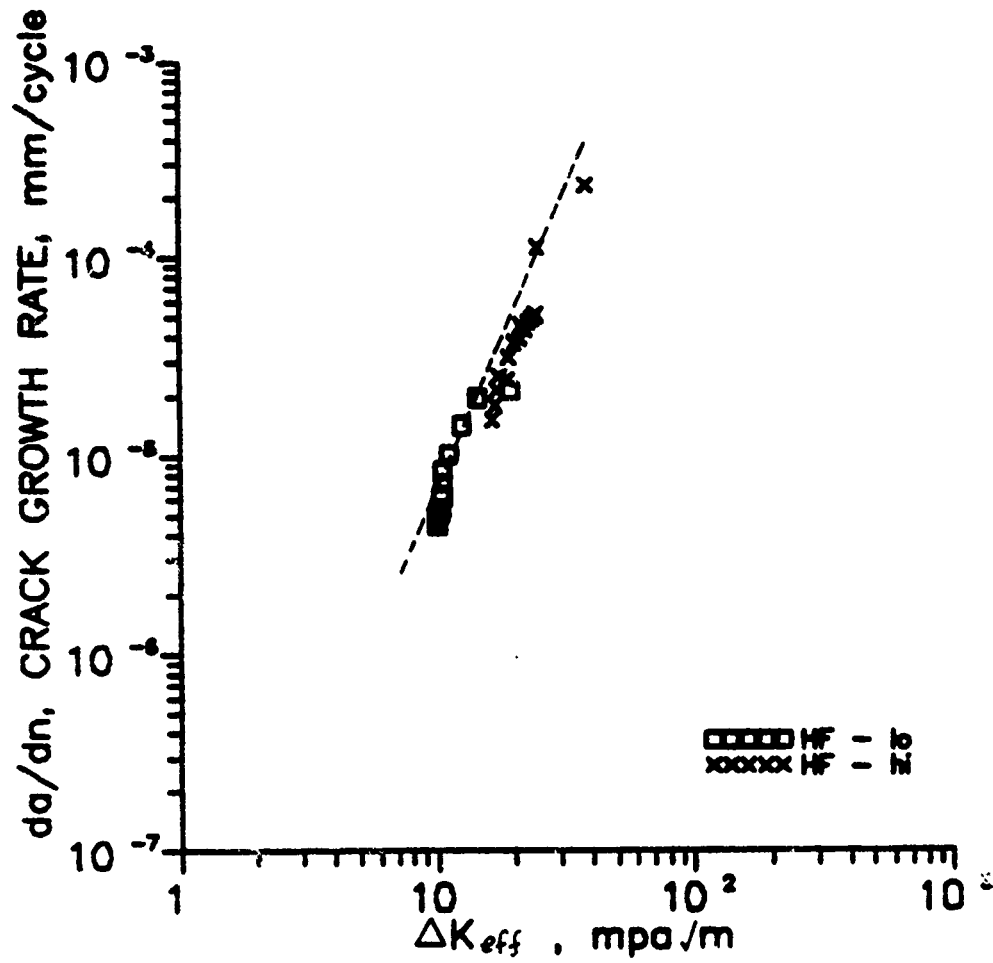


Fig. 4.89 Growth rate,  $da/dn$ , of short cracks at low and high stress levels as a function of  $\Delta K_{eff}$  in HF condition of steel at R ratio of -1.0.

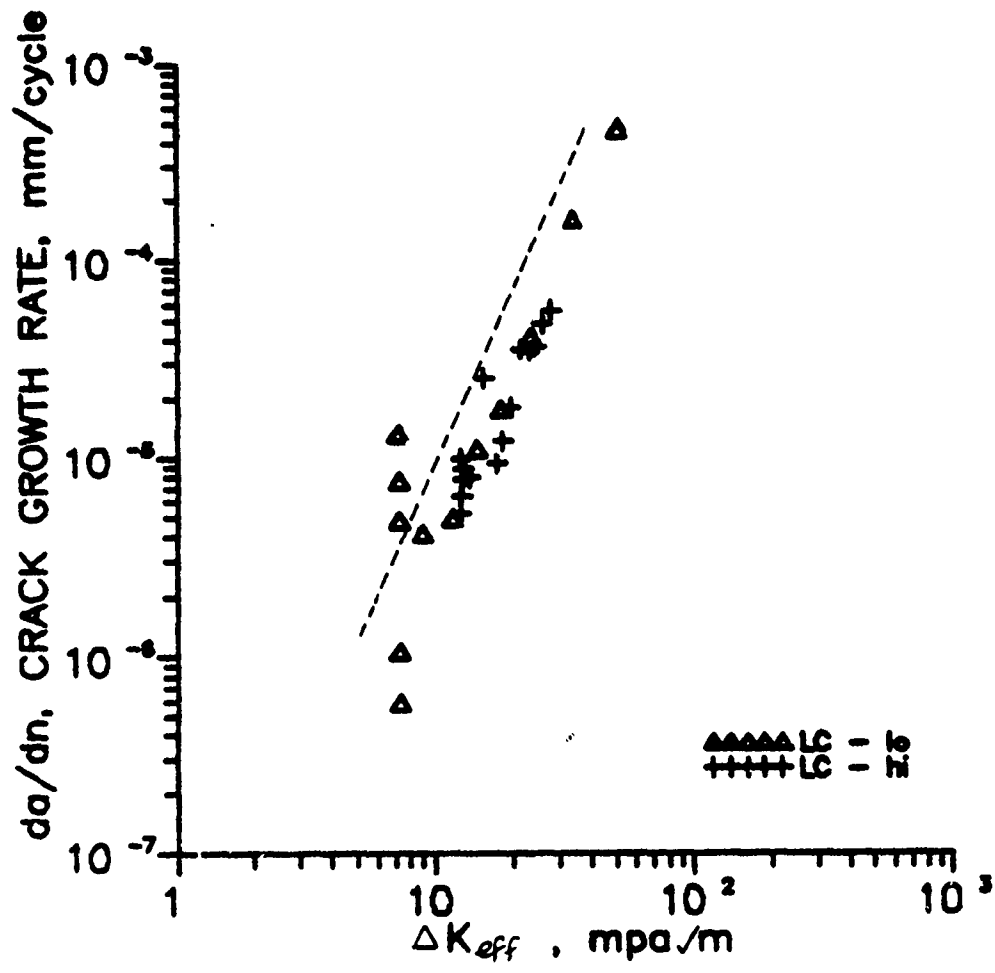


Fig. 4.90 Growth rate,  $da/dn$ , of short cracks at low and high stress levels as a function of  $\Delta K_{eff}$  in LC condition of steel at R ratio of -1.0.

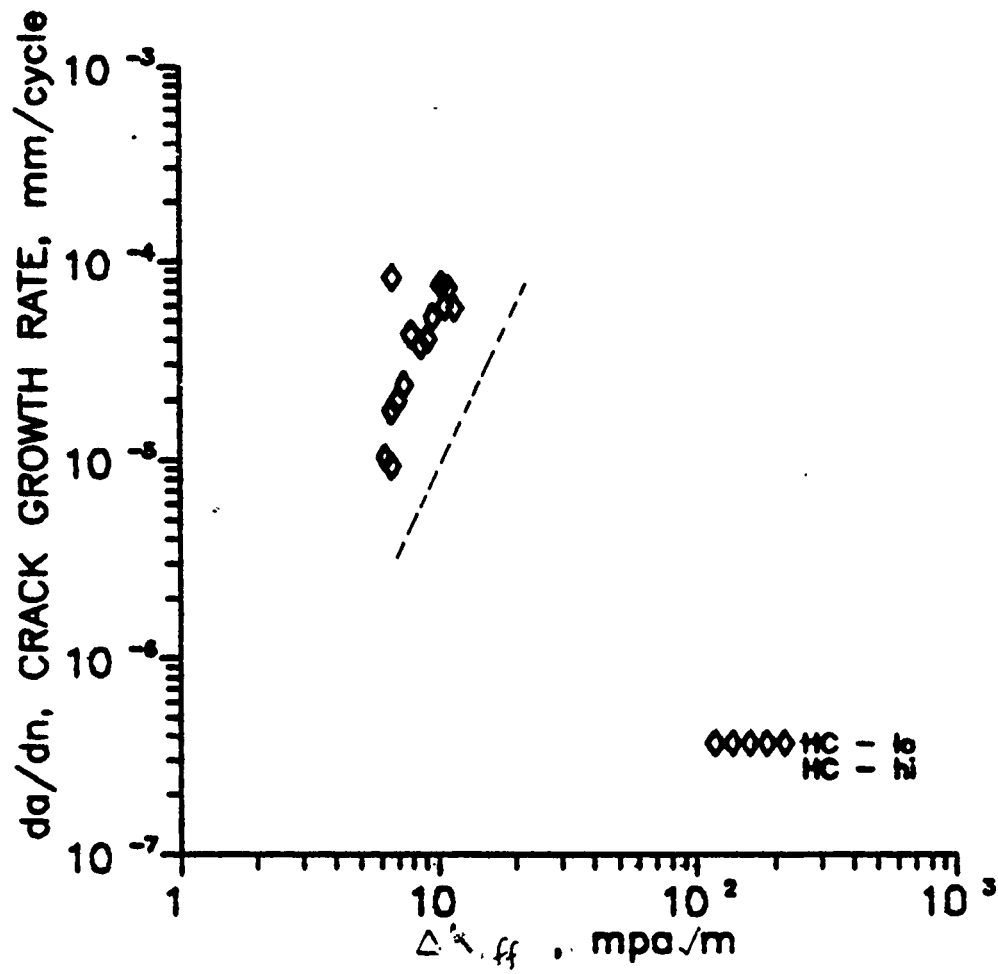


Fig. 4.91 Growth rate,  $da/dn$ , of short cracks at low stress level as a function of  $\Delta K_{eff}$  in HC condition of steel at R ratio of -1.0.

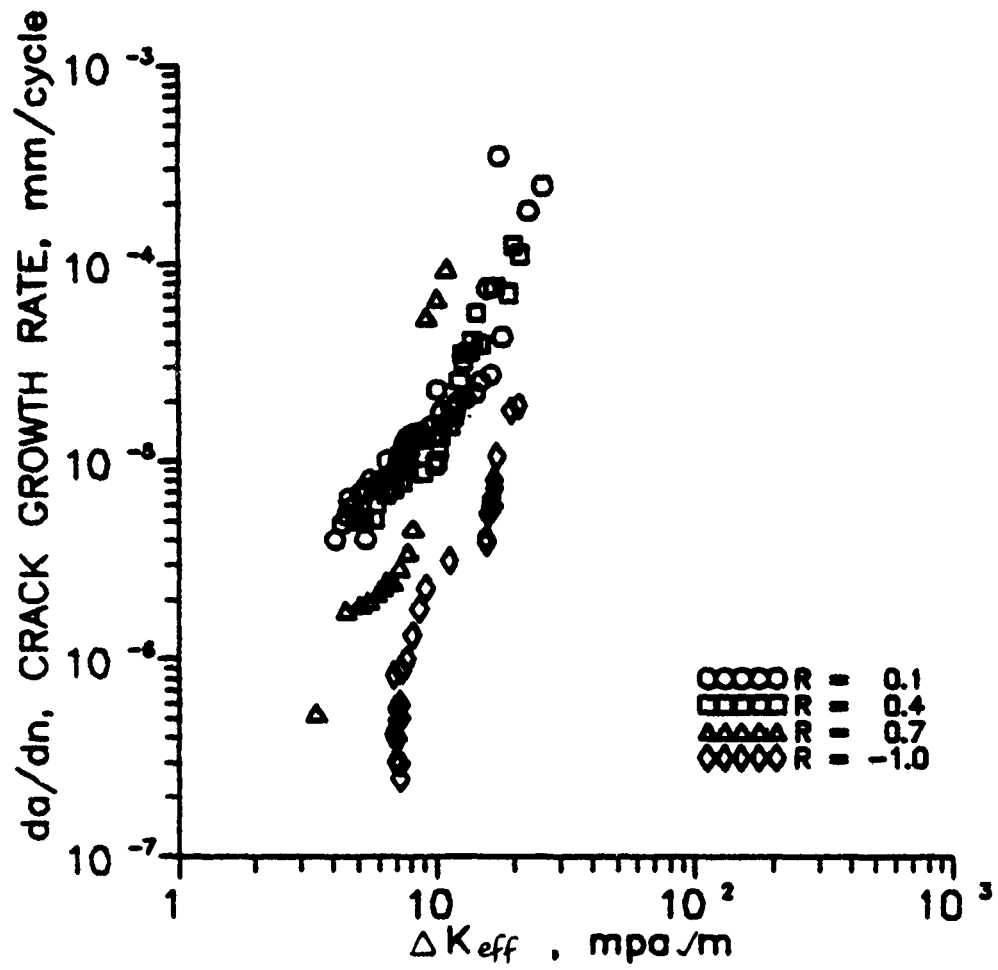


Fig. 4.92 Growth rate of short cracks at different R ratios as a function of  $\Delta K_{eff}$  in LF condition of steel.

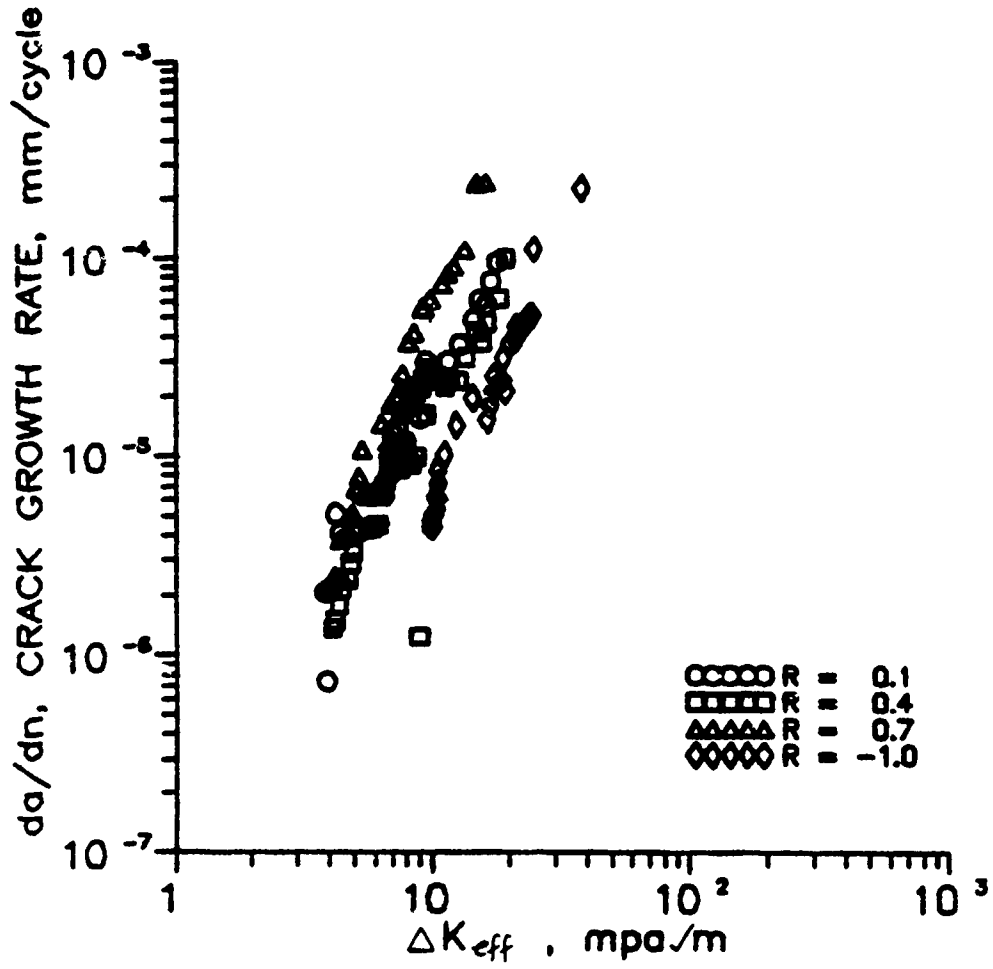


Fig. 4.93 Growth rate of short cracks at different R ratios as a function of  $\Delta K_{eff}$  in HF condition of steel.

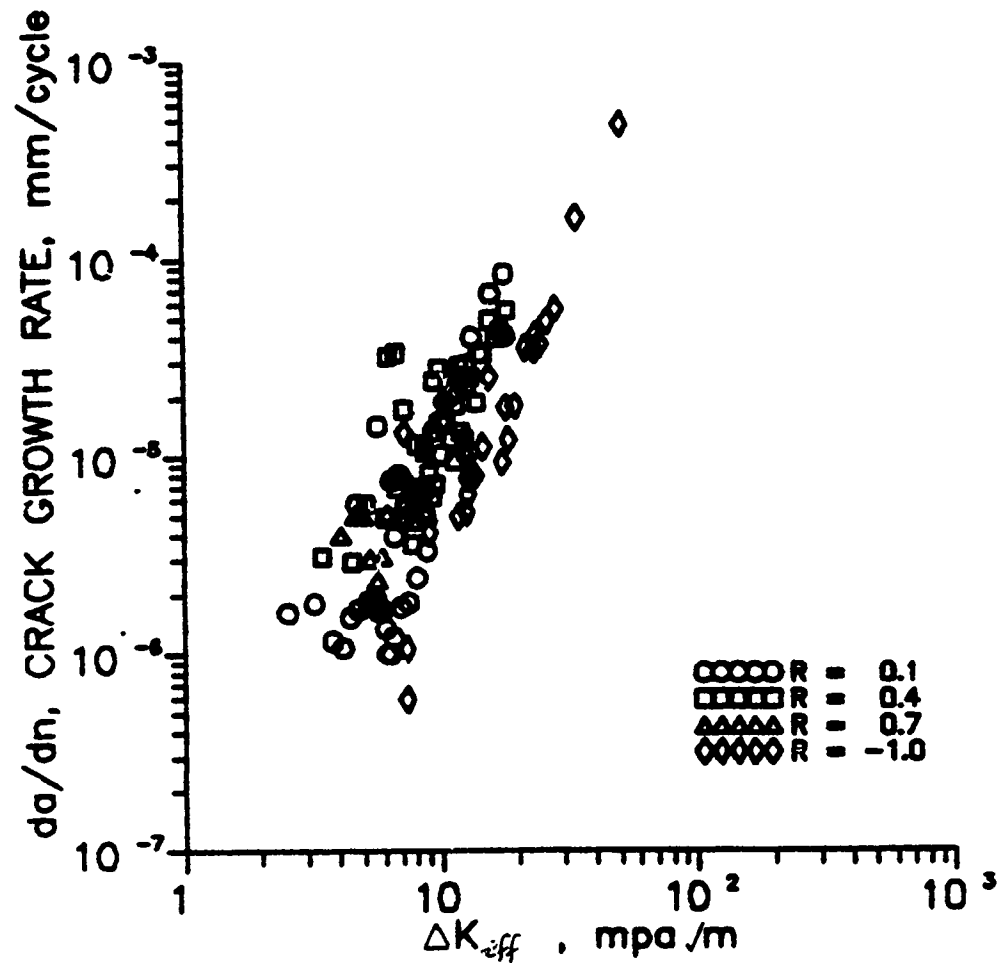


Fig. 4.94 Growth rate of short cracks at different R ratios as a function of  $\Delta K_{eff}$  in LC condition of steel.



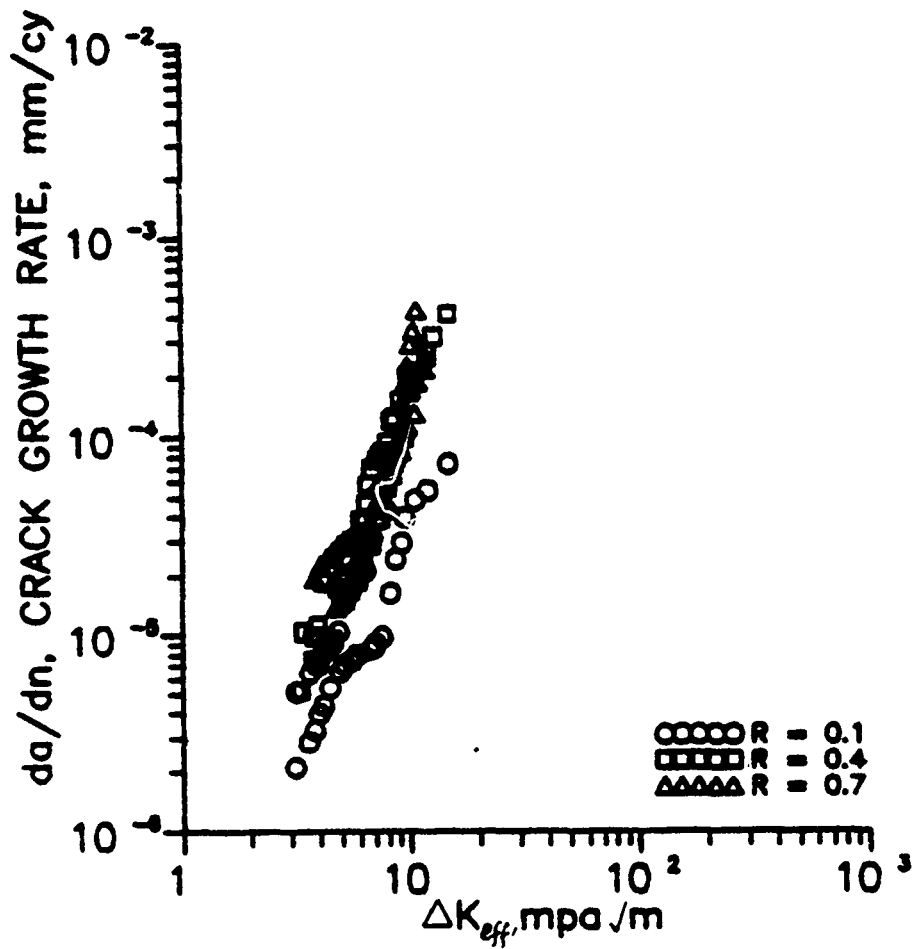


Fig. 4.96 Growth rate of short cracks at different R ratios as a function of  $\Delta K_{eff}$  in aluminum.

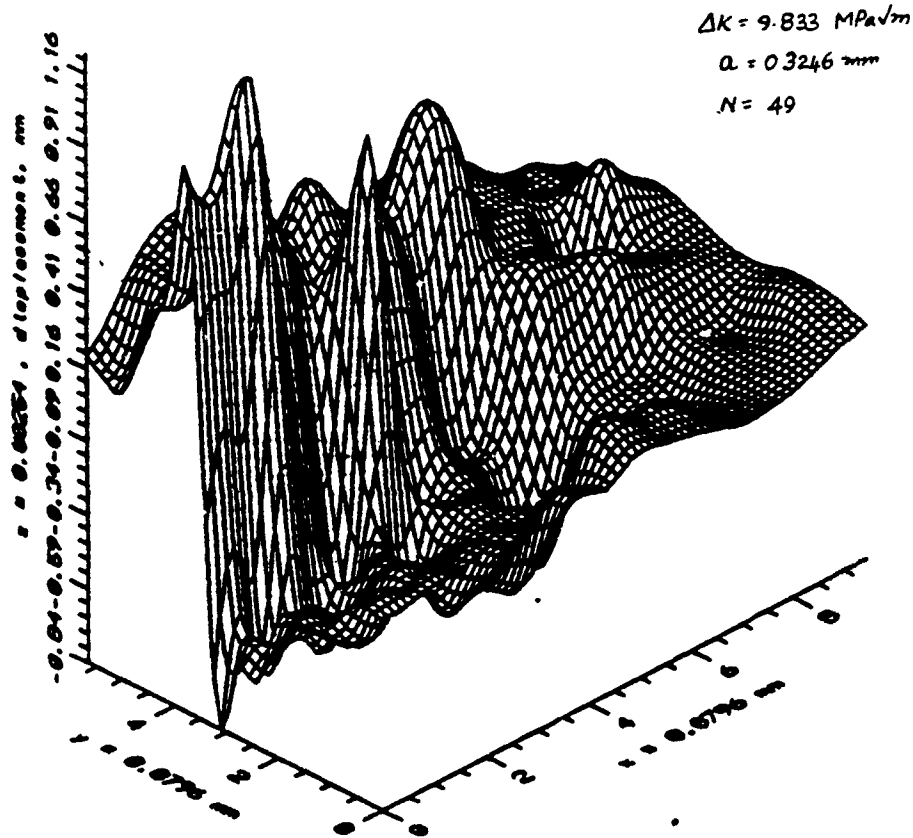


Fig. 4.97 Relative in-plane displacements in the direction perpendicular to the crack axis at  $R=0.1$  in LF condition of steel.

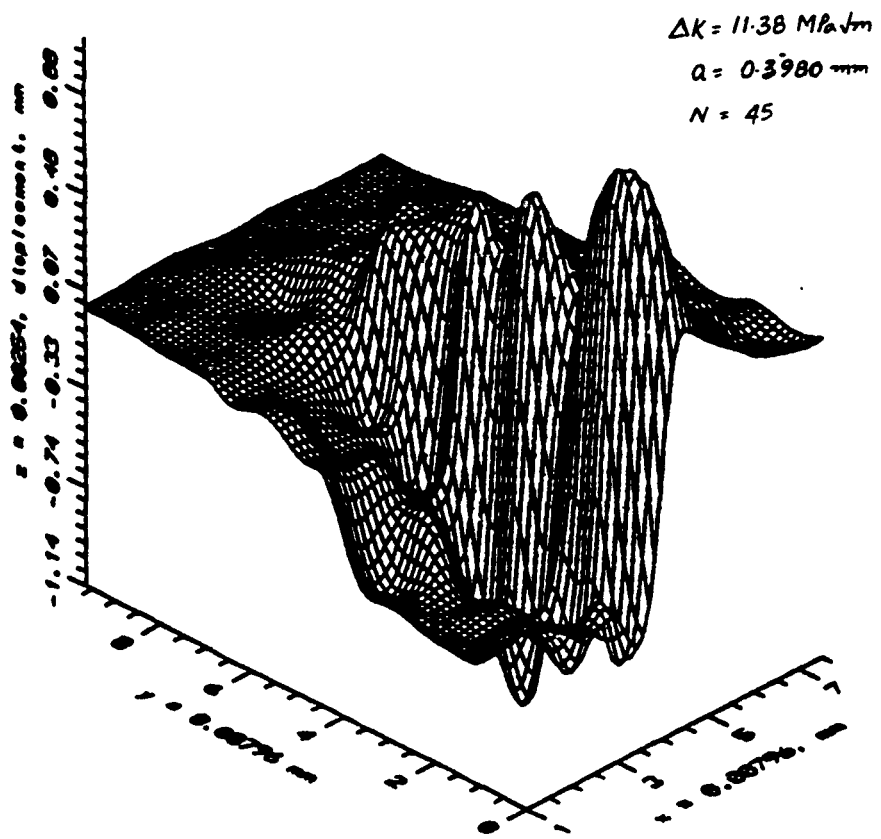


Fig. 4.98 Relative in-plane displacements in the direction perpendicular to the crack axis at  $R = -1.0$  in LF condition of steel.

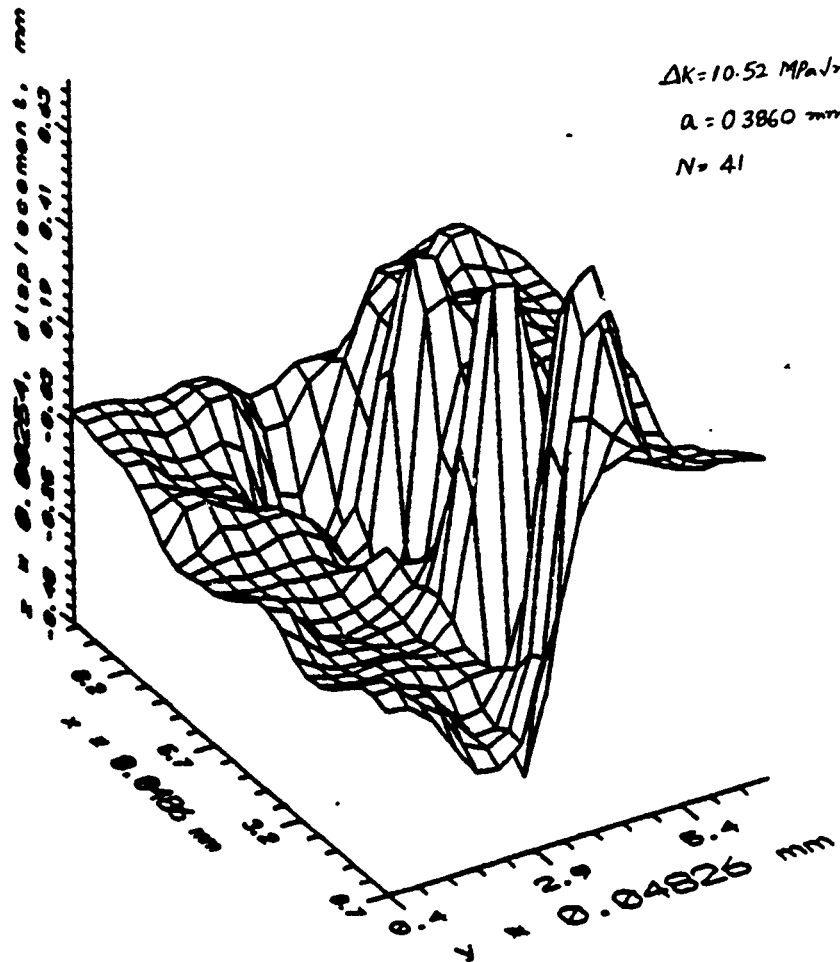


Fig. 4.99 Relative in-plane displacements in the direction perpendicular to the crack axis at  $R = 0.1$  in HF condition of steel.

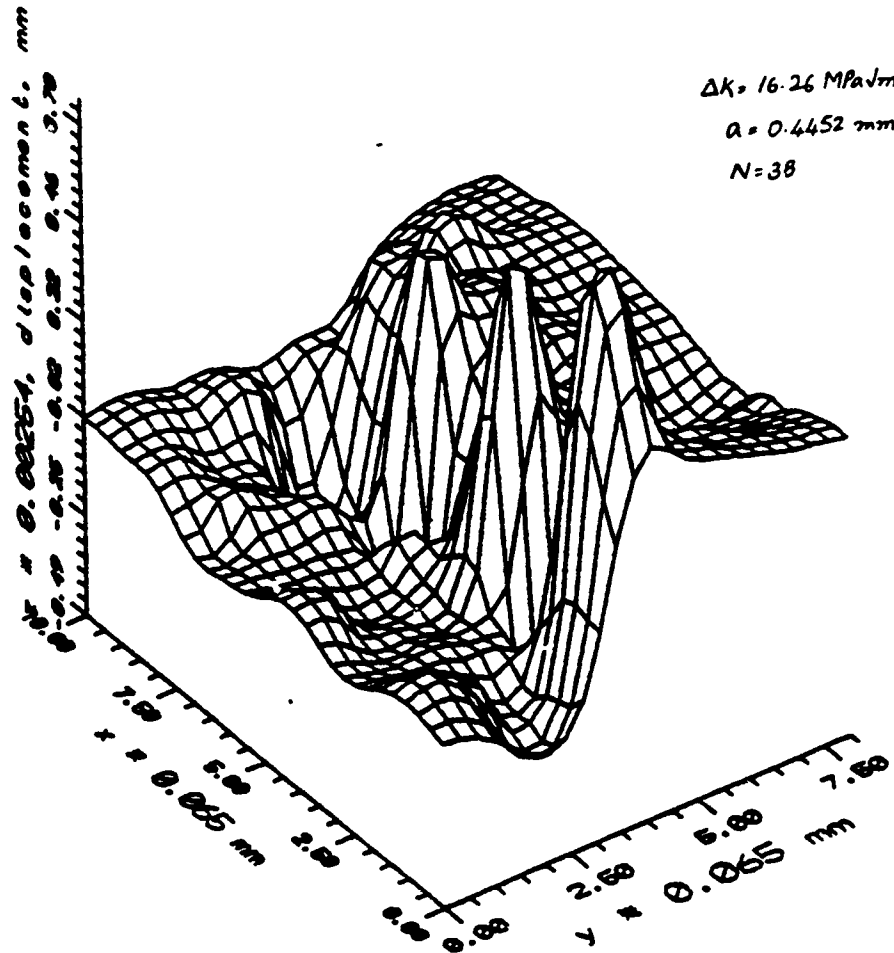


Fig. 4.100 Relative in-plane displacements in the direction perpendicular to the crack axis at  $R = 0.1$  in HF condition of steel.

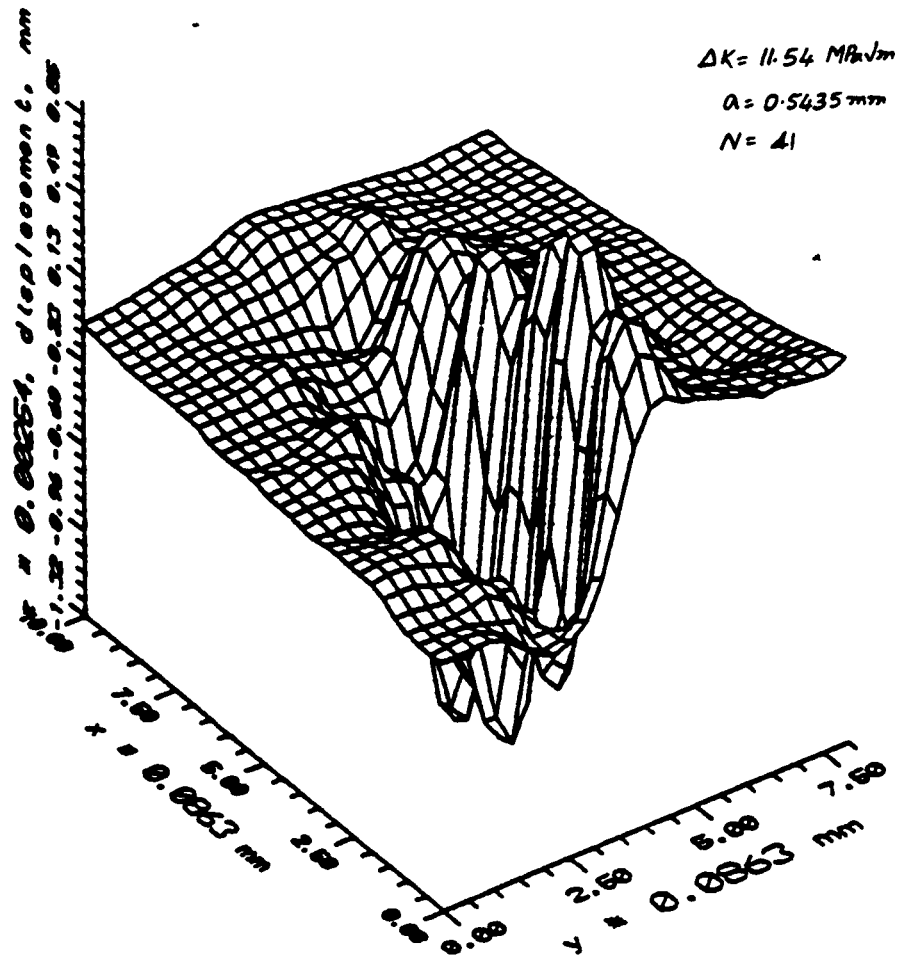


Fig. 4.101 Relative in-plane displacements in the direction perpendicular to the crack axis at  $R = 0.1$  in LC condition of steel.

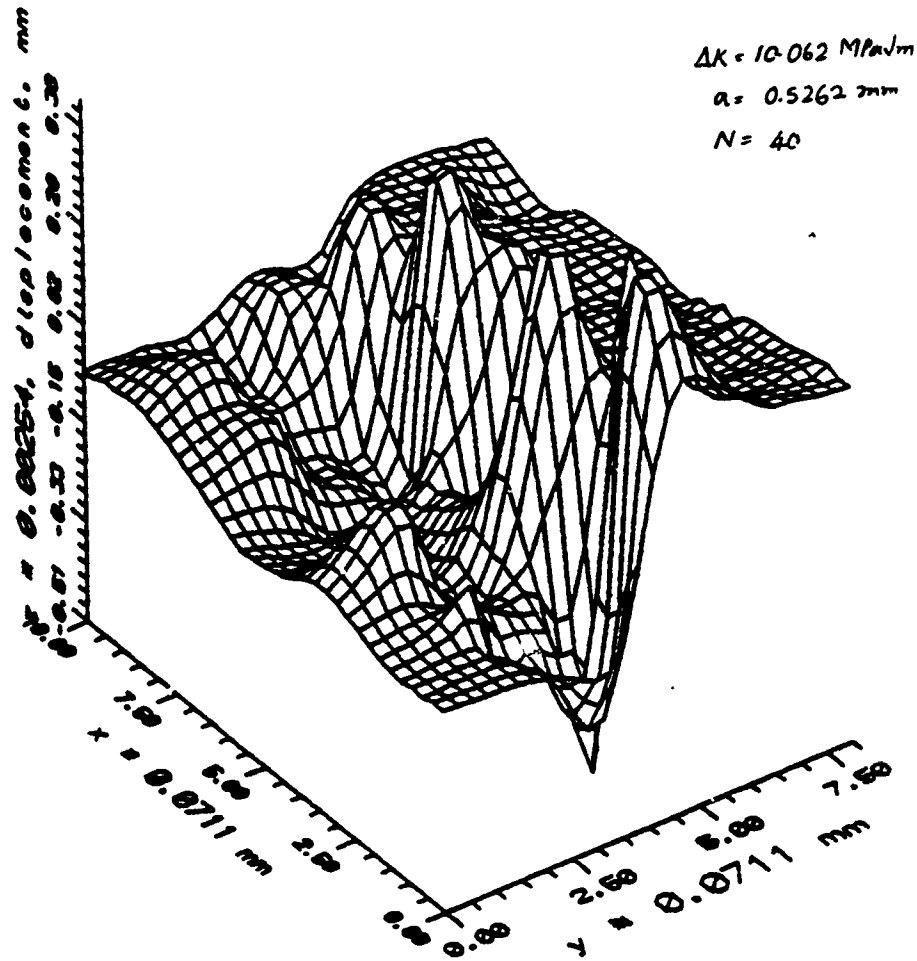


Fig. 4.102 Relative in-plane displacements in the direction perpendicular to the crack axis at  $R = 0.4$  in LC condition of steel.

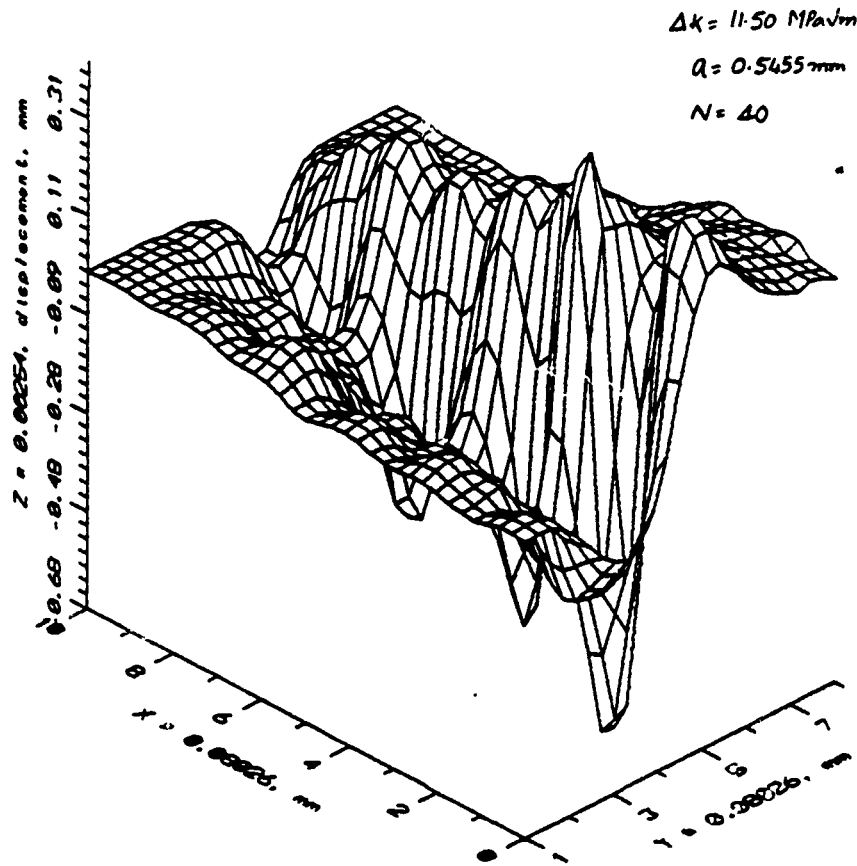


Fig. 4.103 Relative in-plane displacements in the direction perpendicular to the crack axis at  $R = 0.1$  in HC condition of steel.

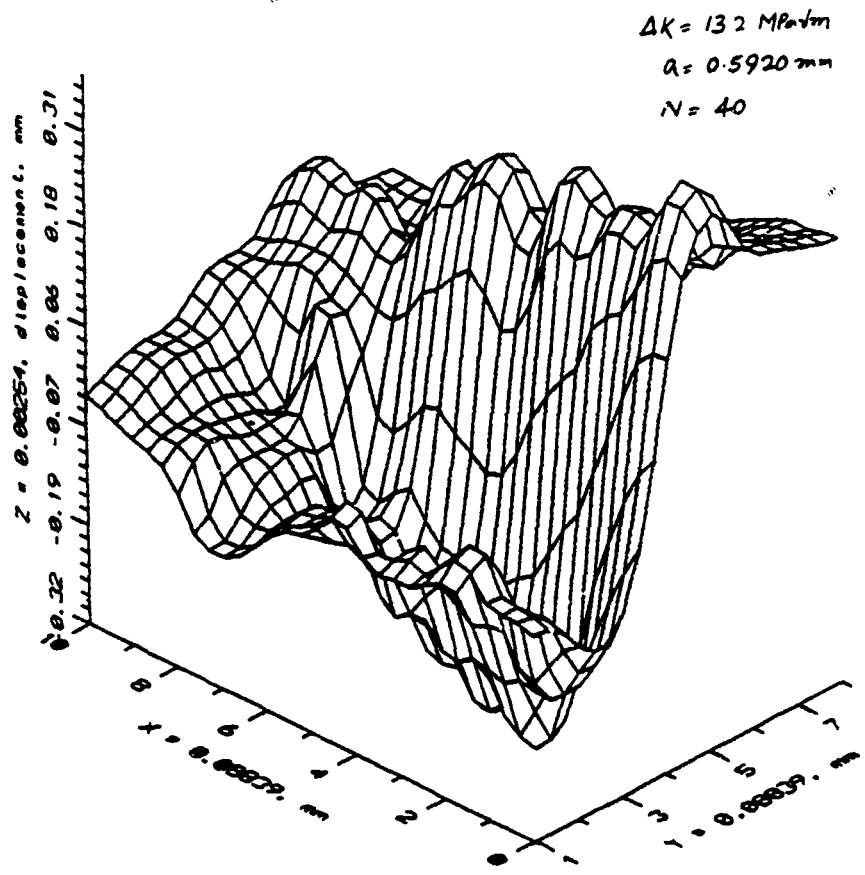


Fig. 4.104 Relative in-plane displacements in the direction perpendicular to the crack axis at  $R = 0.4$  in HC condition of steel.

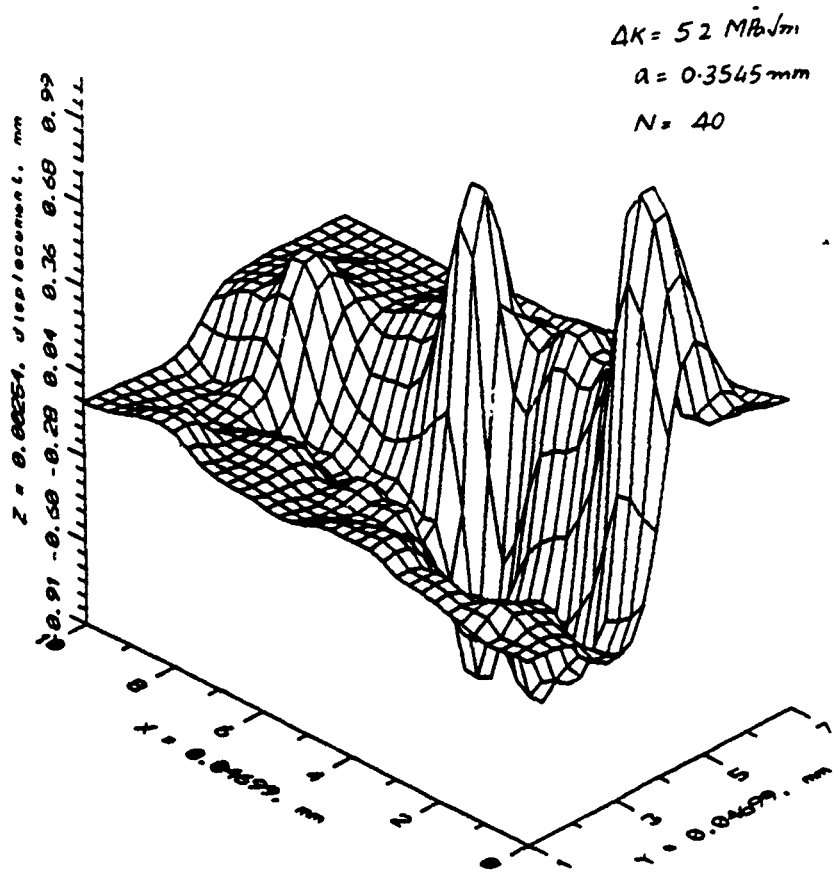


Fig. 4.105 Relative in-plane displacements in the direction perpendicular to the crack axis at  $R = 0.1$  in aluminum.

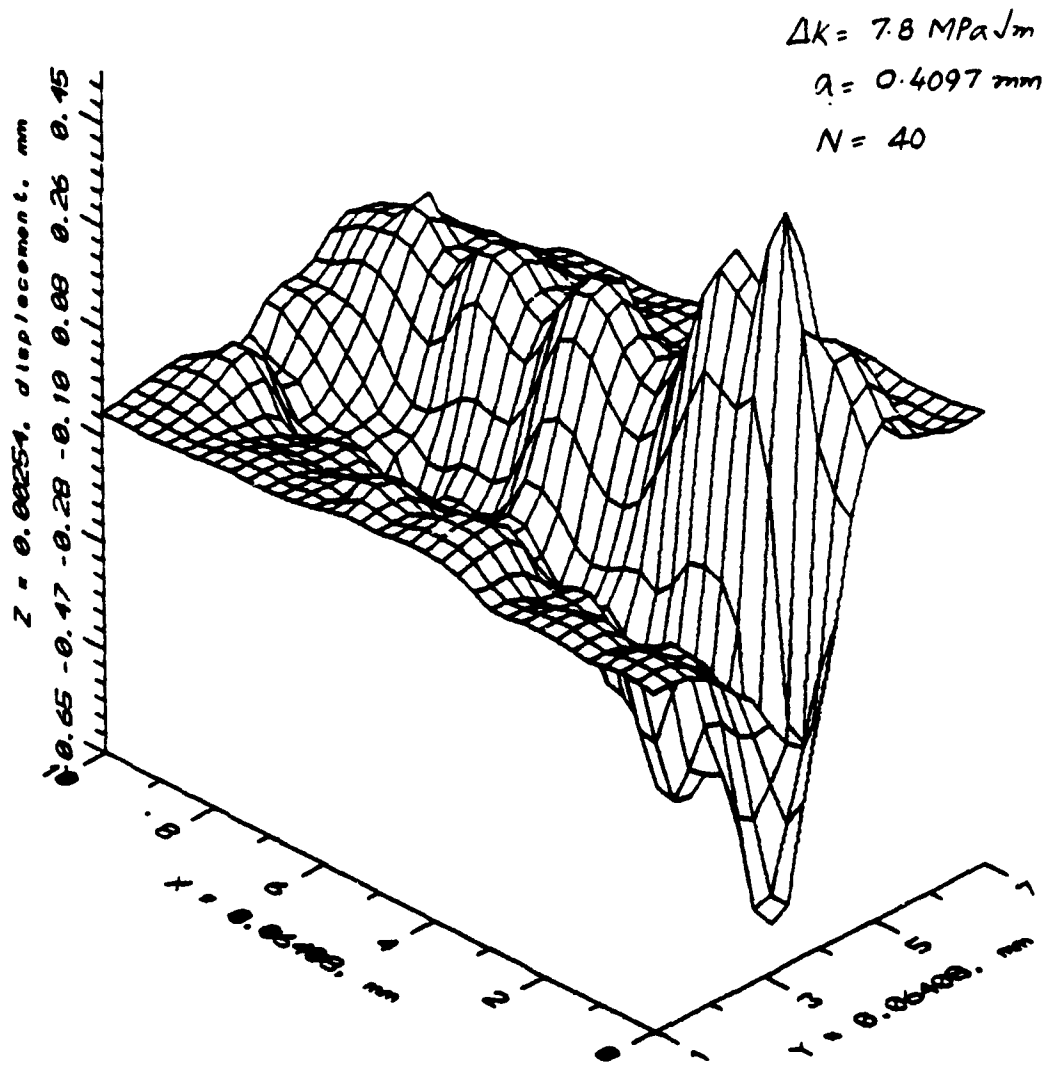


Fig. 4.106 Relative in-plane displacements in the direction perpendicular to the crack axis at  $R = 0.4$  in aluminum.

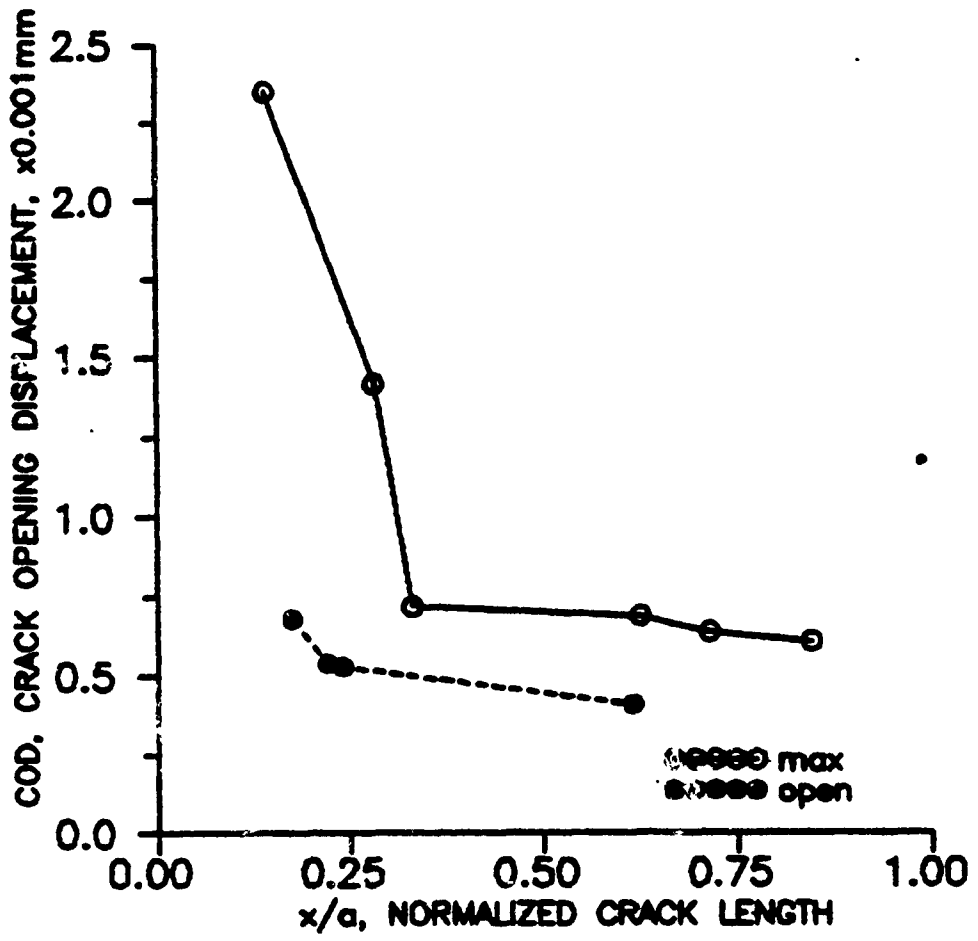


Fig. 4.107 Crack opening displacements corresponding to Fig. 4.97 at maximum and opening points of the loading cycle.

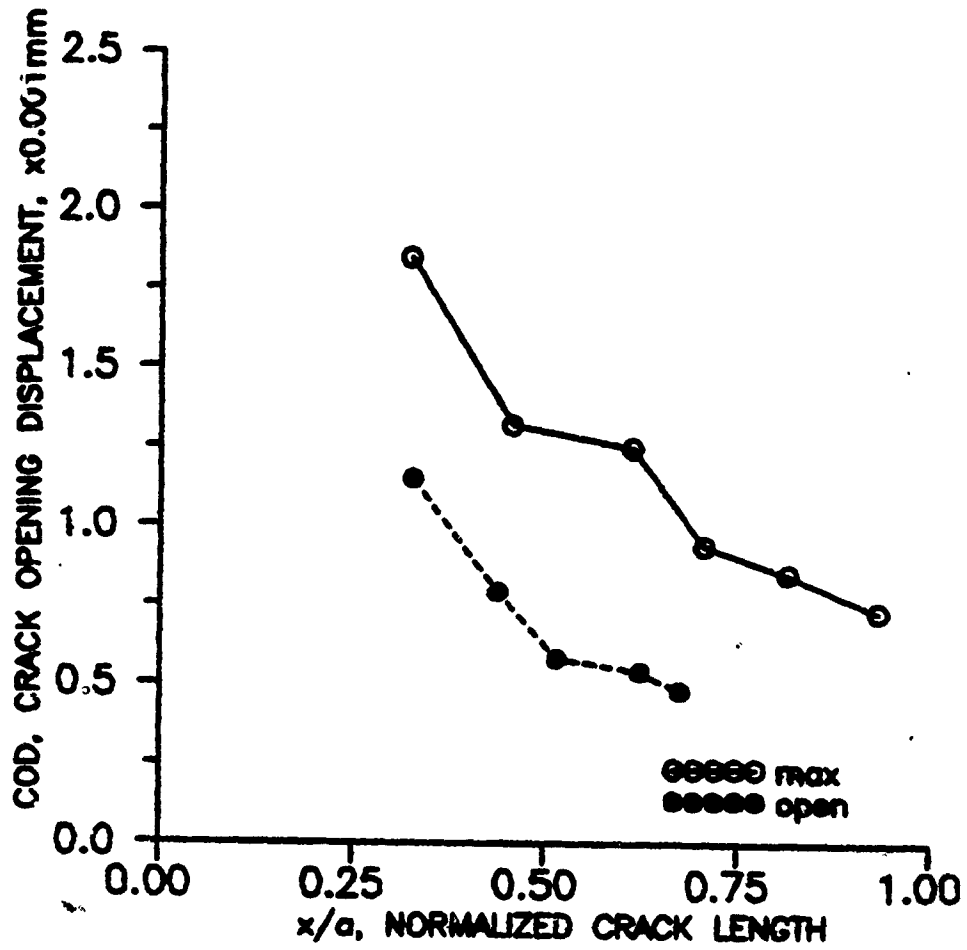


Fig. 4.108 Crack opening displacements corresponding to Fig. 4.98 at maximum and opening points of the loading cycle.

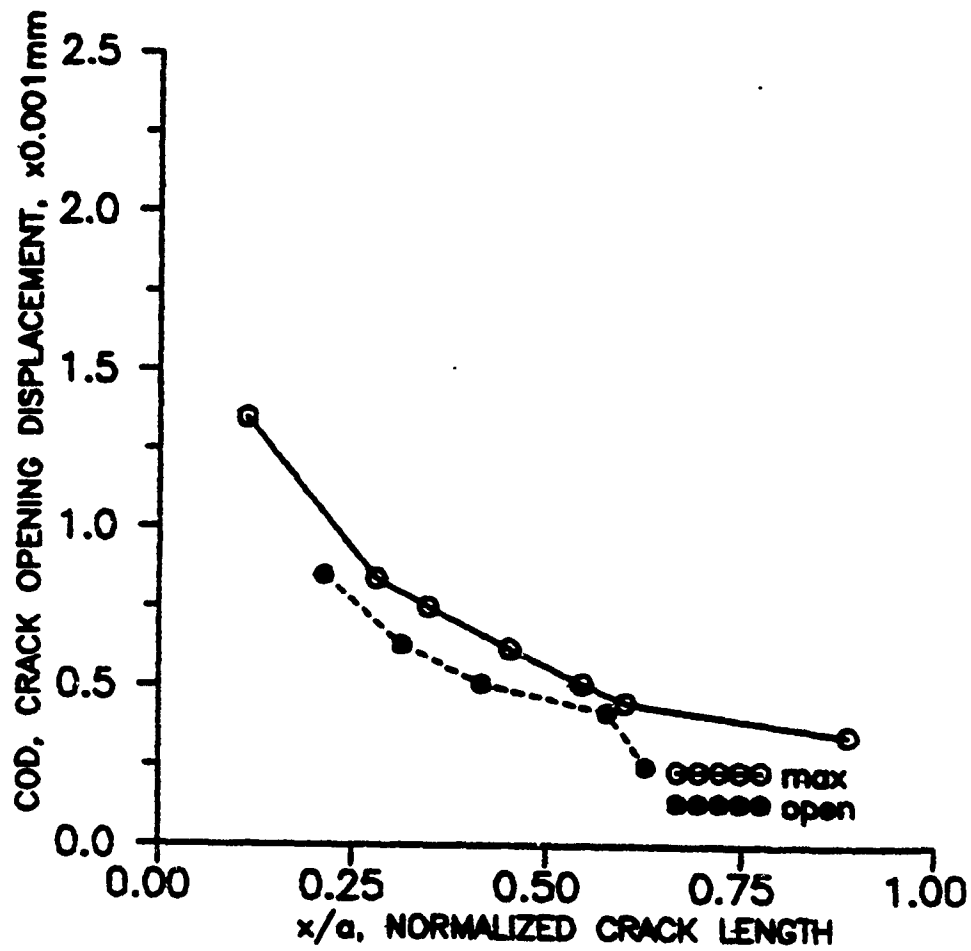


Fig. 4.109 Crack opening displacements corresponding to Fig. 4.99 at maximum and opening points of the loading cycle.

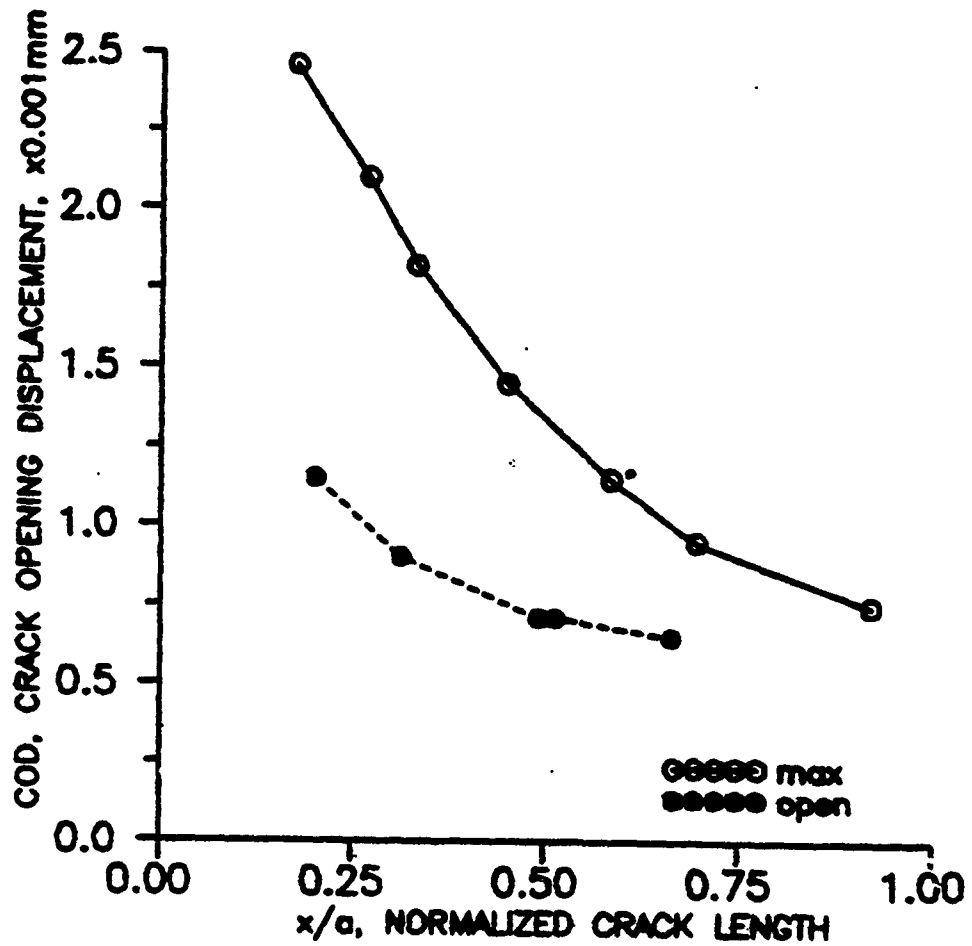


Fig. 4.110 Crack opening displacements corresponding to Fig. 4.100 at maximum and opening points of the loading cycle.

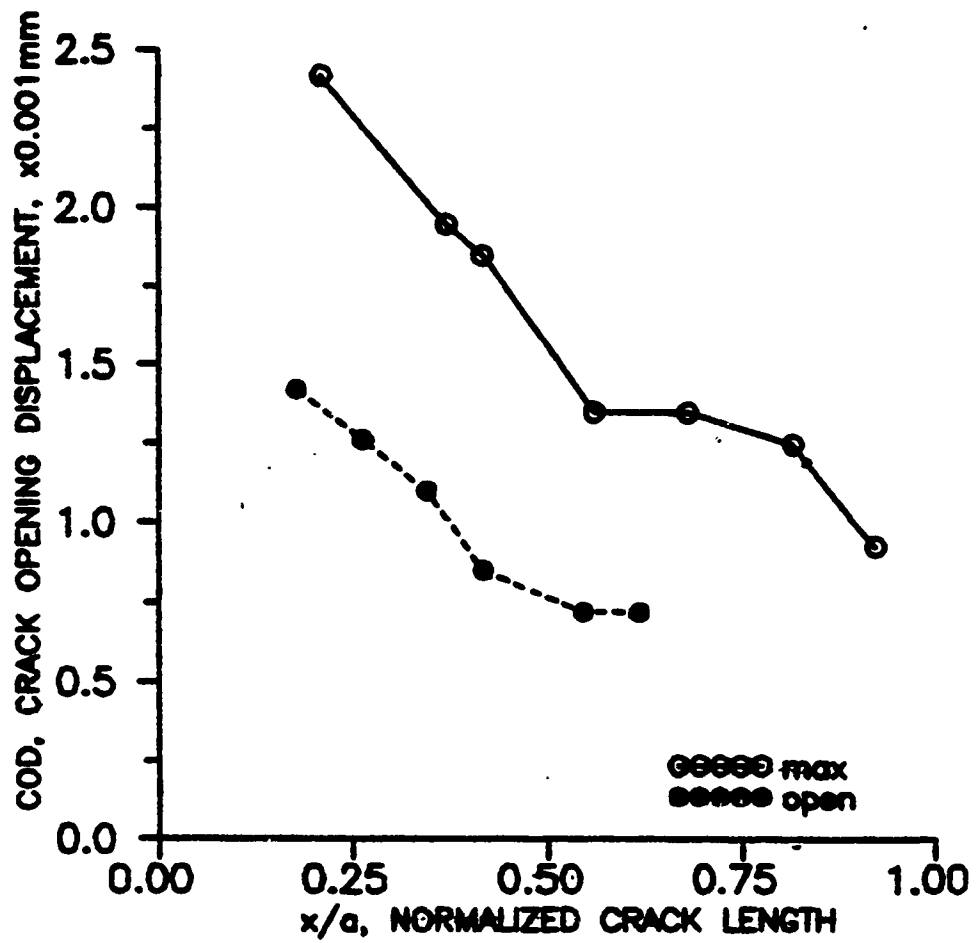


Fig. 4.111 Crack opening displacements corresponding to Fig. 4.101 at maximum and opening points of the loading cycle.

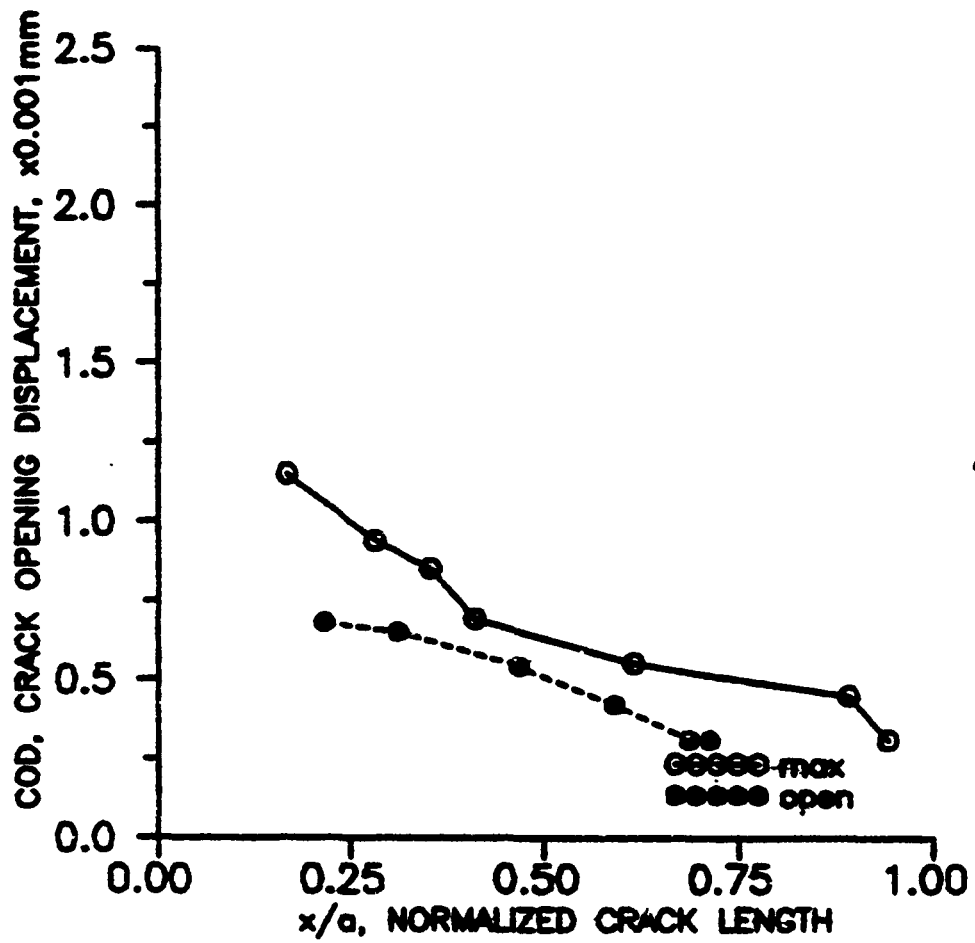


Fig. 4.112 Crack opening displacements corresponding to Fig. 4.102 at maximum and opening points of the loading cycle.

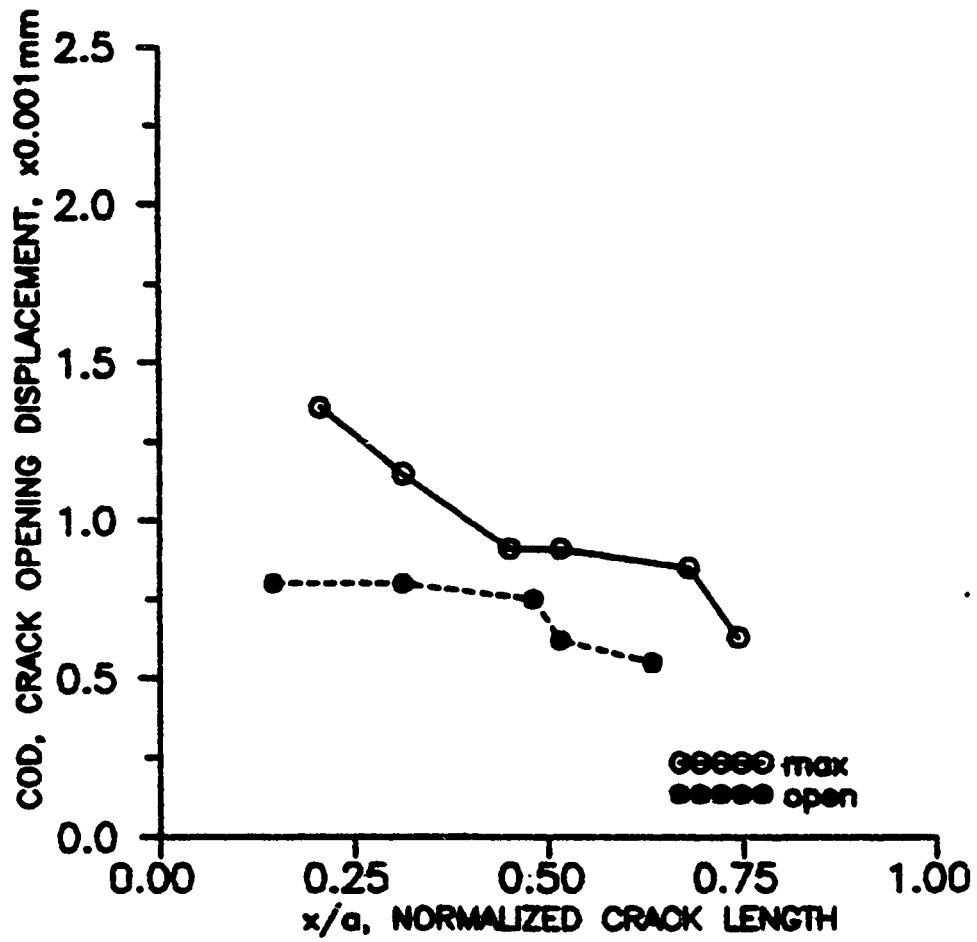


Fig. 4.113 Crack opening displacements corresponding to Fig. 4.103 at maximum and opening points of the loading cycle.

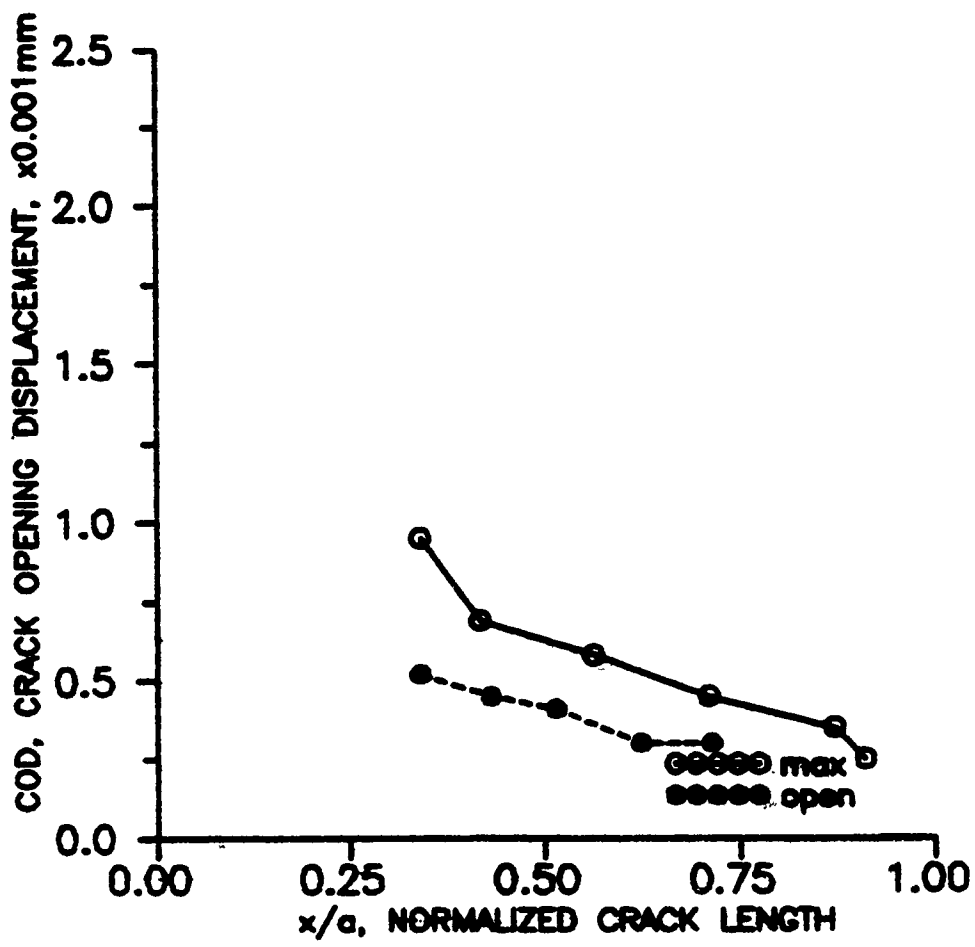


Fig. 4.114 Crack opening displacements corresponding to Fig. 4.97 at maximum and opening points of the loading cycle.

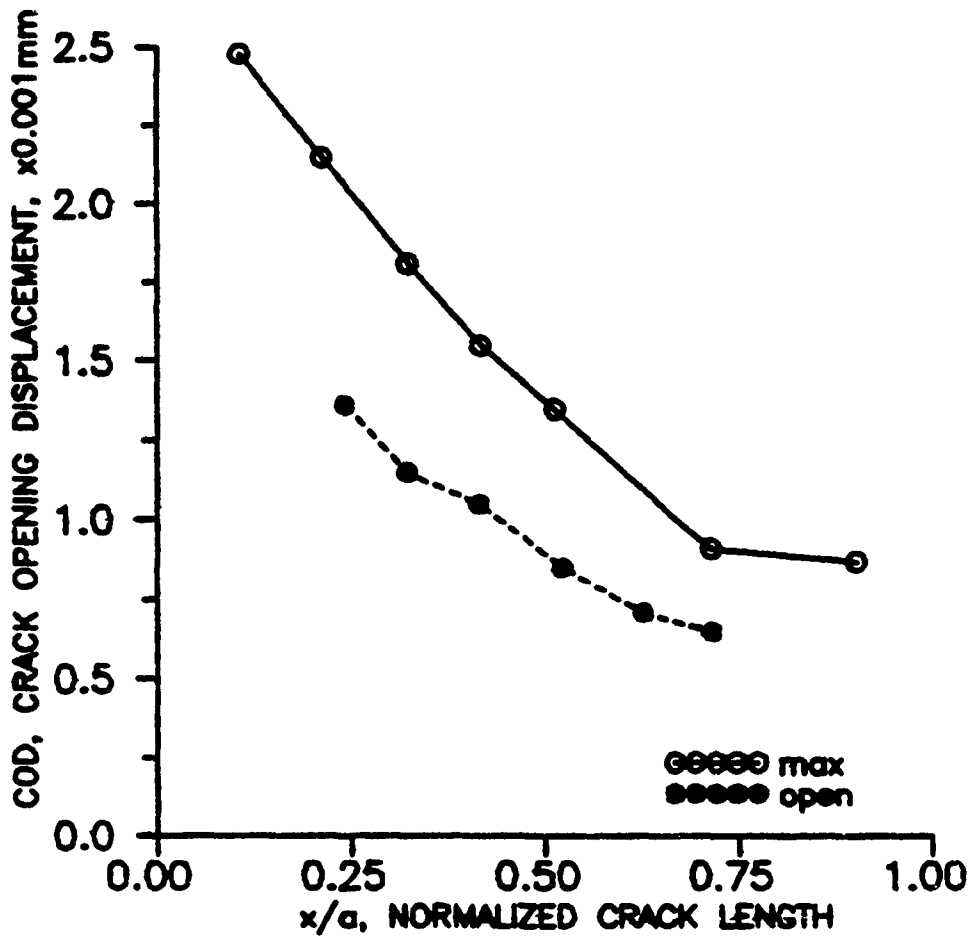


Fig. 4.115 Crack opening displacements corresponding to Fig. 4.105 at maximum and opening points of the loading cycle.

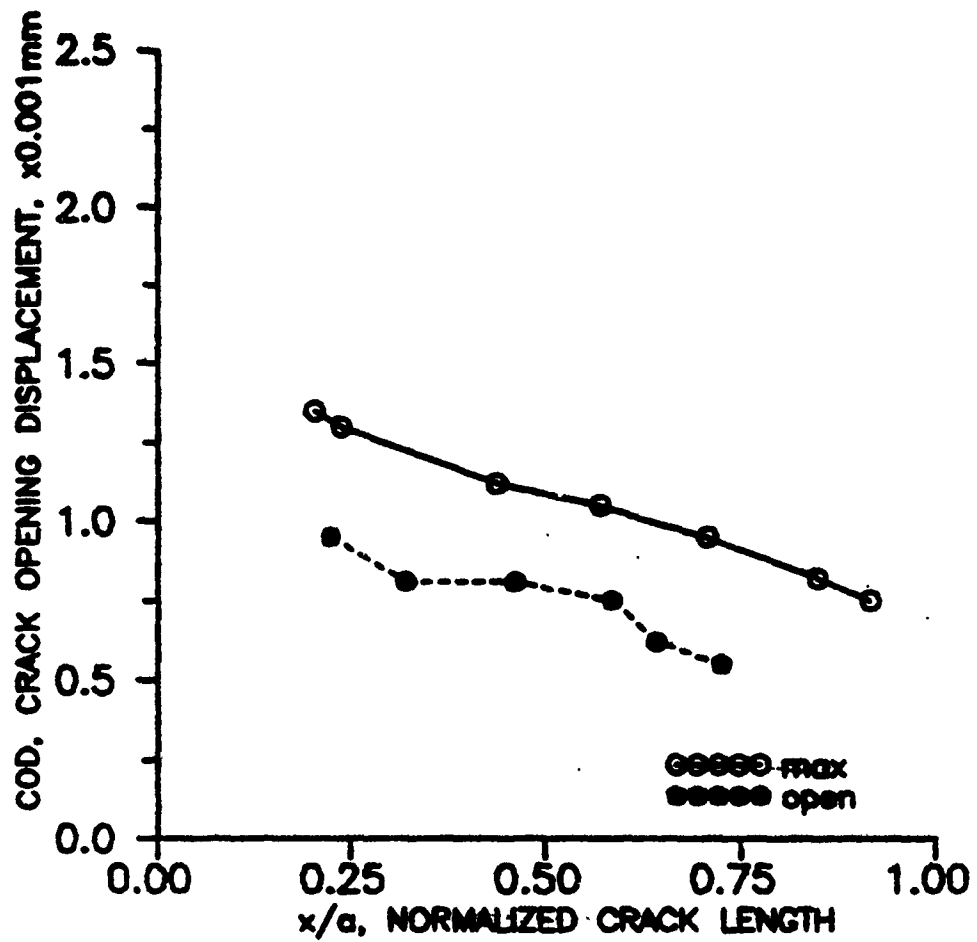


Fig. 4.116 Crack opening displacements corresponding to Fig. 4.106 at maximum and opening points of the loading cycle.

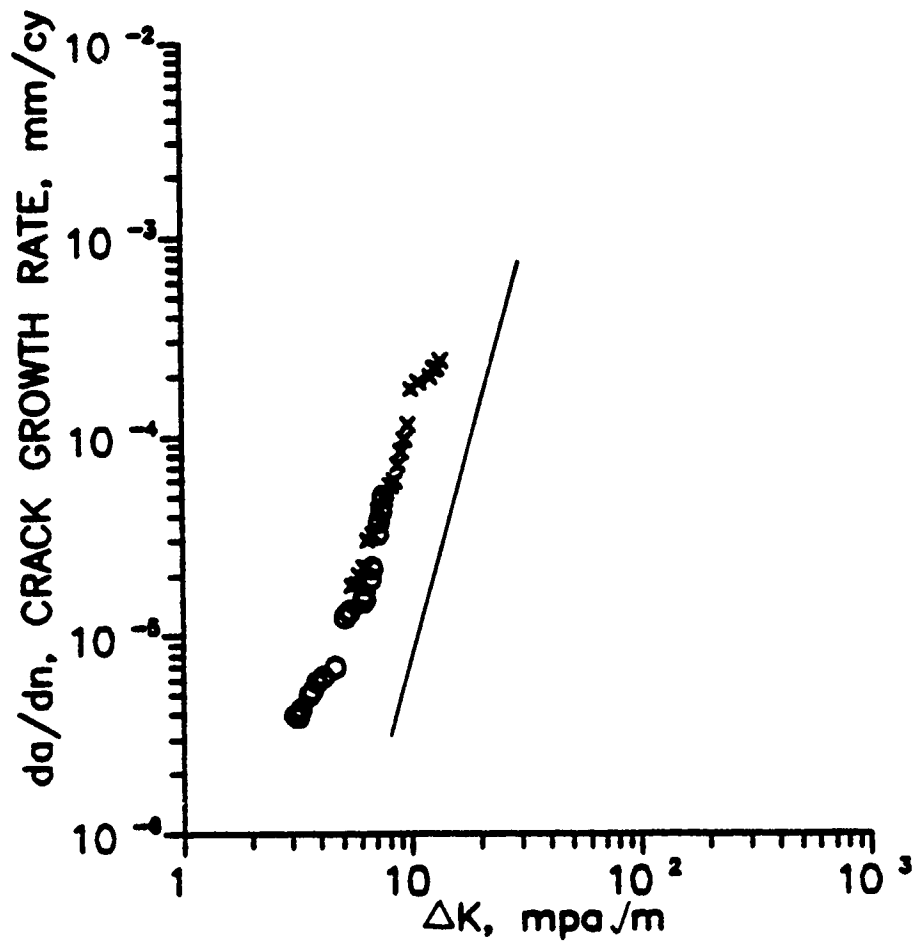


Fig. 4.117 Crack growth rate,  $da/dn$ , versus  $\Delta K$  in notched specimens of aluminum at  $R=0.1$  under negligible notch plasticity effects.

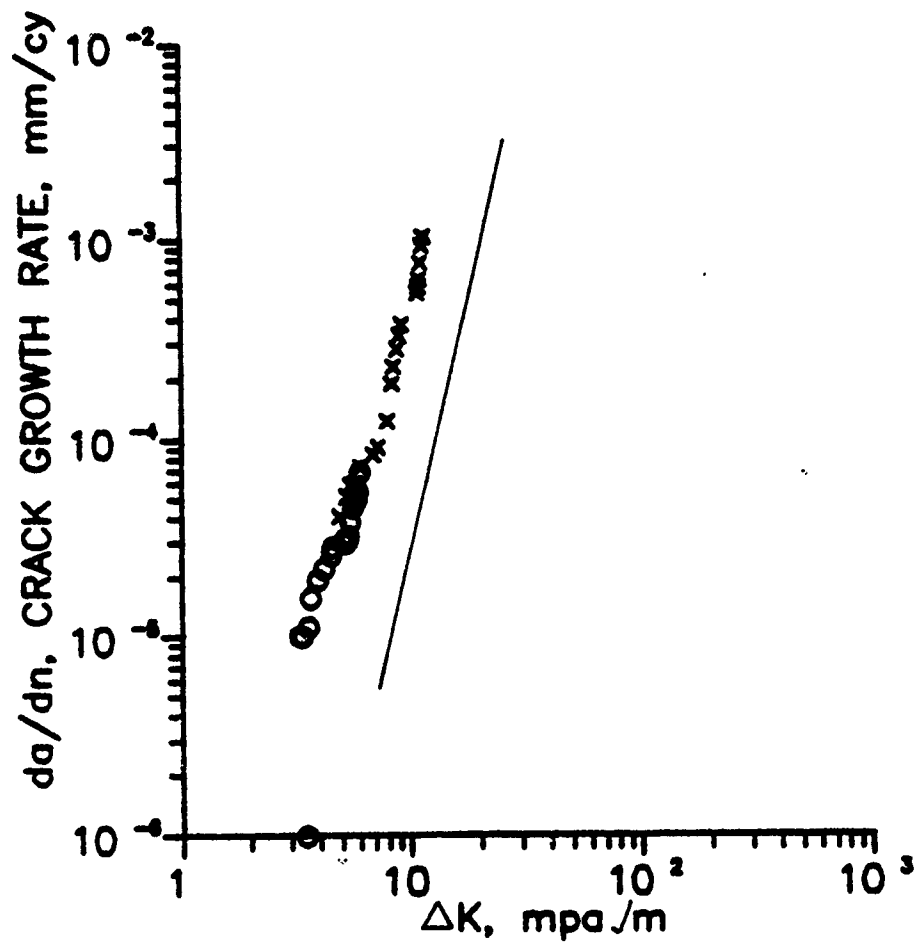


Fig. 4.118 Crack growth rate,  $da/dn$ , versus  $\Delta K$  in notched specimens of aluminum at  $R=0.4$  under negligible notch plasticity effects.

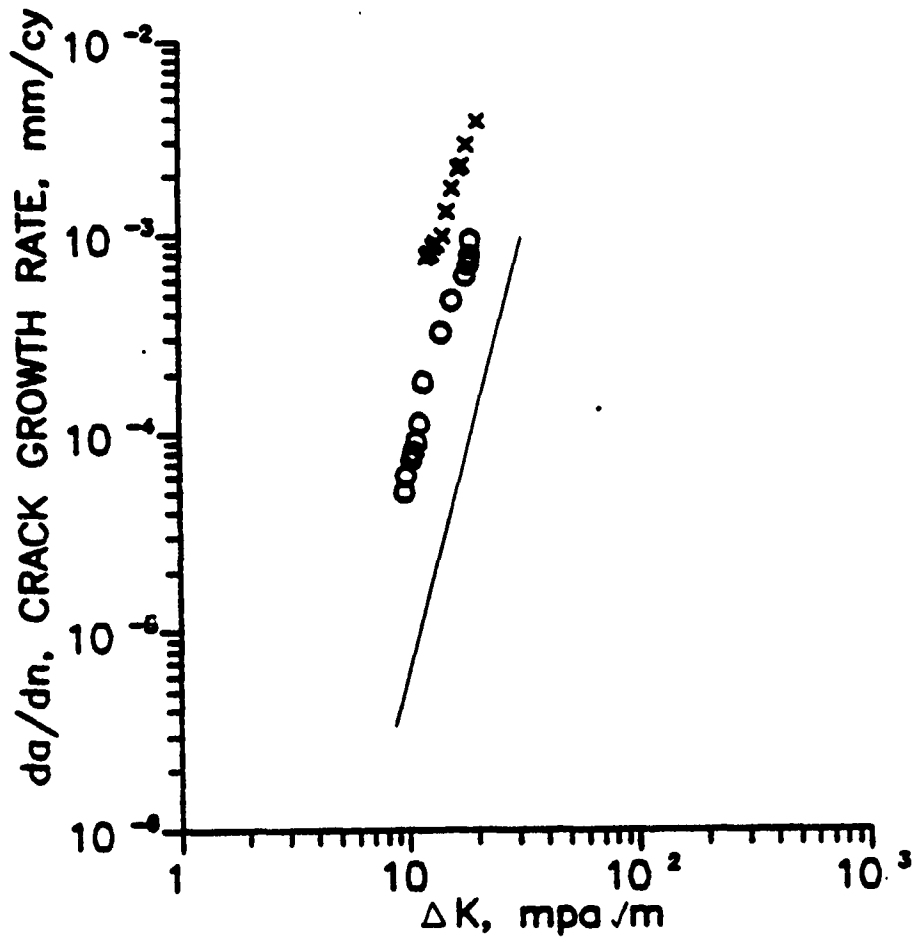


Fig. 4.119 Crack growth rate,  $da/dn$ , versus  $\Delta K$  in notched specimens of aluminum at  $R = 0.1$  under the influence of notch plasticity effects.

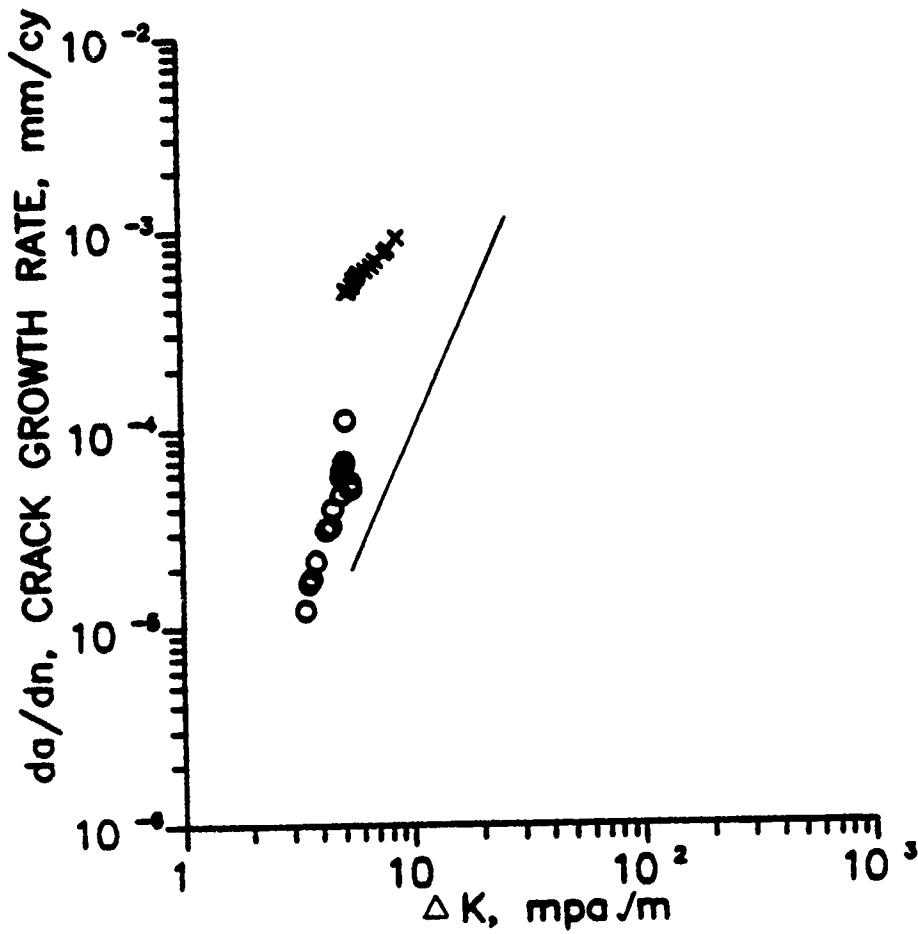


Fig. 4.120 Crack growth rate,  $da/dn$ , versus  $\Delta K$  in notched specimens of aluminum at  $R=0.7$  under the influence of notch plasticity effects.

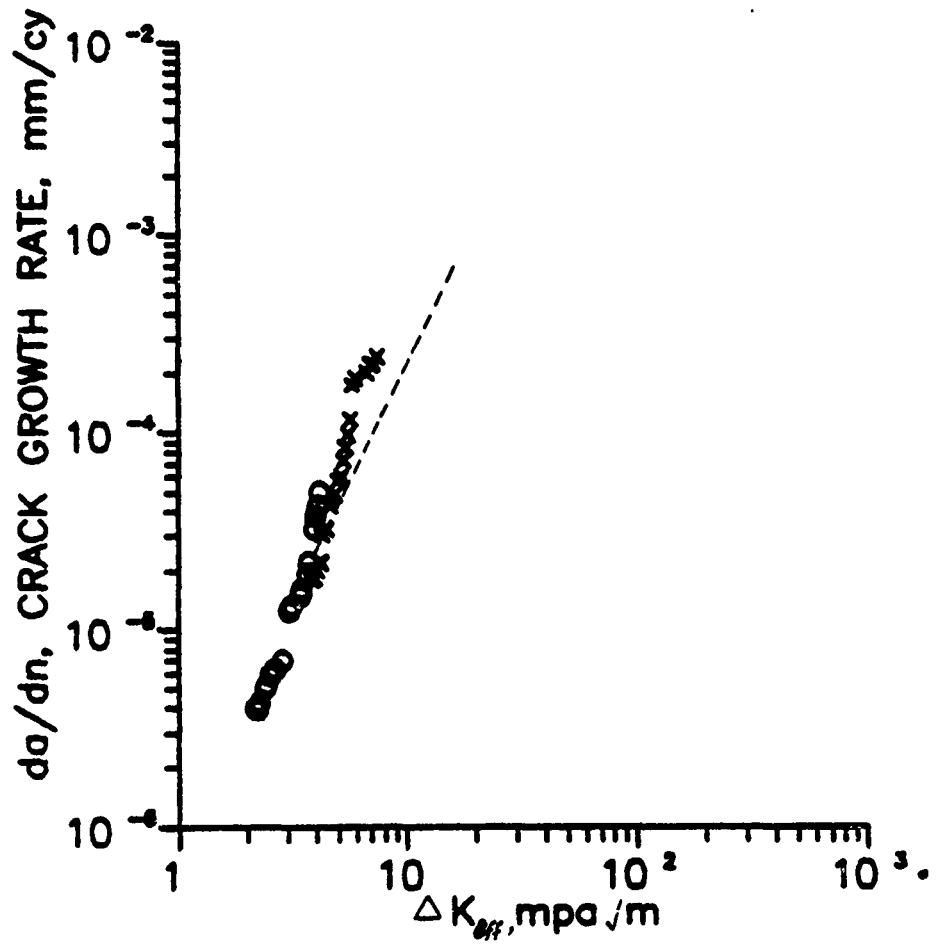


Fig. 4.121 Crack growth rate,  $da/dn$ , as a function of  $\Delta K_{eff}$  corresponding to Fig. 4.117.

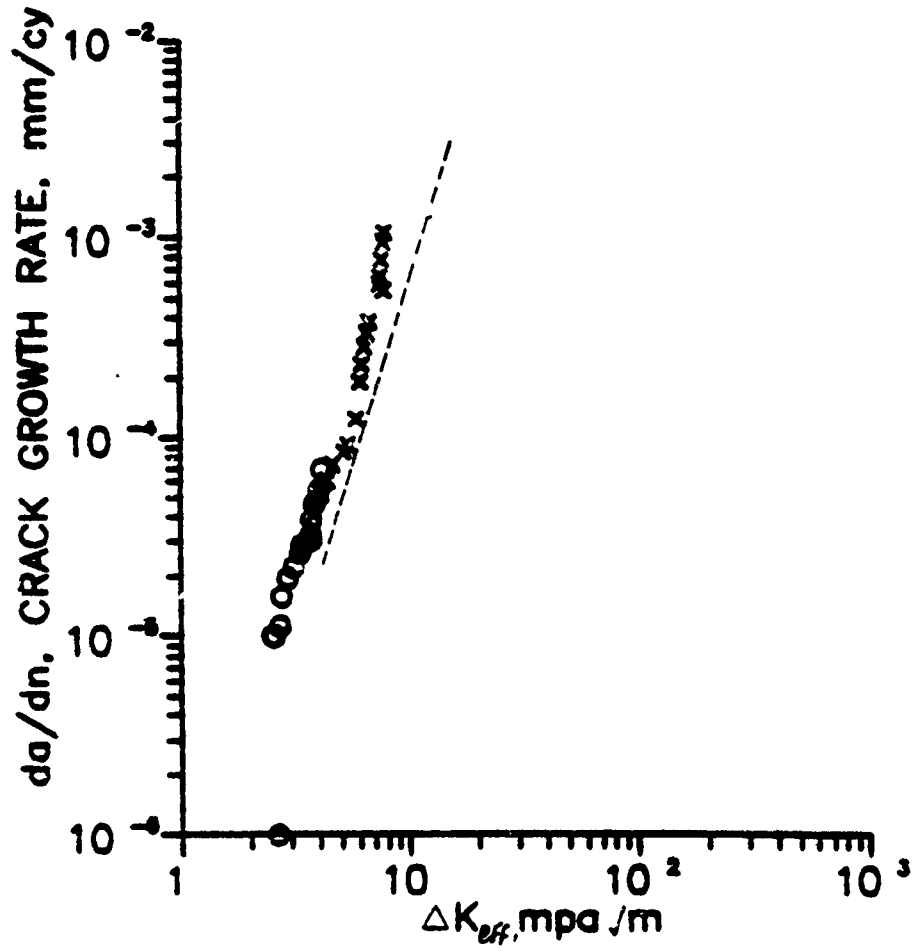


Fig. 4.122 Crack growth rate, da/dn, as a function of ΔK<sub>eff</sub> corresponding to Fig. 4.118.

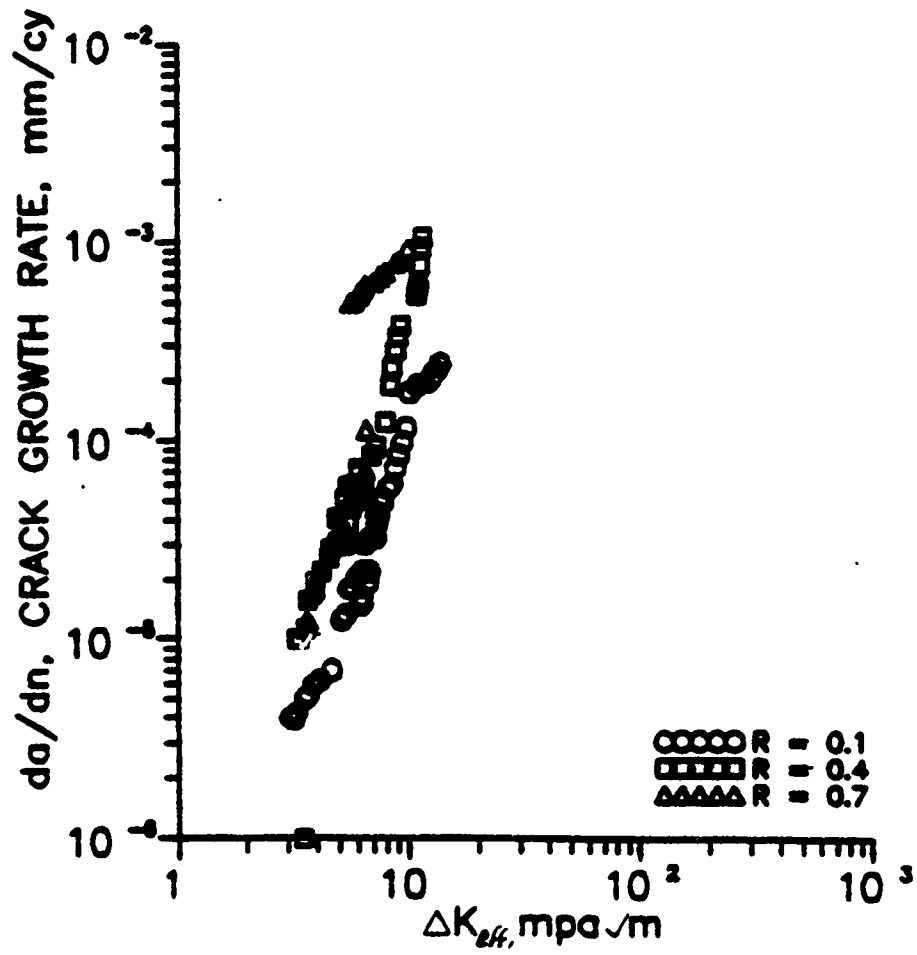


Fig. 4.123 Combined plot showing growth rate of short cracks in front of notches under different conditions.

## **Section 5**

# **DISCUSSION**

The following discussion is focused on four primary aspects of short fatigue crack growth: (1) the equivalent initial flaw size approach, (2) effects of plasticity, (3) crack closure response of long cracks and (4) crack closure response of short cracks.

### **5.1 EQUIVALENT INITIAL FLAW SIZE - DURABILITY ANALYSIS**

Aerospace structures were initially designed on a safe-life approach. The underlying philosophy was to ensure a finite life without any significant fatigue damage. The fail-safe philosophy of aerospace structure design followed the safe-life approach which, besides ensuring service-life, had the additional feature of ensuring operation for a limited time period after significant fatigue damage had occurred. During the 1970's, the United States Air Force developed the damage-tolerance approach which

differed from previous approaches in its assumption of the possibility of cracks being present in any new structure or a component. Also, this approach provided an option for designing structures or components which do not require service inspection during their life. Thus, aircraft structures which are inspected in service can be grouped as fail-safe or as slow-crack growth structures. In these cases, the philosophy of the damage tolerant approach is to ensure that initial fatigue damage grows slowly so that the failure of a component does not take place between inspections.

All structural members and components, when subjected to cyclically varying loads above a certain limit, will develop fatigue cracks leading to the eventual failure of the component. It is thus plausible to assume that there are significant inherent flaws present in certain shapes and sizes within the material which in turn develop into fatigue cracks. This is characterized by the initial fatigue quality of the component. Although this assumption of inherent flaws at a macroscopic scale is subject to discussion, it is very important for durability and reliability studies in the aircraft industry.

The equivalent initial flaw (EIF) is not a physical flaw but an artifact of the method of back extrapolating the crack length versus cycles data to the initial state of zero time. This flaw size, termed equivalent initial flaw size (EIFS), is objectively assumed to be in the direction of the actual crack propagation. This assumed initial flaw size is by definition, a statistical quantity since it is an extrapolated measure. The usual representation of this parameter is by a probabilistic distribution, which is termed the equivalent initial flaw size distribution, EIFSD. Figure 5.1 describes this method of back extrapolation and the EIFSD.

Manning and Yang [90] describe the philosophy of the EIFS concept in detail in their report. This approach has been found to be useful in the U.S. Air Force for durability analysis. This approach of obtaining initial fatigue quality appears to be uncomplicated. Note that the linear elastic long crack data are used in this approach to obtain the back extrapolated initial flaw sizes. In the context of our study, which describes short crack growth and behavior, incremental crack growth from an initial flaw was measured. These data were then back extrapolated to zero time to get initial flaw sizes. This is described in the following paragraphs.

The final crack length and number of cycles from the short crack tests were used in conjunction with the corresponding long crack parameters  $C$  and  $m$  to calculate the initial crack length. A typical method of back extrapolation is shown schematically in Fig. 5.2. Note that the degree of fit utilized to describe the long crack growth rate influences parameters  $C$  and  $m$ . This in turn influences the initial crack sizes obtained by means of the back extrapolation described above.

The results of estimated initial crack lengths for steel, obtained by back extrapolation using linear elastic long crack data, are shown in Figs. 5.3 through 5.6. The solid lines shown in these figures represent the equations

$$a_e = 2 a_i \quad a_e = a_i/2$$

where

$a_e$  is the estimated initial crack length and

$a_i$  is the actual initial crack length

Note that the estimates of initial crack length for tests at  $R = 0.7$  are not shown as the long crack parameters at this ratio were not available. The values of  $C$  and  $m$  for each case are shown in Table 4.1. Besides the actual initial crack length, two other crack lengths were chosen in the history of crack growth, and corresponding estimates were made. These results are also shown in the same figures. The results of fine grain conditions of steel indicate that estimated crack lengths were greater than the initial crack lengths. It was also observed that in the case of coarse conditions of steel, the estimated initial crack lengths were greater than the actual initial crack length except in a few cases. Moreover, the results of estimates of initial crack length lie on or outside the line  $a_e = 2a_i$ . This indicates that the estimates of the initial crack lengths made by using linear elastic data is unconservative for  $R = -1$  tests since real cracks grow faster. Note that no trend could be observed in estimates for different stress levels.

The parameters  $C'$  and  $m'$  describing the long crack growth parameters in terms of  $\Delta K_{eff}$ , were used to get estimates of initial crack length. The results obtained are shown in Figs. 5.7 through 5.10 corresponding to Figs. 5.3 through 5.6. It becomes clear from these figures that in most cases, the estimated crack lengths are smaller than the initial crack length. A schematic diagram illustrating the predictions of crack growth from the use of parameters  $C$  and  $m$  and the parameters  $C'$  and  $m'$  is shown in Fig. 5.11. Results from the estimated crack lengths also reveal that life calculations based on  $C$  and  $m$  would be greater than when using parameters  $C'$  and  $m'$ , for the same initial crack length. The use of parameters  $C'$  and  $m'$  therefore would give conservative results in life predictions.

Thus, the models used to quantify crack growth, such as curve fit or the LEFM adaptation using the Paris' law, seems to be inadequate in supplying necessary information to predict the initial fatigue quality of airframe components. The adaptation of the EIFS approach using linear elastic long crack data is thus relevant to specific conditions for which they are derived and cannot be generalized. To obtain back extrapolated crack lengths in EIFS approaches for cases where short cracks are involved, the use of the parameters  $C'$  and  $m'$  is recommended. The next section will consider the estimates of initial crack length under gross plastic deformation.

## 5.2 SHORT CRACK GROWTH UNDER GROSS PLASTIC DEFORMATION

The importance of short crack growth under gross plastic deformation is relevant to cases where there is high amplitude loading in structural members such as engine disks where cracks of critical lengths are present. The growth rates of cracks in these cases, where significant plasticity effects are involved, cannot be analyzed by LEFM alone. Dowling [91,92] proposed the cyclic J integral  $\Delta J$ , to handle these situations. This  $\Delta J$  is a direct analog of the J-integral for monotonic loading.  $\Delta J$  is defined as follows:

$$\Delta J = \int_{\Gamma} \Delta W dy - \Delta T_i \left[ \frac{\partial \Delta U_i}{\partial x} \right] ds$$

where

$$\Delta W = \int \Delta \sigma_{ij} d\Delta \epsilon_{ij}$$

$$\Delta T_i = \Delta \sigma_{ij} n_j$$

Note that in defining  $\Delta J$ , all stresses, strains, tractions and displacements are replaced by respective ranges in the J-integral definition. In the equations defined above,  $\Gamma$  is a contour line from the lower face of the crack to the upper face of the crack enclosing the crack tip and  $\Delta U$  is the displacement range vector. Strain energy density,  $\Delta W_{ij}$  is defined as a function of stress and strain ranges  $\Delta \sigma_{ij}$  and  $\Delta \epsilon_{ij}$ . The traction vector is defined along  $\Gamma$  by the normal  $n_j$ . As noted in reference [93], there is no fundamental objection to a  $\Delta J$  so defined if the stress ranges for the material could be expressed as a function of current plastic strain ranges and not on deformation history. In other words, the material behaves according to kinematic hardening.  $\Delta J$  so defined, could be interpreted as a measure of the intensity of the cyclic strains near the crack tip.

$\Delta J$  for cracks in infinite bodies is expressed as

$$\Delta J = \Delta J_e + \Delta J_z + \Delta J_p$$

In the above equation for  $\Delta J$ , the first term represents the elastic part, the second term represents the plastic zone correction part and the last term represents the plastic part. A detailed discussion on these estimates and expressions to evaluate each of these parts are given in reference [94]. It was observed in reference [95] that short cracks under gross plastic deformation exhibit less closure. To put it differently, cracks are open for the most part of the cycle. Crack opening was observed below the zero load and crack closure was observed near the minimum strain. Figure 5.12

shows a typical hysteresis loop with opening and closing points for cracks under high strains. Figure 5.13 shows the data of closure so obtained in LF condition of 4340 steel. The hypothetical hysteresis loop b-c-b in Fig. 5.12 was proposed as causing the same amount of crack growth as the loop b-a-b. The stress and strain ranges from this hypothetical hysteresis loop were used to account for closure in the  $\Delta J$  analysis of fatigue short crack growth.

Fatigue crack growth rate data [94] at high cyclic strains in LF condition of steel is shown in Fig. 5.14 as a function of applied  $\Delta K$  without correction for closure and plasticity. The solid line in this figure represents the long crack data fit. The crack growth rate data is plotted as a function of  $\Delta K_{op}$  in Fig. 5.15. Note that  $\Delta K_{op}$  is the modified value of  $\Delta K$  with plasticity and closure effects accounted for. It can be observed from this figure that there is reasonable correlation of crack growth rate data except for a few points at lowest growth rates.

Thus, it is to be noted that  $\Delta J$  is a useful crack growth parameter in handling situations of gross plastic deformation. In the following paragraphs, the estimates of initial crack length based on LEFM and  $\Delta J$  will be made for the data presented in Fig. 5.14. The estimated initial crack lengths based on the linear elastic crack growth parameters are shown in Fig. 5.16 which clearly shows that the estimated crack lengths were always higher than the initial crack lengths at all strain levels. Note that two other crack lengths in the history of the crack growth were also chosen and estimates were made for these crack lengths. These estimates are also shown in the same figure. This reiterates the fact that real cracks under gross plastic deformation grow faster than when predicted by the LEFM analysis.

The estimates of the initial crack length were made by using the  $\Delta J$  approach including closure effects. Specifically, the equation used in back extrapolation was

$$\Delta K_{Jop} = C \Delta \sigma \left[ C_0 \pi a \left( 1 + \frac{0.75 \sqrt{n}}{1 - \nu^2} \frac{\Delta \epsilon_p}{\Delta \epsilon_e} \right) \right]^{1/2} m$$

where

$$C_0 = 0.434$$

$$\nu = 0.29$$

$$n = 6.29$$

$\Delta \epsilon_e$  and  $\Delta \epsilon_p$  are the elastic and plastic strain ranges.

The results of estimated crack lengths based on  $\Delta J$  are shown in Fig. 5.17. Note that estimated crack lengths are still greater than actual initial crack lengths. However, by comparing Fig. 5.17 with Fig. 5.16, it becomes clear that the difference between the actual and estimated initial crack lengths has reduced. This can also be seen in Fig. 5.18 where the ratio of estimated initial crack length to the actual initial crack length based on  $\Delta J$  calculations is plotted against a similar ratio based on  $\Delta K$  calculations. Note that there is an improvement in predicting initial crack lengths by means of  $\Delta J$ . The remaining difference between the estimated crack length and actual initial crack length can be attributed to the local crack tip variations observed in short cracks.

### 5.3 RATIONALIZATION OF LONG CRACK GROWTH

The results of the long crack test data are presented in Figs. 4.39 through 4.42 for LF, HF, LC, and HC conditions of steel and in Fig. 4.43 for aluminum. In these figures the crack growth rate is plotted as a function of the  $\Delta K_{eff}$  at all R ratios. Observe from these figures that the closure is able to consolidate the crack growth rates at different R ratios into a simple relation of the  $\Delta K_{eff}$ . Elber's mechanism in the crack wake is thus dominant in long cracks and hence crack closure explains the decreased driving in front of the crack tip. Figure 5.19 shows a similar plot where results from all four conditions of steel are shown in the same figure. It can be observed from this figure that the crack growth rates of different conditions of steel do not show significant differences in the linear elastic regime and that all data fall within a narrow band. The effect of increased strength therefore has little influence on the crack growth rates of 4340 steel. This has also been observed by Barsom et al [96]. Note that there may be differences in crack growth rates near the threshold region for different conditions of steel. The data obtained do not reveal these differences.

### 5.4 RATIONALIZATION OF SHORT CRACK GROWTH

Short crack growth experiments conducted in this study revealed a transient behavior, which is indicative of the growth processes in the region between microstructurally short and long cracks. In most cases, short cracks in our study exhibited high crack growth rate in this transient region. Note that short crack tests performed on plain specimens did not involve any bulk deformation or net section yielding. Thus, most of the cracks in these tests were growing under small scale yielding conditions.

It is evident from the experimental results that there is a variation in closure level for short cracks as opposed to a near constant value of closure level observed for long cracks. The closure response of short cracks can be due to multiple factors such as plasticity induced, roughness induced etc.

In order to isolate effects of plasticity induced closure, the variation of  $\frac{K_{op}}{K_{max}}$  was studied with respect to the crack length, which was normalized by cyclic plastic zone size. It was observed that the closure level increased with the increase in the normalized crack length at R ratios of -1 and at R ratio of 0.1. The results at R = 0.4 and 0.7 were approximately constant over the entire range. This indicated that there were significant plasticity induced closure mechanisms in our tests.

Crack growth rates at all positive R ratio tests are presented as a function of  $\Delta K_{eff}$  in Figs. 5.20 through 5.23 for different conditions of steel and in Fig. 4.96 for aluminum. Growth rates at different positive R ratios show a single relation within a narrow scatter band for aluminum and fine grain conditions of steel. However, growth rate data for coarse grain conditions of steel do not fall within a narrow band. This is probably due to mechanisms other than the plasticity induced closure such as the roughness induced closure. Figure 5.24 shows the growth rates plotted as a function of  $\Delta K_{eff}$  for all conditions of steel at R = -1. It is clear from this figure that all data except for the test results of HC condition of steel, fall within a narrow band. This implies that plasticity induced closure is able to consolidate the growth rate data into a single relation for fine grain conditions at increased stress ratios. Local microstructural effects, including fracture surface roughness, are believed to be responsible for the large scatter observed in growth rates in coarse grain conditions of steel. In

general, the crack propagation and hence growth rate at  $R=-1$  depends on the micro-morphology of the material. The discontinuous nature of short crack growth in completely reversed cycling can be associated with a multitude of factors including crack deflection, roughness of crack surface, and other mechanisms.

The analyses of cracks growing from notches indicate that cracks growing at stress raisers under negligible notch plasticity effects, show growth behavior similar to that of cracks growing in plain specimens. However, the tests conducted at stress levels where there were considerable notch plasticity effects revealed higher crack growth rates. Although there was no global cyclic creep or ratcheting observed in these tests, this increased growth rate may be attributed to the local mean strain and cyclic creep effects. It was observed that the crack was open throughout the loading cycle in these tests which contained considerable notch plasticity effects. From the results presented in this study, it was not possible to conclude whether there was any exclusive control of growth behavior of cracks by notch plasticity. The estimates of initial crack length by means of long crack parameters are similar to the results presented for steel. In other words, the estimated initial crack lengths are greater than the actual initial crack lengths. The use of long crack parameters, which describe growth rate in terms of effective stress intensity, enable estimated crack lengths to move in closer to or to remain smaller than the actual initial crack lengths.

## 5.5 IMPLICATIONS OF FATIGUE SHORT CRACK GROWTH STUDIES

It is evident from our results that there are differences in the growth behavior of short and long cracks. These differences cannot be accounted for merely by closure. The other mechanisms which are to be considered are  $K$  estimation errors, crack deflection and constraint. Note that the inclusion of higher order terms in the series solution of stress in front of the crack tip changes the stress intensity factor significantly for cracks which are microstructurally short. However, inclusion of higher order terms for cracks which are physically short, or, in other words, for cracks of lengths greater than 0.14mm, will not result in any appreciable difference. In contrast to long crack studies, experimental difficulties in the direct monitoring of short cracks has been a barrier to the understanding of crack growth in terms of quantifiable mechanics parameters. Note that a formal mechanics description of the growth of short cracks is not possible to describe a variety of short crack conditions. In general, short crack growth behavior can be grouped under different headings such as low or high cycle regime in plain or notched specimens.

The findings from this study indicate that through thickness cracks which are physically short cannot be handled by linear elastic fracture mechanics alone. The widespread use of durability methods to assess crack growth by fatigue, depends on its ability to apply to short as well as to long cracks. With the improvement in NDE instruments, it is possible to detect cracks which are physically short in components. In these cases, the durability techniques should be able to account for the increased growth rates of short cracks

Life characterization of fatigue sensitive components forms one aspect of fatigue design. In such a life estimation procedure, use of short crack growth data would improve the results only when other factors such as loading conditions, environment, opening and closing level are well defined. In general, the engineering significance of short cracks may seem to be limited, but with the advancement of technologies in related fields such as non-destructive testing (NDT) techniques, stress analysis, in-service monitoring, safety and reliability the importance of the short crack growth data will increase.

The limits of crack length ranges used in present damage-tolerant methods can be extended to the short crack region by incorporating the effective stress intensity approach in its philosophy. Note that this limit can not be extended to microstructural region because of non-continuum effects. The present study and similar short crack growth studies could be used as a guide line in selecting material, changing existing designs, and approximating inspection intervals.

Small crack data could be used in operational limit analysis, durability design of new structure and fail-safe evaluation of in-service aircraft. It is to be noted that without appropriate experimental data to support small crack predictions, the results would probably be unconservative.

Yet another area where short crack growth behavior can be successfully applied is in the field of alloy development. The difficulties which arise in defining thermomechanical processes for a material to meet important requirements such as fatigue resistance, strength, ductility and corrosion resistance reveal the importance of short crack growth data.

Most experimental data on short cracks is not unique. A statistical approach is hence needed to correlate the data obtained at different conditions. Such a statistical approach which includes both intrinsic (such as ductility) and extrinsic (such as closure mechanisms) parameters will be suitable in handling cases where the crack growth data falls within the microstructural regime.

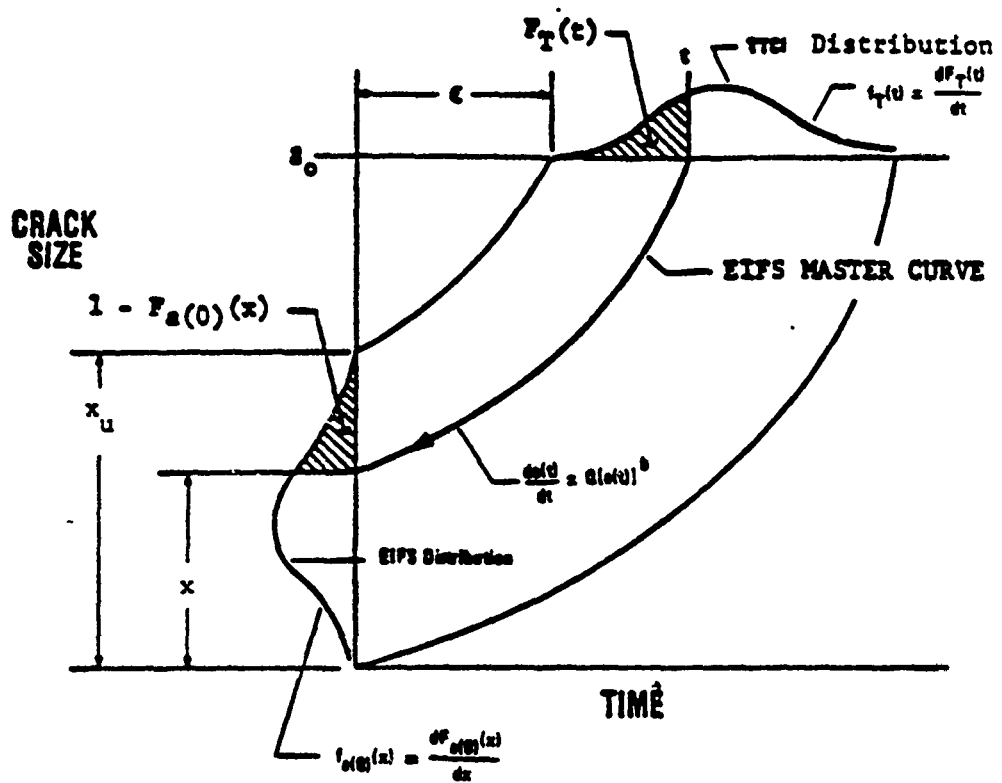


Fig. 5.1 Schematic illustration of the method of back extrapolation

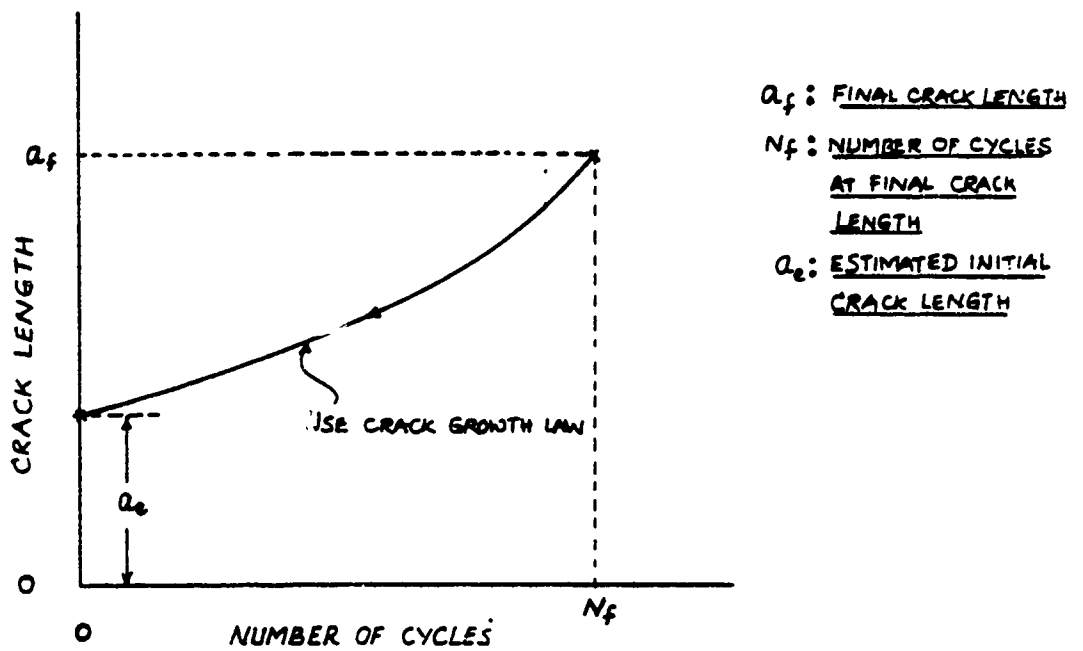


Fig. 5.2 Typical method of back extrapolation adopted.

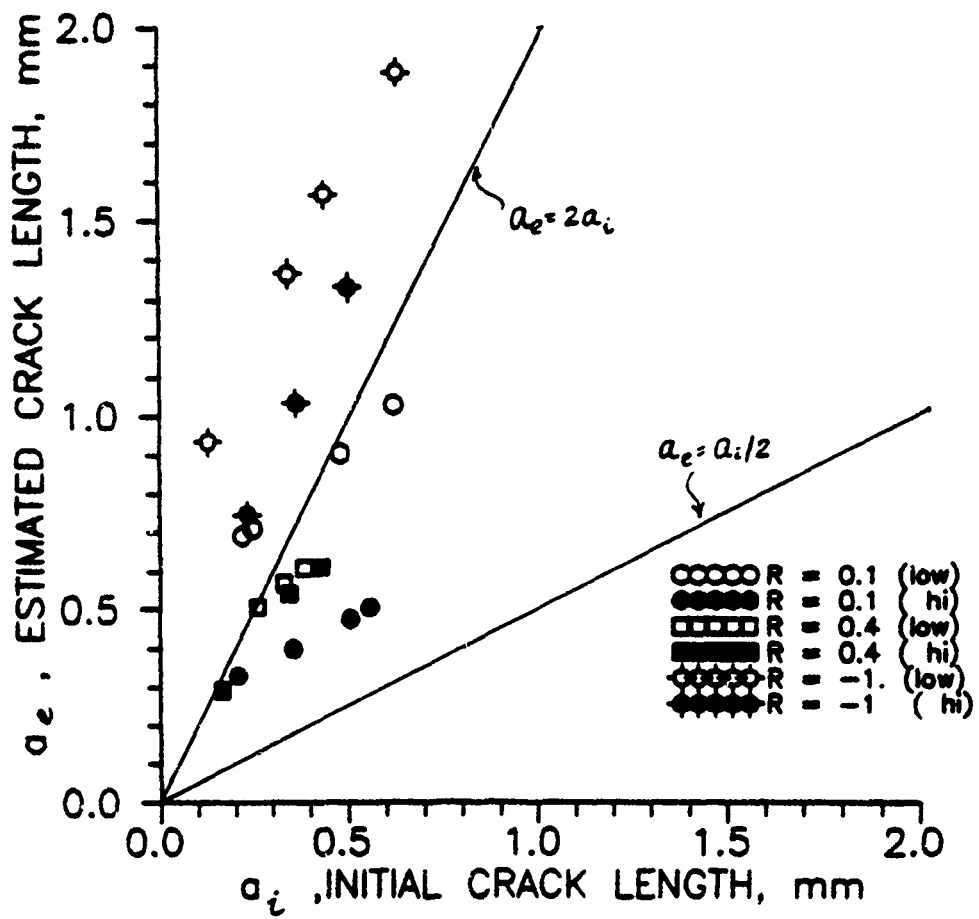


Fig. 5.3  $a_e$  versus  $a_i$  in LF condition of steel at different R ratios using C and m.

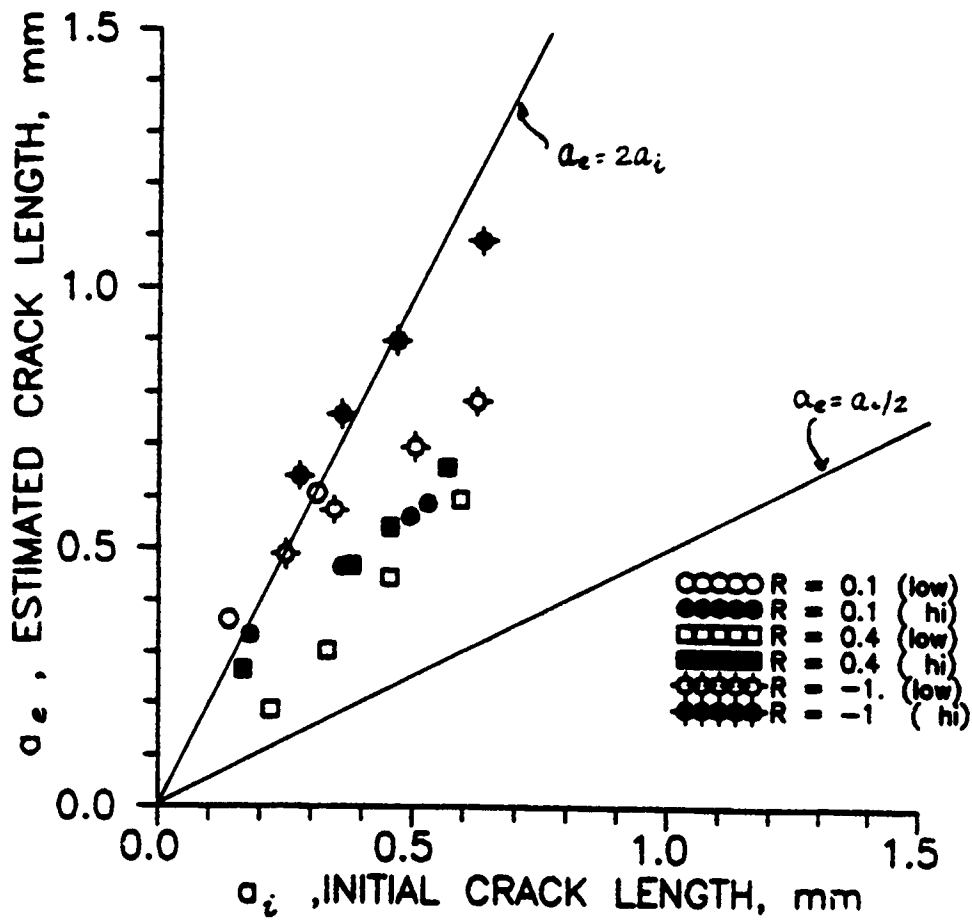


Fig. 5.4  $a_e$  versus  $a_i$  in HF condition of steel at different R ratios using C and m.

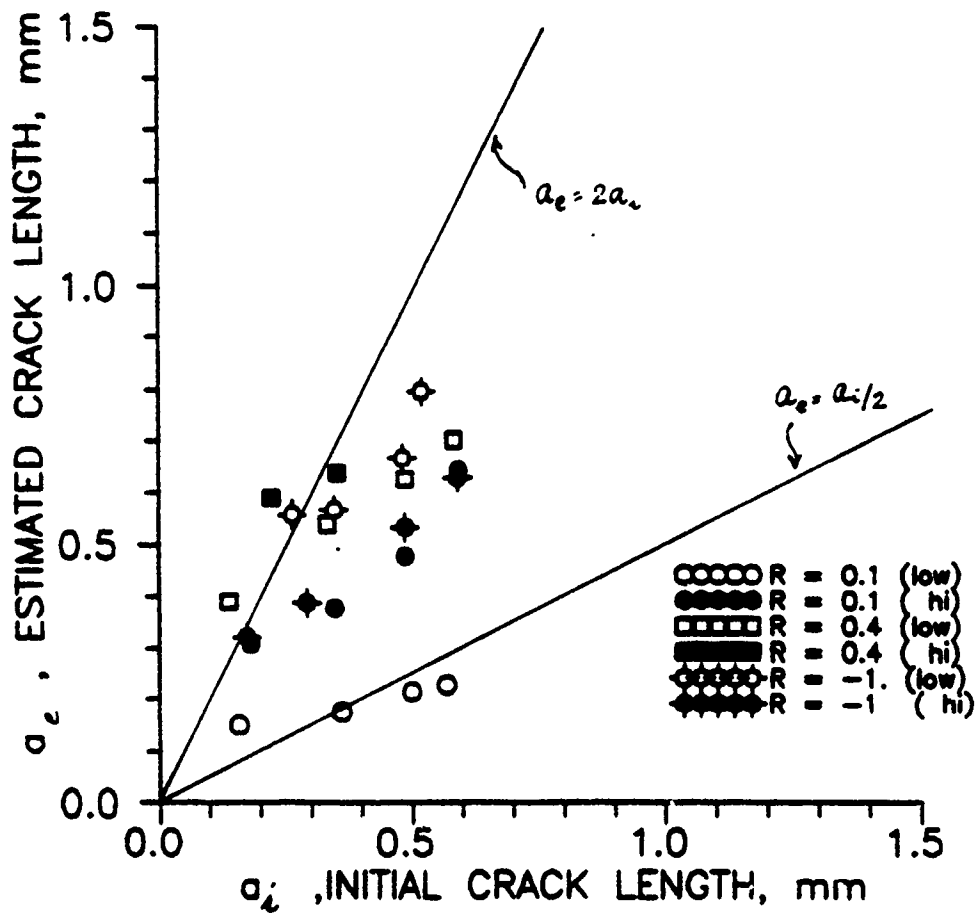


Fig. 5.5 a, versus a, in LC condition of steel at different R ratios using C and m.

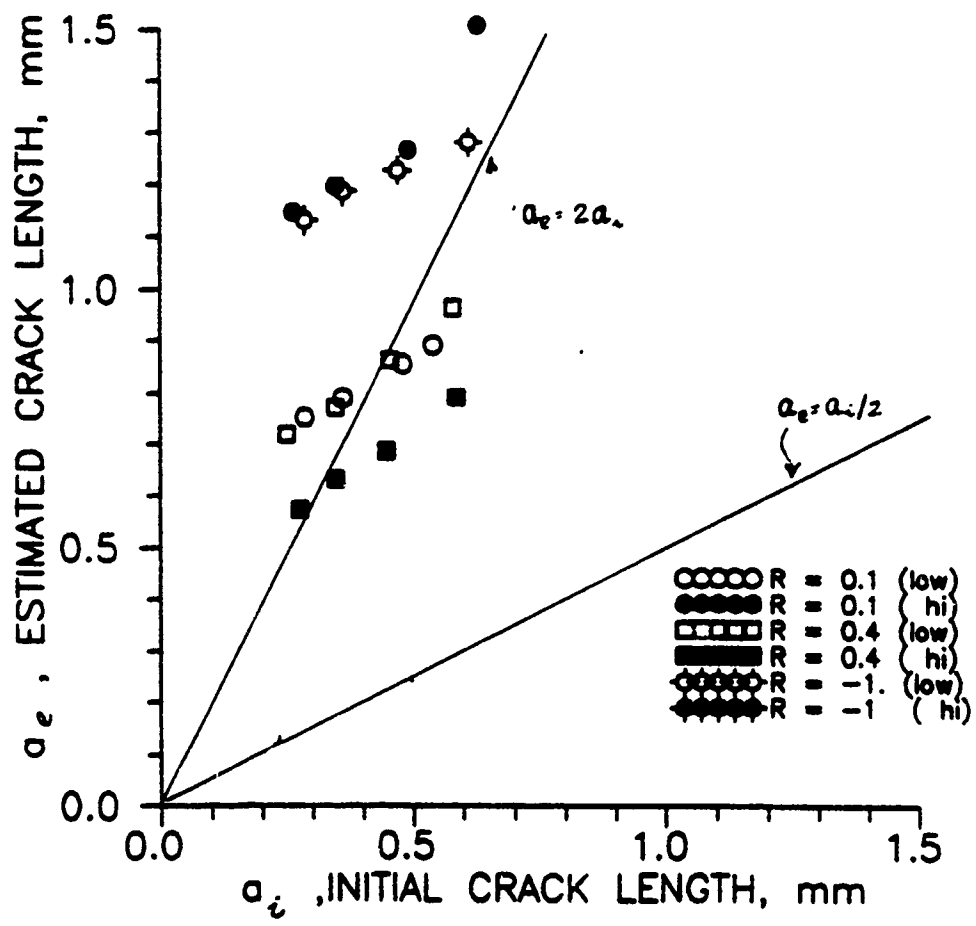


Fig. 5.6  $a_e$  versus  $a_i$  in HC condition of steel at different R ratios using C and m.

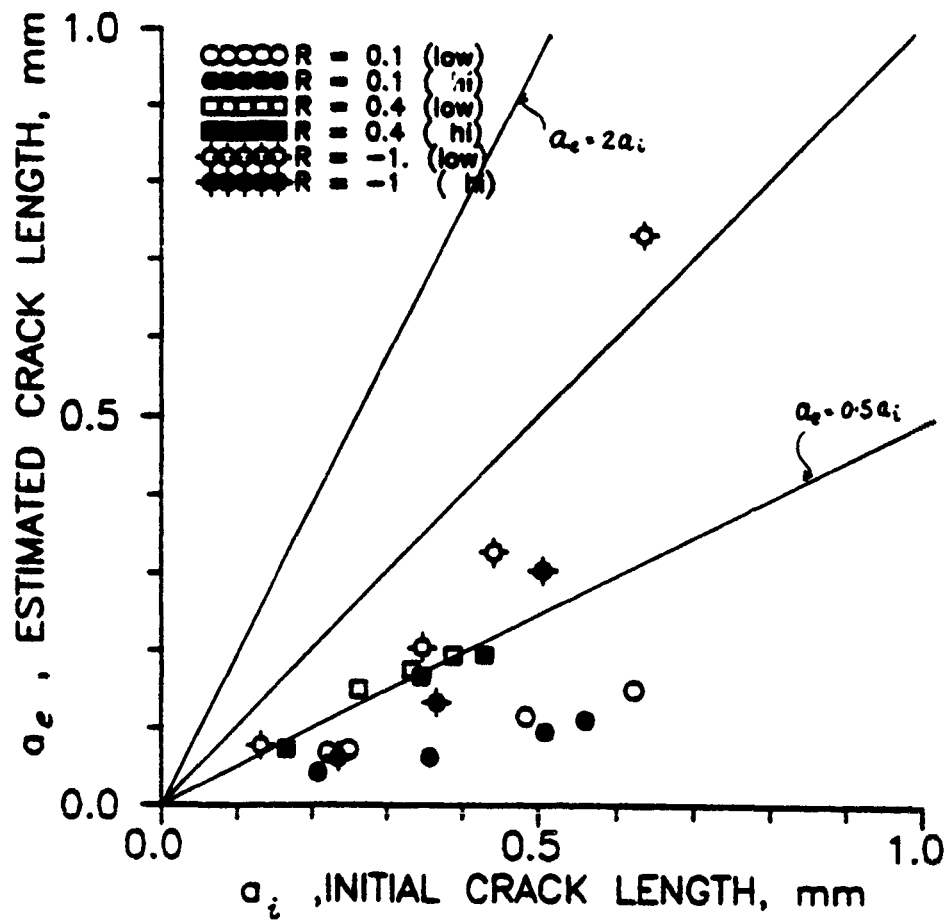


Fig. 5.7  $a_e$  versus  $a_i$  in LF condition of steel at different R ratios using  $C'$  and  $m'$ .



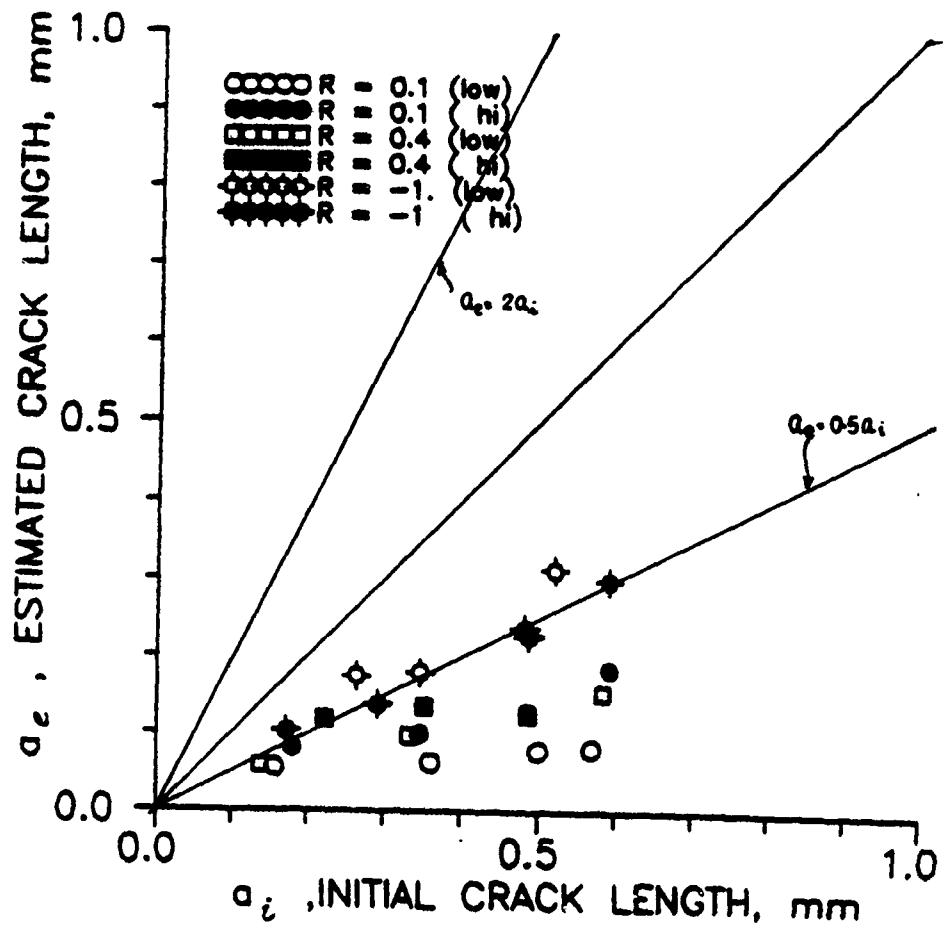


Fig. 5.9 a, versus  $a_i$ , in LC condition of steel at different R ratios using  $C'$  and  $m'$ .

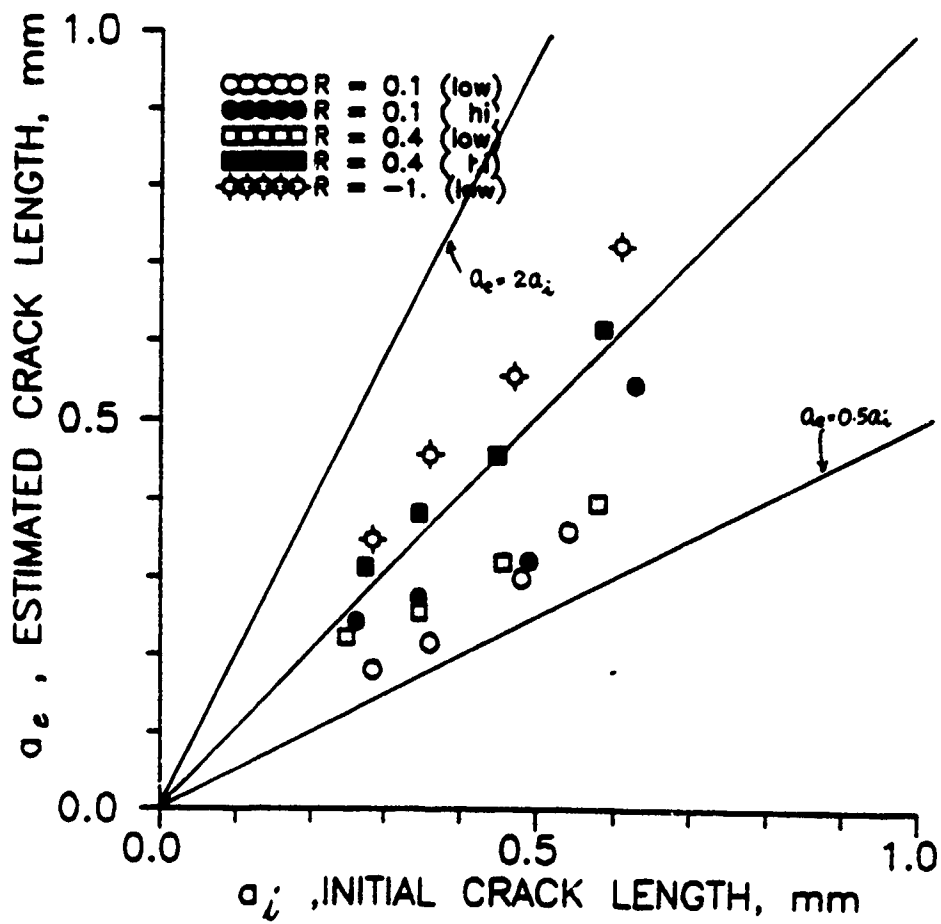


Fig. 5.10  $a_e$  versus  $a_i$  in HC condition of steel at different R ratios using  $C'$  and  $m'$ .

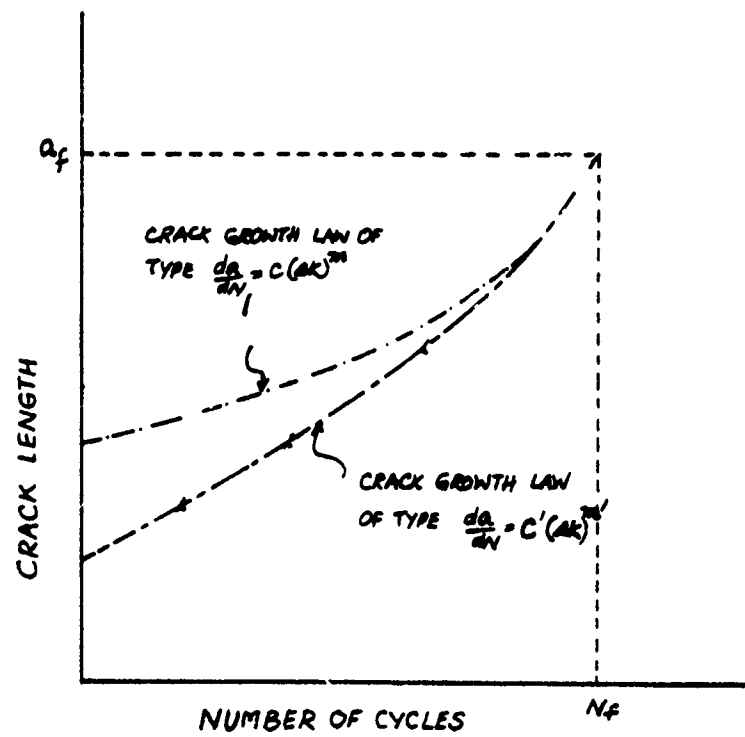


Fig. 5.11 Schematic diagram indicating back extrapolation based on  $C$  and  $m$  and  $C'$  and  $m'$ .

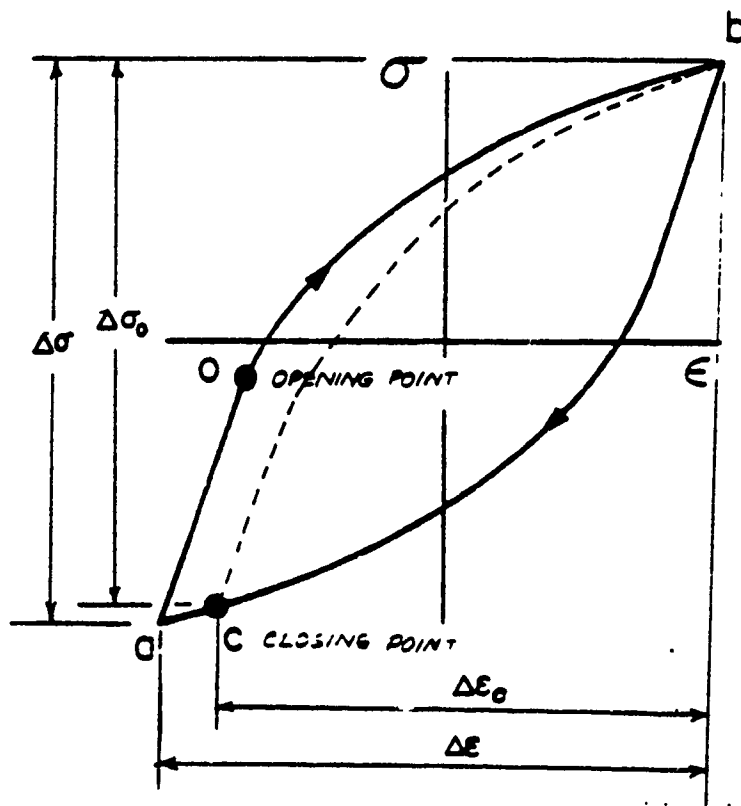


Fig. 5.12 Crack opening and closing at high strain cycling.

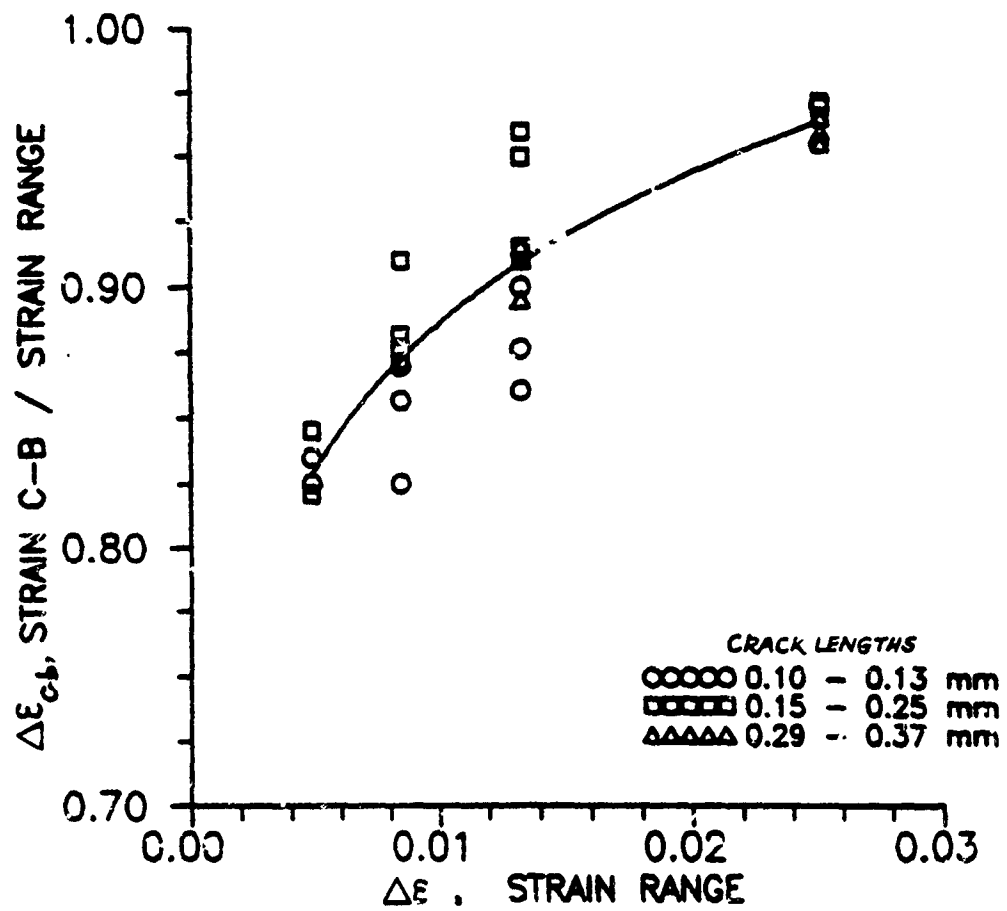


Fig. 5.13 Closure data for LF condition of steel at high strains.

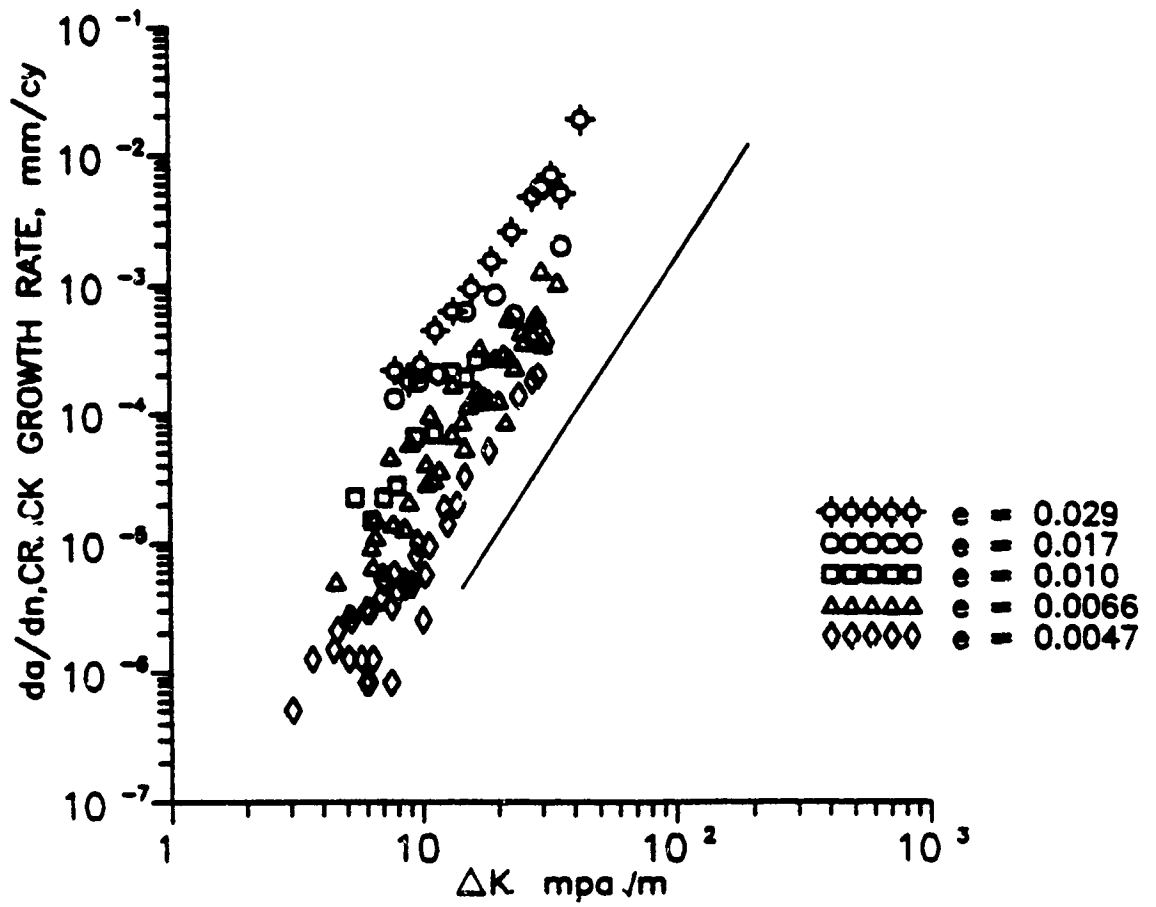


Fig. 5.14 Crack  $\mu$  growth rate as a function of  $\Delta K$  without correction for closure and plasticity.

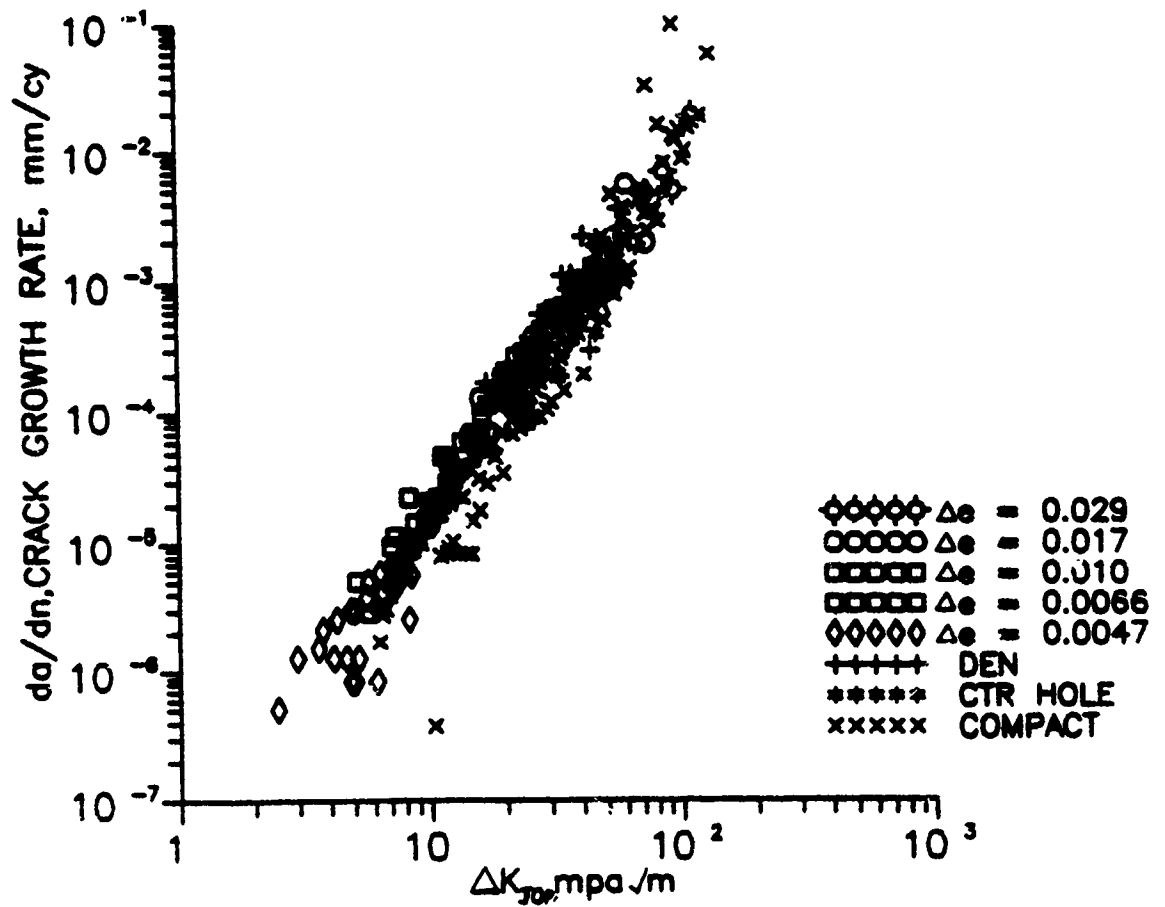


Fig. 5.15 Crack growth rate as a function of  $\Delta K_{Iop}$  with correction for closure and plasticity.

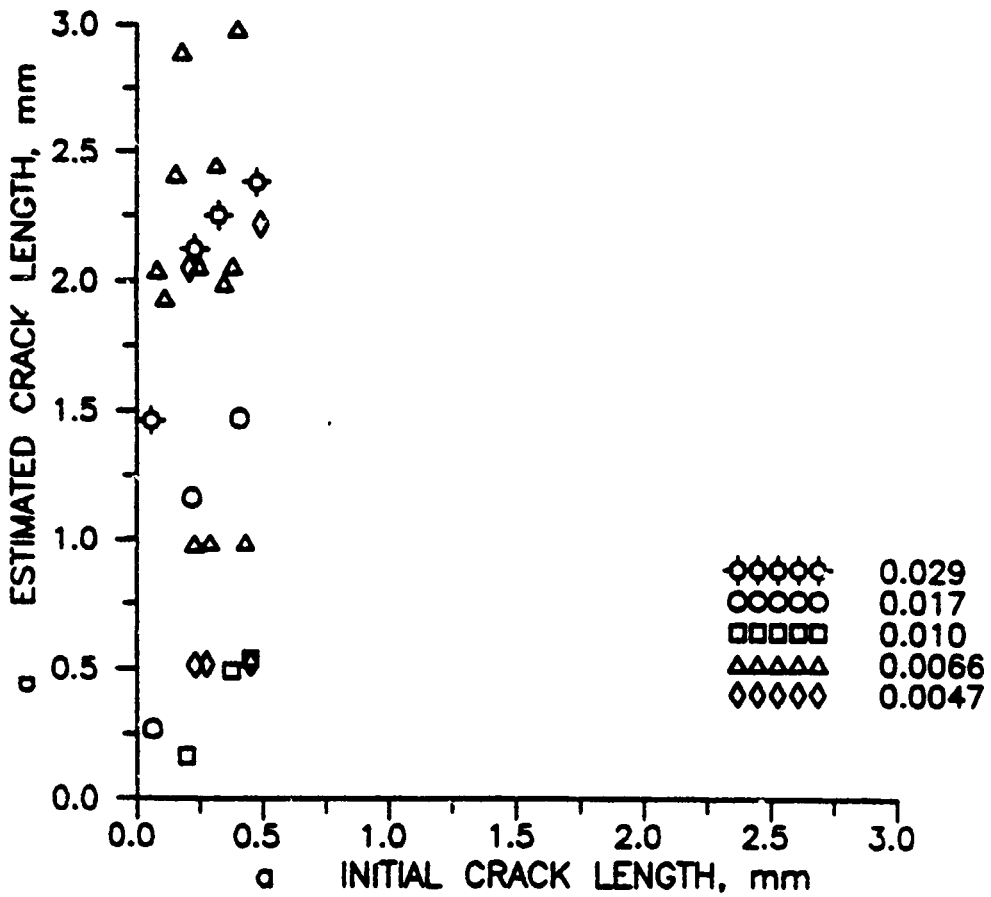


Fig. 5.16 a, versus a, for data of Fig. 5.14 using C and m

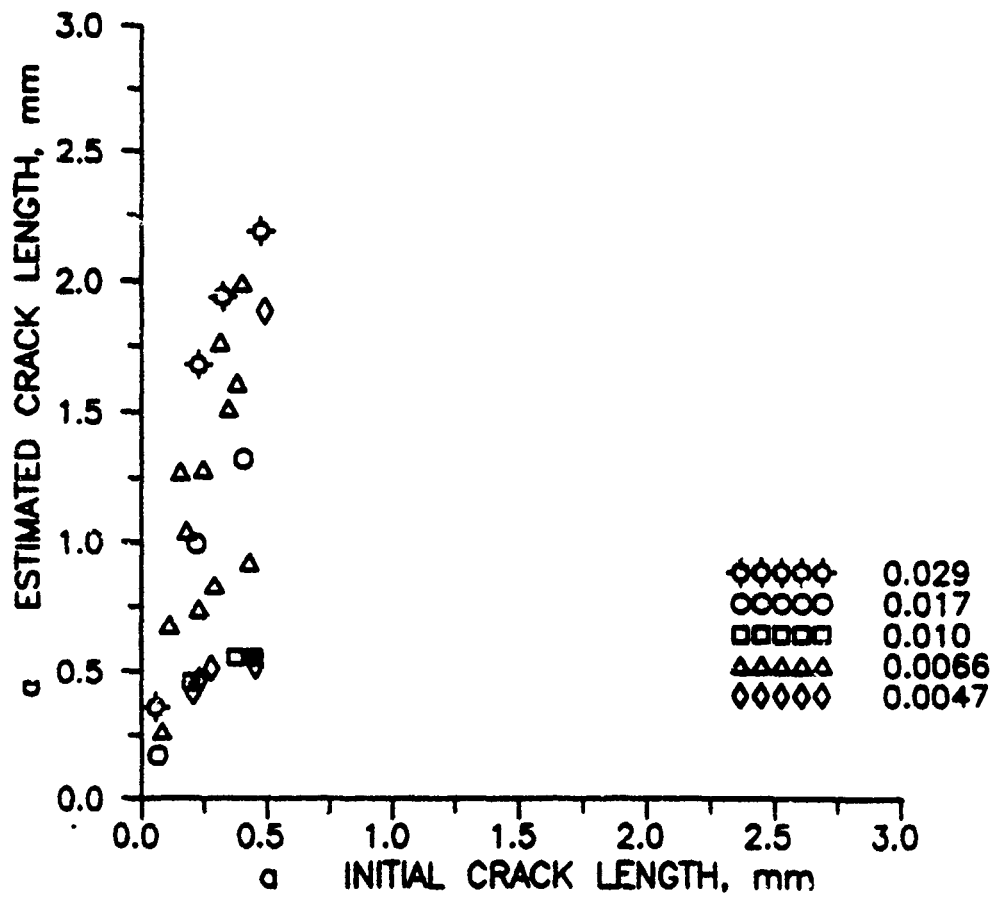


Fig. 5.17  $a_e$  versus  $a_i$  for data of Fig. 5.14 using  $\Delta J$ .

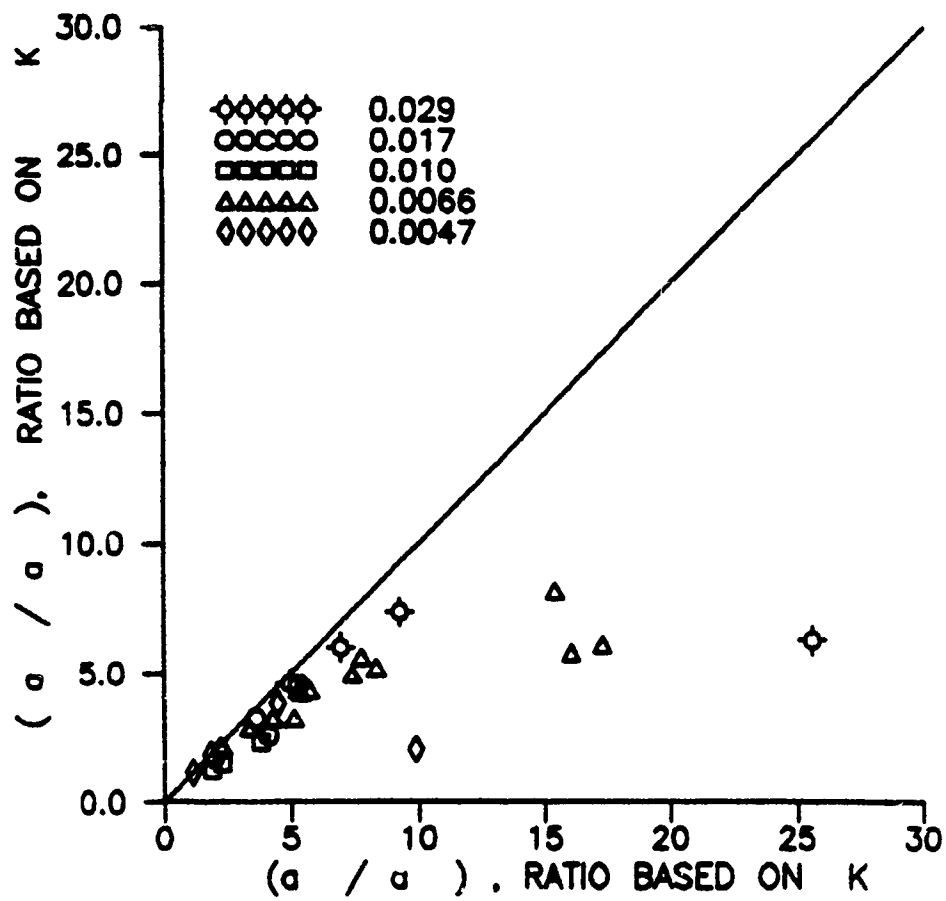


Fig. 5.16 Ratio of  $(\frac{a_e}{a_i})$  based on  $\Delta J$  versus  $(\frac{a_e}{a_i})$  based on  $\Delta K$

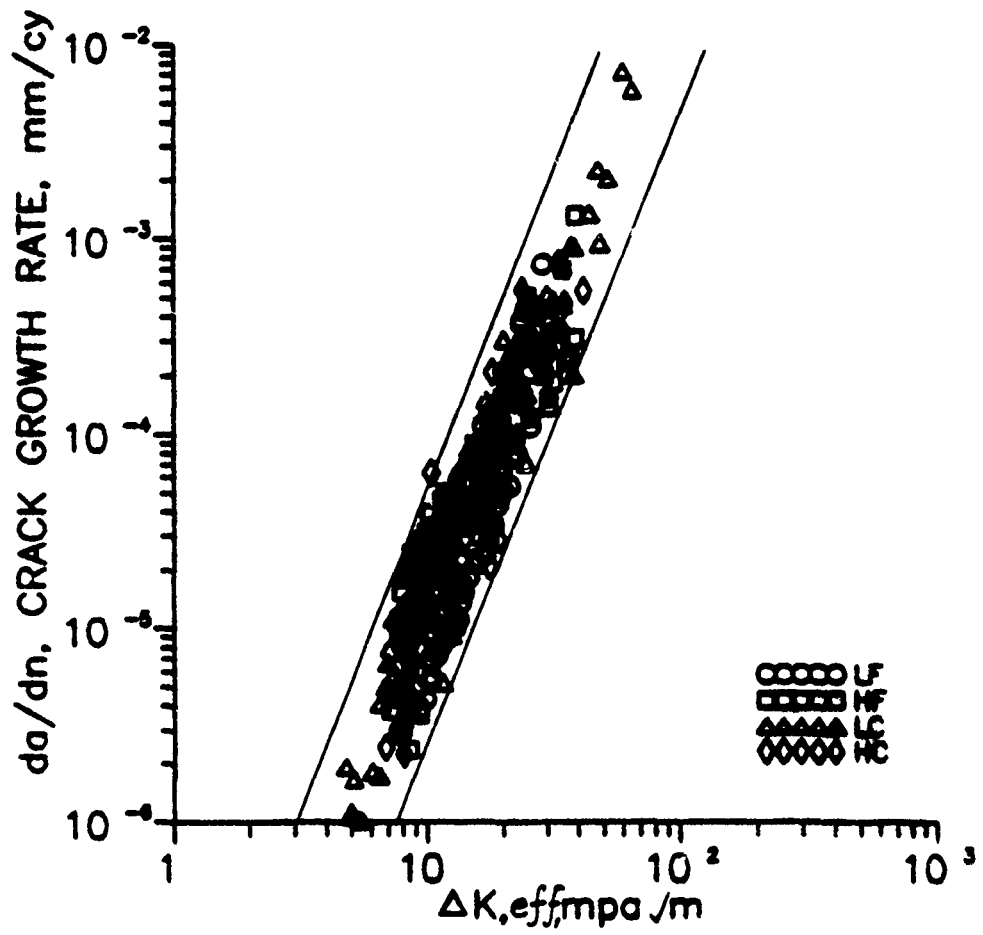


Fig. 5.19 Combined plot showing crack growth rates of long cracks for all conditions of steel as a function of  $\Delta K_{eff}$



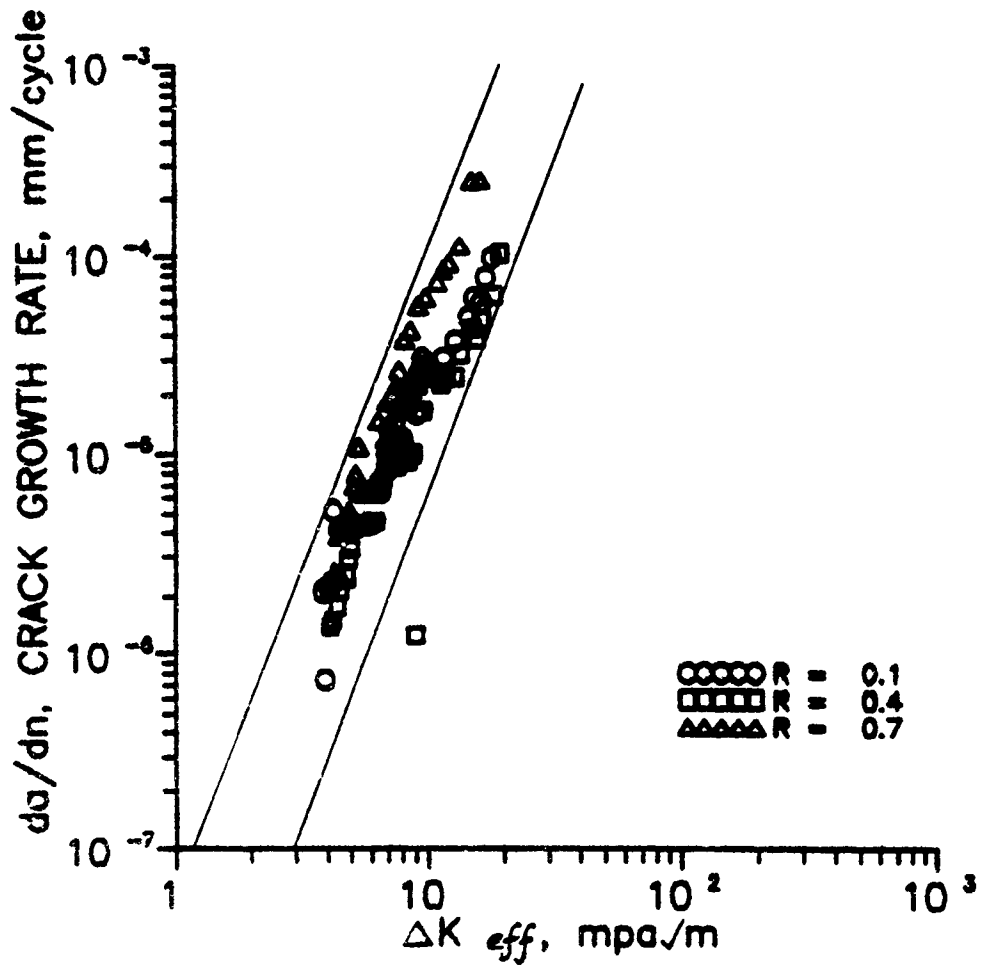


Fig. 5.21  $da/dn$  versus  $\Delta K_{eff}$  for short cracks at positive R ratios in HF condition of steel

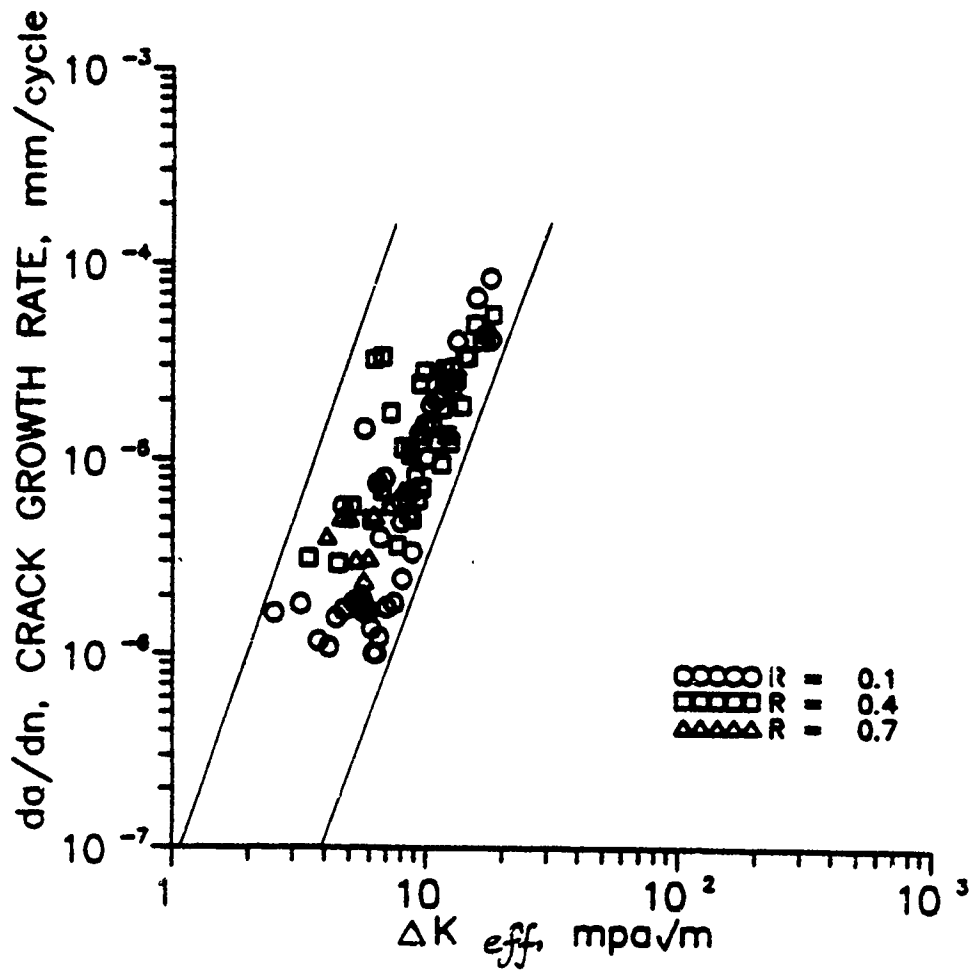


Fig. 5.22  $da/dn$  versus  $\Delta K_{eff}$  for short cracks at positive R ratios in LC condition of steel

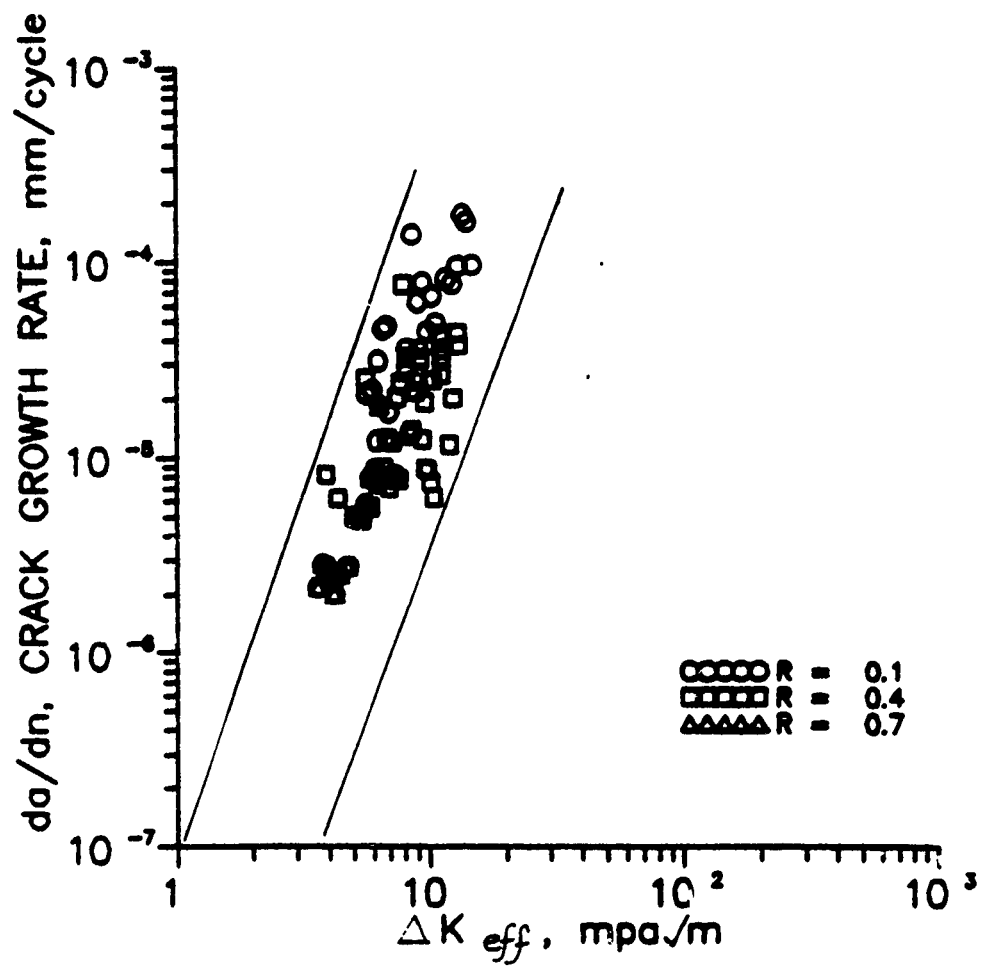


Fig. 5.23  $da/dn$  versus  $\Delta K_{eff}$  for short cracks at positive R ratios in HC condition of steel

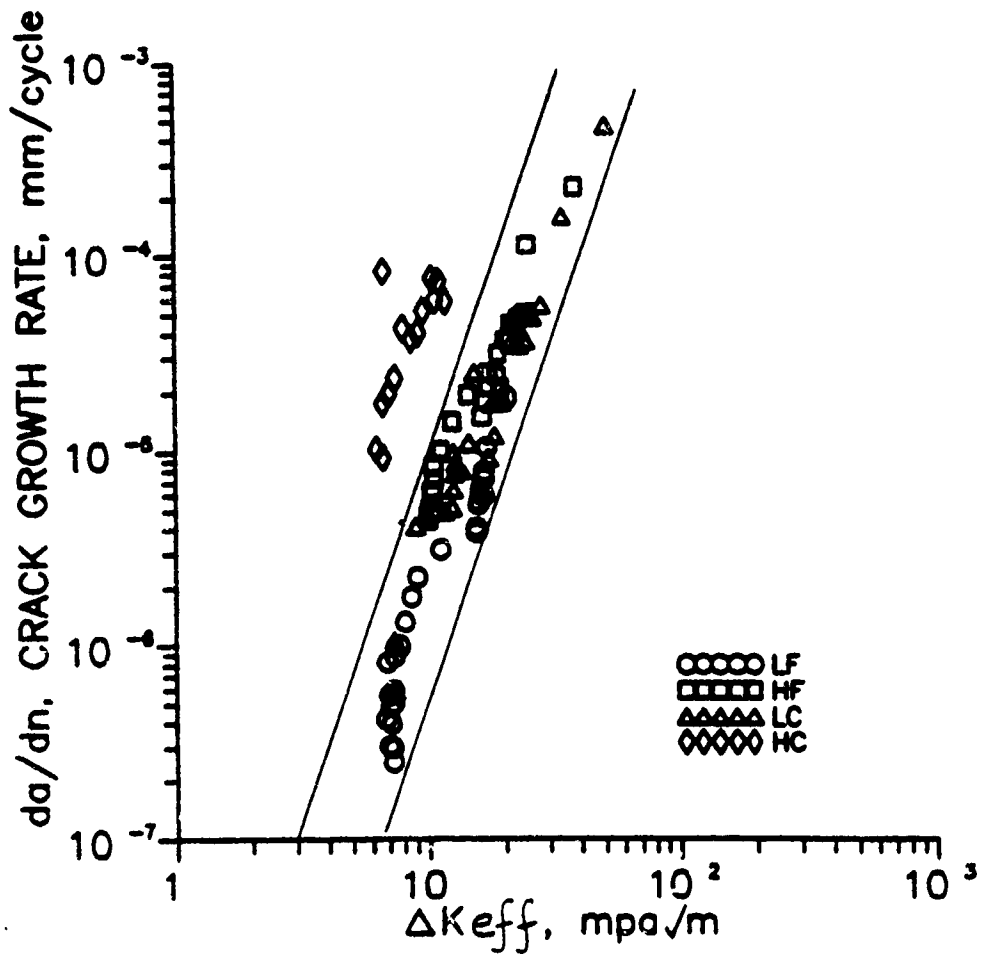


Fig. 5.24  $da/dn$  versus  $\Delta K_{eff}$  for all conditions of steel at  $R = -1$

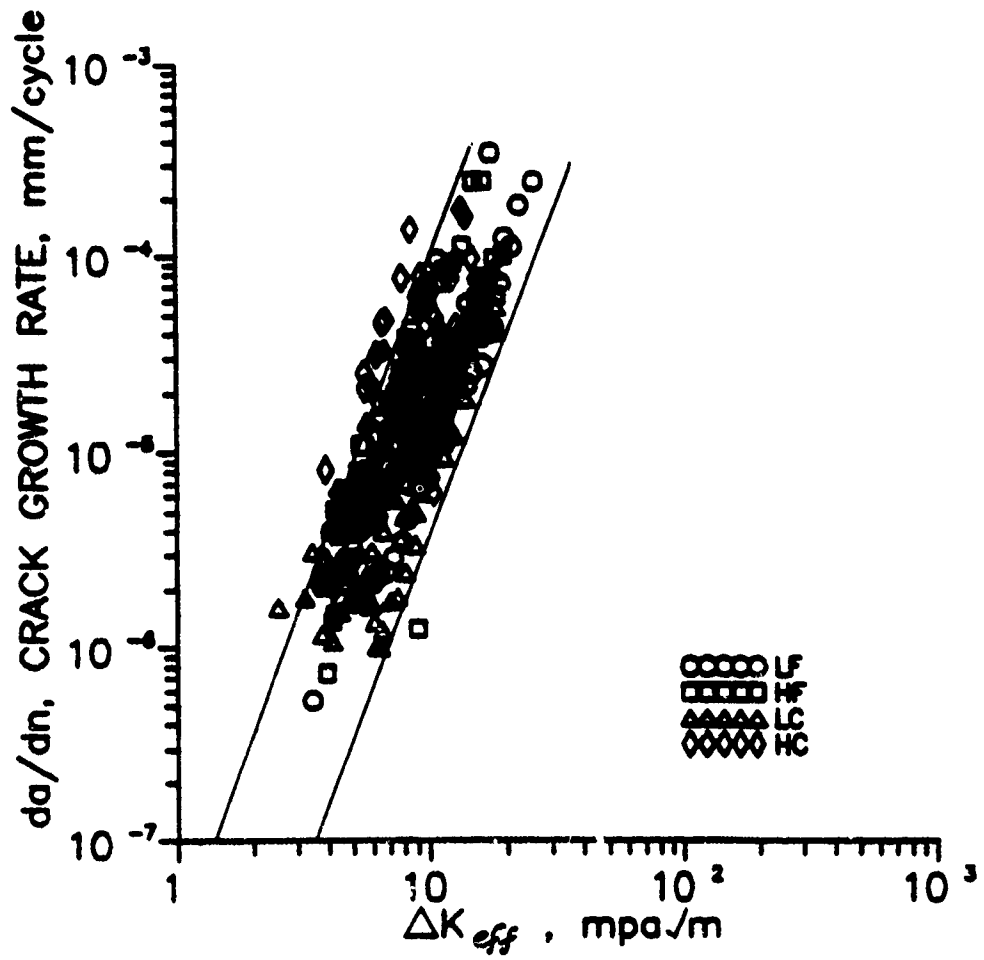


Fig. 5.25  $da/dn$  versus  $\Delta K_{eff}$  for short cracks at positive R ratios for all conditions of steel.

## **Section 6**

### **SUMMARY AND CONCLUSIONS**

This study was undertaken to investigate the growth behavior and closure response of physically short cracks in 2024-T351 aluminum and four different conditions of 4340 steel. The short cracks were of lengths 125-300 $\mu\text{m}$ . These cracks were introduced in specimens by machining material from sides of notches, from specimens containing long cracks produced by compressive loadings.

An extensive literature review was carried out on short fatigue crack growth. A pertinent literature review for this is presented in Section 1. This Section also discusses the objectives of the study and its significance. We observed here that most studies concentrate on "small" or microstructurally short cracks. Very few studies however, report physically short fatigue crack growth, especially short fatigue crack growth in steel. The variables affecting the growth behavior of short cracks were identified and discussed in detail in Section 1. The need to study the effects of stress level, stress

ratio and plasticity in this area was identified. The importance of researching the applicability of linear elastic crack growth data to durability analysis was also highlighted. The difficulties in monitoring short cracks were noted and the differences between various methods of detecting crack closing and opening were pointed out.

An experimental program was designed to study the effects of primary variables such as stress level, stress ratio, plasticity and prior austenitic grain sizes. Fatigue tests were carried out to gather long and short crack growth data. Test procedures and the methodology used to carry them out are discussed in detail in Section 2. It was essential to develop some techniques and procedures prior to fatigue crack growth tests. One of the important procedures developed was to monitor crack tip opening and closing levels, and displacement fields by the stereoimaging technique using a low power microscope. These procedures are discussed in detail in Section 3.

The experimental results for aluminum and four different conditions of steel are presented in Section 4. Linear long crack growth data is presented first, followed by short crack growth data. The stereoimaging technique was employed to determine crack opening and closing levels. The difference between the crack opening and closing level was observed to be less than 10 percent in all cases. Crack opening levels detected at three or four different crack lengths were utilized to get stress effective intensity values. Results of growth rate data are then presented as a function of effective stress intensity.

Effective stress intensity was able to correlate crack growth rate data of steel and aluminum in long cracks. However, in the case of short cracks, effective stress in-

tensity was able to consolidate any differences present at different stress levels in aluminum and fine grain conditions of steel. However, data from coarse grain conditions of steel showed a lot of scatter and could not be consolidated into a simple relation. The growth rate of cracks in coarse grain conditions of steel could not be analyzed in terms of microstructural unit sizes because of the scatter in the data points.

Short cracks growth at stress raisers were also studied. It was observed that the growth rate of short cracks under a negligible notch plasticity influence was similar to the growth rates of cracks in plain specimens without notches. Short cracks which grew under the influence of notch plasticity were open throughout their growth without showing any closure.

A general discussion based on the results obtained is presented in Section 5. The estimates of initial crack lengths were made based on linear elastic crack growth data. It was observed that the estimated crack length tended to be higher than the actual initial crack length in most cases. The estimates at  $R = -1$  were higher than at other  $R$  ratios. It was concluded that estimates based on linear elastic crack growth data would provide unconservative results. There was no discernible trend of the estimates with regard to stress levels. The estimates of initial crack length were made using parameters describing growth rate in terms of effective stress intensity. These estimates yielded results which were conservative. In other words, the estimates of initial crack length were observed to be closer to or smaller than the actual initial crack length.

Short crack growth under gross plastic deformation was then discussed. It was concluded that  $\Delta J$  is able to correlate the growth rate data under these conditions. Estimates of initial crack length were made based on  $\Delta K$  and  $\Delta J$ . It was found that the use of  $\Delta J$  in back extrapolating the initial crack lengths was a significant improvement over  $\Delta K$  approach.

In conclusion, the following inferences were drawn from this experimental study:

- The stereomaging technique developed and adapted for fatigue crack growth studies proved to be an efficient and a simple method of detecting crack closing and opening levels of cracks greater than 150  $\mu\text{m}$ . In addition, this technique also provided the displacement field near the crack tip and COD along the crack length.
- The growth rate of short cracks exhibited a transient behavior showing high crack growth rate in the beginning.
- There were no significant stress level effects for the through thickness cracks investigated in this study.
- Effective stress intensity is able to correlate the long crack growth data at all stress ratios. On the other hand, short crack growth data correlate poorly with each other
- Estimates of initial crack length based on parameters describing growth rate in terms of effective stress intensity provide conservative results.
- $\Delta J$  is able to correlate growth rates of cracks under gross plastic deformation.

## REFERENCES

- [1] Hudak, S.J., "Small Crack Behavior and Prediction of Fatigue Life," J. of Engng. Matls. and Technology, Transactions of ASME, Vol.103, 1981.
- [2] Schijve, J., "Differences Between the Growth of Small and Large Fatigue Cracks: The Relation to Threshold K Values," in Fatigue Thresholds, eds., Backland, J., Blom, A., and Beevers, C.J., EMAS Ltd., Warley, U.K., Vol.2, 1981.
- [3] Lankford, J., "The Effect of Environment on the Growth of Small Fatigue Cracks," Fatigue of Engng. Matls. Structures, Vol.5, 1982.
- [4] Kanninen, M.F., Popellar, C.H., and Broek, D., "A Critical Plastic Fracture to Nuclear Pressure Vessels and Piping," Nuclear Engng. and Design, Vol.67, 1981.
- [5] Taylor, D., and Knott, J.F., "Fatigue and Propagation Behavior of Short Cracks: The Effect of Microstructure," Fatigue of Engng. Matls. Structures, Vol.4, 1981. pp.147-155.
- [6] Smith, R.A., "On the Short Crack Limitations of Fracture Mechanics," Intl. Journal of Fracture, Vol 13, 1977, pp.717-720.
- [7] Leis, B.N., and Forte, T.P., "Fatigue Growth of Initially Physical Cracks in Notched Aluminum and Steel Plates," ASME, STP 743, 1981. pp. 100-124.
- [8] Dowling, N.E., "Crack Growth During Low Cycle Fatigue of Smooth Axial Specimens," Cyclic Stress Strain and Plastic Deformation Aspects of Fatigue Crack Growth, ASTM, STP 637, 1977.
- [9] Kitagawa, H., and Takahashi., Proceedings of the Second International Conference on Mechanical Behavior of Materials. (American Society for Metals), 1976. pp.627-631.
- [10] El Haddad, M.H., Smith, K.N., and Topper, T.H., "Fatigue Crack Propagation of Short Cracks," J. of Engng. Matls. and Technology, Transactions of ASME, Vol.101, No.1, 1979.
- [11] Ohuchida, H., Usami, S., and Nishioka, A., "Fatigue Limit of Steel with Cracks," Bulletin of JSME, Vol.18, No. 125, 1975.

- [12] Lankford, L., Davidson, D.L., and Chan, K.S., "The Influence of Crack Tip Plasticity in Growth of Small Cracks," Metallurgical Transactions A, Vol.15A, Aug.1984, pp.1579-1588.
- [13] El Haddad, M. H., Dowling, N.E., Topper, T.H., and Smith, K.N., "J Integral Applications for Short Fatigue Cracks at Notches," Intl. Jrnl. Fracture Mecchanics, 1980, Vol. 16, pp.15-30.
- [14] Hammouda, M.M., Smith, R.A., and Miller, K.J., "Elastic-Plastic Fracture Mechanics for Initiation and Propagation of Notch Fatigue Cracks," Fatigue of Engng. Matls. Structures, Vol.2, 1979, pp.139-154.
- [15] Newman, J.C., Jr. "A Nonlinear Fracture Mechanics Approach to the Growth of Short Cracks," Proceedings of AGARD Specialists Meeting, Toronto, Canada, 1982.
- [16] Ohji.K., "Cyclic Analysis of a Propagating Crack and its Correlation with Fatigue Crack Growth," Engineering Fracture Mechanics, Vol. 7, pp. 457-464.
- [17] Elber, W., "Fatigue Crack Closure under Cyclic Tension," Engng. Fracture Mechanics, Vol.2, No.1, 1970.
- [18] Ritchie, R.O., and Yu, W., "Short Cracks Effects in Fatigue: A Consequence of Crack Tip Shielding," in Small Fatigue Cracks, Ritchie, R.O., and Lankford, J., eds. The Metallurgical Society - AIME, Warrendale, PA.
- [19] Irwin, G.R., and Wells, A.A., "A Continuum Mechanics View of Crack Propagation," Metallurgical Reviews, Vol.10, No. 38, 1965.
- [20] Tanaka, K., "Short Crack Fracture Mechanics in Fatigue Conditions," in Current Research in Fatigue Cracks, eds., Tanaka, T., Jono, M., and Komai, K., The Society of Materials Science, Japan, 1985, pp.79-100.
- [21] Nakai, Y., Tanaka, K., and Nakanishi, T., "The Effects of Stress Ratio and Grain Size on Near-Threshold Fatigue Crack Propagation in Low Carbon Steel," Engng. Fracture Mechanics, Vol. 3-4, No.15, 1981. pp.291-302.
- [22] McEvily, A.J., and Minakawa, K., "Crack Closure and Conditions for Fatigue Crack Propagation," in Fatigue Crack Growth Thresholds, Davidson, D., and Suresh, S., eds., The Metallurgical Society - AIME, Warrendale, PA, 1984, pp. 517-530
- [23] Katcher, M., and Kaplan, M., in Fracture Toughness and Slow Stable Cracking ASTM, STP, 559, 1974.
- [24] Bell, P.D., and Creager, M., Crack Growth Analysis for Arbitrary Spectrum Loading, AFDEL- TR 74-129, 1974.
- [25] Satish Chand., and Garg, S.B.L., "Crack Closure Studies under Constant Amplitude Loading," Engng. Fracture Mechanics, Vol.18, No.2, 1983. .sk [26] Schijve, J., "Observations on the Prediction of Fatigue Crack Growth Propagation

under Variable-Amplitude Loading," in Fatigue Crack Growth under Spectrum Loads, ASTM, STP, 595, 1976. pp.3-23.

[27] Kikukawa, M., Jono, M., and Tanaka, K., "Fatigue Crack Closure Behavior at Low Stress Intensity Level," Proceedings of the ICM2, Boston, pp.254-277.

[28] Stewart, A.T., "The Influence of Environment and Stress Ratio on Fatigue Crack Growth at Near Threshold Stress Intensities in Low Alloy Steels," Engng. Fracture Mechanics, Vol.13, 1980. pp.463-478.

[29] McClung, R.C. and Sehitoglu, H., "Closure Behavior of Short Cracks Under High Strain Fatigue Histories," Intl. Symposium on Fatigue Crack Closure, Charleston, SC, May, 1986.

[30] Gangloff, R.P., "Crack size Effects on the Chemical Driving Force for Aqueous Corrosion Fatigue," Metallurgical Transactions, 16A, 1985.

[31] Suresh, S., and Ritchie, R.O., "Near Threshold Fatigue Crack Propagation: A Perspective on the Role of Crack Closure," in Fatigue Crack Growth Threshold Concepts, Davidson, D., and Suresh, S., eds., Metallurgical Society of AIME, pp. 227-262.

[32] Cottis, R.A., "The Corrosion Fatigue of Steels in Saline Environments," in Small Fatigue Cracks, Ritchie, R.O., and Lankford, J., eds. The Metallurgical Society - AIME, Warrendale, PA.

[33] Gerdes, C., Gysler, A., and Lutjering, G., "Propagation of Small Surface Cracks in Ti-Alloys, in Fatigue Crack Growth Threshold Concepts, Davidson, D., and Suresh, S., eds., Metallurgical Society of AIME, pp. 465-478.

[34] Zegloul, A., and Pettit, J., "Environmental Sensitivity of Small Crack Growth in 7075 Aluminum Alloy," Fatigue and Fracture of Engineering Materials and Structures, Vol.8, pp.341-348.

[35] Suresh, S., and Vasudevan, A.K., "Application of Fatigue Threshold Concepts to Variable Amplitude Crack Propagation," in Fatigue Crack Growth Threshold Concepts, Davidson, D., and Suresh, S., eds., Metallurgical Society of AIME, pp. 361-378.

[36] Suresh, S., "Micromechanisms of Fatigue Crack Growth Retardation Following Overloads," Engineering Fracture Mechanics, No. 18, 1983, pp.577-593.

[37] Schijve, J., "Prediction Methods for Fatigue Crack Growth in Aircraft Material," Fracture Mechanics: Twelfth Conference, ASTM, STP, 700, 1980, pp.3-34.

[38] Suresh, S., Zamiski, G.F., and Ritchie, R.O., "Oxide-Induced Crack Closure: An Explanation for Near-Threshold Corrosion Fatigue Crack Growth Behavior," Metallurgical Transactions, Vol.12A, 1981, pp.1435-1443.

- [39] Allison, J.E., and Williams, J.C., "The Role of Deformation Character on Fatigue Crack Growth in Titanium Alloys," Strength of Metals and Alloys, ICSMA, 6, Gifkins, R.C., ed., 1983, pp.1219-1224.
- [40] Suresh, S., and Ritchie, R.O., "A Geometric Model for Fatigue Crack Closure Induced by Fracture Surface Roughness," Metallurgical Transactions, Vol.13A, 1982, pp.1627-1631.
- [41] Carlson, R.L., and Beevers, C.J., "A Multiple Asperity Fatigue Crack Closure Model," Engg. Fracture Mechanics, Vol.20, 1984, pp.687-690.
- [42] Brown, R.D., and Weertman, J., "Mean Stress Effects on Crack Propagation Rate and Crack Closure in 7050-T76 Aluminum Alloy," Engng. Fracture Mechanics, Vol.10, 1978, pp.757-771.
- [43] Kikukawa, M., Jono, M., and Tanaka, K., "Fatigue Crack Closure Behavior at Low Stress Intensity Level," Proceedings of the ICM2, Boston, pp.254-277.
- [44] Elber, W., "Fatigue Crack Closure under Cyclic Tension," Engng. Fracture Mechanics, Vol.2, 1970, pp.37-45.
- [45] Buck, O., Ho, C.L., and Marcus, H.L., "Plasticity Effects in Crack Propagation," Engng. Fracture Mechanics, Vol.5, 1973, pp.23-34.
- [46] Unangst, K.D., Shih, T.T., and Wei, R.P., "Crack Closure in 2219-T851 Aluminum Alloy," Engng. Fracture Mechanics, Vol.9, 1977, pp.725-734.
- [47] Frandsen, J.D., Inman, R.V., and Buck, O., "A Comparison of Acoustic and Strain Gauge Techniques for Crack Closure," Int. J. Fracture, Vol.11, 1975.
- [48] Gan, D., and Weertman, J., "Crack Closure and Crack Propagation Rates in 7050 Aluminum," Engng. Fracture Mechanics, Vol.15, 1981, pp.87-106.
- [49] Davidson, D.L., and Nagy, A., "A Low Frequency Cyclic Loading Stage for the SEM," J. of Physics, E, Vol.11, 1978.
- [50] Sharpe, W.N., and Grandt, A.F., in Mechanics of Crack Growth, ASTM, STP, 590, 1976, pp.302-320.
- [51] Cheng, Y.F., and Brunner, H., "Photoelastic Research in Progress on Fatigue Crack Closure," Int. J. Fracture Mechanics, Vol.6, 1970, pp.431-434.
- [52] Bowles, C.Q., and Schijve, J., in Fatigue Mechanisms; Quantitative Measurements of Physical Damage, ASTM, STP, 811, 1983, pp.400-426.
- [53] Fleck, N.A., and Smith, R.A., "Crack Closure - Is It Just A Surface Phenomenon?," Int. J. Fatigue, Vol.4, 1982, pp.157-160.
- [54] Ray, S., Grandt, A.F., Jr. and Andrew, S., paper presented in at the ASTM Symposium on Fundamental Questions and Critical Experiments in Fatigue, Dallas, Texas, 1984.

[55] Kendall, J.M., James, M.N., and Knott, J.F., "The Behavior of Physically Short Fatigue Cracks in Steels," in The Behavior of Short Fatigue Cracks, Miller, K.J., and de los Rios, E.R., eds., EGF Publication 1, 1986, pp.241-258.

[56] Brown, C.W., and King, J.E., "The Relevance of Microstructural Influences in the Short Crack Regime to Overall Fatigue Resistance," in Small Fatigue Cracks, Ritchie, R.O., and Lankford, J., eds. The Metallurgical Society - AIME, Warrendale, PA.

[57] Newman, P., and Beevers, C.J., "Growth of Short Fatigue Cracks in High Strength Ni-Base Superalloys," in Small Fatigue Cracks, Ritchie, R.O., and Lankford, J., eds. The Metallurgical Society - AIME, Warrendale, PA.

[58] Lankford, J., "The Effect of Environment on the Growth of Small Fatigue Cracks," Fatigue Engg. Matl. Structures, Vol.6, 1983, pp.15-31.

[59] Tanaka, K., and Nakai, Y., "Mechanics of Growth Threshold of Small Fatigue Cracks," in Fatigue Crack Growth Threshold Concepts, Davidson, D., and Suresh, S., eds., Metallurgical Society of AIME, pp. 497-516.

[60] Hicks, M.A., and Brown, C.W., "Short Fatigue Crack Growth in Planar Slip Materials," International Journal of Solids, Vol.6, 1982, pp.167-169.

[61] Brown, C.W., and Hicks, M.A., "A Study of Short Fatigue Crack Growth Behavior in Titanium Alloy IMI 685," Fatigue of Engineering Materials and Structures, Vol.6, 1983, pp.67-76.

[62] Bolingbroke, R.K., and King, J.E., "The Growth of Short Fatigue Cracks in Titanium alloys IMI550 and IMI318," in Small Fatigue Cracks, Ritchie, R.O., and Lankford, J., eds. The Metallurgical Society - AIME, Warrendale, PA. 1986.

[63] Daubler, M.A., and Thompson, A.W., "Microstructural Effects on Short Fatigue Cracks in Eutectoid Steels," in Small Fatigue Cracks, Ritchie, R.O., and Lankford, J., eds. The Metallurgical Society - AIME, Warrendale, PA. 1985.

[64] Suresh, S., "Crack Deflection: Implications for the Growth of Long and Short Fatigue Cracks," Metallurgical Transactions, 14A, 1983, pp.2375-2385.

[65] Trantina, G.G., and deLorenzi, H.G., "Elastic Plastic Analysis Fracture Mechanics Analysis of Small Cracks," Proceedings of the Army Symposium on Solid Mechanics. Army Materials and Mechanics Center Research Report, AMMRC-MS-82-4, 1982, pp.203-214.

[66] Clement, P., Angeli, J.P., and Pineau, A., "Short Crack Behavior in Nodular Cast Iron," Fatigue of Engg. Matls and Structures, Vol.7, 1984, pp.251-265.

[67] Grandt, A.F., Jr Perez, R., and Trisch, D.E., "Cyclic Growth and Coalescence of Multiple Fatigue Cracks," in Advances in Fracture Research, ICF6, Vol.3, Valluri, S.R., Taplin, D.M.R., Rama Rao, P., Knott, J.F., and Dubey, R., eds., Pergamon Press, New York, 1984, pp.1571-1578.

[68] Ritchie, R.O., Yu, W., Blom, A.F., and Holm, D.K., "An Analysis of Crack Tip Shielding in Aluminum Alloy 2124: A Comparison of Large, Small, Through-Thickness and Surface Fatigue Cracks," Fatigue Frac. of Engg. Matls. and Structures, Vol.10, No. 5, 1987 pp. 343-362.

[69] Allen, R.J., and Sinclair, J.C., "The Behavior of Short Cracks," Fatigue of Engg. Matl and Structures, Vol.5, pp.343-351.

[70] Taylor, D., "Fatigue of Short Cracks: The Limitations of Fracture Mechanics," in The Behavior of The Behavior of Short Fatigue Cracks, Miller, K.J., and de los Ríos, E.R., eds., EGF Publication 1, 1986, pp.241-258.

[71] Wanhill, R.J.H., "Short Cracks in Aerospace Structures," in The Behavior of The Behavior of Short Fatigue Cracks, Miller, K.J., and de los Ríos, E.R., eds., EGF Publication 1, 1986, pp.241-258.

[72] Dowling, N.E., "Geometry Effects and the J-Integral Approach to Elastic-Plastic Fatigue Crack Growth," in Cracks and Fracture, ASTM, STP. 601, American Society for Testing and Materials, 1976, pp.19-32.

[73] Davidson, D.L., and Lankford, J., "The Role of Metallurgical Factors in Controlling the Growth of Small Fatigue Cracks," in Small Fatigue Cracks, Ritchie, R.O., and Lankford, J., eds. The Metallurgical Society - AIME, Warrendale, PA. 1986.

[74] Salem, J.A., "A Microstructural and Grain Size Characterization of the 4340 steel to be used in Small Crack Program," NASA Lewis Report, 1984.

[75] Khan, K.H., and Wood, W.E., "The Effect of Step Quenching on the Microstructure and Fracture Toughness of AISI 4340 Steel," Metallurgical Transactions, 9A, 1978, pp.899-907.

[76] Bannerji, S.K., McMahon, C.J., Jr. and Feng, H.C., "Intergranular Fracture in 4340-Type Steels: Effects of Impurities and Hydrogen," Metallurgical Transactions, Vol.9A, 1978. pp.237-247.

[77] Ritchie, R.O., and Horn, R.M., "Further Considerations on the Inconsistency in Toughness Evaluation of AISI 4340 Steel Austenitized at Increasing Temperatures," Metallurgical Transactions A, Vol. 9A, 1978. pp.331-341.

[78] Dauebler, M.A., and Thompson, A.W., "Microstructural Effects on Short Fatigue Cracks in Eutectoid Steels," in Small Fatigue Cracks, Ritchie, R.O., and Lankford, J., eds. The Metallurgical Society - AIME, Warrendale, PA. 1986.

[80] Suresh, S., Christman, T., and Bull, C., "Crack Initiation and Growth Under Far Field Cyclic Compression: Theory, Experiments and Applications," in Small Fatigue Cracks, Ritchie, R.O., and Lankford, J., eds. The Metallurgical Society - AIME, Warrendale, PA. 1986.

[81] Pippan, R., "The Growth of Short Cracks Under Cyclic Compression," Fatigue and Fracture of Engg. Matls and Structures, Vol. 9 No. 5, 1987, pp.319-328.

- [82] Holm, D.K., Blom, A.F., and Suresh, S., "Growth of Cracks Under Far Field Cyclic Compressive Loads: Numerical and Experimental Results," Engg. Fracture Mechanics, 23, 1986, pp.1097-1106.
- [83] Davidson, D.L., "The Observation and Measurement of Displacements and Strains by Stereoimaging," Scanning Electron Microscopy, 1979, II, SEM Inc, AMF O'Haire, Illinois, pp.79-86.
- [84] Davidson, D.L., Williams, D.R., and Buckingham, J.E., "Crack Tip Stresses as Computed from Strains Determined by Stereoimaging," Experimental Mechanics, June 1983, pp.242-248.
- [85] Pettigrew, J.D., "The Neurophysiology of Binocular Vision," Scientific American, 227 (2), 1972, pp.84-95.
- [86] Moffitt, F.H., and Mikhail, E.M., "Photogrammetry," 3rd edition, Harper Row, New York, 1980.
- [87] Slama, C.C., Theurer, C.S., and Henricksen, S.W., eds., "Manual of Photogrammetry," American Society of Photogrammetry, 1980.
- [88] Wong, K.W., and Ho, W.H., "Close Range Mapping with a Solid State Camera," Photogrammetric Engineering and Remote Sensing, Vol.52, 1, January, 1986, pp.67-74.
- [89] Ripley, B.D., "Spatial Statistics," John Wiley, 1980.
- [90] Manning S.D., and Yang, J.N., "Advanced Durability Analysis Vol.1, Analytical Methods," AFWAL-TR-86-3017, 1987.
- [91] Dowling, N.E., and Begley, J.A., "Fatigue Crack Growth During Gross Plasticity and the J-Integral," Mechanics of Crack Growth, ASTM, STP, 590, American Society for Testing and Materials, pp.82-103.
- [92] Dowling, N.E., "J-Integral Estimates for Cracks in Infinite Bodies," Engineering Fracture Mechanics, Vol. 26, No.3, 1987. pp.333-348.
- [93] Chan, K.S., "Local Crack Tip Field Parameters for Large and Small Cracks: Theory and Experiment," in Small Fatigue Cracks, Ritchie, R.O., and Lankford, J., eds. The Metallurgical Society - AIME, Warrendale, PA. 1986, pp.407-426
- [94] Dowling, N.E., and Iyyer, N.S., "Fatigue Crack Growth and Closure at High Cyclic Strains," Materials Science and Engineering, 96, 1987, pp.99-107.
- [95] Imhof, E.J., Jr. and Barsom, J.M., "Fatigue and Corrossion Fatigue Crack Growth of 4340 Steel at Various Yield Strengths," Progress in Flaw Growth and Fracture Testing, ASTM, STP, 536, 1973, pp.182-205.